University of Alberta

Sodium MRI Optimization for the Human Head with Application to Acute Stroke

by

Robert Stobbe

A thesis submitted to the Faculty of Graduate Studies and Research
in partial fulfillment of the requirements for the degree of

Doctor of Philosophy

Medical Sciences – Biomedical Engineering

Department of Electrical and Computer Engineering

Spring 2010
Edmonton, Alberta

Examining Committee

Dr. Christian Beaulieu, Biomedical Engineering

Dr. Zoltan Koles, Electrical and Computer Engineering

Dr. Alan Wilman, Biomedical Engineering

Dr. Peter Allen, Biomedical Engineering

Dr. Richard Thompson, Biomedical Engineering

Dr. Roderick Wasylishen, Chemistry

Dr. Robert Bartha, Diagnostic Radiology and Nuclear Medicine, University of Western Ontario

to my family

to Megan
my perfect companion in this journey called life

to David and Matthew
I hope you always know how deeply you are loved

to Bob and Lynda
I'm proud to be your son

to Richard
you continue to inspire me

to Paul and Sally, Margaret and Jack
for your love and encouragement

to Jess, Alison, Seanna, John, Shannon, and Liam
for the laughter and support

to Abraham and Katherine, Jacob and Mary
for the beautiful legacy you have left to follow

Abstract

25 years after the first sodium images of the human brain were created, sodium MRI remains on the periphery of MR research, despite intimate sodium involvement in cellular metabolism and implicated abnormal concentrations in numerous disorders. The difficulties of sodium MRI include not only tissue concentration, ~1750x less than proton, but also rapid biexponential signal decay. The purpose of this work was to optimize human brain sodium MRI and facilitate a study of sodium increase following onset of acute human stroke, with potential 'timing' application for those patients who present with unknown time-of-onset, as effective treatment is currently bound by a 4.5 hour time-window.

Optimization begins with radial 'center-out' k-space acquisition, which minimizes echo time (TE) and signal loss, and in particular concerns the twisted projection imaging (TPI) technique, which has not found wide use. This thesis first considers a new application of TPI, i.e. k-space filtering by sampling density design to minimize detrimental ringing artifact associated with cerebral spinal fluid. Image noise correlation is addressed next, and a method for measuring volumes of statistical noise independence presented, as this correlation together with signal-to-noise ratio (SNR) defines the confidence of signal-averaging measurements. Radial acquisition is then considered with respect to a new imaging metric, i.e. the minimum object volume that can be precisely (with respect to noise) and accurately (with respect to image intensity modulation with object volume) quantified. It is suggested that TPI is a highly beneficial radial acquisition technique when implemented with 'long' readout duration (countering common thought), reduced SNR (i.e. small voxel volumes), and in particular small TPI parameter *p*. Sequence optimization for bulk-tissue sodium analysis demonstrates a large SNR/voxel-volume advantage for TPI implementation in a steady-state approach, even though excitation pulse length and TE must be increased to mitigate power deposition. Finally, an inversion-recovery based fluid-nulling method that facilitates sodium environment separation based on rapid relaxation during soft inversion pulses is presented, with possible application for intracellular weighted imaging.

On 'high quality' sodium images a clear trend of lesion intensity increase with time-after-onset is demonstrated for the first time in acute stroke patients, as expected from animal models.

Acknowledgements

I am very fortunate to have had such an excellent supervisor, Dr. Christian Beaulieu, a brilliant investigator and communicator. Any success I have experienced is directly linked to your extensive knowledge, patience, diligence, and encouragement. Thank you so much.

I am also very fortunate to have had such a great partner for our stroke study, Dr. Shazam Hussain, neurologist extraordinaire and friend. I hope we meet up again. Deep thanks also goes out to: Dr. Yusuf Bhagat, for developing the proton imaging methods used in the stroke study and for his indispensability with regard to working with the patients; Dr. Kenneth Butcher, for his time recruiting and monitoring patients and help fine-tuning the paper; Dr. Derek Emery, for his patient concern and approval; and all the stroke fellows who helped recruit and monitor patients (Dr. Dulka Manawadu, Dr. Nasir Rizvi, Dr. Perkash Maheshwari, and Dr. James Scozzafava). Finally, a sincere thank you is given to the stroke patients who very graciously gave of themselves to facilitate this study.

A special thank you is given to the members of my committee who taught me about NMR, MRI and image processing: Dr. Peter Allen, Dr. Alan Wilman, and Dr. Zoltan Koles. You stand out among the best teachers I have had throughout my university experience. What opportunity, to learn from giants in these fields.

A special thank you is given as well to the remaining members of my examining committee for their time and insight: Dr. Richard Thompson, Dr. Roderick Wasylishen, and Dr. Robert Bartha. In particular I'd like to thank Dr. Richard Thompson who answered many questions throughout my degree. Although not a member of my committee, I'd also like to thank Dr. Richard Snyder for his excellent teaching of biomedical instrumentation and his role as graduate coordinator.

Also well deserving of thanks are Jess Latimer, who built the user interface of the Triple-S simulator and developed RF coil simulation methods in Ansoft's High-Frequency Structure Simulator (HFSS), Nicholas Kalogirou, who constructed the RF head coil used in this thesis, and Woo-Ree Ko, who developed RF sodium coils for our 3T system. It was an honour to work with you.

I'd like to thank Karim Damji for his expert hardware insight and debugging / resolving of hardware problems. I'm also indebted to others that keep (have kept) the 4.7T system and the NMR centre functioning: Dan Georgio, Dr. Chang-Ho Choi, Dr. Chris Hanstock, Peter Seres, Beau Sepach, Michael Kwan, and Carol Hartle.

Special thanks is given to our department chair Dr. Robert Burrell for his encouragement, and to Maisie Goh for the many times she has helped me throughout my degree.

I'd like to thank Adrian Tsang and Ander Watts, my compatriots in this field of sodium imaging. I'm very grateful for the opportunity to work together with such gifted people – go team sodium!

To the many others I have worked alongside and who have helped me throughout my degree, I am very grateful for your time, knowledge, and expertise. More importantly, thank you for your friendship. This list includes: Alison Campbell, (soon to be Dr.) Amir Eissa, Angela Leung, Anthony Tessier, Dr. Atiyah Yahya, (soon to be Dr.) Catherine

Lebel, Corey Baron, Chilo Bonilla, Dan Hallihan, David McAllindon, Dr. David Vuletich, Dr. Donald Gross, Dr. Dongming Zhou, Farnaz Khosrow-Khavar, Dr. Gaolang Gong, Dr. Hyeonjin Kim, Dr. Jacob Ellegood, Jason Mendes, Lindsay Snook, Dr. Nikolai Malykhin, Dr. Jeff Snyder, June Baron, Dr. Keith Wachowicz, Kelvin Chow, Dr. Louise Concha, Dr. Myrlene Gee, (soon to be Dr.) Marc Lebel, Min Liu, Osama Al-Kwifi, Sarah Treit, Sasha Holden, Stijn Michielse, and Xushan Huang.

Many people, and in particular those in the list above, have generously donated their time laying in the magnet. Nothing would be accomplished without volunteers – thank you.

Thank you to the funding agencies that supported me and facilitated our work: NSERC, iCORE, the Province of Alberta, the University of Alberta, the Whitaker Foundation, and the Heart and Stroke Foundation.

I (we – my family) have been so fortunate to have been surrounded by such great community during our time here in Edmonton. We miss you Rob and Heather. I couldn't have asked for a better friend with which to share this Edmonton experience. To the Best Little Group Ever (Aaron and Shelly, Ryan and Pam, and Scott and Niki), you are our family. I don't know how I can state my thankfulness for you more strongly. To James and Mary, Jeff and Kandace, Ben and Heather, thank you for sharing the joys (and struggles) of parenting with us. To Darren and Carlene, Dave and Angela, Dave and Gayle, Dave and Janette, Nattie and Federico, and Raymond and Jacquie, thank you for your friendship. Many of our close friends have already left Edmonton for 'greener pastures' (literally) and we miss you – Ethan and Cadie, Todd and Corrine, Jason and Heidi, Jeff and Jodi. To Central, a church is nothing apart from the people, thank you for becoming - together with us.

Especially thank you Mom and Dad for modelling love: love for God and love for neighbour (and love for me!) – I hope I will always grow in this way. You are my champions and I cherish your continued prayer for me. Rich, thank you for the intimacy of brotherhood. My inherited family, thank you again for your encouragement and support, and for welcoming me into the fold!

Megan, I love you so much, thank you for loving me. I'm woefully incapable of thanking you for everything you are to me – you are as necessary as my own heart. To my boys, every day you make my spirit soar – what an incredible gift! My love for you will never be exhausted.

and to You, my great Father
in whom I live and move and breathe and have my being
I fall down – You pick me up
I fail – You forgive
Above all, Thank you

Table of Contents

1. INTRODUCTION 1

1.1. Thesis Introduction 1
1.2. Acute Stroke 11
1.3. Basic k-Space Acquisition Engineering 16
1.3.1. Creating an MR Image 16
1.3.2. The Discrete Fourier Transform and the MR Image 18
1.3.3. Image Intensity Dependence on Acquisition Parameters and Zero-Filling 25
1.3.4. Image Noise 27
1.3.5. k-Space Acquisition and SNR 29
1.3.6. The Modulation Transfer Function (H(k)) 30
1.3.7. Sampling Efficiency 31
1.4. 3D Twisted Projection k-Space Acquisition 32
1.5. Quantum Mechanics of the Spin 3/2 Sodium Nucleus 37
1.5.1. The Sodium Spin Ensemble in a Large Magnetic Field 37
1.5.2. The Density Matrix / Operator 43
1.5.3. The Quadrupole Hamiltonian 48
1.5.4. The Static Quadrupole Hamiltonian 52
1.5.5. Irreducible Spherical Tensors 55
1.5.6. Density Operator Evolution Under Static Hamiltonians 62
1.5.7. The Fluctuating Quadrupole Hamiltonian 65
1.5.8. Sodium NMR Simulation 72
1.6. Sodium NMR Interactions in Biological Environments 73

2. ADVANTAGE OF SAMPLING DENSITY WEIGHTED APODIZATION OVER POST-ACQUISITION FILTERING APODIZATION FOR SODIUM MRI OF THE HUMAN BRAIN 82

2.1. Introduction 82
2.2. Theory 84
2.2.1. SNR Advantage of Sampling Density Weighted Apodization 84
2.2.2. Design Constraint for Sampling Density Weighting with 3D-Twisted Projection Imaging 85
2.2.3. Apodization Filter 85
2.3. Methods 87
2.4. Results 90
2.5. Discussion 93

3. K-SPACE ACQUISITION COMPARISON WITH RESPECT TO AVERAGE SIGNAL MEASUREMENT WHEN IMAGE NOISE IS SPATIALLY CORRELATED 97

3.1. Introduction 97
3.2. Theory 100
3.2.1. Terms Used in this Paper 100
3.2.2. A Suggested Theory for Correlation Volume Computation 101
3.2.3. The Power Spectral Density of Radial k-Space Acquisition 101
3.3. Methods 104
3.3.1. Correlation Volume Verification using Zero-Filled Uniform k-Space 104
3.3.2. Correlation Volume Calculation Validity with Radial Projections 105
3.3.3. Radial k-Space Acquisition Comparisons 106
3.4. Results 108
3.5. Discussion 115

4. RADIAL K-SPACE SODIUM ACQUISITION OPTIMIZATION FOR OBJECT QUANTIFICATION WITH CONCERN TO THE HUMAN HEAD 121

4.1. Introduction 121
4.2. Theory 125
4.2.1. Relaxation Compensating Sampling Density k-Space Acquisition 125
4.2.2. The Kaiser Function 127
4.2.3. Post-Acquisition Compensation for Sampling Density Deviation from Desired Shape 127
4.2.4. Relative SNR for Radial k-Space Acquisition 128
4.2.5. Assessment of Minimum Object Volumes Required for Measurement Accuracy and Precision 129
4.3. Methods 131
4.3.1. Sodium Imaging Aspects 131
4.3.2. Sodium Phantoms Used for Analysis 131
4.3.3. k-Space Filter Comparison for Imaging the Human Brain 131
4.3.4. Image Intensity Modulation with Object Volume 132
4.3.5. Comparing Approaches to Radial k-Space Acquisition for Minimum Required Object Volume 134
4.3.6. Comparing Radial k-Space Acquisition in Resolution Phantoms and Human Brain 137
4.4. Results 138
4.4.1. k-Space Filter Comparison for Imaging the Human Brain 138
4.4.2. Image Intensity Modulation with Object Volume 141
4.4.3. Comparing Approaches to Radial k-Space Acquisition for Minimum Required Object Volume 143
4.5. Discussion 155
4.6. Conclusion 166

5. SODIUM IMAGING OPTIMIZATION UNDER SPECIFIC ABSORPTION RATE CONSTRAINT 167

5.1. Introduction 167
5.2. Methods 171
5.2.1. Simulation 171
5.2.2. Experiment 175
5.3. Results 177
5.4. Discussion and Conclusions 183

6. SODIUM IMAGING INTENSITY INCREASES WITH TIME AFTER HUMAN ISCHEMIC STROKE 193

6.1. Introduction 193
6.2. Methods 195
6.2.1. Patient Selection 195
6.2.2. MRI acquisition and post-processing 197
6.2.3. Region of Interest Analysis 197
6.2.4. Statistical analysis 198
6.3. Results 199
6.4. Discussion 204

7. IN-VIVO SODIUM MAGNETIC RESONANCE IMAGE OF THE HUMAN BRAIN USING SOFT INVERSION RECOVERY FLUID ATTENUATION (SIRFLA) 208

7.1. Introduction 208
7.2. Methods 211
7.3. Results 215
7.4. Discussion 218

8. DISCUSSION AND CONCLUSION 222

8.1. Thesis Summary 222
8.2. Discussing Aspects Related to this Thesis 224
8.2.1. Concerning Other k-Space Acquisition Methods for Human Brain Sodium MRI 224
8.2.2. Concerning Anisotropic k-Space Acquisition 225
8.2.3. Concerning Projection Twisting 227
8.2.4. Concerning Sodium Relaxation Characterization in Brain Tissue 228
8.2.5. Concerning Residual Quadrupole Effect in Brain Tissue 229
8.2.6. Concerning the PASS Sequence and its Use in the Stroke Study 230
8.2.7. Concerning the Enhancement of Sodium NMR Dependent Contrast 233
8.2.8. Concerning the SIRFLA Sequence 233
8.2.9. Concerning Sodium MRI in Stroke 235
8.2.10. Concerning Other Proposed Sodium Imaging Uses 237
8.3. Final Discussion and Conclusion 239

9. APPENDIX 1: IMPLEMENTING TPI ON THE VARIAN INOVA 245

10. APPENDIX 2: NON-CARTESIAN IMAGE CREATION 259

10.1.1. General Convolution Based Gridding 259
10.1.2. Sampling Density Compensation 260
10.1.3. Image Generation 268

11. APPENDIX 3: ARBITRARY IMAGING DEVELOPMENT (AID) SOFTWARE 272

12. APPENDIX 4: ARBITRARY IMAGE CREATION (AIC) SOFTWARE 274

13. APPENDIX 5: GALILEO (IMAGE ANALYSIS) SOFTWARE 275

14. APPENDIX 6: SODIUM SPIN SIMULATION (TRIPLE-S) SOFTWARE 276

15. APPENDIX 7: 4.7 TESLA SODIUM RADIO FREQUENCY HEAD COIL 277

16. APPENDIX 8: SAMPLING EFFICIENCY DERIVATION 278

17. REFERENCES 281

List of Figures

		Page
1-1	Depiction of the spatial quantization of nuclear angular momentum for spin 3/2	38
1-2	Spin-state energy level shifting as a result of a static residual quadrupole interaction, and the resultant splitting of the sodium spin 3/2 spectrum	54
1-3	Graphical representation of the hermitized irreducible tensor operator basis set using spherical harmonics for a spin 3/2 nucleus	59
2-1	A sodium image of the human brain generated with uniform k-space (3D-TPI) sampling and no post-acquisition filtering demonstrating ringing artifact.	82
2-2	Profiles highlighting sampling density across k-space for uniform k-space acquisition and k-space filtering by sampling density design	88
2-3	Phantom images highlighting the SNR advantage of k-space filtering by sampling density design	90
2-4	The relative SNR advantage of k-space filtering by sampling density design demonstrated in human brain	91
2-5	Multiple image slices from healthy human brain for k-space filtering by sampling density design	92
3-1	Verification of correlation volume computation	108
3-2	Validation of the use of correlation volume computation for radial k-space acquisition	109
3-3	The noise averaging advantage associated with oversampling the centre of k-space when a uniform transfer function is desired	111
3-4	The noise averaging advantage associated with increasing k-space filtering by sampling density design	113
3-5	The noise averaging advantage associated with oversampling the centre of k-space when a k-space filtering shape is desired	114
3-6	A profile through the 3D autocorrelation function for k-space sampled to spherical and cubic extents	118
4-1	CSF ringing artifact dependence on the Kaiser β parameter	139
4-2	Point spread function shape and resolution phantom image dependence on Kaiser β parameter	140

4-3	Image intensity modulation with object volume in spherical 5% agar phantoms	142
4-4	Image intensity modulation with spherical object volume computed for cellular brain tissue	142
4-5	Optimization for minimum spherical object volume required to achieve a given measurement accuracy and precision	145
4-6	Optimization for minimum anisotropic object volume required to achieve a given measurement accuracy and precision	147
4-7	Effect of readout duration increase for standard radial imaging	148
4-8	Effect of readout duration increase for radial evolution altered k-space acquisition	150
4-9	The critical requirement of small value of *p* when readout duration is long	151
4-10	The marginal effect of increased k-space filtering by sampling density design	152
4-11	Radial k-space acquisition approach PSF and resolution phantom image comparison	153
4-12	Radial k-space acquisition approach comparison in healthy human brain	154
4-13	The k-space ‘time-bending’ advantage of radial evolution altered acquisition	158
5-1	Sodium magnetization relaxation curves plotted from relaxation model	172
5-2	Simulated stead-state sodium sequence analysis under SAR constraint	179
5-3	The SNR advantage of a spoiled steady-state approach to sodium imaging with radial acquisition implemented under SAR constraint	181
5-4	Representative sodium images for healthy human brain demonstrating the Na-PASS sequence	182
5-5	Simulated sequence analysis when SAR constraints at field strengths other than 4.7 Tesla are considered	188
5-6	Optimal flip angle deviation from the Ernst angle under SAR constraint	189

5-7	Relative SNR from simulation for three different approaches to sodium imaging	190
6-1	Representative images acquired from stroke patients 7 – 52 hours post onset	199
6-2	Representative sodium images and water apparent diffusion coefficient maps from a single patient	200
6-3	Sodium MRI signal intensity increases non-linearly with time over the first week after stroke onset	201
6-4	Relative sodium intensity increase during first 40 hours post stroke onset	202
6-5	Signal intensity within the DWI defined lesion increases in a different manner on sodium images than it does on T_2 and FLAIR images	203
7-1	The effect of relaxation on the longitudinal and transverse magnetization associated with soft inversion pulses	215
7-2	The SNR enhancing effects of soft inversion pulses in an inversion recovery experiment	216
7-3	CSF suppressed images acquired from healthy human brain	217
7-4	The SNR advantage of the SIRFLA sequence demonstrated in healthy human brain	219
8-1	Visual comparison of a SIRFLA image and a triple quantum filtered image of healthy human brain	234
8-2	Visual comparison with other sodium MRI images presented by other groups	240
8-3	Multiple axial slices of a sodium image generated using the proposed sodium imaging methodology presented in this thesis	241
8-4	Multiple sagittal slices of a sodium image generated using the proposed sodium imaging methodology presented in this thesis	242
8-5	Multiple coronal slices of a sodium image generated using the proposed sodium imaging methodology presented in this thesis	243
8-6	Sodium image re-highlighting stroke lesion depiction	244
A1-1	A TPI projection demonstrating gradient quantization	249
A1-2	Measured gradient field step responses	251

A1-3	Effect of gradient field step response on the sampled k-space locations	254
A1-4	Image effects of using linear gradient slew models	255
A1-5	A saline resolution phantom image produced before the gradient upgrade	256
A2-1	Effect of the number of sampling density compensation generation iterations	264
A2-2	k-Space error with increasing iterations for non-accelerated and accelerated approach to sampling density compensation	266
A2-3	Profiles through weighted and convolved sampling functions	266
A2-4	The indistinguishable effect of convolution kernel quantization	267
A2-5	Relative replication contribution to the FoV and associated amplification error	269
A2-6	Convolution kernel comparison	271
A3-1	Screenshot of the Arbitrary Imaging Development (AID) user interface	273
A4-1	Screenshot of the Arbitrary Image Creation (AIC) user interface	274
A5-1	Screenshot of the Galileo (Image Analysis) user interface	275
A6-1	Screenshot of the Sodium Spin Simulation (Triple-S) user interface	276
A7-1	A picture of the sodium birdcage head coil constructed and used during this thesis.	277
A7-2	The balun matching circuit used in the sodium birdcage head coil	277

List of Tables

		Page
1-1	Irreducible tensor operator matrices	57
4-1	Projection set parameters used for k-space filtering comparison	132
4-2	Projection set parameters for radial k-space acquisition approach comparison	133
4-3	Projection set parameters for analysis of readout duration with standard radial k-space acquisition	135
4-4	Projection set parameters for analysis of readout duration with radial evolution altered k-space acquisition	136
4-5	Projection set parameters for analysis of *p* with radial evolution altered k-space acquisition	136
5-1	The SAR Constrained RF Pulse Parameters Used in Simulation to Generate the Relative SNR Charts in Figure 5-7	191
6-1	Clinical and imaging characteristics of the 21 stroke patients	196

List of Symbols

a	Centripetal acceleration
a_m	Quantum mechanical probability of finding a spin in state *m*
afib	Arterial fibrillation
A	Dimension of k-space sampled
ADC	Apparent Diffusion Coefficient
ALIAS	Albumin in Acute Stroke
ATP	Adenosine Triphosphate
β	Kaiser function design parameter
B_0	Static magnetic field
B_1	Rotating transverse magnetic field
BBB	Blood brain barrier
BW	Bandwidth (anti-aliasing filter)
c_m	'Simplified' quantum mechanical probability of finding a spin in state *m*
C	Convolution Kernel
chol	Cholesterol
CHF	Congestive Heart Failure
CI	Confidence Interval
CSF	Cerebral Spinal Fluid
CV	Correlation Volume
DM	Density Matrix (Chapter 1.3)
DM	Diabetes Mellitus (Chapter 6)
DFT	Discrete Fourier Transform
DNA	Deoxyribonucleic Acid
DWI	Diffusion Weighted Imaging
D(r)	A post-acquisition filter shape
E	Energy
EFG	Electric Field Gradient
F(k)	Spatial frequency profile of a one-dimensional image (Chapter 1.3)
F(k)	Desired apodization filter shape for theoretical analysis (Chapter 2)
$\mathcal{F}$	Fourier Transform
FDA	Food and Drug Administration
FLAIR	Fluid Attenuated Inversion Recovery
FLASH	Fast Low-Angle Shot
FoV	Field of View
FT	Fourier Transform
γ	Gyromagnetic ratio
Γ	Acquisition design transfer function ($\Gamma = \mathrm{SD} \cdot \mathrm{W}$)
G	Gradient field strength (mT/m)
GRE	Gradient Recalled Echo
$\hbar$	Plank's constant
H(k)	Modulation Transfer Function
$\mathcal{H}_Z$	Zeeman Hamiltonian
$\mathcal{H}_Q$	Quadrupole Hamiltonian
$\mathcal{H}_{QS}$	Static quadrupole Hamiltonian
$\mathcal{H}_{QF}$	Fluctuating quadrupole Hamiltonian

HTN	Hypertension
θ	Spherical azimuthal angle
θ	Excitation flip angle (Chapter 5)
I	Nuclear spin
$\boldsymbol{I}$	Nuclear angular momentum vector
I_X, I_Y, I_Z	Cartesian nuclear angular momentum operators
I_+, I_-	Raising and lowering operators
Im	A one-dimensional image
IR	Inversion Recovery
IV	Intra-venous
ISMRM	International Society for Magnetic Resonance in Medicine
J_0, J_1, J_2	Spectral density parameters relaxation to relaxation
k	Spatial frequency in (1/m)
k	Boltzmann's constant
k_{step}	Distance between sampled k-space locations (1/m)
k_{max}	Maximum extent of k-space sampled (1/m)
k-space	spatial frequency space
K	Total number of Cartesian k-space grid points (Chapter 2)
λ	Describes an individual sampling point
L	Total number of sampling points
LR	Long Readout duration radial evolution altered k-space acquisition approach
μ	Nuclear magnetic moment
m	Eigenvalues of I_Z nuclear angular momentum (Chapter 1.5)
m	'Generalized Hamming' filter design parameter (Chapter 2)
M	Dimension of k-space and image matrices
M_0	Fully relaxed value for the longitudinal magnetization vector.
M_{xy}	Transverse Magnetization
$Mask_{ROI}$	Mask of ones defined by the volume of the ROI
MCA	Middle Cerebral Artery
MI	Myocardial Infarction
MINUTES	Multiple Interventions for Neuroprotection Utilizing Thermal-regulation in the Emergent Treatment of Stroke
MNR	Measurement to Noise Ratio
MTF	Modulation Transfer Function
MRI	Magnetic Resonance Imaging
n	'Generalized Hamming' filter design parameter (Chapter 2)
Na-PASS	Projection Acquisition in the Steady-State for Sodium Imaging
N_{eff}	Number of effectively uncorrelated noise volumes in an ROI
N_{ROI}	Number of acquisition voxels within an ROI
NIHSS	National Institutes of Health Stroke Scale
NINDS	National Institute of Neurological Disorders and Stroke
NMR	Nuclear Magnetic Resonance
ϕ	Spherical polar angle
OP	A quantum mechanical operator
PCA	Posterior Cerebral Artery
PICA	Posterior Inferior Cerebellar Artery
PG	Processing Gain
PSD	Power Spectral Density

PSF	Point Spread Function
PWI	Perfusion Weighted Imaging
rect	Rectangular function
ρ	Design operator (Chapter 1.5)
ρ	Nuclear charge distribution (Chapter 1.5)
R	Acquisition voxel volume dimension $R = 1/(2 \cdot k_{max})$ (Chapter 1.3)
R	Autocorrelation function (Chapter 3)
R	Cartesian sampling function (Appendix 2)
RW	Relaxation Weighting
r	Radial fraction of the sampled k-space extent
r_x	Continuous autocorrelation function (Chapter 1.3)
r_D	Discrete autocorrelation function (Chapter 1.3)
RF	Radio Frequency
ROI	Region of Interest
rtPA	Recombinant Tissue Plasminogen Activator
p	Radial fraction of the sampled k-space extent at which radial evolution alteration is initiated
Q	Nuclear electric quadrupole moment
σ_o^2	Total noise variance
σ_s^2	Sampled noise variance
σ_n^2	Image noise variance
σ_{PAW}^2	Image noise variance – post acquisition weighting
σ_{SD}^2	Image noise variance – sampling density design
s	Real time conversion factor $s = T_{RO}/\tau_{Tot}$
S	Non-Cartesian sampling function (Appendix 2)
$S_{(x_0)}$	Signal produced by a point-source at location x_o (Chapter 1.3)
SAR	Specific Absorption Rate
SCA	Superior Cerebellar Artery
SD	Sampling Density
SDC	Sampling Density Compensation
SDWA	Sampling Density Weighted Apodization
SP	Standard Projection imaging approach
SNR	Signal to Noise Ratio
SIRFLA	Soft Inversion Recovery Fluid Attenuation
SQ	Single Quantum
SR	Short Readout duration radial evolution altered k-space acquisition approach
SW	Sampling bandwidth (inverse of sampling dwell time)
τ	Dimensionless fraction of the time required for a projection to reach the sampled extent of k-space when radial evolution is not altered
τ_c	Characteristic time of an exponential autocorrelation function
τ_{Tot}	Dimensionless total length of a radial evolution altered projection in proportion to that of a standard straight projection.
τ_{RF}	RF pulse length
τ_{samp}	Sampling dwell time
t	Time
T	Tesla
T	Temperature (Chapter 1.5)
T_{nq}	Irreducible tensor operator (rank ‘n’, coherence ‘q’)
T_1	Longitudinal magnetization relaxation time

T_2	Transverse magnetization decay time
T_2*	Transverse magnetization decay time including dephasing envelope
T_{IM}	Scanning Time
T_{RO}	Readout Duration
TE	Echo Time
TPI	Twisted Projection Imaging
TQF	Triple Quantum Filtering
TR	sequence Repetition Time
TSC	Tissue Sodium Concentration
TWIRL	Twisted Radial Lines
UPFA	Uniform k-space sampling with Post-acquisition Filtering Apodization
USD	Uniform Sampling Density
χ	Quadrupole coupling constant
v_{acq}	Acquisition voxel volume defined as: $v_{acq} = 1/(2 \cdot k_{max})^3$
v_{ZF}	Zero-filled image voxel
ω_0	Larmor frequency
ω_{RF}	Frequency of applied transverse magnetization
ω_Q	Quadrupole interaction frequency
$\bar{\omega}_Q$	Residual quadrupole interaction frequency
V	Electric potential at nucleus due to external sources (Chapter 1.5)
V_{s_i,s_j}	Electric field gradient terms
W	Post-acquisition weighting
Ψ	Nuclear spin wave-function (Chapter 1.5)
$\Psi(r)$	A desired transfer function shape (Chapter 4)
X	Dimension of an image voxel
Z	Number of spin

Chapter 1

Introduction and Background

1.1. Thesis Introduction

In biological systems the ubiquitous sodium ion plays many critical roles, and in many disorders sodium concentrations are directly altered as a result of the pathology; the ability to non-invasively assess these sodium concentration changes may provide insight related to the nature of disorders, the action and efficacy of treatment, and the pathophysiological status of patients. However, since the first demonstration of human sodium MR images in 1985 (1), there have been only 22 published studies of pathology in humans with sodium MRI (including preliminary studies), these include studies of: tumour (2-10), stroke (11-13), myocardial infarction (14-16), paramyotomia (5,17,18), osteoarthritis (19-21), haemorrhage (22), and Alzheimer's disease (23). Perhaps the greatest reason for the paucity of medical research in this field is that sodium MRI is complicated not only by low tissue sodium concentrations ~ 0.05% to 0.25% that of tissue water protons (1,24), a sensitivity 35% that of water protons, and a Larmor frequency roughly ¼ that of protons (requiring capable hardware), but also by much different nuclear spin dynamics leading to very rapid inherent biexponential transverse magnetization decay (T_2 relaxation) and rapid longitudinal magnetization recovery (T_1 relaxation) in macro-molecular tissue (see Chapters 1.5 and 1.6). Due to sodium's relatively low concentration and sensitivity, it could be said that sodium MRI remains on the cusp of utility, producing images with resolution considerably lower than expected from standard MRI. In order to 'squeeze' as much as possible from the sodium nuclei, the purpose of the work presented in this thesis was to optimize non-conventional imaging strategies with regard to rapid relaxation for sodium MRI of the human head within the context of a beneficial 'high' static magnetic field. The goal of this optimization was to facilitate a study of the time course of intensity on human brain sodium MR images following the onset of stroke with implication to

provide a timing mechanism for this pathology. Acute stroke has a very time-dependent treatment window, and a timing mechanism may 'open' a treatment option for those patients with unknown stroke onset (see Chapter 1.2). The field of sodium MRI research has also always had a strong component seeking intracellular [^{23}Na] analysis capability, and so to address the current gamut of sodium MRI consideration for human brain, novel potential intracellular sodium imaging methodology is also suggested.

There have been 28 papers published concerning sodium imaging of human brain since 1985 (1,3,5-13,22,23,25-40) apart from the 4 published and presented in this thesis (41-44). It was understood in the first published paper of human brain sodium MRI (1) that because the T_1 of sodium in cellular brain tissue ($\sim$ 37 ms at 4.7 Tesla (45)) is much shorter than that of protons ($\sim$ 800 ms – 1300 ms), three dimensional k-space acquisition techniques, enabled by short repetition times (TR), could be used to enhance image signal-to-noise ratio (SNR) (see Chapter 1.3 for an introduction to k-space and its acquisition in an MRI experiment). Standard proton images must typically be acquired in a two dimensional fashion as a result of time constraints. Although the sodium nuclei in cellular tissue exhibit a fast signal decay component of T_{2f} = 0.7 ms – 3.0 ms (60%) and a slow component of T_{2s} = 16 ms – 30 ms (40%) (25,37,46-53), the first and many early papers implemented a multiple spin-echo technique with delay between excitation and the acquisition of the centre of k-space (labelled echo-time – TE) of 3 ms – 13 ms (1,10,13,22,31-34); increased TE results in signal loss within the image. Addressing the desire for shorter TE, the gradient echo (GRE) technique was also implemented very early for human brain sodium imaging (9,40). This technique acknowledges that dephasing as a result of local magnetic field inhomogeneity within a voxel at short echo times is inconsequential, and the transverse magnetization refocusing of the 180^o RF pulse associated with the spin-echo technique, unnecessary; the 180^o RF refocusing pulse simply adds additional delay before acquisition and unwanted power deposition. The 3D-GRE technique remains in use as of 2009 (23) for sodium imaging of the human head with echo

times ranging from TE = 0.9 ms – 11 ms (3,8,9,23,25-27,37,40). For introduction to the standard spin-echo and GRE sequences the reader is referenced to (54) or any other introductory MRI textbook.

The standard sodium 3D-GRE technique acquires one line of k-space per excitation along a Cartesian dimension beginning at the edge of the sampled k-space extent, or somewhere in-between the edge and the centre for asymmetric echoes. As a result, minimum TE values are limited by minimum phase-encode times (selecting the k-space line to be acquired), and the time required to 'rewind' and 'play-out' each k-space line until acquisition of the centre of k-space. An alternative is 'centre-out' radial k-space acquisition where the centre of k-space directly follows RF excitation. For radial k-space acquisition TE is solely dependent on the length of the RF excitation pulse and any system delays, as TE is (and T_2 signal loss can be) measured from the centre of the RF pulse. Standard radial acquisition samples k-space along straight lines with constant velocity from the centre of k-space to its sampled extent, and perhaps surprisingly has been implemented only once, quite recently (2007), for sodium MRI of the human brain (5).

The lack of use of standard radial k-space acquisition for sodium MRI likely stems from fact that non-Cartesian k-space acquisition techniques (of which radial acquisition is a member) are typically not well supported on MRI systems and often require development. Another reason is that standard radial k-space acquisition 'suffers' from extreme sampling density variation across k-space, i.e. the centre is sampled much more frequently than the edges (where the qualification of 'suffering' points to work presented in this thesis). The effective sampling density transfer function of radial acquisition is far from ideal and is typically post-acquisition compensated. This process is SNR inefficient (55).

In 1997 a radial k-space acquisition technique named 3D twisted projection imaging (TPI) was introduced by F.E. Boada for sodium MRI (30) to achieve

uniform sampling density throughout the majority of k-space (beyond radial fraction *p*) and hence minimize SNR inefficiency. This technique, which is a three-dimensional implementation of an earlier two-dimension technique named 'twisted radial lines' (or TWIRL) (56), was also originally implemented as a means to reduce the number of projections required to critically fill k-space (for an introduction to TPI see Chapter 1.4). This technique has been used quite often by its original contributors (7,11,12,28,35), achieving a small TE of typically ~ 0.4 ms.

Only one other group outside the original contributors to TPI has used this technique to image sodium in the human brain (6) (and the original sequence was provided to this group by Boada). The reason likely arises from the 'complexity' of TPI and unanswered questions pertaining to its merit. A fairly recent (2003) paper suggests TPI is hindered by both lengthy TR and lengthy readout duration (T_{RO}), the former decreasing SNR and the latter causing blurring (26). However, it is an intention of this thesis to point out that this suggestion is incorrect. Although TPI has been used exclusively with full T_1 recovery following 90^o excitation, an SNR enhancing steady-state approach with short TR can also be used with TPI k-space acquisition (Chapter 5), and in Chapter 4 optimization suggests that TPI actually *benefits* from lengthy T_{RO}, given appropriate implementation. It is suggested in this thesis that the advantage of TPI k-space acquisition for sodium imaging is very large, but as suggested in Chapter 3, not necessarily related to the reason of SNR efficiency for which it was originally introduced by Boada (30).

Sodium MRI is somewhat unique in that optimization can effectively be separated into two distinct aspects: NMR related optimization, and k-space acquisition related optimization. NMR optimization begins with the static magnetic field strength (B_0), as SNR following an ideal RF excitation pulse is directly proportional to B_0. A majority of human brain sodium imaging papers used what has been the standard clinical field strength of 1.5 Tesla (1,5,6,9,10,13,22,31-34), one used a 2T system (27), eight used increasingly standard 3T systems

(7,12,23,28-30,35,36), five used 4T systems (3,8,25,26,39), and one used a 7T system (37). The field strength used for the sodium MRI studies in this thesis was 4.7T, a now 'moderately-high' field system. NMR optimization also concerns what is typically described as the 'pulse sequence.' In this thesis, optimization of the NMR pulse sequence concerns optimization of excitation flip-angles, RF pulse length (in effect TE), and TR for a maximal SNR/voxel-volume relationship, given that imaging sequences will be constrained by power deposition (resulting in tissue heating) within the human head (a problem increasing as B_0^2) (57). k-Space acquisition optimization in this thesis is concerned with the 'production' of k-space immediately prior to Fourier transform and includes: post-acquisition filtering, sampling density design, projection evolution through k-space, readout duration, and the optimal SNR at which to perform sodium imaging. k-Space acquisition optimization also requires relevant image metrics for quantitative imaging which are introduced in this thesis.

The first published paper presented in this thesis (Chapter 2) describes the value of sampling density design to generate a k-space filtering shape for human head sodium imaging. Because k-space is sampled to a finite extent, the image point spread function (PSF) will have a sinc shape (or jinc shape for a spherical sampled k-space extent), manifesting as ringing in the image (see Chapter 1.3). Although it may be expected that the rapid signal decay of brain tissue may provide an inherent k-space filter, sodium T_2 in cerebral spinal fluid (CSF), which wraps the brain and fills the ventricles at its centre, is substantially longer than in brain tissue ($T_{2f} = T_{2s} \sim 64$ ms at 4.0 T (25)). Given that the sodium concentration in CSF is roughly 3x larger (~150 mM) than in brain tissue (~ 50 mM) (6,31,32,58,59), ringing lobes arising from CSF substantially contaminate the brain tissue; this problem is exacerbated by the low resolution of sodium imaging which spatially extends the ringing lobes, and by the spherical geometry of the head which generates ringing superposition. The idea that k-space filtering is required to minimize sodium brain tissue measurement errors related to CSF has not been previously mentioned in the literature (it is possible that filtering may be

commonly used without being mentioned). Sampling density shape design other than uniform was also introduced by Boada in 1997 (60), however his concern was with shortening readout duration under a hardware constraint and only very mild k-space roll-off was produced. In this paper a 'Hamming-like' k-space filter shape is presented which can be generated by sampling density design without violating the Nyquist criterion. The intention of this paper is to demonstrate and quantify from theory and experiment the SNR efficiency of k-space filtering by sampling density design rather than with post-acquisition weighting. A 'noise colouring' advantage of filtering by sampling density design is also highlighted.

In Chapter 3 (unpublished) this thesis considers the minimum region of interest (ROI) volume required to attain a desired confidence interval for a measurement of average signal intensity in an ROI with respect to image noise. Although proton MRI is typically unconcerned with the measurement of average ROI signal intensity (proton MRI has historically been concerned with pathology *detection* rather than signal intensity quantification), average ROI signal intensity measurements are of primary interest for sodium imaging. The minimum ROI volume required for a desired absolute confidence interval and a given standard deviation of image noise is trivial to calculate if one understands how noise is averaged (61). For non-zero-filled images with uniform noise power spectral density (PSD) (the bulk of standard Cartesian images) the noise autocorrelation is a delta function, i.e. image noise is uncorrelated, and the standard deviation of noise in a signal averaging ROI measurement is decreased in proportion to the square root of the number of voxels in the ROI (62). However, when the noise PSD is not uniform, as it is for radial k-space acquisition, image noise will be correlated between voxels. To the author's knowledge, no method to measure correlation volume (CV), or the effective volume of statistical independence in terms of voxels, has been presented other than the 'trivial' case when the ROI encompasses 'all' of the autocorrelation function and the PSD is of unit value at its centre (63). A theory is presented in Chapter 3 for the computation of correlation volume given any PSD shape and ROI volume. Several interesting

results are demonstrated, including an additional advantage for k-space filtering by sampling density design. This chapter also highlights that although TPI was developed in the context of improving SNR efficiency, standard radial imaging with its excessive oversampling at the centre of k-space and dramatic reduction of low frequency noise is actually (substantially) better than TPI in terms of signal averaging within an ROI, requiring smaller ROI volumes to attain a desired confidence with respect to image noise.

Chapter 4 (unpublished) concerns optimization of radial k-space acquisition for the directly relevant quantitative imaging metric introduced. Signal drop-off toward the sampled extent of k-space, exacerbated by long readout duration in the presence of rapid T_2 decay, produces a smearing (down and out) of the PSF and blurring in the image. It is for this reason that T_{RO} reduction has been considered beneficial (5,29). However, image noise standard deviation will also be reduced in proportion to the square root of the readout duration. The following question remains: assuming voxel volumes are reduced in proportion to T_{RO} increase such that SNR remains constant, how are image quality and the effects of PSF smearing to be measured? An optimization for radial ('TPI related') readout duration was very recently performed (36), however, it is the contention of this thesis that this recent paper does not use a particularly informative image metric with regard to quantitative imaging for their optimization – the optimization of SNR in a point source object. Chapter 4 demonstrates that image intensity is modulated by object volume when object volumes are small in comparison to the spatial extent of the PSF, and the image metric introduced in Chapter 4 is thus the minimum object volume in which both a desired measurement confidence (with respect to image noise – Chapter 3) and a desired average measurement accuracy (with respect to PSF-related image intensity modulation with object volume) can be attained within an ROI. Using this metric, three approaches to radial k-space acquisition are compared: standard radial imaging with short ~ 2 ms T_{RO} (5), TPI with short 4 ms T_{RO} (29), and TPI with long ~ 17 ms T_{RO} (as used in Chapters 2, 5 and 6 of this thesis). Also included in this chapter is consideration of: k-space

filtering shape, the T_2 decay 'reshaping' advantage of TPI related k-space acquisition (also very recently highlighted to some extent by (36)), CSF containment within its bounds, and ideal implementation SNR.

Chapter 5 diverges from discussion of k-space acquisition to tackle NMR sequence optimization, and was published in 2008 (42). This chapter describes that there is much to be gained from a steady-state approach to imaging, and that use of TPI does not preclude one from using a steady-state approach, as can be implied from (26). TR reduction facilitates increased averaging and proportional noise variance reduction, however, reduced TR is also associated with increased power deposition. A new approach to NMR sequence optimization is presented – optimization for SNR under power deposition constraint. This optimization includes the three parameters of a single-quantum sodium MR sequence that govern SNR and power deposition, i.e. excitation RF pulse length, flip angle, and TR. Although a prevailing notion for optimal sodium imaging includes use of the shortest TE possible to avoid signal loss, it is shown in this chapter that a large SNR increase is associated with some TE increase (as a result of RF pulse length increase) which facilitates steady-state imaging under power deposition constraint.

As previously mentioned, the purpose of the sodium imaging optimization of this thesis was to enable the creation of 'optimal' sodium images of human stroke and so evaluate a sodium signal intensity time-line following stroke onset. This is the subject of Chapter 6. The value of a potential timing mechanism is given in Chapter 1.2, along with a brief introduction to the pathophysiological increase of sodium ions within an ischemic lesion during acute stroke. Two previous papers have studied sodium imaging during acute human stroke. The first (1993 – 7 patients) observed general intensity increase on a sodium image at an earliest time of 38 hours post-onset, and no intensity increase on three images within 13 hours. It was concluded that "^{23}Na MRI is insensitive to early ischemic changes and not clinically useful for diagnosis" (13). The second paper (1999 – 26 patients)

showed a relatively large sodium increase as early as 4 hours but no clear potentially diagnostic trend with respect to the timing of stroke (12). Because numerous animal studies have demonstrated time-dependent accumulation of sodium within the acute phase of stroke (12,64-68), a study of sodium imaging in human stroke was again reconsidered in this thesis. The resulting paper, published in 2009 (41), highlights for the first time in humans a time-dependent trend for sodium MR intensity similar to that observed in animal models.

The ability to selectively assess intracellular sodium concentrations would be particularly valuable for the study of many disease processes, and it has been hypothesized that significant sodium relaxation differences may exist between intra- and extracellular spaces (see Chapter 1.6). Considerable research ((28,49,69-74) are a selection of papers since 1998) has been devoted to the use of triple quantum filtered (TQF) sodium NMR since it was presented in 1986 (75) that triple quantum spin-ensemble polarizations could be produced as a result of biexponential relaxation for spin 3/2 nuclei (for a brief description of triple quantum filtered spin 3/2 NMR see Chapter 1.5). The theory of the use of TQF sodium NMR for selective intracellular imaging is that sodium ions in the extracellular space are in a considerably more fluid environment and do not exhibit biexponential relaxation, and hence do not produce signal (or produce considerably less signal). However, difficulties of TQF sodium MRI for human brain include the power deposition of the minimum three 90^{o} RF pulses of the TQF sequence, and low signal yield (28). No paper has ever used TQF sodium MRI to study pathology in the human brain. A novel NMR sequence presented in Chapter 7 may be an alternative selective imaging method, and is based on inversion recovery. Although a 180^{o} RF inversion pulse is required (along with a 90^{o} excitation pulse), the power deposition of this inversion pulse is greatly mitigated by making the pulse relatively long (or 'soft'). Unlike the TQF methodology where increasing RF pulse length reduces yield, the Soft Inversion Recovery Fluid Attenuation (SIRFLA) sequence benefits from *increased* yield with RF inversion pulse softening.

Before presenting the published (or to be published in some form) chapters of this thesis some time will be taken to introduce some relevant background material. In Chapter 1.2 acute stroke is introduced along with current treatment and current understanding of pathophysiological sodium ion increase within the stroke lesion. Chapter 1.3 covers the basics of k-space acquisition engineering, and in Chapter 1.4 TPI-related k-space acquisition is introduced. Chapters 1.5 and 1.6 cover the quantum mechanics of the spin 3/2 sodium nuclei and their interactions in biological environments respectively. Appendices 1 and 2 concern implementation and image creation of the non-Cartesian TPI k-space acquisition. Appendices 3 – 6 highlight software created for this thesis, and Appendix 7 concerns derivation of sampling efficiency for k-space filtering.

1.2. Acute Stroke

According to a 2008 American Heart Association report, ischemic stroke is the leading cause of disability, and the third leading cause of mortality after heart disease and cancer (as stated in (76)). Conceptually, ischemic stroke is a very simple disease involving the blockage of blood flow to the brain, typically as the result of a blood clot, however, until 1996 there was no direct treatment to mitigate the extent of neurological damage following stroke onset. In 1996 the Food and Drug Administration (FDA) approved the use of intravenous recombinant tissue plasminogen activator (rtPA, also alteplase) for treatment of ischemic stroke within the window of 3 hours following the onset of symptoms (the use of rtPA was granted approval in Canada in 1999 (77) and in Europe in 2002 (78)). Administration of rtPA, a protein that cleaves the plasma proenzyme plasminogen to form clot dissolving plasmin (24), within the 3 hour window remains (as of 2008) the international standard of care for acute stroke (78,79). FDA approval was based on a large scale study funded by the National Institute of Neurological Disorders and Stroke (NINDS), which suggested absolute increases of 11% - 13% for favourable outcomes, and a 32% relative increase in number of patients who were more likely to have minimal or no disability at 3 months when treated with rtPA (50% of patients for rtPA and 38% for no treatment, based on the Barthel index measuring performance of daily activities) (80). However, the rate of symptomatic intracerebral haemorrhage was increased from 0.6% to 6.4% (80). Subsequent reanalyses of this study confirmed the beneficial nature of treatment with rtPA (81) and suggested for every 100 patients treated 32 will have better final outcome and 3 a worse final outcome (82), with 1 having a severely disabled or fatal outcome as a result of treatment (83). Efforts to expand the treatment window beyond 3 hours are ongoing (84-87), and a pooled study analysis (88) and recent large scale study (89) suggest value up to 4.5 hours.

The value of rtPA arises from the rescue of tissue at risk of preceding to infarction, or cell death as a result of ischemia. The ‘core’ of an ischemic lesion, or regions having undergone anoxic depolarization (discussed below), can be

detected using diffusion weighted magnetic resonance imaging (DWI) within minutes following the onset of stroke (90-92). DWI contrast is facilitated by the restricted diffusion of water associated with anoxic depolarization and the resultant cytotoxic edema. The DWI defined ischemic core (or typically portions thereof) may be salvageable, but this rescue is highly dependent on early recanalization (93). The 'penumbra' of the ischemic cerebral lesion was originally defined as that portion exhibiting 'electrical failure' (or electro-encephalogram silence) but not anoxic depolarization (94), with ATP levels 50% – 70% of control values (95). Within the context of MRI, the penumbra is defined by the extent of under-perfused areas as detected on perfusion weighted MRI (PWI), or the PWI-DWI mismatch (96-98), although PWI may overestimate tissue at risk of proceeding to infarction, i.e. tissue with benign oligemia or hypo-perfusion. Recent stroke trials have addressed expansion of the rtPA treatment time-window to 6 hours by using PWI-DWI mismatch to identify patients with salvageable tissue at risk who may be likely to benefit from recanalization (99,100).

While considerable attention has been focussed on identifying the potential benefits of thrombolysis for individual stroke patients, there is currently no recommended methodology to decipher the elapsed time since symptom onset if it is unknown. This is problematic, given the time requirement of current regulatory approval, as ~ 1/3 of patients present within an uncertain time of onset making them ineligible for rtPA (101). Several 'classic' non-NMR non-human studies have demonstrated time-dependent increases in sodium concentration following stroke onset (58,68,102-108). More recently, several non-human studies have demonstrated time-dependent increases in signal intensity measured with sodium NMR (12,64-67,109-111). Although there may be potential for sodium with respect to assessment of time after stroke (112), there have been only two human studies of sodium MRI in acute stroke (12,13), neither demonstrating a clear evolution timeline.

In this thesis the time-course of sodium accumulation during ischemic stroke is studied within a human population using sodium MRI, with intention to assess a potential means for inclusion of patients with unknown time of onset as eligible for thrombolytic treatment. Although this thesis is not concerned with the pathophysiology of acute stroke, current understanding of Na^+ and water accumulation within the ischemic lesion of acute stroke is briefly introduced below.

It is well known that cells actively maintain a large sodium concentration gradient across their cell membrane, continually 'pumping out' three Na^+ ions (while simultaneously 'pumping in' two K^+ ions through the Na,K-ATPase) to maintain an intracellular sodium concentration of ~ 15 mM against the ~ 150 mM concentration in the homeostatically buffered interstitial space (24). This concentration gradient and the resting membrane potential of -5 to -100 mV produced as a combined result of the Na^+, K^+, and Cl^- concentration gradients and the respective permeability of the cell membrane to each species are vital to the function of each cell, and are directly responsible for transport of other ions and metabolites across the cell membrane as well as the initiation and propagation of action potentials in nervous tissue (24). Within the human brain at least 40% of the energy released by respiration is required by the Na,K-ATPase for the maintenance of concentration gradients (113).

Following the 'cessation' of blood flow, or the reduction of ATP levels to ~ 25% of baseline values (95), the ischemic cascade could be said to begin with 'anoxic depolarization,' a very rapid depolarization of the cell membrane associated with large compartmental ion shifts (interstitial Na^+ decreases to ~ 50 mM and intracellular Na^+ increases to ~ 100 mM have been measured) (95,114,115). Given limited energy reserves in the brain, anoxic depolarization occurs within minutes following onset of severe ischemia (95,113-115). Several pathways have been suggested for the rapid influx of sodium associated with anoxic depolarization. These pathways may include non-selective cation channels gated

by glutamate (116-122). Elevation of intracellular calcium through voltage-gated calcium channels and inactivation of the ATP dependent calcium pumps, along with the impairment of Na^+ concentration gradient dependent reuptake of glutamate in the post-synaptic terminal and surrounding glial cells (123), results in a flooding of the synapse with glutamate (increases > 150 fold (124)). Pathways of sodium influx associated with anoxic depolarization may also include (non-inactivating) voltage gated sodium channels (114,125-129) and other ion co-transport channels (130-133). The large compartmental ion shifts and increased cellular osmolality are most certainly associated with the *cellular* swelling of cytotoxic edema (it should be noted that there is no *tissue* swelling, or tissue water increase associated with cytotoxic edema as defined here) (130,134-136). While cellular recovery from anoxic depolarization is possible if ischemic conditions are shortly resolved (within 30 minutes for neurons, 60 minutes for astrocytes (137)), the cellular swelling and calcium influx, concomitant with sodium influx (121,126,129,138), among other mechanisms are typically tied to cell death (137).

The sodium ion shift of anoxic depolarization produces a new concentration gradient between the depleted interstitial space of the lesion core (that part of the ischemic lesion having undergone anoxic depolarization) and ultimately the vasculature (67,130). Sodium flux across the endothelial cells of the vasculature while the blood brain barrier remains intact has been suggested to be the primary source of water accumulation within the lesion core during the period directly following anoxic depolarization, and as such water accumulation during this period has been labelled ionic edema (58,102,106,130,135). The transcapillary sodium flux associated with ionic edema may require active transport through the Na,K-ATPase on the abluminal side of the endothelial cells (68,106,135), along with the stimulation of other co-transporters (139) and up-regulation of non-selective cation channels (130,133). However, one seminal (non-MRI) rat model study found no significant correlation between sodium and water concentration in this period following the onset of stroke; water concentrations were statistically

elevated prior to sodium increase (68). Lack of correlation between tissue sodium and water was also observed at 1 and 3 hours following stroke onset in another large scale rat model study (107). It has alternatively been suggested that sodium ions are not the sole source of osmoles driving tissue water increase during this period, a marked increase in catabolic products may also significantly contribute (68,102).

The period of ionic edema has been suggested to last for 3 to 6 hours and is succeeded by vasogenic edema, a process of tissue water accumulation in which the blood brain barrier becomes indiscriminately porous to blood ultrafiltrate, allowing passage of brain proteins such as albumin (106,130,139,140). Several mechanisms may be responsible for the increased permeability of the blood brain barrier, which retains its integrity with respect to the containment of erythrocytes within the vasculature. These include disruption of tight junctions and reverse pinocytosis (130,135). During vasogenic edema the capillaries of the blood brain barrier behave like fenestrated capillaries, and hydrostatic pressure gradients contribute to the tissue infiltration of water, ions and other molecules (130). Ischemic tissue sodium and water concentrations continue to increase in vasogenic sense over a period of several days (68,106).

It is suggested that the time-dependent tissue sodium increase throughout the periods of time associated with ionic and vasogenic edema following the onset of acute stroke may provide information pertaining to time past stroke onset. In this thesis an attempt is made to characterize intensity increase on sodium images following onset in acute human stroke.

1.3. Basic k-Space Acquisition Engineering

A brief description of MR image acquisition is given below, followed by introduction to relevant aspects of MR image acquisition engineering. To simplify the equations, one dimensional images are considered (a 1D image can be viewed as an object profile). Extension to two and in particular three dimensions for this thesis is straight-forward. The description of MR image formation below and its relevant aspects to this thesis draw from the following references (54,141-143)

1.3.1. Creating an MR Image

Assume that an object we wish to scan in an MRI experiment is a point-source with location $(\mathrm{x_o})$ (with respect to the bore centre) and signal intensity $\left(\mathrm{S_{(x_o)}}\right)$. The image $\left(\mathrm{Im}(x)\right)$ we would hope to attain from this MRI experiment is

$$\mathrm{Im}(x) = \mathrm{S_{(x_o)}} \cdot \delta(x - \mathrm{x_o})\,. \qquad [1\text{-}1]$$

If an MRI scanner simply consisted of a constant magnetic field generating solenoid there would be no way of knowing the location of the object within the bore other than by physically measuring it. Fortunately, a 'beautiful' method of MR imaging has be developed that makes MR image acquisition particularly interesting for 'signal processing' engineers. The Fourier transform $\left(\mathrm{F}(k)\right)$ of the image we would hope to attain from the MR experiment above is given in Eq. [1-2], where *k* is in 1/m (it should be noted that spatial frequency space is labelled k-space).

$$\mathrm{F}(k) = \mathrm{S_{(x_o)}} \cdot \mathrm{e}^{-\mathrm{j}2\pi \mathrm{x_o} k} \qquad [1\text{-}2]$$

If it were possible to make the phase of the signal from each point-source within an object evolve with sampling according to its location, then this sampling could be mapped into k-space. An inverse Fourier transform of the acquired k-space data would produce the desired image.

In an NMR experiment the received signal is a result of rotating (transverse) magnetization which produces an oscillating EMF within a tuned receive antenna (or coil). The rate of oscillation (named the Larmor frequency) is dependent on the magnitude of the static magnetic field (B_0) and the gyromagnetic ratio of the nuclei (γ). For sodium nuclei $\gamma = 11.26$ MHz/Tesla, and at 4.7 Tesla the Larmor frequency is ~53 MHz. The received signal is demodulated before discrete sampling and requires a MR system with a tuneable local oscillator (such as the Varian Inova used throughout this thesis). For more information on the quantum mechanical production of rotating transverse magnetization for spin 3/2 nuclei see Chapter 1.5.

Because the frequency of signal oscillation is dependent on the magnetic field, a spatially varying magnetic field can be used to make the signal phase of a point-source evolve with time according to its position. Three solenoids producing orthogonal, (linearly) spatially varying magnetic fields are included in each MRI scanner. These magnetic fields are aptly named the gradient fields (G) and have a value of zero at the centre of the bore and units of mT/m. When a gradient field is applied, the signal phase of a point-source will evolve with time and position according to

$$\phi(t) = 2\pi x_o \gamma G t \,. \qquad [1\text{-}3]$$

It is immediately apparent from Eq. [1-2] and Eq. [1-3] that the magnitude of the gradient field and length of time it is applied provide a direct mapping into k-space,

$$k = \gamma G t \,. \qquad [1\text{-}4]$$

To produce an MR image, the values of k-space are simply acquired through application of gradient fields and subsequently inverse Fourier transformed. The use of gradient fields to produce an MR image won Mansfield and Lauterbur the Nobel prize in Medicine in 2003.

There are essentially two methods of 'getting around' in k-space to acquire its values. The first is labelled 'phase-encoding' and consists of the application of a gradient for a specific period of time prior to acquisition (i.e. k-space locations in a specific dimension are developed *before* the signal is acquired). The second method is labelled 'frequency-encoding' and consists of acquisition of k-space locations during the application of a gradient. Most standard Cartesian imaging methods use a combination of phase and frequency encoding (i.e. frequency along one dimension and phase along the other one or two). Phase-encoding is disadvantageous for imaging the rapidly decaying signal of the sodium nuclei as time is required to perform this encoding, during which the signal decays. A pure frequency-encoding technique is primarily used in this thesis in which the centre of k-space (i.e. $k = 0$) is acquired directly following excitation while a gradient field is simultaneously applied. k-Space is acquired on spokes projecting from the centre (often labelled radial or projection imaging).

1.3.2. The Discrete Fourier Transform and the MR Image

An image directly representing any object to be scanned in an MR experiment can be perfectly produced if the entirety of its continuous k-space, without any external modulation, can be Fourier transformed to produce the image. In practice, k-space must be discretely sampled to a finite extent in the presence of external modulation. Practical k-space acquisition is given in Eq. [1-5], following the point-source introduction to MR image generation in Eq. [1-2]. The distance in 1/m between sampled k-space locations is labelled k_{step}, k_{max} is the maximum value of k-space sampled, and $H_{(x_o)}(k)$ (also called the modulation transfer function – MTF) includes modulation of the point-source signal at location x_o.

$$F(k) = \sum_{m=-\infty}^{\infty} \left(S_{(x_o)} \cdot e^{-j2\pi x_o k}\right) \cdot H_{(x_o)}(k) \cdot \mathrm{rect}\left(\frac{k}{2 \cdot k_{max}}\right) \cdot \delta\left(k - \left(m \cdot k_{step}\right)\right) \quad [1\text{-}5]$$

The term $S_{(x_o)}$ is defined to be the NMR signal acquired at zero spatial frequency, or at the centre of k-space. Ideally the magnitude of the NMR signal produced by each point-source would remain constant throughout the acquisition of k-space, but this is rarely the case. Alterations in the NMR signal from its value at the centre of k-space are reflected in $H_{(x_o)}(k)$, which is defined to have a value of 1 at the centre of k-space in this description. The modulation of $H_{(x_o)}(k)$ can include the effects of local transverse magnetization relaxation, along with k-space sampling density and post-acquisition weighting.

The inverse Fourier transform of the sampled k-space of Eq. [1-5] is given below ('$*$' denotes convolution, and the scaling factor of the inverse Fourier transform has been left out)

$$\mathrm{Im}(x) = S_{(x_o)}\delta(x - x_o) * PSF_{(x_o)}(x) * \frac{1}{R}\mathrm{sinc}\left(\frac{x}{R}\right) * FoV \sum_{i=-\infty}^{\infty} \delta(x - i \cdot FoV)\,. \qquad [1\text{-}6]$$

Several new terms are introduced in Eq. [1-6], the first is the point spread function (PSF) which is the inverse Fourier transform of the MTF. If $H_{(x_o)}(k)$ is uniform across k-space, $PSF_{(x_o)}(x)$ will be a delta function, however, as mentioned above this is rarely the case. If $H_{(x_o)}(k)$ drops-off away from the centre of k-space the $PSF_{(x_o)}(x)$ will be spatially 'smeared' (down and out). In this case each point-source will contribute intensity to a larger volume in the image than a delta function. However, the total contribution of each point-source to the image will remain constant as the integral of $PSF_{(x_o)}(x)$ remains constant and equal to the value of $H_{(n_0X)}(0)$ = 1 (as will be discussed below). Because the total contribution of each point-source to the image is solely dependent on the acquired value at the centre of k-space, NMR contrast timings (such as TE) are always considered with respect to the centre of k-space.

The term (R) introduced in Eq. [1-6] is equal to $1/(2 \cdot k_{max})$, and often R^3 is listed as the voxel volume. Sampling k-space to a finite extent will result in an

additional convolution of the point source with a sinc function having a main-lobe width of 2R. When k-space is sampled to an infinite extent this sinc function will reduce to a delta function, however, this is far from practical. Sampling k-space to a reduced extent will broaden and scale the sinc function, spatially spreading the contribution of each point-source to the image. It should be noted that differences in k-space sampling extent do not alter the integral sum of values within the sinc function, and as such do not affect the total point-source contribution to the image.

The sinc function convolution will spread the signal contribution of each point-source to distant regions of the image. In a large uniform object the side-lobes of the sinc function will be 'cancelled' by integral summation of point-source contributions, however, sharp signal transitions in the object will generate visible ringing in the image (named Gibbs' ringing). To reduce the spatial extent of signal contribution to the image associated with sinc function convolution, a k-space filter (which would be included in the MTF of Eq. [1-5]) can be implemented (Chapters 2 - 4).

The term (FoV) introduced in Eq. [1-6] is equal to $1/\mathrm{k}_{\mathrm{step}}$, and is labelled the field of view. The result of the discrete k-space sampling requirement is that the image produced will be replicated at intervals of FoV. Point-sources at a distance greater than FoV/2 will contribute to the space within –FoV/2 to FoV/2 as a result of this replication, superimposing with other point-source contributions inside FoV. This well known problem is defined as aliasing, and $1/\left(2 \cdot \mathrm{k}_{\mathrm{step}}\right)$ must be less than the greatest signal contributing distance (the 'spatial' Nyquist criterion). For the frequency-encoding k-space sampling of this thesis, maximum signal contributing distances are bound by the Varian Inova's anti-aliasing filter. When a gradient G is applied during frequency-encoding, the phase of point-sources at $\mathrm{FoV}/2$ will evolve with frequency $\gamma \mathrm{G}(\mathrm{FoV}/2)$. This frequency can be set as the cut-off frequency (or frequency bandwidth – BW) for the anti-aliasing filter. It is

trivial to show that this frequency is half of the sampling frequency (SW) which produces k_{step} (Eq. [1-7], where τ_{samp} is the frequency encoding sampling dwell time), thus satisfying the 'temporal' Nyquist criterion.

$$BW = \gamma G \frac{FoV}{2} = \gamma G \frac{1}{2 \cdot k_{step}} = \gamma G \frac{1}{2\gamma G \tau_{samp}} = \frac{1}{2} SW \qquad [1\text{-}7]$$

It should be noted that the effects of replication associated with the sampling of k-space are not completely eliminated even with perfect filtering and critical sampling according to the Nyquist criterion. Both the PSF and the sinc functions will be continuous functions with infinite spatial extent (i.e. each point-source will contribute everywhere in the infinite image space as a result of these convolutions). The portions of the convolved signal intensity beyond FoV will contribute to the space within FoV as a result of replication. These replication contributions are typically very small, but do have some impact in the context of Non-Cartesian gridding (Appendix 2).

Practical computation of the inverse Fourier transform of Eq. [1-5] requires a practical limit on *m*, i.e.

$$Im(x) = \int_{-\infty}^{\infty} \sum_{m=-M/2}^{M/2-1} S_{(x_o)} \cdot e^{-j2\pi x_o k} \cdot H_{(x_o)}(k) \cdot rect\left(\frac{k}{2k_{max}}\right) \cdot \delta\left(k - \left(m k_{step}\right)\right) e^{j2\pi x k}\, dk\,. \qquad [1\text{-}8]$$

Replacing *k* with $m \cdot k_{step}$, Eq. [1-8] can be rewritten as

$$Im(x) = \sum_{m=-M/2}^{M/2-1} S_{(x_o)} \cdot e^{-j2\pi x_o m k_{step}} \cdot H_{(x_o)}[m k_{step}] \cdot rect\left[\frac{m k_{step}}{2k_{max}}\right] \int_{-\infty}^{\infty} \delta\left(k - \left(m k_{step}\right)\right) e^{j2\pi x k}\, dk\,, \qquad [1\text{-}9]$$

or as

$$\mathrm{Im}(x) = \sum_{m=-\mathrm{M}/2}^{\mathrm{M}/2-1} \mathrm{S}_{(\mathrm{x_o})} \cdot \mathrm{e}^{-\mathrm{j}2\pi \mathrm{x_o} m \mathrm{k_{step}}} \cdot \mathrm{H}_{(\mathrm{x_o})}\left[m\mathrm{k_{step}}\right] \cdot \mathrm{rect}\left[\frac{m\mathrm{k_{step}}}{2\mathrm{k_{max}}}\right] \mathrm{e}^{\mathrm{j}2\pi x m \mathrm{k_{step}}} . \quad [1\text{-}10]$$

Acknowledging that the image produced will be discrete, Eq. [1-10] can be rewritten as in Eq. [1-11] with $x = n\mathrm{X}$ (where X is the pixel / voxel size in the image), and $\mathrm{X} = 1/\left(\mathrm{k_{step}} \cdot \mathrm{M}\right)$, yielding what looks like the discrete Fourier transform (DFT).

$$\mathrm{Im}[n\mathrm{X}] = \sum_{m=-\frac{\mathrm{M}}{2}}^{\mathrm{M}/2-1} \mathrm{S}_{(\mathrm{n_0X})} \cdot \mathrm{e}^{-\mathrm{j}2\pi(\mathrm{n_0X}) m \mathrm{k_{step}}} \cdot \mathrm{H}_{(\mathrm{x_o})}\left[m\mathrm{k_{step}}\right] \cdot \mathrm{rect}\left[\frac{m\mathrm{k_{step}}}{2\mathrm{k_{max}}}\right] \mathrm{e}^{\mathrm{j}2\pi\frac{nm}{\mathrm{M}}} \quad [1\text{-}11]$$

$$\{0 \le n \le \mathrm{M}-1\}$$

The commonly used inverse DFT (which includes the scaling factor 1/M to reflect standard computation of the inverse DFT) is given in Eq. [1-12]. Inclusion of the variable b reflects the required summation limits of the DFT, and involves an effective swapping of sampled k-space halves (or 'fftshift' in Matlab).

$$\mathrm{Im}[n\mathrm{X}] = \frac{1}{\mathrm{M}} \cdot \sum_{m=0}^{\mathrm{M}-1} \mathrm{S}_{(\mathrm{n_0X})} \cdot \mathrm{e}^{-\mathrm{j}2\pi(\mathrm{n_0X}) b(m) \mathrm{k_{step}}} \cdot \mathrm{H}_{(\mathrm{n_0X})}\left[b(m)\mathrm{k_{step}}\right] \cdot \mathrm{rect}\left[\frac{b(m)\mathrm{k_{step}}}{2\mathrm{k_{max}}}\right] \mathrm{e}^{\mathrm{j}2\pi\frac{nm}{\mathrm{M}}} \quad [1\text{-}12]$$

$$\left\{b(m) = m \ (\mathrm{mod\ N}), \qquad -\frac{\mathrm{M}}{2} \le b \le \frac{\mathrm{M}}{2} - 1, \qquad 0 \le n \le \mathrm{M}-1\right\}$$

The inverse DFT of Eq. [1-12] governs MRI image formation. It can also be written in the alternative form of Eq. [1-13] below. It should be noted that M must be greater than or equal to $\mathrm{A} = 2\mathrm{k_{max}}/\mathrm{k_{step}}$ (or the sampled matrix dimension) for physical meaning.

$$\mathrm{Im}[n\mathrm{X}] = \frac{1}{\mathrm{M}} \cdot \sum_{m=0}^{\mathrm{M}-1} \mathrm{S}_{(\mathrm{n_0X})} \cdot \mathrm{e}^{-\mathrm{j}2\pi(\mathrm{n_0X})\frac{b(m)}{\mathrm{FoV}}} \cdot \mathrm{H}_{(\mathrm{n_0X})}\left[\frac{b(m)}{\mathrm{FoV}}\right] \cdot \mathrm{rect}\left[\frac{b(m)}{\mathrm{FoV}} \cdot \mathrm{R}\right] \mathrm{e}^{\mathrm{j}2\pi\frac{nm}{\mathrm{M}}} \quad [1\text{-}13]$$

$$\left\{b(m) = m \ (\mathrm{mod\ M}), \qquad -\frac{\mathrm{M}}{2} \le b \le \frac{\mathrm{M}}{2} - 1, \qquad 0 \le n \le \mathrm{M}-1\right\}$$

While the periodicity (at the rate of FoV) of the image produced has been absorbed into the inverse DFT equation, one should be aware that this periodicity is still present. The discrete image produced by inverse DFT is essentially a sampling of continuous image Eq. [1-6] (within the limits defined by FoV), and the functions in Eq. [1-6] without finite spatial extent (i.e. the sinc function, and for most practical cases the PSF function) will contribute values to the discrete image from replications beyond the extent of the image.

When M is greater than $\mathrm{A} = 2\mathrm{k}_{\max}/\mathrm{k}_{\mathrm{step}}$ (or the sampled matrix dimension), discrete k-space can be said to be zero-filled beyond $\mathrm{k}_{\max}$. The result is finer sampling of signal contributions to the image. Note, however, that the shape of each signal contribution does not change, i.e. the smearing of the PSF is not altered by zero-filling.

The inverse DFT of Eq. [1-13] can also be re-expressed as Eq. [1-14], where $\otimes$ denotes circular convolution

$$\mathrm{Im}_{(\mathrm{n_0X})}[n\mathrm{X}] = \mathrm{S}_{(\mathrm{n_0X})}(\mathrm{n_0X}) \otimes \mathrm{PSF}'_{(\mathrm{n_0X})}[n\mathrm{X}]\,. \qquad [1\text{-}14]$$

As with the continuous image of Eq. [1-6], the discrete image produced by DFT will be the integral sum of all the infinitesimal point-source contributions within the object scanned during the MRI experiment. For each point-source signal contribution, the $\mathrm{PSF}'_{(\mathrm{n_0X})}$ is effectively centred at continuous location n_0 in image space, multiplied with $\mathrm{S}_{(\mathrm{n_0X})}$, and sampled at the image matrix locations defined by n. The definition of $\mathrm{PSF}'_{(\mathrm{n_0X})}$ is given as

$$\mathrm{PSF}'_{(\mathrm{n_0X})}[n\mathrm{X}] = \frac{1}{\mathrm{M}} \cdot \sum_{m=0}^{\mathrm{M}-1} \mathrm{H}_{(\mathrm{n_0X})}\left[\frac{b(m)}{\mathrm{FoV}}\right] \cdot \mathrm{rect}\left[\frac{b(m)}{\mathrm{FoV}} \cdot \mathrm{R}\right] \mathrm{e}^{\mathrm{j}2\pi\frac{\mathrm{mn}}{\mathrm{M}}}\,, \qquad [1\text{-}15]$$

where the prime represents the fact that the inverse DFT produces a function that is not simply the convolution of the inverse Fourier transforms of the sampled $\mathrm{H}_{(\mathrm{n_0X})}$ and rect functions, but rather the circular convolution of the two inverse

DFT transforms. The inverse DFT of the rect function is also not simply a sinc function, but approaches one within image space when 'replication folding' is minimal (as is typically the case in practice). It should be noted that the inverse DFT produces a sampling of $\mathrm{PSF}'_{(\mathrm{n_0X})}$ at matrix locations *n*. The values of $\mathrm{PSF}'_{(\mathrm{n_0X})}$ at fractional locations of the image matrix can be found from zero-filling the k-space matrix (i.e. increasing M).

As mentioned previously, truncation of k-space yields convolution with a sinc function in image space. The sinc function has null locations spaced at distance R, and when R = X (i.e. no zero-filling) and $\mathrm{n_0}$ is an integer, a point-source contribution centred at $\mathrm{n_0}$ will contribute solely to the $\mathrm{n_0}$ matrix location. However, this is not the case when $\mathrm{n_0}$ is not an integer. When k-space is zero-filled the sinc function will be sampled more finely, and the effects of sinc function convolution may be more visible than when R = X (i.e. it is more likely that minimum and maximum values of the troughs and valleys associated with sinc function convolution will be sampled).

Because the DFT and the inverse DFT are transform pairs, the DFT of a discrete image produced in an MRI experiment can be directly stated as below.

$$\sum_{n=0}^{\mathrm{M}-1} \mathrm{Im}[n\mathrm{X}]\, \mathrm{e}^{-\mathrm{j}2\pi\frac{mn}{\mathrm{M}}} = \mathrm{S}_{(\mathrm{n_0X})} \mathrm{e}^{-\mathrm{j}2\pi(\mathrm{n_0X})\frac{b(m)}{\mathrm{FoV}}} \cdot \mathrm{H}_{(\mathrm{n_0X})}\left[\frac{b(m)}{\mathrm{FoV}}\right] \cdot \mathrm{rect}\left[\frac{b(m)}{\mathrm{FoV}} \cdot \mathrm{R}\right] \qquad [1\text{-}16]$$

$$\left\{ b(m) = m \ (\mathrm{mod\ M}), \qquad -\frac{\mathrm{M}}{2} \le b \le \frac{\mathrm{M}}{2} - 1, \qquad 0 \le m \le \mathrm{M} - 1 \right\}$$

By considering $m = 0$, it is readily apparent that the total signal contribution of any point-source to the discrete image is directly the acquired signal value at the centre of k-space (as stated previously for Eq. [1-6]). For this reason, when designing NMR pulse sequences for maximum signal or contrast, the value at the centre of k-space is of primary concern (as mentioned above). It is again noted that the shape of H(k) will not alter the total signal contribution of each point-

source to the image; the shape of H(k) will, however, change the shape of each signal contribution to the image, potentially smearing it out.

1.3.3. Image Intensity Dependence on Acquisition Parameters and Zero-Filling

While the total signal contribution to a discrete MR image is solely dependent on the associated signal value at the centre of k-space, image intensity can depend on the k-space acquisition parameters k_{step} and k_{max} (or FoV and R) along with the inverse DFT parameter M. The dependence of the value at the centre of the $PSF'_{(n_0X)}$ is given below

$$PSF'[0] \propto \frac{FoV}{R \cdot M} \ . \qquad [1\text{-}17]$$

When the MTF remains constant, Eq. [1-17] describes PSF scaling and the effects on image intensity can be introduced as below.

When M is increased (i.e. the case of zero-filling) the magnitude of the PSF will be reduced in inverse proportion to this increase, however, the PSF will be more finely sampled in direct proportion to this increase. The decrease in image intensity maintains a constant total signal contribution. This intensity decrease also follows from solution to Parseval's theorem, which is stated below for the DFT where $Im[n]$ is the inverse DFT of $F[m]$.

$$\sum_{n=0}^{M-1} |Im[n]|^2 = \frac{1}{M} \sum_{m=0}^{M-1} |F[m]|^2 \qquad [1\text{-}18]$$

From Eq. [1-17] it is apparent that image intensity is directly dependent on FoV. A decrease in FoV when all else remains constant yields a decrease in the value of X and increased sampling of any signal contribution. The decrease in image intensity again maintains a constant total signal contribution. Note, however, that the shape of $PSF'_{(n_0X)}$ (particularly in its periphery) can be (very slightly) altered

by change in FoV. Direct scaling of the entire signal contribution with FoV assumes minimum contribution to 'replication space' beyond the FoV, which (in general) is effectively the case.

Although each point-source contribution to the image is also inversely scaled by R (when all else remains constant in Eq. [1-17]), within a sufficiently large uniform object the final image intensity (or the integral sum of each point-source contribution) remains 'constant.' When R is decreased, the shape of each point-source signal contribution to the image is spatially stretched, and inversely scaled in proportion to the increase in R (maintaining a constant total signal contribution). However, the spatially stretched signal contribution from each infinitesimal point-source will contribute to a greater number of matrix locations within the image. If a uniform object is sufficiently large, the average total sum of contributions at matrix locations 'sufficiently within' the object (i.e. not at the edges) remains the 'same' (the term *average* is included as superimposed ringing throughout the object will be altered with change in R).

For any 'sufficiently large' uniform (with respect to signal) object, its image intensity will be inversely scaled by M, 'directly' scaled by FoV (assuming minimal replication folding), but remain 'unmodulated' by R. This is perhaps a break from the traditional way of thinking about image intensity dependence on voxel volume (where $R_{(x,y,z)}$ would typically define a 3D voxel). Traditionally, image intensity in an MRI experiment is thought of as being proportional to voxel volume, but this is a 0-dimensional 'spectroscopy' way of thinking about things, where signal intensity is simply proportional to the total number of spins excited. For the MRI experiment, the total number of spins excited remains constant regardless of how their signal phase is made to evolve or how k-space is sampled.

1.3.4. Image Noise

It is generally considered that the noise present at the input to the discrete sampler (or the analog to digital converter) in an MRI experiment is additive white Gaussian noise with variance σ_s^2 (zero mean is implied). This noise is dependent on the resistive load of the coil, which includes the series resistance of the linear components, as well as (and predominantly for typical in-vivo experiments) the effective resistance associated with the object in the coil. Sampled noise is also dependent on the noise figure of the system receive chain, and isolation from additional additive sources such as the transmit power amplifier. Finally, the sampled noise power is dependent on the bandwidth of the anti-aliasing filter (BW), which is of primary concern to this introduction. The power spectral density (PSD) of the input noise will be expressed as Eq. [1-19], where σ_o^2 represents the sum of thermal noise contributions and their dependencies as described above.

$$\mathrm{PSD}(f) = \sigma_s^2 = \sigma_o^2 \cdot \mathrm{BW} \qquad [1\text{-}19]$$

If every location of the k-space matrix is sampled exactly once, each location will be associated with a noise power of σ_s^2. As σ_o^2 and BW (typically) remain constant throughout an MRI experiment, a discrete spatial PSD associated with each k-space matrix location for an MRI experiment can be given as Eq. [1-20].

$$\mathrm{PSD}[m] = \sigma_o^2 \cdot \mathrm{BW} \qquad [1\text{-}20]$$

The discrete spatial PSD can be modified by two means. One is the additional sampling of each k-space matrix location (or sampling density, given as $\mathrm{SD}[m]$), and the other is post-acquisition weighting ($\mathrm{W}[m]$), or the scaling of each matrix location. Noise power is directly related to noise summing and proportional to the square of noise scaling. The discrete, windowed, spatial PSD is given in Eq. [1-21], where A is the number of sampled k-space matrix locations ($\mathrm{A} = 2\mathrm{k}_{max}/\mathrm{k}_{step} = \mathrm{FoV/R}$).

$$\mathrm{PSD}[m] = \sigma_o^2 \cdot \mathrm{BW} \cdot \mathrm{SD}[b(m)] \cdot \mathrm{W}^2[b(m)] \cdot \mathrm{rect}[b(m)/\mathrm{A}] \qquad [1\text{-}21]$$

Inverse Fourier transform of the continuous spatial noise power spectral density yields the autocorrelation function $\mathrm{r}(x)$.

$$\mathrm{r}_x(x) = \mathrm{FT}^{-1}\{\mathrm{PSD}(k)\} \quad [1\text{-}22]$$

Inverse DFT of the discrete PSD yields the discrete autocorrelation function $\mathrm{r}_\mathrm{D}[n]$.

$$r_\mathrm{D}[n] = \frac{(\sigma_o^2 \cdot \mathrm{BW})}{\mathrm{M}^2} \sum_{m=0}^{\mathrm{M}-1} \mathrm{SD}[b(m)] \cdot \mathrm{W}^2[b(m)] \cdot \mathrm{rect}[b(m)/\mathrm{A}] e^{\mathrm{j}\frac{2\pi}{\mathrm{M}}nm} \quad [1\text{-}23]$$

The subscript 'D' is used to indicate that $\mathrm{r}_\mathrm{D}[n]$ does not have the same shape as $\mathrm{r}(x)$ but contains the effects of 'replication folding' associated with PSD sampling (however, the shape of $\mathrm{r}_\mathrm{D}[n]$ will approach that of $\mathrm{r}(x)$ when A is large). The factor $1/\mathrm{M}^2$ accounts for the scaling associated with typical calculation of the inverse DFT. The value of the autocorrelation function at zero is the variance of the noise in image space (σ_n^2).

$$\sigma_n^2 = r[0] = \frac{(\sigma_o^2 \cdot \mathrm{BW})}{\mathrm{M}^2} \sum_{m=0}^{\mathrm{M}-1} \mathrm{SD}[b(m)] \cdot \mathrm{W}^2[b(m)] \cdot \mathrm{rect}[b(m)/\mathrm{A}] \quad [1\text{-}24]$$

Image noise variance dependence can be re-expressed by replacing the anti-aliasing filter BW with its Nyquist link to sampling rate, i.e. $\mathrm{BW} = \mathrm{A}/2\mathrm{T}_\mathrm{RO}$.

$$\sigma_n^2 \propto \frac{\mathrm{A}}{\mathrm{T}_\mathrm{RO} \cdot \mathrm{M}^2} \sum_{m=0}^{\mathrm{M}-1} \mathrm{SD}[b(m)] \cdot \mathrm{W}^2[b(m)] \cdot \mathrm{rect}[b(m)/\mathrm{A}] \quad [1\text{-}25]$$

Introducing the relative power spectral density (rPSD), Eq. [1-25] can be re-stated as

$$\sigma_n^2 \propto \frac{\mathrm{A}^2}{\mathrm{T}_\mathrm{RO} \cdot \mathrm{M}^2} \sum_{m=0}^{\mathrm{A}-1} \mathrm{rPSD}[b(m)] \quad [1\text{-}26]$$

where,

$$\mathrm{rPSD}[b(m)] = \mathrm{SD}[b(m)] \cdot \frac{\mathrm{W}^2[b(m)]}{\mathrm{A}}. \quad [1\text{-}27]$$

Replacing A with the dependency $\mathrm{A} = \mathrm{FoV}/\mathrm{R}$ yields

$$\sigma_n^2 \propto \frac{\mathrm{FoV}^2}{\mathrm{T_{RO}} \cdot \mathrm{R}^2 \cdot \mathrm{M}^2} \sum_{m=0}^{\mathrm{A}-1} \mathrm{rPSD}[b(m)] \,. \qquad [1\text{-}28]$$

Finally, expressing the effects of 'global' k-space averaging with its dependence on total scan time ($\mathrm{T_{IM}}$)

$$\sigma_n^2 \propto \frac{\mathrm{FoV}^2}{\mathrm{T_{IM}} \cdot \mathrm{T_{RO}} \cdot \mathrm{R}^2 \cdot \mathrm{M}^2} \sum_{m=0}^{\mathrm{A}-1} \mathrm{rPSD}[b(m)] \qquad [1\text{-}29]$$

gives the direct dependency of image noise on the k-space acquisition attributes and zero-filling.

1.3.5. k-Space Acquisition and SNR

As described previously, image intensity is 'directly' proportional to FoV/M. As the standard deviation of noise produced in the image is also proportional to FoV/M it can be stated that altering FoV (assuming imaging times remain constant) and k-space zero-filling have no effect on image SNR. However, given that image intensity remains 'constant' with change in R for objects that are sufficiently large, it can also be stated that within sufficiently large objects SNR will be proportional to R. The resultant SNR dependence of k-space acquisition design is given in Eq. [1-30].

$$\mathrm{SNR} \propto \mathrm{R} \cdot \sqrt{\mathrm{T_{IM}} \cdot \mathrm{T_{RO}}} \left(1 \Big/ \sum_{m=0}^{\mathrm{A}-1} \mathrm{rPSD}[b(m)] \right) \qquad [1\text{-}30]$$

1.3.6. The Modulation Transfer Function (H(k))

The function $H_{(n_0X)}(k)$ is given the label 'modulation transfer function' and can be split into two parts (Eq. [1-31]).

$$H_{(n_0X)}\left[\frac{b(m)}{FoV}\right] = M_{xy(n_0X)}\left[\frac{b(m)}{FoV}\right] + \Gamma\left[\frac{b(m)}{FoV}\right] \quad [1\text{-}31]$$

The function $M_{xy(n_0X)}$ is used to define NMR signal dependency with time for each point-source in the object. As stated previously, it is assigned the value of one at the centre of k-space (i.e. the NMR signal intensity at the centre of k-space is included in the $S_{(n_0X)}$ constant). For standard single-quantum sodium imaging (which typically does not involve spin-echo refocusing) $S_{(n_0X)}M_{xy(n_0X)}$ can be effectively defined by T_2* decay and the time following excitation at which the k-space locations are sampled. However, it should be noted that $M_{xy(n_0X)}$ for sodium imaging is not necessarily the sum of intrinsic T_2 decay and the dephasing envelope T_2', the development of other spin 3/2 coherences and their evolution into observable single quantum coherence can affect the $M_{xy(n_0X)}$ shape. An example is triple quantum filtering, briefly described in Chapter 1.5.

The function $\Gamma[m]$ includes both sampling density, $SD[m]$, and post-acquisition weighting, $W[m]$, and is very often designed to be uniform.

$$\Gamma[m] = SD[m] \cdot W[m] \quad [1\text{-}32]$$

In this introduction $\Gamma[m]$ is assumed to retain a value of one at the centre of k-space. The trivial scaling of the $\Gamma[m]$ function (and the modulation transfer function) by post-acquisition weighting will increase image signal and noise in equal proportion. Scaling the $\Gamma[m]$ function by sampling density is equivalent to global averaging producing the associated SNR increase.

1.3.7. Sampling Efficiency

Sampling efficiency is concerned with the generation of a desired $\Gamma[m]$ in the most SNR efficient manner (for constant scan duration). It has been shown that sampling efficiency is maximal when sampling density matches the desired $\Gamma[m]$ shape (55). Any requirement for non-uniform post-acquisition weighting of sampling points will reduce SNR from the value that could have been attained if sampling density had been altered as desired. The relative increase in noise variance associated with post-acquisition weighting is given in Eq. [1-33] (from (55)), where σ^2_{PAW} is the image noise variance in the post-acquisition weighted case and σ^2_{SD} is the image noise variance in the sampling density designed case. The variable λ is used to describe each sampling point, and L reflects the total number of sampling points.

$$\frac{\sigma^2_{\mathrm{PAW}}}{\sigma^2_{\mathrm{SD}}} = \frac{\mathrm{L} \cdot \sum_\lambda \mathrm{W}^2[\lambda]}{(\sum_\lambda \mathrm{W}[\lambda])^2} \qquad [1\text{-}33]$$

Derivation (not presented to the author's knowledge) of a similar equation with respect to the sampling efficiency of k-space filtering is given in Appendix 7.

1.4. 3D Twisted Projection k-Space Acquisition

As previously mentioned, standard 3D radial k-space acquisition 'suffers' from large sampling density variation across k-space. Sampling density can be defined for radial imaging as the time spent sampling a spherical shell in proportion to the volume of that shell

$$\frac{\mathrm{d}\tau}{\mathrm{dV}} = \frac{\mathrm{d}\tau}{4\pi \mathrm{k}_{\mathrm{max}}^2 r^2 \mathrm{d}r}, \qquad [1\text{-}34]$$

where the variable τ is a dimensionless fraction of the time required for a projection to reach the extent of k-space, and r is a radial fraction of the sampled k-space extent. Within a Cartesian k-space matrix Eq. [1-34] could be rewritten as

$$\frac{\mathrm{d}\tau}{\mathrm{dV}} = \frac{\mathrm{d}\tau}{4\pi((\mathrm{A}-1)/2)^2 r^2 \mathrm{d}r}, \qquad [1\text{-}35]$$

where A is the number of matrix locations across the Cartesian k-space matrix. When $4\pi\big((\mathrm{A}-1)/2\big)^2$ uniformly spaced projections are implemented the sampling density is

$$\mathrm{SD}(r) = \frac{\mathrm{d}\tau}{r^2 \mathrm{d}r}. \qquad [1\text{-}36]$$

At the edge of the sampled k-space sphere the sampling density will be 1, describing critical Nyquist sampling. Uniform 'over-projectioning' is equivalent to a uniform averaging of k-space and can be included as such in noise variance calculation. For standard radial imaging $\mathrm{d}\tau/\mathrm{dr} = 1$, and the sampling density throughout k-space is proportional to $1/\mathrm{r}^2$.

If a uniform $\Gamma(r)$ is desired, each acquired sampling point must be post-acquisition weighted as r^2 according to its relative radial location. It is simple to calculate the sampling inefficiency of standard radial imaging for the generation of a uniform $\Gamma(r)$ using an integral form of Eq. [1-33] (from the previous

section). This is highlighted below where the volume of the k-space sphere is proportional to the total number of k-space matrix locations within the sphere, and the total number of radial spokes (or 'projections') implemented is proportional to the surface area of the sampled sphere (k_{max} is the radius of the sampled k-space sphere).

$$\frac{\sigma_{\mathrm{PAW}}^2}{\sigma_{\mathrm{SD}}^2} = \frac{\frac{4}{3}\pi k_{\max}^3 \cdot 4\pi k_{\max}^2 \int_0^{k_{\max}} (r^2)^2 \, dr}{\left(4\pi R^2 \int_0^{k_{\max}} r^2 \, dr\right)^2} = 5/3 \qquad [1\text{-}37]$$

For standard radial imaging the standard deviation of noise will be 29% greater when compared to a case where the entirety of the sphere was sampled uniformly.

Into the context of standard radial acquisition's sampling inefficiency and large number of required projections, 3D twisted projection imaging (TPI) was presented in 1997 for sodium imaging (30). The concept is to slow the radial evolution of each projection beyond a given fraction of sampled k-space (labelled *p*) such that sampling density beyond *p* remains the constant value of that at *p*. This is done while maintaining a constant sampling speed, and to maintain a constant sampling speed projections are made to twist. As a result, each projection samples much more of k-space before reaching the edge of the sampled extent, and the required number of projections to critically fill k-space is decreased. 3D TPI is an implementation of 2D TWIRL (56) on sets of cones. A brief derivation and description of the equations governing TPI are given below.

The required projection radial evolution to maintain a desired sampling density beyond radial fraction *p* can be solved from solution to Eq. [1-36], i.e.

$$\frac{dr}{d\tau} = \frac{1}{\mathrm{SD}(r) \cdot r^2}, \quad r(\tau = 0) = p \qquad [1\text{-}38]$$

with the requirement that

$$\mathrm{SD}(p) = \frac{1}{p^2}. \qquad [1\text{-}39]$$

This requirement reflects the fact that at the initiation of radial evolution alteration the sampling density must be equal to that of standard radial acquisition.

If uniform sampling density is to be maintained beyond *p*, then Eq. [1-38] must be solved for a constant value of SD = $1/p^2$, yielding

$$r(\tau) = (3p^2\tau + p^3)^{1/3}, \qquad [1\text{-}40]$$

where Eq. [1-40] describes the radial evolution beginning at $r = p$. The total relative projection length (τ_{Tot}), in proportion to that of a standard straight projection, can be found from solution to Eq. [1-40] for $r(\tau) = 1$ and the addition of the relative time required to sample the initial straight segment before the initiation of radial evolution.

$$\tau_{\mathrm{Tot}} = \frac{1 - p^3}{3p^2} + p \qquad [1\text{-}41]$$

For small values of p the relative length of each projection will be substantially increased from that of standard radial imaging.

Although TPI was initially introduced for the generation of uniform sampling density, Eq. [1-38] can be used to solve radial evolution for a very wide range of sampling densities. This was also proposed by Boada in 1997 (29). While Boada's purpose was to facilitate reduced readout duration under a hardware constraint, it is proposed in this thesis that the logical radial evolution altered design is one that produces a k-space filtering shape for the minimization of ringing artifact (Chapter 2). Another radial evolution altered design is also presented in this thesis and involves the *compensation* of the T_2 relaxation with sampling density to produce any desired MTF in the presence of relaxation (Chapter 4). For the 'non-

trivial' SD(r) shapes presented in this paper Eq. [1-38] is solved numerically (using Matlab).

While radial evolution slows to achieve a desired sampling density for TPI, the speed of sampling throughout k-space is designed to remain constant and equal to that before the initiation of radial evolution alteration $(\mathrm{d}r/\mathrm{d}\tau = \upsilon = 1)$. The speed of positional evolution in terms of spherical coordinates is given in Eq. [1-42], where (ϕ) and (θ) are the polar and azimuthal angles respectively (from http://mathworld.wolfram.com/SphericalCoordinates.html).

$$\upsilon = 1 = \sqrt{\dot{r}^2 + r^2\dot{\theta}^2\sin^2(\phi) + r^2\dot{\phi}^2} \qquad [1\text{-}42]$$

When 3D TPI is implemented on sets of cones, as suggested by (30) (and done in this thesis), the polar angle is held constant throughout each trajectory. In this case the azimuthal angle must evolve according to Eq. [1-43].

$$\frac{\mathrm{d}\theta}{\mathrm{d}\tau} = \sqrt{\frac{1 - \left(\frac{\mathrm{d}r}{\mathrm{d}\tau}\right)^2}{r^2(\tau)\sin^2(\phi)}} \qquad [1\text{-}43]$$

Formal solution to Eq. [1-43] for the case of uniform sampling density production is given in (30). For the 'non-trivial' SD(r) shapes presented in this paper Eq. [1-43] was solved numerically together with Eq. [1-38]. See Appendix 1, **Figure A1-1** for an image of a three dimensional twisted projection.

The advantage of twisting each projection, or designing each projection to maintain constant sampling speed while radial evolution slows to produce the desired sampling density, is that with increased projection length each projection will sample many more locations within the k-space sphere than standard straight projections. The maintenance of constant sampling density of $1/p^2$ beyond p implies that k-space will be globally oversampled beyond p to the extent of $1/p^2$

when $4\pi\left((A-1)/2\right)^2$ projections are implemented. Global oversampling is unnecessary and as a result the number of projections required to critically fill k-space can be reduced. In theory, if the sample density at p is maintained throughout k-space the number of projections required to meet the Nyquist criterion is related to the relative radius p (rather than $r = 1$) and could be reduced as p^2 from the case of standard radial imaging. For TPI, the Nyquist criterion within each cone requires that the number of projections filling the cone can only be reduced by the factor p, and the number of cones required cannot be reduced. However, a reduction in the number of required projections by the factor p can be substantial especially when p is small.

Although a reduction in the number of projections required to fully sample k-space may be beneficial in some cases, this is not necessarily the case for in-vivo sodium imaging. Because sodium imaging is a low signal (low concentration) application, k-space matrix dimensions are typically small and scan times typically long (for the purpose of increasing SNR). Because sodium in-vivo T_1 values are also short (< 65 ms @ 4.7T), in many practical in-vivo sodium imaging scenarios the entirety of k-space can be filled with straight (un-twisting) projections in a 'reasonable' scan time. For this reason the twisting aspect of TPI with its associated reduction in number of required projections is not its most important aspect. Of much greater importance is simply the alteration of radial evolution. 3D radial sampling density altered k-space acquisition without twisting has been very recently presented (36), and is essentially TPI without the maintenance of constant sampling speed.

As an aside, a novel technique that allows both the polar *and* azimuthal angles to evolve during the projection readout and facilitates projection reduction toward that of p^2 was developed and presented at the ISMRM non-Cartesian workshop in Sedona (Stobbe, Beaulieu, 2007, (144)), While this technique may find value in a proton MRI setting, no particular value is suggested for sodium imaging.

1.5. Quantum Mechanics of the Spin 3/2 Sodium Nucleus

Although this thesis is by no means intended to be one of a quantum mechanical nature, the quantum mechanics of spin 3/2 nuclei are nevertheless introduced to provide some consideration of the unique aspects of spin 3/2 NMR. This section provides some background to the Sodium Spin Sequence ("Triple-S") simulator created during this thesis, which involves a direct implementation of coupled differential equations defining the evolution of the density operator given by (71,145,146) (Appendix 6).

The ^{23}Na nucleus has 11 protons and 12 neutrons, and it is from the eleventh unpaired nucleon that the nucleus derives its net angular momentum (147). The combination of angular momentum and intrinsic proton spin yields a nuclear spin for ^{23}Na of $I = {}^{3}/_{2}$ (148,149). Discussion of the consequences of spin $^{3}/_{2}$ and its difference from that of Hydrogen (^{1}H, i.e. proton, $I = {}^{1}/_{2}$) will begin with discussion of the sodium spin ensemble within a large magnetic field. Following description of the density matrix and operator, the quadrupole Hamiltonian (the preponderant interaction experienced by sodium nuclei in biological environments) will be introduced and its effect on spectral splitting and relaxation given. Finally, evolution of the density operator describing the polarization of the spin ensemble will be addressed in the context of the particularly useful irreducible tensor operators.

1.5.1. The Sodium Spin Ensemble in a Large Magnetic Field

The sodium nucleus has four 'spin-states' associated with the orientation of the spatially quantized nuclear angular momentum vector ($\boldsymbol{I}$), which has a magnitude $|\boldsymbol{I}| = \sqrt{I(I+1)} = \sqrt{15}/2$, and a z-component ($I_z$) quantized according to its eigenvalues: $m = -{}^{1}/_{2}, {}^{1}/_{2}$ for proton and $m = -{}^{3}/_{2}, -{}^{1}/_{2}, {}^{1}/_{2}, {}^{3}/_{2}$ for sodium (**Figure 1-1**) (150-152).

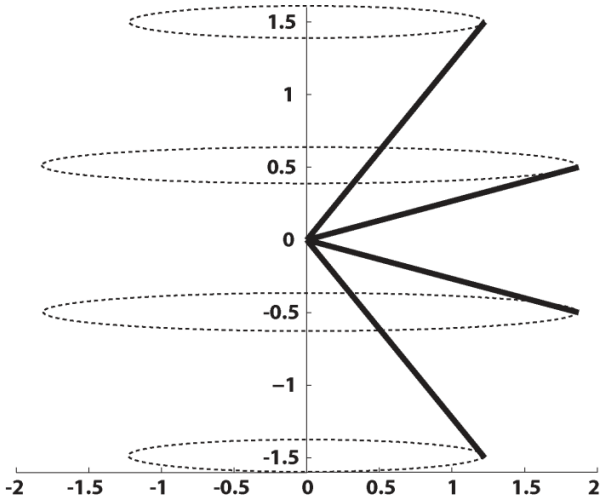

Figure 1-1: Depiction of the spatial quantization of nuclear angular momentum for spin 3/2. While the z-component (along the vertical axis) and magnitude values are defined for each spin-state, the x and y components are not (depicted by the dotted ellipsoids).

The wave-function for each nuclear spin can be expressed as Eq. [1-44] (152-154),

$$\Psi = \sum_j a_{m_j} |m_j\rangle \qquad [1\text{-}44]$$

where the a_m terms are complex constants associated with the probabilities of each spin-state (that differ for each nuclear spin within an ensemble), and the $|m\rangle$ terms represent the spin-states. The quantum mechanical probability of finding a spin in state $|m\rangle$ is equal to the magnitude of a_m, and can be found from the inner product $\langle\Psi_m|\Psi\rangle$ (where the angle brackets define the inner product), as the spin-states are orthonormal, i.e. $\langle m_j|m_{j=k}\rangle = 1$, and $\langle m_j|m_{j\neq k}\rangle = 0$.

$$\langle\Psi_m|\Psi\rangle = a_m^*\langle m|\Psi\rangle = a_m^* a_m \qquad [1\text{-}45]$$

The use of angle brackets in quantum mechanics is defined as the Dirac notation (152,153), and often the 'bra' $\langle\Psi|$ and 'ket' $|\Psi\rangle$ terms are separated to label wave-

functions or spin-states as above. The term $\langle\Psi|OP|\Psi\rangle$ defines the inner product following operation on the ket by a given operator 'OP' (for example, the operator I_z given above weights each spin-state (or ket term) by its z-component of angular momentum). If the operator is associated with a physical observable, $\langle\Psi|OP|\Psi\rangle$ yields the quantum mechanical expectation of that observable.

The interaction energy associated with a nuclear magnetic moment μ and a magnetic field B_o is given by the scalar product below:

$$E = -\mu \cdot B_o \quad [1\text{-}46]$$

where

$$\mu = \hbar\gamma I \quad [1\text{-}47]$$

and γ is the gyromagnetic ratio, which for sodium is 11.26 MHz/T (roughly ¼ that of proton). Assigning the z-axis to be along the direction of B_0, the (Zeeman) Hamiltonian can be defined as:

$$\mathcal{H}_Z = \hbar\gamma I_z B_o \quad [1\text{-}48]$$

In the presence of the static Zeeman Hamiltonian each wave-function will evolve with time according to Schrodinger's equation,

$$i\hbar\dot{\Psi} = \mathcal{H}\Psi \quad [1\text{-}49]$$

with solution given below (153)

$$\Psi(t) = \sum_j a_{m_j} \exp\left(i m_j \gamma B_0 t\right)|m_j\rangle \quad [1\text{-}50]$$

The quantum mechanical expectation value of a magnetic dipole along the z-axis (labelled $\langle\mu_z\rangle$), where $\mu_z = \hbar\gamma I_z$, is given in Eq. [1-51] for a sodium nucleus within a large magnetic field.

$$\langle\mu_z\rangle = \gamma\hbar\langle\Psi(t)|I_z|\Psi(t)\rangle = \gamma\hbar\sum_j m_j \cdot a^*_{m_j} a_{m_j} \quad [1\text{-}51]$$

The time-dependent phase term of Eq. [1-50] is cancelled, and the expectation value for a magnetic dipole along the z-axis in a large magnetic field is solely associated with the I_z eigenvalues and probabilities of each spin-state (Eq. [1-52] for proton and Eq. [1-53] for sodium).

$$\langle \mu_z \rangle_{\text{proton}} = \frac{\gamma\hbar}{2}\left(a_{m_1}^* a_{m_1} - a_{m_2}^* a_{m_2}\right) \quad [1\text{-}52]$$

$$\langle \mu_z \rangle_{\text{sodium}} = \frac{\gamma\hbar}{2}\left(3 \cdot a_{m_1}^* a_{m_1} + a_{m_2}^* a_{m_2} - a_{m_3}^* a_{m_3} - 3 \cdot a_{m_4}^* a_{m_4}\right) \quad [1\text{-}53]$$

Given the orientation of nuclear angular momentum associated with each spin-state, a magnetic moment projection along the transverse plane is also to be expected for each nuclear spin. To calculate the expectation value $\langle \mu_x \rangle = \gamma\hbar\langle I_x \rangle$, the raising and lowering operators, I_+ and I_-, are introduced with function to increase or decrease the wave-function spin-state (i.e. to states with greater or less projection along the z-axis respectively) (Eqs. [54, 55]).

$$I_\pm |m_j\rangle = \left(\sqrt{I(I+1) - m_j\left(m_j \pm 1\right)}\right)|m_{j\pm1}\rangle \quad [1\text{-}54]$$

$$I_+ |m_{max}\rangle = 0 \quad \& \quad I_- |m_{min}\rangle = 0 \quad [1\text{-}55]$$

The I_x and I_y operators can be expressed as linear combinations of these raising and lowering operators (Eq. [1-56]) (152,153,155).

$$I_x = \frac{1}{2}(I_+ + I_-) \quad \& \quad I_y = \frac{-i}{2}(I_+ - I_-) \quad [1\text{-}56]$$

The expectation value for a magnetic moment along the x-axis is given below:

$$\langle \mu_x \rangle = \gamma\hbar\langle \Psi(t)|I_x|\Psi(t)\rangle = \gamma\hbar \sum_{j,j'} a_{m_{j'}}^* a_{m_j} \langle m_{j'}|I_x|m_j\rangle \exp\left(i\gamma B_0\left(m_{j'} - m_j\right)t\right) \quad [1\text{-}57]$$

For a proton spin system with two spin-states the expectation value $\langle \mu_x \rangle_{\text{proton}}$ is given in Eq. [1-58]. If the complex $'a'$ constants are expressed according to Eq. [1-59], then $\langle \mu_x \rangle_{\text{proton}}$ can be expressed according to Eq. [1-61]. As can be seen,

for nuclei within a large magnetic field the expectation value of a magnetic dipole in the x – y plane rotates at the Larmor frequency with phase determined by the combination of adjacent spin-state probability constants.

$$\langle \mu_x \rangle_{\text{proton}} = \frac{\gamma\hbar}{2}\left(a^*_{m_2}a_{m_1} + a^*_{m_1}a_{m_2}\right)\exp(i\omega_0 t) \quad [1\text{-}58]$$

$$a_{m_j} = \mathrm{A_j}e^{-i\alpha_j} \quad [1\text{-}59]$$

$$\phi_{21} = \alpha_2 - \alpha_1 \quad [1\text{-}60]$$

$$\langle \mu_x \rangle_{\text{proton}} = \gamma\hbar \mathrm{A_1A_2}\cos(\phi_{21} + \omega_0 t) \quad [1\text{-}61]$$

$$\langle \mu_y \rangle_{\text{proton}} = -\gamma\hbar \mathrm{A_1A_2}\sin(\phi_{21} + \omega_0 t) \quad [1\text{-}62]$$

Likewise, the sodium expectation value $\langle \mu_x \rangle_{\text{sodium}}$ can be expressed as below, and is the sum of three oscillating components.

$$\langle \mu_x \rangle_{\text{sodium}} = \frac{\gamma\hbar}{2}\{\sqrt{3}\left(a^*_{m_2}a_{m_1} + a^*_{m_1}a_{m_2}\right) + 2\left(a^*_{m_3}a_{m_2} + a^*_{m_2}a_{m_3}\right) + \sqrt{3}\left(a^*_{m_4}a_{m_3} + a^*_{m_3}a_{m_4}\right)\}\exp(i\omega_0 t) \quad [1\text{-}63]$$

$$\langle \mu_x \rangle_{\text{sodium}} = \gamma\hbar\{\sqrt{3}\mathrm{A_1A_2}\cos(\phi_{21} + \omega_0 t) + 2\mathrm{A_2A_3}\cos(\phi_{32} + \omega_0 t) + \sqrt{3}\mathrm{A_4A_3}\cos(\phi_{43} + \omega_0 t)\} \quad [1\text{-}64]$$

In practice we are concerned with not one, but many, many spins. In this case the statistical expectation value associated with a given spin-state for the spin system, or ensemble, is written as $\overline{a^*_m a_m}$. In thermal equilibrium within a large magnetic field the ensemble expectation values for each spin-state will not be equal, but will follow the Boltzmann distribution with probability $\propto \exp(-\mathrm{E}_m/\mathrm{kT})$, where E_m is the energy associated with each eigenstate (152). Because the distribution differences between spin-states will be extremely small, the exponential can be expanded as Eq. [1-65] (where $Z = (2I + 1)$ is the number of spin-states, 2 for proton and 4 for sodium).

$$\overline{a_m^* a_m} \approx \frac{1}{Z}(1 + m\hbar\gamma \mathrm{B}_0/\mathrm{kT}) \quad [1\text{-}65]$$

To simplify calculation, the ensemble spin-state expectation values are generally given in terms of deviation from equilibrium while removing the extraneous (to calculation) constants. As can be seen, with this expression the ensemble spin-state expectation values in thermal equilibrium within a large magnetic field are directly the I_z eigenvalues.

$$\overline{c_m^* c_m} = m \quad [1\text{-}66]$$

As a result of the ensemble spin-state expectation differences, an ensemble average magnetic dipole (or longitudinal magnetization) will be generated along the z-axis in a large magnetic field. This magnetization, which is proportional to the maximum signal that can be produced in an NMR experiment, is directly dependent on B_0. It is for this reason that greater static magnetic fields have been sought in which to do NMR experiments.

From experiment it is well known that at thermal equilibrium there is no net ensemble magnetization rotating in the x-y plane at the Larmor frequency (transverse magnetization), as such a rotating magnetic field would produce an EMF in the detection coil (tuned to the Larmor frequency). Although the expectation value of a transverse magnetic dipole for a single wave function oscillates in time at the Larmor frequency, it must be the case that the phase terms of Eq. [1-64] are randomly distributed amongst the spins in the ensemble at equilibrium.

1.5.2. The Density Matrix / Operator

The density matrix is a matrix of the average spin ensemble products of state probability values, $\overline{c_{m_j}^* c_{m_k}}$, which for spin $^3/_2$ is of size 4 x 4. The ensemble average expectation value for an observable such as a magnetic dipole along the z-axis or $\overline{\langle \mu_z \rangle}$ is then proportional to the trace of the density matrix multiplied with the operator matrix (shown in Eq. [1-67] for sodium).

$$\overline{\langle \mu_z \rangle} \propto \overline{\langle I_z \rangle} = \mathrm{Tr}\left\{ \begin{bmatrix} \overline{c_{m_1}^* c_{m_1}} & \cdots & \overline{c_{m_4}^* c_{m_1}} \\ \vdots & \ddots & \vdots \\ \overline{c_{m_1}^* c_{m_4}} & \cdots & \overline{c_{m_4}^* c_{m_4}} \end{bmatrix} \cdot \begin{bmatrix} \langle m_1|I_z|m_1\rangle & \cdots & \langle m_1|I_z|m_4\rangle \\ \vdots & \ddots & \vdots \\ \langle m_4|I_z|m_1\rangle & \cdots & \langle m_4|I_z|m_4\rangle \end{bmatrix} \right\} \quad [1\text{-}67]$$

At thermal equilibrium within a large magnetic field the density matrix (labelled DM) for the sodium nucleus is given in Eq. [1-68].

$$\mathrm{DM}_{\mathrm{equilbrium}} = \frac{1}{2}\begin{bmatrix} 3 & 0 & 0 & 0 \\ 0 & 1 & 0 & 0 \\ 0 & 0 & -1 & 0 \\ 0 & 0 & 0 & -3 \end{bmatrix} \quad [1\text{-}68]$$

Of particular importance to the computation of the evolution of the spin ensemble is that quantum mechanical operators can be associated with the density matrix; this was shown above for the I_z operator related to the system in thermal equilibrium. As such, not only are quantum mechanical operators associated with their direct operation on the wave-function, but also with the statistical ensemble distribution. The density operator (ρ) is introduced as a linear sum of orthonormal basis operators, and is associated with density matrix according to Eq. [1-69] below.

$$\overline{c_{m_j}^* c_{m_k}} = \langle m_k|\rho|m_j\rangle \quad [1\text{-}69]$$

In this sense, the density operator is a descriptor of the ensemble 'status', or the ensemble distribution of spin-states and coherence between each oscillation terms. From the definition of the density operator the ensemble average expectation value for any observable associated with an operator (*OP*) can be given as Eq. [1-70].

$$\overline{\langle OP\rangle} = \mathrm{Tr}\begin{bmatrix} \langle m_1|\rho OP|m_1\rangle & \cdots & \langle m_1|\rho OP|m_4\rangle \\ \vdots & \ddots & \vdots \\ \langle m_4|\rho OP|m_1\rangle & \cdots & \langle m_4|\rho OP|m_4\rangle \end{bmatrix} \quad [1\text{-}70]$$

This equation is written in shorthand below.

$$\overline{\langle OP\rangle} = \mathrm{Tr}(\rho OP) \quad [1\text{-}71]$$

At thermal equilibrium in a large magnetic field $\rho = I_z$ and $\overline{\langle I_z\rangle} = \mathrm{Tr}(I_z^2)$. For spin 3/2, $\overline{\langle I_z\rangle}$ is 10x that of proton (for which $\overline{\langle I_z\rangle} = 0.5$).

$$\overline{\langle I_z\rangle} = \mathrm{Tr}(I_z^2) = \frac{1}{4}\mathrm{Tr}\begin{bmatrix} 9 & 0 & 0 & 0 \\ 0 & 1 & 0 & 0 \\ 0 & 0 & 1 & 0 \\ 0 & 0 & 0 & 9 \end{bmatrix} = 5 \quad [1\text{-}72]$$

However, the gyromagnetic ratio of sodium is roughly ¼ that of proton. When the proportionality constants from $\langle \mu_z\rangle = \hbar\gamma\langle I_z\rangle$ and the population distribution in a large magnetic field ($\hbar\gamma \mathrm{B}_0/Z\mathrm{kT}$) are re-introduced, the ensemble longitudinal magnetization expectation value (Eqs. [73, 74]) is 35% that of proton.

$$\overline{\langle \mu_z\rangle} = \left(\frac{\hbar^2\gamma^2\mathrm{B}_0}{\mathrm{ZkT}}\right)\mathrm{Tr}(I_z^2) \quad [1\text{-}73]$$

This result can be re-expressed as below using $\mathrm{Tr}(I_z^2) = (1/3)I(I+1)(2I+1)$ (54,153).

$$\overline{\langle \mu_z\rangle} = \left(\frac{\hbar^2\gamma^2\mathrm{B}_0}{3\mathrm{kT}}\right)\big(I(I+1)\big) \quad [1\text{-}74]$$

Of central importance to the calculation of the evolution of the spin ensemble, as described by the density operator, is the Liouville – Von Neumann equation (152,154,156)

$$\frac{d\rho}{dt} = \frac{-i}{\hbar}[\mathcal{H}, \rho] \quad [1\text{-}75]$$

where the square brackets denote operator commutation.

$$[\mathcal{H}, \rho] = \langle m_j|\mathcal{H}\rho|m_k\rangle - \langle m_j|\rho\mathcal{H}|m_k\rangle \quad [1\text{-}76]$$

Operators commutation relationships for the Cartesian projection operators are given below. If the order of the operators within the commutator changes the sign of the resultant operator changes. All operators commute with themselves and with expressions of the same operator.

$$[I_z, I_x] = iI_y \quad [1\text{-}77]$$

$$[I_z, I_y] = -iI_x \quad [1\text{-}78]$$

$$[I_x, I_y] = iI_z \quad [1\text{-}79]$$

For the spin ensemble within a large magnetic field the Liouville – Von Neumann equation takes the form below, where $\mathcal{H}_p(t)$ is a perturbing Hamiltonian much smaller in magnitude than the Zeeman interaction (note that it is typical to remove $\hbar$ from each of the Hamiltonians when presenting the evolution of the density operator (154,157)).

$$\frac{d\rho}{dt} = -i[\mathcal{H}_Z + \mathcal{H}_p(t), \rho] \quad [1\text{-}80]$$

To remove the constant Zeeman interaction from this calculation the 'interaction representation' (153,157) is used such that

$$\frac{d\rho^*}{dt} = -i[\mathcal{H}_p^*(t), \rho^*] \quad [1\text{-}81]$$

where

$$\rho^* = \exp(\mathrm{i}\mathcal{H}_Z t)\rho\exp(-\mathrm{i}\mathcal{H}_Z t) \quad [1\text{-}82]$$

and

$$\mathcal{H}_p^*(t) = \exp(\mathrm{i}\mathcal{H}_Z t)\mathcal{H}_p(t)\exp(-\mathrm{i}\mathcal{H}_Z t) \quad [1\text{-}83]$$

It is apparent that use of the interaction representation represents a coordinate transformation to a frame rotating about the z-axis in a negative sense at the Larmor frequency. The rotating frame will be used for all subsequent equations involving the density operator.

One of the great values of re-casting the Liouville – Von Neumann equation within the rotating frame is that the well known RF excitation Hamiltonian (an applied magnetic field, of magnitude B_1, rotating in the transverse plane, with frequency ω_{RF}, producing classical magnetic dipole 'flipping') is independent of time within this frame. In the rotating frame the RF excitation Hamiltonian can be given as below:

$$\mathcal{H}_{RF}^{*} = \hbar(\gamma B_o - \omega_{RF})I_z - \hbar\gamma B_1 I_y \qquad [1\text{-}84]$$

If ω_{RF} is equal to the Larmor frequency, i.e. the case of 'on-resonance', the I_z term can be dropped. The effect of the I_z term, or 'off-resonance' excitation, is 'flipping' on a cone not equal to the x-z plane, and the inability to produce a complete inversion pulse.

The formal solution to the Liouville – Von Neumann equation for time-independent Hamiltonians is given in Eq. [1-85]

$$\frac{d\rho^*}{dt} = \exp(-i\mathcal{H}t)\rho^*(0)\exp(+i\mathcal{H}t) \qquad [1\text{-}85]$$

and in many cases a formal solution is of great value to describe the evolution of a spin sequence and design NMR pulse sequences. However, a formal solution is not required and is often not practical for the evaluation of the evolution of the spin 3/2 density operator under multiple Hamiltonians, as will be discussed further in this introduction. The formal solution for an on-resonance RF pulse, given initial thermal equilibrium conditions (i.e. $\rho^*(0) = I_z$), is given below (152).

$$\rho^*(t) = I_z\cos(\gamma B_1 t) + I_x\sin(\gamma B_1 t) \qquad [1\text{-}86]$$

If the spin ensemble following a 90° RF pulse can be described by $\rho^* = I_x$ then the density matrix $\left(\mathrm{DM}(\rho^*)\right)$ will be as given in Eq. [1-87].

$$\mathrm{DM}(\rho^* = I_x) = \frac{1}{2}\begin{bmatrix} 0 & \sqrt{3} & 0 & 0 \\ \sqrt{3} & 0 & 2 & 0 \\ 0 & 2 & 0 & \sqrt{3} \\ 0 & 0 & \sqrt{3} & 0 \end{bmatrix} \quad [1\text{-}87]$$

The first thing of note is that when the spin ensemble can be described by $\rho^* = I_x$ the statistical distribution of spin-states throughout the ensemble are equal, as denoted by the zeros along the diagonal. However, the one-off-diagonal terms $\overline{c^*_{m_k} c_{m_{k\pm1}}}$ are non-zero. These terms are the ensemble averages of the products of the complex spin-state probabilities describing the expectation of a nuclear dipole in the transverse plane of Eq. [1-63], and non-zero values specify phase correlation between spins in the ensemble. When $\rho = I_x$ the magnitude of the expected ensemble magnetization along the x-axis is equal to the magnitude of longitudinal magnetization in thermal equilibrium.

$$\overline{\langle \mu_x \rangle} \propto \overline{\langle I_x \rangle} = \mathrm{Tr}(I_x^2) = 5 \quad [1\text{-}88]$$

The I_x^2 term is written out below where the order of operations is important.

$$I_x^2 = \frac{1}{4}(I_+I_+ + I_-I_+ + I_+I_- + I_-I_-) \quad [1\text{-}89]$$

It should be remembered that the expected ensemble transverse magnetization will be oscillating in accordance with the rotating frame.

For spin 3/2 nuclei, the expectation value of a transverse nuclear dipole is associated with three oscillating terms. As spin 3/2 nuclei possess four energy states, each oscillating term can be ascribed to transition between adjacent states. When the ensemble average phases of the oscillating terms are non-zero, these oscillations are said to be coherent. The one-off-diagonal terms are specified as single-quantum coherence terms. The propagated coherence along the diagonal (or 'super-coherence') of the density matrix when $\rho^* = I_x$ is associated with an

observable transverse magnetization. However, it is possible for spin 3/2 nuclei to produce an 'observable' with positive coherence between the outer spin-states, but negative coherence between the inner spin-states, the linear sum (or 'super-coherence') of which yields no ensemble transverse magnetization. Transitions of 2 and 3 quanta, producing oscillation terms at 2 and 3 times the Larmor frequency (related to operators $(I_{\pm})^2$ and $(I_{\pm})^3$) are also possible for sodium nuclei with ensemble double and triple quantum coherence terms filling the remaining diagonals / corners of the density matrix. The production of a density operator that contains these terms will be discussed later in this introduction.

The beauty of the density operator is that one need only follow its evolution to fully describe the state of the spin system, or the spin ensemble magnetic polarization, during an NMR pulse sequence. In the following sections the quadrupole Hamiltonian is introduced, a dominant interaction unique to nuclei other than spin ½, along with its effect on relaxation and energy level shifting. A particularly useful basis set in which to express the density operator given the quadrupole Hamiltonian will then be introduced along with sets of coupled differential equations 'completely' describing the sodium spin system during an NMR pulse sequence.

1.5.3. The Quadrupole Hamiltonian

As mentioned above the quadrupole Hamiltonian is the preponderant interaction experienced by sodium nuclei in a biological environment. While the charge distributions of spin ½ nuclei are spherically symmetric, the charge distributions of nuclei with spin > ½ are not (they are ellipsoidal), and as a result these nuclei will be preferentially oriented in an electric field gradient (EFG) (153). It is the energy associated with this orientation that produces the rapid relaxation commonly known to be possessed by sodium in biological environments such as the human brain as well as typically 'ignored' (for imaging the human brain)

energy level shifting. The source of the electric field gradients in biological systems such as the human brain will be introduced in the subsequent chapter section 1.6. Derivation of the quadrupole interaction in this section will closely follow Allen (152) and Slichter (153).

The electric potential energy between a nuclear charge distribution and an electric potential, arising from the environment surrounding the nucleus and mediated at the nuclear site by the electron cloud (through the Sternheimer anti-shielding factor) (153,157,158), is given by the equation below where ρ is the nuclear charge distribution (not to be confused with the density operator) and V is the mediated electric potential at the nucleus due to external sources.

$$\mathrm{E} = \int \rho(\boldsymbol{r})\mathrm{V}(\boldsymbol{r})\, d^3r \qquad [1\text{-}90]$$

Because $\mathrm{V}(\boldsymbol{r})$ is determined by electronic charge distributions that are much greater than the nuclear dimensions, it is assumed the derivatives of $\mathrm{V}(\boldsymbol{r})$ do not change over the dimensions of the nucleus and as a result this interaction can be expanded in a multipole sense over the nucleus. A 3D Taylor series expansion is used, however, this interaction can also be expanded in terms of spherical harmonics (157). The first three terms of the Taylor expansion of $\mathrm{V}(\boldsymbol{r})$ are written below,

$$\mathrm{V}(\boldsymbol{r}) = \mathrm{V}(0) + \sum_{\mathrm{s_i=x,y,z}} \mathrm{s}_i \frac{\partial \mathrm{V}(\boldsymbol{r})}{\partial \mathrm{s}_i}\bigg|_{r=0} + \frac{1}{2!} \sum_{\mathrm{s_i,s_j=x,y,z}} \mathrm{s}_i \mathrm{s}_j \frac{\partial^2 \mathrm{V}(\boldsymbol{r})}{\partial \mathrm{s}_i\, \partial \mathrm{s}_j}\bigg|_{r=0} + \cdots \qquad [1\text{-}91]$$

and the interaction energy re-expressed as:

$$\mathrm{E} = \mathrm{V}(0) \int \rho(\boldsymbol{r})\, d^3r + \sum_{\mathrm{s_i}} \mathrm{V}_{\mathrm{s_i}} \int \mathrm{s_i}\rho(\boldsymbol{r})\, d^3r + \frac{1}{2!} \sum_{\mathrm{s_i,s_j}} \mathrm{V}_{\mathrm{s_i s_j}} \int \mathrm{s_i s_j}\rho(\boldsymbol{r})\, d^3r \qquad [1\text{-}92]$$

where

$$\mathrm{V}_{\mathrm{s_i}} = \frac{\partial \mathrm{V}(\boldsymbol{r})}{\partial \mathrm{s}_i}\bigg|_{r=0} \qquad [1\text{-}93]$$

and

$$V_{s_i s_j} = \left.\frac{\partial^2 V(\boldsymbol{r})}{\partial s_i \, \partial s_j}\right|_{r=0} \qquad [1\text{-}94]$$

The first and second terms of Eq. [1-92], which involve the electrostatic interaction energy of the nucleus considered as a point source and a nuclear dipole moment respectively, are irrelevant to this discussion. The first term will simply produce spatial drift, while the second term will be zero as nuclear dipole moments are non-existent (the nuclear centre of mass and centre of charge coincide (153)). The third term, however, concerns the nucleus orienting interaction associated with its electric quadrupole moment in an electric field gradient.

Continuing to follow (153) the electric quadrupole moment, $Q_{s_i s_j}$, can be introduced (where $\delta_{s_i s_j}$ is the Kronecker delta function):

$$Q_{s_i s_j} = \int \left(3 s_i s_j - \delta_{s_i s_j} r^2\right) \rho(\boldsymbol{r}) d^3 r \qquad [1\text{-}95]$$

The integral of the third term in the energy interaction equation (Eq. [1-91]) can then be expressed in terms of $Q_{s_i s_j}$ as:

$$\int s_i s_j \rho(\boldsymbol{r}) \, d^3 r = \frac{1}{3}\left(Q_{s_i s_j} + \int \delta_{s_i s_j} r^2 \rho(\boldsymbol{r}) d^3 r\right) \qquad [1\text{-}96]$$

The subsequent quadrupole interaction energy, i.e the relevant third term of Eq. [1-92], is given below:

$$E = \frac{1}{6} \sum_{s_i, s_j} V_{s_i s_j} Q_{s_i s_j} + V_{s_i s_j} \delta_{s_i s_j} \int r^2 \rho(\boldsymbol{r}) \, d^3 r \qquad [1\text{-}97]$$

It should be noted that the electric field in which the nucleus is present must (in general) satisfy Laplace's equation, $\nabla^2 V = 0$ (i.e. the electric field at the location of the nucleus should not contain an electronic charge independent of the

nucleus). As a result, the second term of Eq. [1-97] will be zero, yielding the interaction energy of Eq. [1-98] below.

$$\mathrm{E} = \frac{1}{6}\sum_{\mathrm{s_i},\mathrm{s_j}} \mathrm{V_{s_i s_j}} \mathrm{Q_{s_i s_j}} \qquad [1\text{-}98]$$

The delta function in the equation defining the nuclear quadrupole moment (Eq. [1-95]), involves subtraction of a term that is independent nuclear orientation, or the subtraction of spherical electric symmetry from the nucleus, the interaction with which we are not interested.

To obtain the associated quadrupole Hamiltonian, $\mathcal{H}_Q$, the quadrupole moment can be replaced by an operator term dependent on the sum of protons within the nucleus. Without attempting to describe the underlying quantum mechanics (the reader is referenced to (153)) the quantum mechanical operator $\mathrm{Q}^{(\mathrm{op})}_{\mathrm{s_i s_j}}$ is simply given below (Eq. [1-99]) (where the constant Q is defined as the quadrupole moment of the nucleus: 1.04 x 10^{-25} cm^2 for ^{23}Na (159)).

$$\mathrm{Q}^{(\mathrm{op})}_{\mathrm{s_i s_j}} = \frac{eQ}{I(2I-1)}\left(\frac{3}{2}\left(I_{\mathrm{s_i}} I_{\mathrm{s_j}} + I_{\mathrm{s_j}} I_{\mathrm{s_i}}\right) - \delta_{\mathrm{s_i s_j}} I^2\right) \qquad [1\text{-}99]$$

Following algebraic manipulation, and noting that principal axes can always be defined such that $\mathrm{V_{s_i s_j}} = 0$ for $\mathrm{s_i} \neq \mathrm{s_j}$, the quadrupole Hamiltonian can be stated in terms of these principal axes.

$$\mathcal{H}_Q = \frac{eQ}{4I(2I-1)}\left[\mathrm{V_{zz}}\left(3I_{\mathrm{z}}^2 - I(I+1)\right) + \left(\mathrm{V_{xx}} - \mathrm{V_{yy}}\right)\left(I_{\mathrm{x}}^2 - I_{\mathrm{y}}^2\right)\right] \qquad [1\text{-}100]$$

An alternative representation is given in Eq. [1-101] in terms of the operators I_z and $I_\pm$, highlighting one and two quanta transition terms in the Hamiltonian (153,157).

$$\mathcal{H}_Q = \frac{eQ}{4I(2I-1)}\left[\mathrm{V}_0 2\left(3I_z^2 - I(I+1)\right) + \mathrm{V}_{\pm 1}\sqrt{6}(I_\pm I_z + I_z I_\pm) + \mathrm{V}_{\pm 2}\sqrt{6}(I_\pm)^2\right] \qquad [1\text{-}101]$$

where

$$V_0 = 1/2\, V_{zz} \quad [1\text{-}102]$$

$$V_{\pm 1} = 1/\sqrt{6}\left(V_{zx} \pm iV_{zy}\right) \quad [1\text{-}103]$$

$$V_{\pm 2} = \left(1/\left(2\sqrt{6}\right)\right) \cdot \left(V_{xx} - V_{yy} \pm 2iV_{xz}\right) \quad [1\text{-}104]$$

As can be seen the quadrupole Hamiltonian involves a 'complicated' combination of I_z and $I_\pm$ operators. However, this preponderant spin 3/2 Hamiltonian can be greatly simplified for calculation of the evolution of the density operator by recasting spin 3/2 quantum mechanics in terms of a beneficial tensor operator basis set. Before this is done, it should be noted that the EFG terms experienced by the sodium nuclei in a biological environment will most certainly be time dependent (the source of the EFG terms and their time dependency is the topic of chapter section 1.6). However, in certain environments a non-zero-mean component to the fluctuating EFG may persist over the relevant NMR time-course. In this case the quadrupole Hamiltonian can be split into effectively static $(\mathcal{H}_{QS})$ and fluctuating $(\mathcal{H}_{QF})$ components. Introduction of the static quadrupole Hamiltonian and its effect will precede consideration of the evolution of the density operator under influence of the static quadrupole Hamiltonian, followed by consideration of the fluctuating Hamiltonian.

1.5.4. The Static Quadrupole Hamiltonian

To calculate the effect of the 'static' (or non-zero-mean time-averaged) quadrupole Hamiltonian in a strong magnetic field (B_0) the case of axial symmetry is assumed for the time-averaged components of the EFG, labelled $\overline{V_{xx}(t)}$, $\overline{V_{yy}(t)}$, and $\overline{V_{zz}(t)}$, such that $\overline{V_{xx}(t)} = \overline{V_{yy}(t)}$ (a good approximation for an environment with lots of motion as a biological system) (152,153,160), and $\overline{V_{zz}(t)}$ is assigned the magnitude $e\overline{(q(t))}$, where $\left|\overline{V_{zz}(t)}\right| \geq \left|\overline{V_{xx}(t)}\right| = \left|\overline{V_{yy}(t)}\right|$.

However, it is unlikely that the 'z' axis of B_0 will coincide with the 'z' axis of the EFG (labelled z′). The static quadrupole Hamiltonian is expressed below in Eq. [1-105] together with the Zeeman Hamiltonian.

$$\mathcal{H} = \gamma\hbar B_0 I_z + \frac{e^2 Q\overline{(q(t))}}{4I(2I-1)}\left(3I_{z'}^2 - I(I+1)\right) \quad [1\text{-}105]$$

Given the overwhelming magnitude of the Zeeman interaction in proportion to the quadrupole interaction, the quadrupole Hamiltonian can be expressed as a first order perturbation in terms of the principal axes of B_0 as below (where θ is the polar angle between z and z′) (147,153). However, the orientation of the EFG experienced by the sodium nucleus in a biological environment will also certainly change will time. The 'static' quadrupole interaction will be proportional to the time average of this orientation (over the relevant NMR time-course).

$$\mathcal{H} = \gamma\hbar B_0 I_z + \frac{e^2 Q\overline{(q(t))}}{4I(2I-1)}\left[\frac{1}{2}\left(3\cos^2\overline{\theta(t)} - 1\right)\left(3I_z^2 - I(I+1)\right)\right] \quad [1\text{-}106]$$

Before discussing the effect of the static quadrupole Hamiltonian perturbation in a large magnetic field two common terms will be introduced. The term

$$\chi(t) = \frac{e^2 Q q(t)}{\hbar} \quad [1\text{-}107]$$

is defined as the quadrupole coupling constant, and the term

$$\omega_Q(t) = \frac{\chi(t)}{4}(3\cos^2\theta(t) - 1) \quad [1\text{-}108]$$

is defined as the quadrupole interaction frequency. The term $\overline{\omega}_Q$, labelled the residual quadrupole interaction frequency, is used to represent the non-zero-mean time-averaged (or static) component of the quadrupole interaction (160,161).

Using the residual quadrupole term the static quadrupole Hamiltonian can be expressed as Eq. [1-109].

$$\mathcal{H}_{QS} = \hbar \frac{\bar{\omega}_Q}{6}\left(3I_z^2 - I(I+1)\right) \quad [1\text{-}109]$$

The corresponding spin-state energy eigenvalues can be written as below

$$E_m = \hbar\omega_o m + \frac{1}{2}\hbar\bar{\omega}_Q[m^2 - 5/4] \quad [1\text{-}110]$$

with the result of spin-state energy level shifting as demonstrated in **Figure 1-2**. While the frequency of the central transition is unaffected by the quadrupole interaction, the quadrupole interaction produces equally spaced satellite resonances in the spectrum. The static quadrupole interaction is highly dependent on the angle of orientation of the EFG, or $\overline{V_{zz}(t)}$, with respect to the main magnetic field. If $\overline{\theta(t)} = 54.7^o$ the quadrupole interaction will be eliminated.

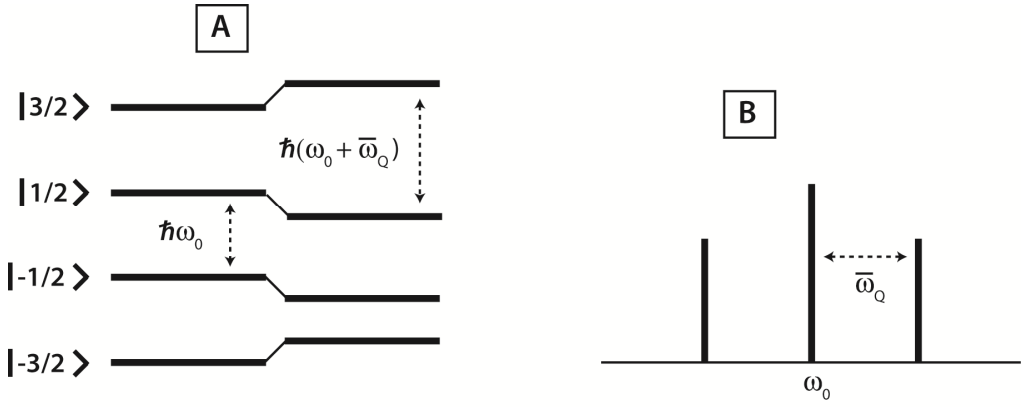

Figure 1-2: Spin-state energy level shifting as a result of a static residual quadrupole interaction (A), and the resultant splitting of the sodium spin 3/2 spectrum (B).

It should be noted that in the case where time-averaged non-zero-mean electric field gradients experienced by sodium nuclei are randomly distributed in 3D space throughout a voxel the distribution of $\overline{\theta(t)}$ is not uniform. Rather, it has a

probability density $\propto \sin(\overline{\theta(t)})$ (i.e. there is only one infinitesimal EFG orientation associated with $\overline{\theta(t)} = 0^{o}$, but much greater orientation 'freedom' through the azimuthal angle as $\overline{\theta(t)}$ is increased) (162). As a result, the average $\bar{\omega}_Q$ in a voxel with randomly distributed static EFGs will be zero (in this environment the powder spectrum will be produced) (153). It should also be noted that the coherence between the outer spin orientation eigenstates each produce 30% of the observable transverse magnetization, and the coherence between the central eigenstates – 40% (163). This follows from observation of Eq. [1-63].

Although discussion of energy level shifting as a result of the quadrupole Hamiltonian may seem specifically related to spectroscopy, the secular quadrupole interaction can also have significant impact on signal intensity measured with NMR sequences intending to assess spin density. This interaction, which is briefly introduced below, has generally been ignored for imaging the human brain. However, it was recently shown at ISMRM Hawaii (Stobbe, Beaulieu, 2009) (164) that some signal loss on sodium images may be the result of a static residual quadrupole interaction.

1.5.5. Irreducible Spherical Tensors

The use of irreducible tensor operators (T_{nq}) (150,153,154,157,165-168) as a basis set in which to express the density operator is particularly helpful for sodium NMR analysis as they allow for simple expression of the quadrupole Hamiltonian and full representation of all possible spin 3/2 ensemble coherences (71,145). The commutation relations for these operators have been tabulated (169), facilitating 'simple' derivation of the Liouville – Von Neumann equation (Eq. [1-74]) under the influence of the quadrupole Hamiltonian. The use of irreducible tensor operators also provides a visual understanding of sodium spin ensemble multipoles, or spin 'polarizations' (170,171).

Irreducible tensor operators are defined as operators that transform under rotation in the same manner as spherical harmonics of order l, and have operator matrices defined by the Wigner-Eckart Theorem, which states that the matrix elements are related to the Clebsch-Gordan coefficients as below (150,166,167):

$$\langle m|T_{nq}|m'\rangle = (2I+1)^{-1/2}\langle Im'nq|Im\rangle\langle I||T_n||I\rangle \quad [1\text{-}111]$$

Within the Wigner-Eckart Theorem, the Clebsch-Gordan coefficients, typically written $\langle j_1 m_1 j_2 m_2|JM\rangle$, are used outside their 'derived application' of coupling two angular momenta. If desired, the values of these coefficients can be found from any online table or calculator. It can be noted that matrix elements are non-zero only when $m' + q = m$. The scaling term $\langle I||T_n||I\rangle$ is labelled the 'reduced matrix element' and is given below.

$$\langle I||T_n||I\rangle = \left[\frac{n!\,n!\,(2I+n+1)!}{2^n(2n)!\,(2I-n)!}\right]^{1/2} \quad [1\text{-}112]$$

The definition of the irreducible tensor operators, and the equation specifying their matrix elements is given above for completeness. However, full understanding of the derivation of these tensor operators is not required to appreciate their use. The matrix elements associated with each T_{n+q} operator relevant to spin 3/2 nuclei have been tabulated and are given in **Table 1-1** (from (168)). The T_{n-q} operators have negative matrix elements mirrored along the diagonal. In reference to the tensor operators, (n) is defined as the operator rank and (q) its coherence in association with related spin-state transitions (sometimes q is labelled as irreducible tensor 'order').

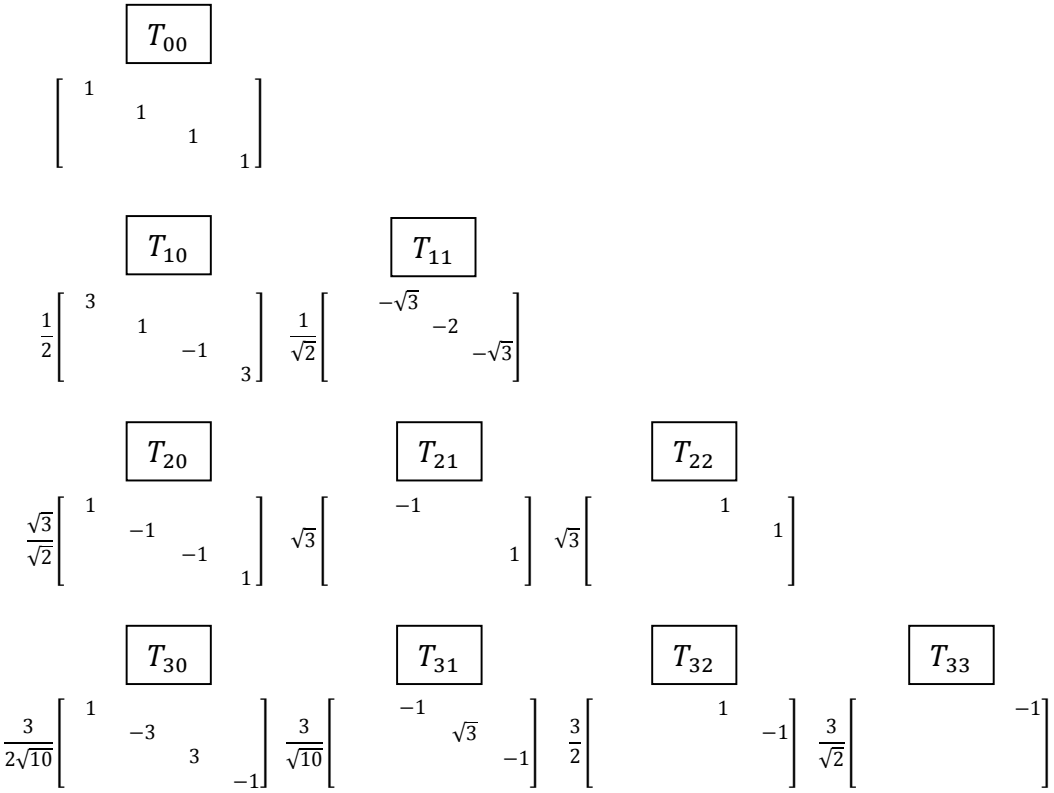

Table 1-1: Irreducible tensor operator matrices with rank increasing from top to bottom and coherence increasing from left to right. As can be seen, the T_{10} operator is equal to the I_Z operator and the T_{11} operator is proportional to the I_+ operator introduced previously. When used as a basis set for the density operator, the remaining orthogonal operators describe other ensemble spin-state distributions: quadrupolar - T_{20}, and octopolar - T_{30}; as well as other ensemble coherence combinations.

Following from the operator matrices, the irreducible tensor operators can also expressed in terms of I_Z and $I_\pm$. These expressions are given below from (145,167,168), where $[A,B]_+$ represents anti-commutation (i.e. $[A,B]_+ = AB + BA$). Given the definition of the irreducible tensor operators, it is not surprising these operators have similar form to the spherical harmonics. For this reason they are often called irreducible *spherical* tensor operators. Although expression of the irreducible tensor operators in terms of I_Z and $I_\pm$ may be interesting, expression in this manner is not necessary for their use.

$$T_{00} = 1 \qquad \text{[1-113:1-122]}$$

$$T_{10} = I_Z$$

$$T_{1\pm1} = \mp\left(1/\sqrt{2}\right)I_{\pm}$$

$$T_{20} = \left(1/\sqrt{6}\right)\left(3I_{\mathrm{Z}}^2 - I(I+1)\right)$$

$$T_{2\pm1} = (1/2)(I_{\pm}I_Z + I_Z I_{\pm})$$

$$T_{2\pm2} = (1/2)I_{\pm}^2$$

$$T_{30} = \left(1/\sqrt{10}\right)(5I_{\mathrm{Z}}^3 - (3\mathrm{I}(\mathrm{I}+1) - 1)\mathrm{I}_{\mathrm{Z}})$$

$$T_{3\pm1} = \mp(1/4)\left(\sqrt{3/10}\right)[5I_{\mathrm{Z}}^3 - \mathrm{I}(\mathrm{I}+1) - 1/2\,, I_{\pm}]_{+}$$

$$T_{3\pm2} = (1/2)\left(\sqrt{3/4}\right)\left[I_Z, I_{\pm}^2\right]_{+}$$

$$T_{3\pm3} = \mp(1/2)\left(1/\sqrt{2}\right)I_{\pm}^3$$

As a basis set for the density operator, the matrix associated with a $T_{n\mathrm{q}}$ operator specifies the density matrix, or the sum of ensemble spin-state coherence $\left(\overline{c_{m_j}^* c_{m_k}}\right)$ terms, when the density operator can be expressed solely by that $T_{n\mathrm{q}}$ operator. As such, each $T_{n\mathrm{q}}$ operator specifies an ensemble 'super-coherence' or spin polarization. The use of the irreducible tensors as a basis set provides a means to graphically depict this polarization, given their relationship to the spherical harmonics (170,171). The ensemble spin magnetization polarizations associated with each irreducible tensor operator forming a basis for density operator are shown from (170) in **Figure 1-3**. Although the individual T_{nq} tensor operators themselves do not represent physical observables, as their associated operator matrices are not hermitian (i.e. no conjugate symmetry about the

diagonal), hermitian T_{nq} operators can be generated from a linear combination of individual T_{nq} operators. The hermitizing procedure used for this graphical depiction is given below, producing polarizations that differ by a phase ϕ for each coherence.

$$T_{nq\phi} = \frac{1}{2}\left(e^{iq\phi}T_{n-q} - e^{-iq\phi}T_{nq}\right) \quad [1\text{-}123]$$

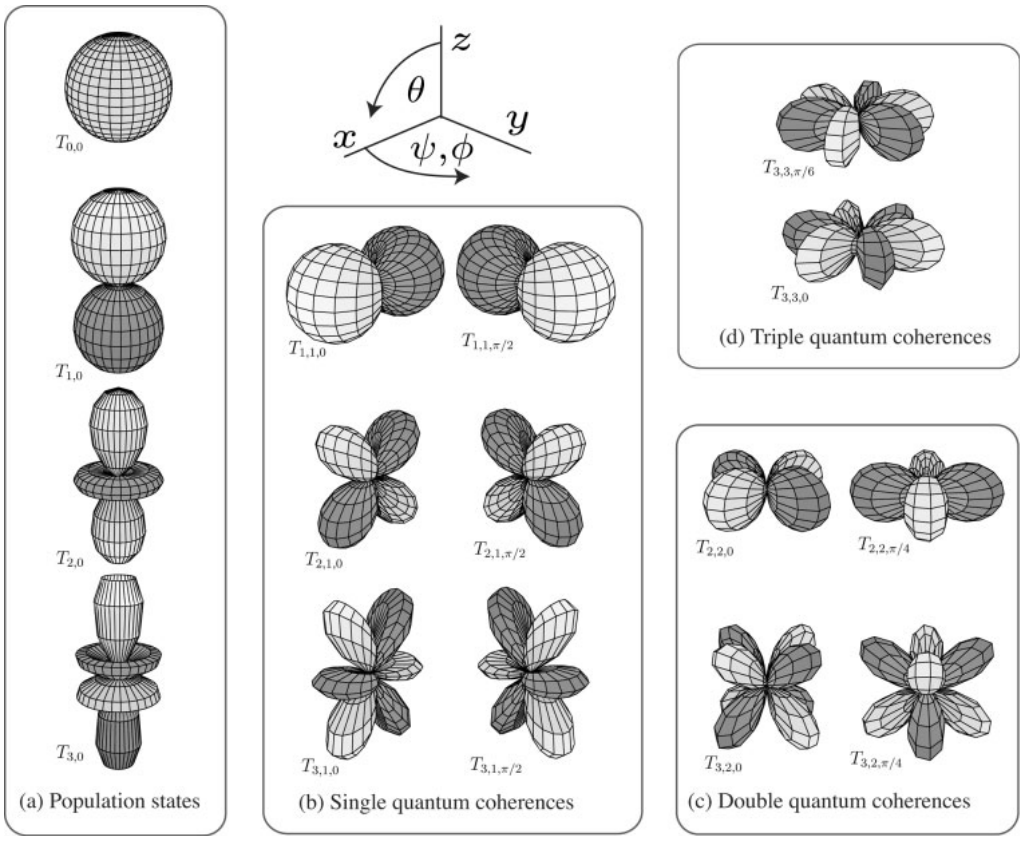

Figure 1-3: "Graphical representation of the (hermitized irreducible tensor operator) basis set using spherical harmonics for a spin I = 3/2 nucleus. Any density matrix representing an ensemble of spin I = 3/2 nuclei can be illustrated as a linear combination of these states. The (irreducible tensor operators) are specified by their rank (n), order (coherence) (q), and phase ϕ..." The other angles have meaning specifically related to (170). "...The population states (a) are rotationally symmetric about the z axis, and are not coherences. The single quantum coherences (b) have a single plane of symmetry through the z axis; the double quantum coherences (c) have two such planes; and (d) the triple quantum coherences have three." (170)

It is informative to consider that when the density operator is considered within the rotating frame, each nuclear spin ensemble polarization in **Figure 1-3** will rotate at the Larmor frequency. It is the rotation of the magnetic dipole (T_{11}) that produces the EMF within the receive coil. Each of the other polarizations are rotationally balanced about the z-axis and will not generate an EMF. A polarization rotation rate at 2 and 3 times the Larmor frequency can also be observed for the double and triple quantum coherences. Throughout an NMR sequence the density operator will consist of changing linear combinations of these irreducible tensor operators, and visualization of the nuclear spin ensemble polarizations during different NMR sequences are further shown in (170).

Before discussing the evolution of the density operator it should also be noted that in order to form a basis set for the density operator, the irreducible tensor operators must satisfy an orthonormal relationship. While they are orthogonal, they must be scaled to be of unit length. The scaling required to produce unit spin 3/2 irreducible tensors operators $(\hat{T}_{nq})$ is given in Eqs. [124 - 128] (145,167,168).

$$\hat{T}_{n\mathrm{q}} = \left[\frac{(2n+1)(2I-n)!\,2^n(2n)!}{(2I+n+1)!}\right]^{1/2} T_{n\mathrm{q}} \qquad [1\text{-}124]$$

$$\hat{T}_{00} = (1/2)T_{00} \qquad [1\text{-}125]$$

$$\hat{T}_{1q} = \left(1/\sqrt{5}\right)T_{1q} \qquad [1\text{-}126]$$

$$\hat{T}_{2q} = \left(1/\sqrt{6}\right)T_{2q} \qquad [1\text{-}127]$$

$$\hat{T}_{3q} = \left(\sqrt{2}/3\right)T_{3q} \qquad [1\text{-}128]$$

Symmetric (s) and antisymmetric (a) combinations of these unit operators are also formed for calculation to reflect the hermitian requirement for an observable (145,167).

$$\hat{T}_{nq}(s) = \left(1/\sqrt{2}\right)\left(\hat{T}_{n-q} + \hat{T}_{nq}\right) \qquad [1\text{-}129]$$

$$\hat{T}_{nq}(a) = (1/\sqrt{2})(\hat{T}_{n-q} - \hat{T}_{nq}) \qquad [1\text{-}130]$$

The symmetric and antisymmetric combinations produce magnetic polarizations 90^o out of phase from each other, such that $T_{11}(a) = I_x$, and $T_{11}(s) = -iI_y$ (note that the Cartesian projection operators are not of unit length for spin 3/2). The magnitude of the transverse ensemble magnetization is then proportional to $|\hat{T}_{11}(a) - \hat{T}_{11}(s)|$. During 'on-resonant' conditions the symmetric and antisymmetric terms for each $\hat{T}_{nq}$ are un-coupled.

Perhaps the greatest advantages of considering the evolution of the density operator in the basis set of the irreducible tensor operators is that the quadrupole operator can be directly expressed in terms of this basis set. From observation of Eq. [1-101] and Eq. [1-116 – 1-118] it is apparent that $Q_{2q} = T_{2q}$. The full quadrupole Hamiltonian is expressed below where the electric field gradients V_m have been defined above and are now written to reflect their time dependency.

$$\mathcal{H}_Q = \frac{eQ}{\sqrt{6}} \sum_{-2}^{2} T_{2m} V_m(t) \qquad [1\text{-}131]$$

The calculation of the evolution of the density operator under influence of RF pulses and the quadrupole Hamiltonian used to build the sodium spin simulator used in this thesis (Appendix 6) is based on the sets of coupled differential equations derived by Van Der Maarel (71,145,146,172-176). These equations will be briefly described below, first for the static and then the time-dependent Hamiltonians.

1.5.6. Density Operator Evolution Under Static Hamiltonians

Using the irreducible tensor operators the static residual quadrupole Hamiltonian can be expressed very simply as Eq. [1-132].

$$\mathcal{H}_{QS} = \hbar\bar{\omega}_Q \hat{T}_{20} \qquad [1\text{-}132]$$

Transformation to the rotating frame does not affect the static quadrupole Hamiltonian as it commutes with $\mathcal{H}_Z$.

$$\mathcal{H}_{QS}^* = U\mathcal{H}_{QS}U^{-1} = \mathcal{H}_{QS} \qquad [1\text{-}133]$$

$$U = \exp(-i\mathcal{H}_Z t) \qquad [1\text{-}134]$$

In the rotating frame the Hamiltonian for an on-resonance RF pulse is also independent of time and can be expressed as below.

$$\mathcal{H}_{RF}^* = \hbar\gamma B_1 I_x = \hbar\omega_1\left(\sqrt{5}\right)\hat{T}_{11}(a) \qquad [1\text{-}135]$$

Evolution of the density operator in the rotating frame under the influence of these two relevant static Hamiltonians experienced by the spin ensemble during an NMR experiment is given below (from Eq. [1-75], note that in this representation the $\hbar$ has again been removed from the Hamiltonians).

$$\frac{d\rho^*}{dt} = -i\left[\mathcal{H}_{RF}^* + \mathcal{H}_{QS}^*, \rho^*\right] \qquad [1\text{-}136]$$

Derivation of the Liouville – Von Neuman equation for these static Hamiltonians simply requires knowledge of the irreducible tensor operator commutation relations for spin 3/2 which are given in (169). The two coupled differential equations describing the evolution of the density operator under the influence RF irradiation are given below. It can be seen that the effect of an RF pulse on the density operator is to couple the $\hat{T}_{nq}$ operators of different coherence (q) within their rank (n). An RF pulse cannot produce $\hat{T}_{nq}$ operators of rank different than

those present prior to the RF pulse, however, an RF pulse can produce all the $\hat{T}_{nq}$ operators of different coherence within the rank of those present prior to the RF pulse. If the spin system is in thermal equilibrium $\left(\rho^* = \hat{T}_{10}\right)$ prior to the RF pulse, only single quantum coherences (or observable transverse magnetization) will be produced. Formal solutions to the Liouville – Von Neuman equation under the influence of an RF pulse (or under a hard RF pulse) are given in (145) for each case that density operator is initially one of the 15 irreducible tensor operators. Although not shown in this introduction, it is interesting to note that RF 'flipping' rates between coherences can be 2x and 3x greater than ω_1 for the rank 2 and rank 3 operators.

$$\frac{d}{dt}\begin{pmatrix} \hat{T}_{10} \\ \hat{T}_{11}(s) \\ \hat{T}_{21}(a) \\ \hat{T}_{22}(a) \\ \hat{T}_{30} \\ \hat{T}_{31}(s) \\ \hat{T}_{32}(s) \\ \hat{T}_{33}(s) \end{pmatrix} = \begin{pmatrix} 0 & -i\omega_1 & 0 & 0 & 0 & 0 & 0 & 0 \\ -i\omega_1 & 0 & 0 & 0 & 0 & 0 & 0 & 0 \\ 0 & 0 & 0 & -i\omega_1 & 0 & 0 & 0 & 0 \\ 0 & 0 & -i\omega_1 & 0 & 0 & 0 & 0 & 0 \\ 0 & 0 & 0 & 0 & 0 & -i\sqrt{6}\omega_1 & 0 & 0 \\ 0 & 0 & 0 & 0 & -i\sqrt{6}\omega_1 & 0 & -i\sqrt{5/2}\,\omega_1 & 0 \\ 0 & 0 & 0 & 0 & 0 & -i\sqrt{5/2}\,\omega_1 & 0 & -i\sqrt{3/2}\,\omega_1 \\ 0 & 0 & 0 & 0 & 0 & 0 & -i\sqrt{3/2}\,\omega_1 & 0 \end{pmatrix} \begin{pmatrix} \hat{T}_{10} \\ \hat{T}_{11}(s) \\ \hat{T}_{21}(a) \\ \hat{T}_{22}(a) \\ \hat{T}_{30} \\ \hat{T}_{31}(s) \\ \hat{T}_{32}(s) \\ \hat{T}_{33}(s) \end{pmatrix} \quad [1\text{-}137a]$$

$$\frac{d}{dt}\begin{pmatrix} \hat{T}_{11}(a) \\ \hat{T}_{20} \\ \hat{T}_{21}(s) \\ \hat{T}_{22}(s) \\ \hat{T}_{31}(a) \\ \hat{T}_{32}(a) \\ \hat{T}_{33}(a) \end{pmatrix} = \begin{pmatrix} 0 & 0 & 0 & 0 & 0 & 0 & 0 \\ 0 & 0 & -i\sqrt{3}\omega_1 & 0 & 0 & 0 & 0 \\ 0 & -i\sqrt{3}\omega_1 & 0 & -i\omega_1 & 0 & 0 & 0 \\ 0 & 0 & -i\omega_1 & 0 & 0 & 0 & 0 \\ 0 & 0 & 0 & 0 & 0 & -i\sqrt{5/2}\,\omega_1 & 0 \\ 0 & 0 & 0 & 0 & -i\sqrt{5/2}\,\omega_1 & 0 & -i\sqrt{3/2}\,\omega_1 \\ 0 & 0 & 0 & 0 & 0 & -i\sqrt{3/2}\,\omega_1 & 0 \end{pmatrix} \begin{pmatrix} \hat{T}_{11}(a) \\ \hat{T}_{20} \\ \hat{T}_{21}(s) \\ \hat{T}_{22}(s) \\ \hat{T}_{31}(a) \\ \hat{T}_{32}(a) \\ \hat{T}_{33}(a) \end{pmatrix} \quad [1\text{-}137b]$$

The two coupled differential equations describing the evolution of the density operator under the influence of the residual quadrupole interaction are given in Eq. [1-138] below. The effect of the isolated residual quadrupole interaction is somewhat opposite to that of the RF pulse in that it couples the $\hat{T}_{nq}$ operators of different rank within a specified coherence.

$$\frac{d}{dt}\begin{pmatrix}\hat{T}_{10}\\ \hat{T}_{11}(s)\\ \hat{T}_{21}(a)\\ \hat{T}_{22}(a)\\ \hat{T}_{30}\\ \hat{T}_{31}(s)\\ \hat{T}_{32}(s)\\ \hat{T}_{33}(s)\end{pmatrix}=\begin{pmatrix}0&0&0&0&0&0&0&0\\ 0&0&i\sqrt{3/5}\,\bar{\omega}_Q&0&0&0&0&0\\ 0&i\sqrt{3/5}\,\bar{\omega}_Q&0&0&0&i\sqrt{2/5}\,\bar{\omega}_Q&0&0\\ 0&0&0&0&0&0&i\bar{\omega}_Q&0\\ 0&0&0&0&0&0&0&0\\ 0&0&i\sqrt{2/5}\,\bar{\omega}_Q&0&0&0&0&0\\ 0&0&0&i\bar{\omega}_Q&0&0&0&0\\ 0&0&0&0&0&0&0&0\end{pmatrix}\begin{pmatrix}\hat{T}_{10}\\ \hat{T}_{11}(s)\\ \hat{T}_{21}(a)\\ \hat{T}_{22}(a)\\ \hat{T}_{30}\\ \hat{T}_{31}(s)\\ \hat{T}_{32}(s)\\ \hat{T}_{33}(s)\end{pmatrix} \quad [1\text{-}138a]$$

$$\frac{d}{dt}\begin{pmatrix}\hat{T}_{11}(a)\\ \hat{T}_{20}\\ \hat{T}_{21}(s)\\ \hat{T}_{22}(s)\\ \hat{T}_{31}(a)\\ \hat{T}_{32}(a)\\ \hat{T}_{33}(a)\end{pmatrix}=\begin{pmatrix}0&0&i\sqrt{3/5}\,\bar{\omega}_Q&0&0&0&0\\ 0&0&0&0&0&0&0\\ i\sqrt{3/5}\,\bar{\omega}_Q&0&0&0&i\sqrt{2/5}\,\bar{\omega}_Q&0&0\\ 0&0&0&0&0&i\bar{\omega}_Q&0\\ 0&0&i\sqrt{2/5}\,\bar{\omega}_Q&0&0&0&0\\ 0&0&0&i\bar{\omega}_Q&0&0&0\\ 0&0&0&0&0&0&0\end{pmatrix}\begin{pmatrix}\hat{T}_{11}(a)\\ \hat{T}_{20}\\ \hat{T}_{21}(s)\\ \hat{T}_{22}(s)\\ \hat{T}_{31}(a)\\ \hat{T}_{32}(a)\\ \hat{T}_{33}(a)\end{pmatrix} \quad [1\text{-}138b]$$

Formal solution to the evolution of the density operator under the influence of the residual quadrupole interaction given an initial $\hat{T}_{11}(s)$ state is given below from (177). Fourier transform of the evolution of $\hat{T}_{11}(s)$ with time, $g_{11}(t)$, yields the split spectrum of **Figure 1-2**.

$$\hat{T}_{11}(s) \rightarrow g_{11}(t)\hat{T}_{11}(s) + g_{21}(t)\hat{T}_{21}(a) + g_{31}(t)\hat{T}_{31}(s) \quad [1\text{-}139]$$

where

$$g_{11}(t) = \frac{1}{5}\left(2 + 3\cos\left(\bar{\omega}_Q t\right)\right) \quad [1\text{-}140]$$

$$g_{21}(t) = \frac{\sqrt{3}}{\sqrt{5}}\sin\left(\bar{\omega}_Q t\right) \quad [1\text{-}141]$$

$$g_{31}(t) = \frac{\sqrt{6}}{5}\left(1 - \cos\left(\bar{\omega}_Q t\right)\right) \quad [1\text{-}142]$$

To search for the presence of residual quadrupole interactions in biological tissue (and underlying tissue 'order' as will be introduced in chapter section 1.6) an RF pulse following transverse evolution under the residual quadrupole interaction can

be applied to convert $\hat{T}_{21}(a)$ into $\hat{T}_{22}(a)$. A subsequent RF pulse will convert $\hat{T}_{22}(a)$ back into $\hat{T}_{21}(a)$ which will then evolve back into $\hat{T}_{11}(s)$ which can be observed. Of value is that multiple averages with appropriate flip-angles and phase cycling can be used to cancel signal from sodium nuclei that do not produce the $\hat{T}_{21}(a)$ spin polarization. This is facilitated by the fact that an RF pulse with a given phase will 'interact' with the double quantum coherence at 2x that phase. There are many different double quantum filtering variants that have been used to assess sodium nuclei in biological environments (177-179). Although double quantum filtering was not used in this thesis, a brief description is given as it is referenced at various times.

In the presence of both RF and residual quadrupole Hamiltonians formal solutions to the combined differential equations become exceedingly cumbersome if the RF pulse is not sufficiently hard that its effect can be considered in isolation. Solutions that would fill much of this page are given in (180,181). However, of particular interest to sodium NMR experiments attempting to assess sodium concentrations is that soft RF pulses applied in the presence of a residual quadrupole interaction may 'selectively produce only' the central single quantum coherence. In this case the transverse magnetization generated will not directly reflect the underlying sodium concentration even if relaxation effects could be 'eliminated.'

1.5.7. The Fluctuating Quadrupole Hamiltonian

While the T_{20} term of the quadrupole Hamiltonian is involved in spin-state energy level shifting when the electric field gradient contains a 'static' (or non-zero time-averaged) component, each term of the quadrupole Hamiltonian is involved in the production of relaxation associated with the superimposed EFG fluctuation. The zero-mean fluctuating component of the quadrupole Hamiltonian is given below:

$$\mathcal{H}_{QF}(t) = \frac{eQ}{\sqrt{6}} \sum_{-2}^{2} T_{2m} \left[\mathrm{V_m}(t) - \overline{(\mathrm{V_m}(t))} \right] \qquad [1\text{-}143]$$

The fluctuating quadrupole Hamiltonian produces very efficient relaxation for sodium nuclei in biological environments, and the much weaker dipole-dipole interaction associated with proton relaxation can effectively be ignored. There are three state transitions for spin 3/2 associated with the production of transverse magnetization, and ensemble coherence need not be 'disrupted' at the same rate for each transition. In fact, the outer and inner transition coherences are reduced to thermal equilibrium at different rates (biexponential transverse relaxation) as given by (182) (describing electron spin coupling). The ensemble spin-state probabilities are also returned to thermal equilibrium at different rates (biexponential longitudinal relaxation) as reported by (183). The first mathematical expressions of biexponential relaxation for spin 3/2 nuclei were given by Hubbard in 1970 (184). It is also of particular interest that the fluctuating quadrupole Hamiltonian can also *produce* coherence for the spin 3/2 system rather than simply destroy it (75).

The equation of motion for the density operator is re-stated below from Eq. [1-136] with the "relaxation superoperator" added.

$$\frac{d\rho^*}{dt} = -i[\mathcal{H}^*_{\mathrm{Static}}, \rho^*] + f(\rho^*) \qquad [1\text{-}144]$$

The evolution of the density operator under the influence of a fluctuating Hamiltonian follows from consideration of the fluctuating Hamiltonian as a second order perturbation (154,157), and assumes that changes in the density operator are small on the time scale of the fluctuations (145,157). The quadrupole relaxation superoperator is given below in Eq. [1-145] for the sodium spin ensemble and includes the static (in the rotating frame) RF and residual quadrupole perturbations (145).

$$f(\rho^*) = \int_0^\infty \overline{\left[\mathcal{H}_{QF}^*(t), \left[\exp\left(-\imath\left(\mathcal{H}_{RF}^* + \mathcal{H}_{QS}^*\right)\tau\right)\mathcal{H}_{QF}^*(t-\tau)\exp\left(\imath\left(\mathcal{H}_{RF}^* + \mathcal{H}_{QS}^*\right)\tau\right), \rho^*(t)\right]\right]} \, d\tau \quad [1\text{-}145]$$

The effect of the relaxation superoperator on the density operator will first be introduced in the absence of RF and residual quadrupole perturbations; the effect of these static interactions will be briefly addressed following analysis of the fluctuating Hamiltonian in isolation (145).

Because evolution of the density operator is considered within the rotating frame, an expression for the fluctuating Hamiltonian within the rotating frame is required. The basis frame transformation is re-stated below

$$\mathcal{H}_{QF}^*(t) = U\mathcal{H}_{QF}(t)U^{-1} \quad [1\text{-}146]$$

where

$$U = \exp(-i\mathcal{H}_Z t) \quad [1\text{-}147]$$

Unlike the static quadrupole Hamiltonian, not all components of the fluctuating quadrupole Hamiltonian commute with $\mathcal{H}_Z$. However, the irreducible spherical tensor operators are of particular value to facilitate this basis frame transformation (150,166). An irreducible tensor is defined by its transformation under rotation as:

$$RT_{nq}R^{-1} = \sum_{q'} D_{q'q}^l(\alpha, \beta, \gamma)\, T_{nq'} \quad [1\text{-}148]$$

In this definition R is the Euler rotation operator, with rotation operation first about the z-axis (angle α), then about redefined y-axis (angle β) and finally about the redefined z-axis (angle γ). The term $D_{q'q}^l(\alpha\beta\gamma)$ is the Wigner rotation matrix, or the operator matrix associated with R in the nq representation of the tensor operators. For the rotating frame transformation only the first rotation term is non-zero and $R = U^*$. For this case (166)

$$D_{q'q}^l(\omega_0 t, 0, 0) = \exp(-iq\omega_0 t)\delta_{q'q} \quad [1\text{-}149]$$

and

$$RT_{nq}R^{-1} = \exp(-iq\omega_0 t)T_{nq} \qquad [1\text{-}150]$$

The result of transforming the fluctuating quadrupole operator to the rotating frame is simply multiplication with an exponential having rotation rate proportional to the quantum value of the operator. The fluctuating quadrupole Hamiltonian is stated below (145), where the $(-1)^q$ term (and other sign changes) result from rotating frame evolution in a negative sense.

$$\mathcal{H}^*_{QF} = \frac{eQ}{\hbar\sqrt{6}}\sum_{-2}^{2}(-1)^q T_{2q}\left[\mathrm{V}_{-\mathrm{q}}(t) - \overline{\left(\mathrm{V}_{-\mathrm{q}}(t)\right)}\right]\exp(iq\omega_0 t) \qquad [1\text{-}151]$$

The relaxation superoperator is expressed below in the rotating frame for the isolated fluctuating quadrupole Hamiltonian, where the dagger represents the Hermitian adjoint $T^{\dagger}_{2q} = (-1)^q T_{2-q}$ (145,157).

$$f(\rho^*) = -\sum_{-2}^{2}\left[T_{2q},\left[T^{\dagger}_{2q},\rho^*(t)\right]\right]\int_0^{\infty}\left(\frac{eQ}{\hbar\sqrt{6}}\right)^2\overline{\left[\mathrm{V}_{-\mathrm{q}}(t) - \overline{(\mathrm{V}_{-\mathrm{q}})}\right]\left[\mathrm{V}_{\mathrm{q}}(t-\tau) - \overline{(\mathrm{V}_{\mathrm{q}})}\right]}\exp(iq\omega_0\tau)d\tau \qquad [1\text{-}152]$$

The integral term looks very much like the Fourier transform of an auto-correlation function, or the power spectral density of the fluctuating interaction. However, as the integral limits do not extend to -∞ this term contains both real and imaginary components. The real terms are the relevant quadrupole interaction power spectral densities, $J_q(\omega)$, sampled at $\omega = q\omega_0$. The imaginary terms result in very small shifts in the spin-states energy levels (dynamic frequency shift) and are generally ignored (145). The relaxation super-operator is restated in Eq. [1-153] in terms of the quadrupole interaction power spectral densities.

$$f(\rho^*) = -\sum_{-2}^{2}\left[T_{2q},\left[T^{\dagger}_{2q},\rho^*(t)\right]\right]J_q(q\omega_0) \qquad [1\text{-}153]$$

The coupled differential equations describing the evolution of the density operator under the influence of a fluctuating quadrupole Hamiltonian (calculated from the

double commutation) are given below from (145), where $J_0 = J_0(0)$, $J_1 = J_1(\omega_0)$, and $J_2 = J_2(2\omega_0)$

$$\frac{d}{dt}\begin{pmatrix}\hat{T}_{10}\\ \hat{T}_{11}(s)\\ \hat{T}_{21}(a)\\ \hat{T}_{22}(a)\\ \hat{T}_{30}\\ \hat{T}_{31}(s)\\ \hat{T}_{32}(s)\\ \hat{T}_{33}(s)\end{pmatrix} = \mathbf{A}\begin{pmatrix}\hat{T}_{10}\\ \hat{T}_{11}(s)\\ \hat{T}_{21}(a)\\ \hat{T}_{22}(a)\\ \hat{T}_{30}\\ \hat{T}_{31}(s)\\ \hat{T}_{32}(s)\\ \hat{T}_{33}(s)\end{pmatrix} \quad \& \quad \frac{d}{dt}\begin{pmatrix}\hat{T}_{11}(a)\\ \hat{T}_{20}\\ \hat{T}_{21}(s)\\ \hat{T}_{22}(s)\\ \hat{T}_{31}(a)\\ \hat{T}_{32}(a)\\ \hat{T}_{33}(a)\end{pmatrix} = \mathbf{B}\begin{pmatrix}\hat{T}_{11}(a)\\ \hat{T}_{20}\\ \hat{T}_{21}(s)\\ \hat{T}_{22}(s)\\ \hat{T}_{31}(a)\\ \hat{T}_{32}(a)\\ \hat{T}_{33}(a)\end{pmatrix} \qquad [1\text{-}154A\text{-}C]$$

$$\mathbf{A} = -\begin{pmatrix}
2/5J_1 + 8/5J_2 & 0 & 0 & 0 & 4/5J_1 - 4/5J_2 & 0 & 0 & 0\\
0 & 3/5J_0 + J_1 + 2/5J_2 & 0 & 0 & 0 & \sqrt{6}/5J_0 - \sqrt{6}/5J_2 & 0 & 0\\
0 & 0 & J_0 + J_1 + 2J_2 & 0 & 0 & 0 & 0 & 0\\
0 & 0 & 0 & J_0 + 2J_1 + J_2 & 0 & 0 & 0 & 0\\
4/5J_1 - 4/5J_2 & 0 & 0 & 0 & 8/5J_1 + 2/5J_2 & 0 & 0 & 0\\
0 & \sqrt{6}/5J_0 - \sqrt{6}/5J_2 & 0 & 0 & 0 & 2/5J_0 + J_1 + 3/5J_2 & 0 & 0\\
0 & 0 & 0 & 0 & 0 & 0 & J_0 + J_2 & 0\\
0 & 0 & 0 & 0 & 0 & 0 & 0 & J_1 + J_2
\end{pmatrix}$$

$$\mathbf{B} = -\begin{pmatrix}
3/5J_0 + J_1 + 2/5J_2 & 0 & 0 & 0 & \sqrt{6}/5J_0 - \sqrt{6}/5J_2 & 0 & 0\\
0 & 2J_1 + 2J_2 & 0 & 0 & 0 & 0 & 0\\
0 & 0 & J_0 + J_1 + 2J_2 & 0 & 0 & 0 & 0\\
0 & 0 & 0 & J_0 + 2J_1 + J_2 & 0 & 0 & 0\\
\sqrt{6}/5J_0 - \sqrt{6}/5J_2 & 0 & 0 & 0 & 2/5J_0 + J_1 + 3/5J_2 & 0 & 0\\
0 & 0 & 0 & 0 & 0 & J_0 + J_2 & 0\\
0 & 0 & 0 & 0 & 0 & 0 & J_1 + J_2
\end{pmatrix}$$

Although this thesis is not concerned with the use of higher order coherences to filter NMR, it is useful to understand the evolution of the polarization of the spin ensemble. As a mathematical result of double commutation the zero quantum $\hat{T}_{10}$ and $\hat{T}_{30}$ operators as well as the single quantum $\hat{T}_{11}$ and $\hat{T}_{31}$ operators are linked through relaxation:

$$\hat{T}_{10} \rightarrow \hat{T}_{10}\left[0.2\exp\left(\frac{-t}{T_{1f}}\right) + 0.8\exp\left(\frac{-t}{T_{1s}}\right)\right] + \hat{T}_{30}\frac{2}{5}\left[\exp\left(\frac{-t}{T_{1f}}\right) - \exp\left(\frac{-t}{T_{1s}}\right)\right] \qquad [1\text{-}155]$$

where

$$T_{1f} = \frac{1}{2J_1}; \quad T_{1s} = \frac{1}{2J_2} \qquad [1\text{-}156]$$

and

$$\hat{T}_{11}(s,a) \rightarrow \hat{T}_{11}(s,a)\left[0.6\exp\left(\frac{-t}{T_{2f}}\right) + 0.4\exp\left(\frac{-t}{T_{2s}}\right)\right] + \hat{T}_{31}(s,a)\frac{\sqrt{6}}{5}\left[\exp\left(\frac{-t}{T_{2f}}\right) - \exp\left(\frac{-t}{T_{2s}}\right)\right] \qquad [1\text{-}157]$$

where

$$T_{2f} = \frac{1}{J_0 + J_1}; \quad T_{2s} = \frac{1}{J_1 + J_2} \qquad [1\text{-}158]$$

An appropriately phased RF pulse can be used to convert the rank 3 signal quantum coherence into a rank 3 triple quantum coherence, and a subsequent appropriately phased RF pulse can be used to reproduce $\hat{T}_{31}$ which will evolve back into $\hat{T}_{11}$ under the influence of relaxation. This is the essence of triple quantum filtering, where appropriate phase cycling (related to the more rapidly rotating triple quantum coherence) and sequence averaging can be used to cancel all signal in cases where $\hat{T}_{31}$ is not generated (75). The operator $\hat{T}_{31}$ is not produced when $T_{2f} = T_{2s}$, or when the transverse relaxation is monoexponential. This technique has been used 'extensively' in attempts to probe sodium concentration and relaxation differences between intracellular and extracellular space. In this thesis an alternative, potentially higher yield methodology is proposed for this task (Chapter 7). The nature of the spectral density function for sodium in a biological environment will be introduced in chapter section 1.6.

The coupled differential equations describing the evolution of the density operator above (Eq. [1-154]) are given in the absence of static RF and residual quadrupole perturbations. If a residual quadrupole interaction persists it will commute with the $q = 0$ term in the fluctuating Hamiltonian, and its dependence removed from the relaxation super-operator with respect to this term. The effect of a residual quadrupole interaction related to the $q = \pm 1, \pm 2$ terms is a shift in the sampling

of the interaction power spectral density functions J_1 and J_2 in proportion to $\bar{\omega}_Q$. However, this shift in comparison to the Larmor frequency is insignificant. In the presence of an RF field the static quadrupole Hamiltonian no longer commutes and many more terms are introduced into the coupled differential equations above (Eq. [1-154]). These terms are dependent on the power spectral density function J_0 sampled not only at 0 Hz, but at the two additional frequencies below (71):

$$\lambda_1 = \sqrt{\bar{\omega}_Q^2 + 2\omega_1\bar{\omega}_Q + 4\omega_1^2} \quad [1\text{-}159]$$

$$\lambda_2 = \sqrt{\bar{\omega}_Q^2 - 2\omega_1\bar{\omega}_Q + 4\omega_1^2} \quad [1\text{-}160]$$

It is assumed for the simulations performed in this thesis that the dispersion of J_0 at low frequency is negligible. When $J_0(0) \approx J_0(\lambda_1) \approx J_0(\lambda_2)$ the coupled differential equations of Eq. [1-154] remain valid in the presence of the static RF and residual quadrupole Hamiltonians. An absence of low frequency spectral dispersion is also assumed by the group that derived and presented the coupled differential equation describing the evolution of sodium spin ensemble given above (71). Measurements of low frequency spectral density dispersion do not exist for cellular tissue, but it is likely, given the lack of discrete long-term sodium ion binding sites in biological environments, the type of which may contribute energy solely to $J_0(0)$ (chapter section 1.6), that dispersion within this frequency range is small.

Although evolution of the density operator within the irreducible spherical tensor basis set completely describes relaxation for the spin ensemble, it does not highlight the 'source' of the two components of biexponential transverse relaxation. Solution to the Redfield relaxation matrix which describes the time dependence of the three (for sodium) single quantum coherences highlights that the T_{2f} component of transverse relaxation is associated with coherence between

the outer states and T_{2s}, coherence between the inner states (75). The Redfield relaxation matrix for a four state system is derived in (182).

1.5.8. Sodium NMR Simulation

The evolution of the density operator for the spin 3/2 sodium nuclei during an NMR experiment involves solution to the sum of the three coupled differential equations under the influence of RF (Eq. [1-137]), static residual quadrupole (Eq. [1-138]), and fluctuating quadrupole (Eq. [1-154]) Hamiltonians. While formal solutions in special cases may be used for sequence design, for general sequence analysis formal solutions can be quite impractical. Numerical solution provides a means to observe and optimize the evolution of the density operator for 'complicated' sequence scenarios. The numerical solution is given below, where V is the modal matrix whose columns are the eigenvectors of the summed differential equation matrices, and D is a diagonal matrix of associated eigenvalues (71).

$$\rho(t) = V\exp(\mathrm{Dt})V^{-1}\rho(0) \qquad [1\text{-}161]$$

Eigenvectors and eigenvalues for the coupled differential equations were solved in Matlab. The NMR simulator built during this thesis is shown in Appendix 6.

1.6. Sodium NMR Interactions in Biological Environments

For sodium NMR in biological environments the preponderant quadrupole interaction, $\omega_Q(t)$, will be time dependent, as both the quadrupole coupling constant, $\chi(t)$, and the angle of orientation of the 'experienced' electric field gradients with respect to the main magnetic field, $\theta(t)$, will change with time (Eq. [1-162]).

$$\omega_Q(t) = \frac{\chi(t)}{4}(3\cos^2\theta(t) - 1) \qquad [1\text{-}162]$$

In an environment where the EFGs are randomly distributed in 3D space and the fluctuations of $\omega_Q(t)$ are very rapid on the scale of the Larmor period (ω_0^{-1}), the time averaged $\omega_Q(t)$ will be zero. This is the case of sodium in a simple saline solution, where the origin of the EFG arises from instantaneous asymmetries in the hydration shell (160,185,186). Although the average power of these interactions is very large $\upsilon_{Qrms} \cong 1$Mhz (161), the interaction correlation time constant (τ_c) is very short $(< 1$ ps) (where τ_c is the characteristic time of an exponential autocorrelation function, $\exp(-\tau/\tau_c)$, a reasonable approximation for an aqueous NaCl solution (160)).

In biological environments it is possible that much slower fluctuations of $\omega_Q(t)$ may be superimposed on the rapid variations arising from the 'thermal' distortions of the hydration shell (the source of these slower fluctuations is discussed below). If the duration of an effective half-period of the slow fluctuation approaches ω_0^{-1} but is still less than the inverse of the time-averaged $\omega_Q(t)$ during a half-period, spectral splitting remains non-existent (i.e. $\omega_Q(t)$ is still time-averaged to zero over the NMR time scale) (160,161). The slow fluctuating contribution will, however, increase the interaction energy at low frequencies, with consequence for relaxation (i.e. the power spectral density at 0 Hz will be increased resulting in biexponential transverse relaxation). If the effective period of the superimposed $\omega_Q(t)$ fluctuations become quite long,

and/or the magnitude of $\omega_Q(t)$ associated with these slow fluctuations becomes quite large, $\omega_Q(t)$ will not be time-averaged to zero over the NMR time scale and the spectrum will be split according to the 'residual quadrupole interaction' – $\bar{\omega}_Q$ (i.e. the time-averaged $\omega_Q(t)$) (187). It should be noted that the biexponential transverse relaxation process will also be very efficient in the case of 'very' slow superimposed EFG fluctuations.

While the rapid EFG fluctuations produced by the hydration shell surrounding the sodium ion in an aqueous environment are well known (186), the sources of slow EFG fluctuations experienced by sodium nuclei in biological environments are not as clear, and diverse mechanisms are likely involved. Sodium ions may be 'bound' to sites within large macromolecules such as the grooves of DNA (188-192). Cation binding is essential for the folding and stability of large RNA molecules (193), and the binding of Na^+ and K^+ in particular is essential for the proper function of many enzymes (194,195). Sodium nuclei directly and statically bound to large stationary macromolecules would likely experience large constant electric field gradients. However, binding to biological macromolecules is most likely a very transient process, as binding sites on the minor groove of DNA are suggested to be occupied for only 50 ns (189).

Models of rapid exchange between 'bound' and 'free' ions states (discrete exchange models) have been used to describe sodium NMR dynamics and assess sodium interactions with specific macromolecules (in particular DNA) (188,189,196-199). However, the 'binding' of sodium ions in a biological environment can take many forms including inner-sphere (or direct), outer-sphere (coordination through a water molecule) and atmospheric (200). While 'strong' binding may exist for molecules of nucleic acid, weaker and non-specific (or 'territorial') binding is associated with other prevalent biological macromolecules such as carbohydrate chains, proteoglycans or glycosaminoglycans (201,202). As binding weakens, the residence duration of an ion within an EFG produced by association with the macromolecule is reduced. In this way the rate and

magnitude of EFG fluctuations may be related to the type, strength and availability of sodium ion binding sites within the environment (199). In biological tissue, the concentration of 'strong' binding sights is suggested to be very much less than the concentration of ions (160,161).

Slow EFG fluctuations experienced by sodium nuclei in biological environments will also be influenced by the diffusion of the sodium ion through the time-span of its NMR coherence (161,163,203,204). Repeated 'encounters' with EFGs having the same spatial orientation will greatly increase the interaction energy at low frequencies. While these 'encounters' may be short-lived, in an ordered environment the probability of similar 'encounters' may be quite high. In this sense the rate of the slow EFG fluctuation can be discussed in terms of local 'order.' Saline solutions can be described as 'zero order' environments, while 'medium-range order' environments produce slow fluctuating $\omega_Q(t)$ components but no spectral splitting. It is in environments with 'long-range order' that residual quadrupole interactions remain.

The EFGs 'encountered' by the sodium nucleus throughout its nuclear NMR coherence may involve the specific transient binding of a sodium ion to a molecule such as DNA; they may also involve 'territorial interaction.' Of particular importance to the discussion of the latter is the role of the hydration shell in the EFG experienced by the nucleus. It has been considered that the water surrounding the sodium ion simply acts to screen a territorial electrostatic macromolecular-generated EFG, as a result of fixed-charges, at the nuclear site (i.e. the water simply has a dielectric effect) (205). However, this continuous solvent model has been considered insufficient to fully describe the EFG at the nuclear site, as perturbations of the hydration shell itself, beyond random thermal fluctuation, brought about by short-range interaction with large macromolecules are also involved in the production of EFG fluctuation (206-208). At surface interfaces, perturbation of the hydration shell from symmetry may result from the preferential orientation of the water molecules as a result of hydrogen bonding

(209). Elsewhere, perturbations of the hydration shell are simply discussed as outer-sphere collisions with macromolecules, with the EFGs generated being perpendicular to the surface (161). It has been suggested that along surfaces, fixed macromolecular charges may have little to do with the EFGs experienced by sodium nuclei other than the adsorption of ions along the surface, being overshadowed by hydration shell distortion (210,211). Large, slow-fluctuating electric field gradients with long correlation times may arise from the diffusion of sodium ions in tightly confined and highly anisotropic environments. It should also be noted that macromolecular density will also influence slow EFG fluctuation (209), increasing frequency of interaction.

When discrete exchange models are used to assess ion interactions with macromolecules, quadrupole interaction in each ion 'pool' (either 'free' or 'bound') is defined by an exponential autocorrelation function with characteristic time constant, or a Debye model, and the resultant relaxation described according to a population weighted mean. While this methodology may be functional for the NMR analysis of molecules with specific binding sites (199), it is somewhat awkward to characterize EFG fluctuation twice, i.e. within the autocorrelation functions defining each site and within the 'chemical exchange,' especially given the very transient binding in even the strongest binding cases. The discrete exchange model can be replaced by a continuous diffusion model in which distinct Debye models of autocorrelation are abandoned and replaced by a single autocorrelation function for the diffusing nuclei (161,204,210). Within this thesis a single autocorrelation function is considered for all sodium NMR environments simulated, with power spectral density values extrapolated from relaxometry measurements via Eqs. [156, 158]. Apart from the case of saline, these power spectral density values specify autocorrelation functions that are not exponential (or Debye). While others have attempted to create non-exponential single autocorrelation models for sodium nuclei in biological environments, this sort of interaction modeling is not relevant to this thesis (210). It should be noted,

however, that in complex environments such as cellular tissue different ‘domains’ or ‘compartments’ may be present with limited sodium exchange between them.

The purpose of single quantum sodium imaging has typically not been concerned with the use of quadrupolar interactions (i.e. relaxation and residual splitting) to describe the nature of biological environments; it has generally been concerned with the assessment of tissue sodium concentration. However, it is important to have some understanding of the nature of sodium quadrupole interactions in-vivo. It is informative to note that studies of yeast cells suggest an intracellular space containing an effective single NMR population of sodium nuclei exhibiting biexponential relaxation but no spectral splitting (210). This suggests no local regions within the (yeast) cell producing ‘experienced’ EFG fluctuations slower (and possibly greater) than the rest of the cell where sodium nuclei are ‘held’ over the lifetime of the transverse coherence. Such regions would exhibit a more rapid short component of biexponential relaxation and possibly residual splitting. While local regions producing slower EFG fluctuations may exist within the cell, such as the nucleus (isolated DNA has been shown to produce spectral splitting (163)) or the mitochondria with its many membrane folds (mitochondrial suspensions have also been shown to produce spectral splitting (212)), intracellular sodium ions may only ‘sample’ these regions for limited periods of time. The discussion of ‘pools’ of sodium ions in biological environments is an old one. Early sodium NMR studies in biological tissue suggested a large component (65%) of sodium in muscle, brain and kidney was complexed to macromolecules while the remainder was free (213,214), but these early studies lacked understanding of the nature of biexponential relaxation produced by a quadrupole nuclei (34). More recently, distinct intracellular sodium pools were suggested for rat liver using a combination of shift reagent multiple quantum coherence to assess intracellular sodium (53). Distinct intracellular pools have also been suggested for perfused rat heart, based on single quantum relaxation fitting, with the hypothesis that one pool contains those ions in the subsarcolemmal space (52). Finally, differences in single and triple quantum measures of intracellular T_{2f} for implanted gliosarcoma

(49,50) and perfused rat heart (46,52,215-217) also suggest distinct intracellular pools.

In general, sodium nuclei within intracellular space are simply assumed to form a homogenous pool with respect to quadrupole interaction, however, considerable effort has been applied to measure quadrupole interaction differences between this intracellular pool and the presumed different extracellular (or interstitial) pool or sodium nuclei. Extracellular sodium, present in a concentration ~ 10x that of intracellular sodium and buffered by the body's homeostatic mechanisms, may obscure intracellular sodium concentration changes that may be of note, such as elevation related to the rate of cell proliferation (218,219), or increases related to early anoxic depolarization in ischemia (95). As such, the ability to selectively acquire signal from intracellular sodium based on sodium NMR characteristics would be highly beneficial. The discrimination of intracellular and extracellular sodium NMR characteristics requires a separation mechanism such as a shift reagent, and several have been used (220-222). In implanted gliosarcoma (49,50), perfused rat heart (46,216), and perfused rat liver (223) relaxation differences were measured between intra and extracellular space. Unfortunately, although the blood-brain-barrier has been broken in two studies to facilitate the invasion of interstitial space with shift reagent (224,225), no measures of intracellular and extracellular relaxation in brain tissue have been made. However, different NMR characteristics in the two spaces have been implied from differences in the signal intensity timelines of single and multiple-quantum filtered methods following onset of ischemia (74,111,226). The anatomy of interstitial space in the brain which facilitates bulk transport (227-229), also suggests a less dense environment. A technique is presented in this thesis which may be useful in the discrimination of intracellular and extracellular space if significant relaxation differences do actually exist (Chapter 7).

When bulk tissue sodium concentrations are to be assessed, the compartmentalization of sodium nuclei has importance in terms of sodium

'invisibility;' if a portion of the tissue sodium population is 'undetectable' by NMR, the NMR signal will not accurately reflect concentration. It has been suggested that > 20% of intracellular sodium remains undetected by NMR spectroscopy in a range of mammalian erythrocytes when compared to sodium measurement by flame photometry (230,231). A similar study with rat muscle suggested an intracellular sodium 'invisibility' of ~ 30% (232). 'Invisibility' is an awkward term and is really a measure of signal loss as a result of the NMR measurement method and the sodium quadrupole interactions. There are two sources of sodium NMR signal loss, which as described above reflect a continuum of microscopic 'order': rapid biexponential relaxation, and residual quadrupole splitting (233). If all compartments within a tissue simply exhibit biexponential relaxation without quadrupole splitting, minimization of signal loss is relatively 'simple' and involves, for imaging, a minimization of TE (234). It should, however, be noted that bulk tissue relaxation measurements may not reflect different compartmental relaxation rates, and it is possible, when TE is not extremely short, that signal loss may vary for potentially different tissue compartments.

While the minimization of tissue sodium signal loss with respect to biexponential relaxation has been discussed at great length (7,12,30,234,235) the effect of quadrupole splitting on acquired sodium signal has essentially been ignored. This is likely for good reason as no residual quadrupole interactions where found in a comprehensive study of the yeast cell (210), or within porcine skeletal muscle or cat brain (236). However, with more recent use of the double quantum filtering (237) and Jeener-Broekaert techniques (238) with increased sensitivity (to quadrupole splitting), residual quadrupole interactions have been observed in cartilage (178,238-241), in erythrocyte cells (242-244), and most importantly for this thesis in human skeletal muscle and brain in-vivo (245). As mentioned previously, residual quadrupole interactions have also been measured in mitochondrial suspensions (212) and isolated DNA (163). It is possible that signal loss related to sodium 'invisibility' is a result of residual quadrupole splitting; this

is an old hypothesis (246). In an imaging sense, the satellite-related signal in any voxel having sodium nuclei in macroscopically disordered compartments with residual quadrupole interactions will be rapidly dephased following its production (i.e. in a spectroscopy sense this refers to the spreading of the satellite peaks – with the production of a powder spectrum). The rate of dephasing of this 60% of the transverse magnetization coherence will be dependent on the average magnitude of the EFG interaction. Another source of signal loss related to residual splitting arises from insufficient excitation of the satellite resonances when soft or narrow bandwidth RF excitation pulses are implemented. When the central transition is selectively irradiated the maximum transverse magnetization that can be produced is only 20% of the longitudinal magnetization in thermal equilibrium (181,247,248).

There is only one early study (1987) of signal loss related to residual quadrupole interactions in the brain (cat) and sodium was determined to be 100% 'visible' (236). When the central transition is selectively irradiated it will 'flip' at a rate of $2\omega_1$. This early study searched for a flip-angle dependent effect but did not find one, implying no residual quadrupole related signal loss. At ISMRM Hawaii (Stobbe, Beaulieu, 2009) preliminary data was presented for a similar experiment using 'high resolution' short TE imaging in the human brain with the result of positive flip-angle dependent effect, especially in white matter tracts running parallel to the main magnetic field (164). It was suggested that the residual quadrupole interaction observed may be dependent on the high degree of diffusion anisotropy associated with myelinated axons.

There is a paucity of knowledge concerning sodium quadrupole interactions in brain tissue. While it has generally been assumed that residual splitting is not present in the human brain, recent double quantum experiments suggest otherwise. This residual splitting likely represents a source of signal loss not considered in recent tissue sodium concentration measurements that attempt to minimize biexponential relaxation. Whether or not sodium 'pools' with different

quadrupole interactions exist, such as intracellular vs. extracellular, or within different cellular compartments, or within different cell types, or within the myelination, remains to be determined. In this thesis for our stroke study (Chapter 6) we chose to accept some known signal loss with respect to biexponential relaxation in exchange for reduced noise variance (Chapter 5). 'Full' elimination of all quadrupole NMR related weighting may require very short RF pulses with very short echo times; this requirement is problematic with respect to SNR and SAR constraints at high field. Although attaining an in-vivo measure for a physical parameter such as sodium concentration is very alluring, correlation of sodium signal intensity which includes the quadrupole dependence on macromolecular structure with disease state may be just as valuable (or even more so, given increased SNR and potentially beneficial added contrast). In the future, sodium quadrupole NMR contrast could possibly be *exploited*, in both its forms, to assess macromolecular structure and tissue anisotropy in the human brain rather than *minimized* which appears to be the current norm for sodium imaging. A sodium imaging technique attempting to enhance contrast related to long-range order was recently presented at ISMRM Toronto (Stobbe, Beaulieu, 2008) (249).

Chapter 2

Advantage of Sampling Density Weighted Apodization Over Post-acquisition Filtering Apodization for Sodium MRI of the Human Brain

A version of this thesis has been published
(R.S. Stobbe, C. Beaulieu, Magn Reson Med, 60, 981-986, 2008)

2.1. Introduction

Perhaps the greatest detriment to sodium MRI of the human brain is the low sodium concentration in-vivo (~50 mM for ^{23}Na vs. ~ 80 M for ^{1}H). Because of this concentration deficit, sodium imaging voxel sizes must be considerably larger than those generally acquired for proton imaging; an increased voxel size is required in order to generate an adequate signal to noise ratio (SNR). One consequence of implementing large voxels (and low matrix size) is that Gibbs' ringing extends relatively far (in space) beyond the sharp transition that generated the ringing artifact. The affect of this ringing on sodium image quality can be seen in **Figure 2-1**; it not only degrades image appearance, it may also confound tissue and lesion region of interest (ROI) analysis.

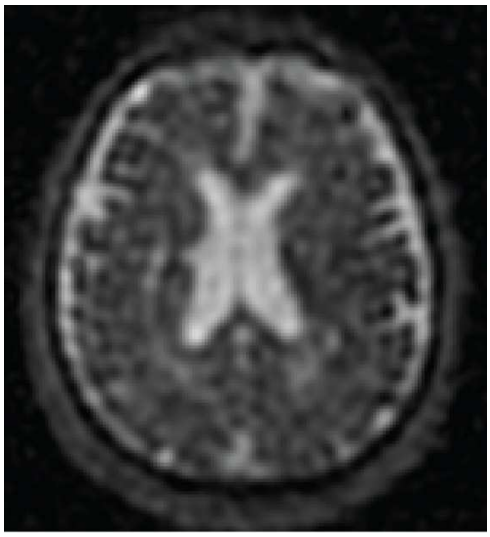

Figure 2-1: A sodium image of the human brain generated with uniform k-space (3D-TPI) sampling and no post-acquisition filtering. This image highlights the effect of Gibbs' ringing, which appears to originate along the inner circumference of the head and propagate toward the centre.

One approach to minimize ringing is to post-acquisition filter a uniformly sampled k-space with an appropriate apodizing function just prior to Fourier transform (UPFA – Uniform k-space sampling with Post-acquisition Filtering Apodization). Another approach is to sample k-space in such a manner that the acquisition sampling density matches the desired apodizing function (SDWA – Sampling Density Weighted Apodization). SDWA for Gibbs' ringing removal is not a new concept; it was proposed in 1987 (250,251) and can be implemented for low signal, low resolution applications such as spectroscopic imaging, where multiple averaging is common (252-257). SDWA was recently implemented for 3D pure phase-encode sodium imaging of the heart (258,259). A previous sodium imaging paper of the human brain using 3D twisted projection imaging (3D-TPI) (30) implemented sampling density weighting with the intention to reduce readout length and T_2^* attenuation (using a 'mild' sampling density shape) (29). In the current paper sampling density weighting was implemented for 3D-TPI with the different intention of producing effective, SNR efficient, image apodization.

The purpose of the current paper is to directly quantify the SNR advantage of SDWA over UPFA with sodium 3D twisted projection imaging (3D-TPI) of the human head, and to compare this SNR increase with theory. This was accomplished with the creation of two 3D-TPI projection sets, one producing uniform sampling density, and the other a 'generalized Hamming' sampling density which conforms to 3D-TPI design constraints for full k-space sampling (the SDWA projection set produces an effective redistribution of the global over-sampling inherent in uniformly sampled 3D-TPI). Both projection sets sampled k-space to the same extent with an identical number of projections, readout length, and number of sampled points along each projection (TE, TR, and flip angle were also constant for this comparison). The SNR advantage of SDWA (when compared to UPFA) was quantified, and a significant noise coloring benefit demonstrated in sodium images acquired from a saline phantom and healthy human brain.

2.2. Theory

2.2.1. SNR Advantage of Sampling Density Weighted Apodization

The relative image noise variance advantage of SDWA ($\sigma^2_{SDWA}/\sigma^2_{UPFA}$) is given in Eq. [2-1] , where $\mathrm{F}(k)$ is the desired shape of the k-space 3D modulation transfer function (MTF) generated by sampling density for the SDWA approach and post acquisition filtering for the UPFA approach. K is the total number of Cartesian k-space grid-points within the MTF. This equation is conceptually the same as that given by Pipe and Duerk to quantify the relative image noise variance increase associated with (non-uniform) post-acquisition weighting of individual data points (55).

$$\frac{\sigma^2_{SDWA}}{\sigma^2_{UPFA}} = \frac{(\sum_K \mathrm{F}(k))^2}{K \sum_K \mathrm{F}(k)^2} \qquad [2\text{-}1]$$

The noise power spectral density (PSD) is given for both SDWA and UPFA in Eq. [2-2] and Eq. [2-3], where *M*K* describes the total number of data samples collected for the case of uniform sampling (which is identical for the sampling density weighted case), and σ_S^2 is the noise variance associated with each data sample collected.

$$\mathrm{PSD}_{\mathrm{UPFA}}(k) = \frac{\mathrm{F}(k)^2}{M}\sigma_S^2 \qquad [2\text{-}2]$$

$$\mathrm{PSD}_{\mathrm{SDWA}}(k) = \frac{\sum_K \mathrm{F}(k)}{MK}\mathrm{F}(k)\sigma_S^2 \qquad [2\text{-}3]$$

2.2.2. Design Constraint for Sampling Density Weighting with 3D-Twisted Projection Imaging

A 3D radial sampling density shape, $\Gamma(r)$, can be generated with 3D-TPI (beyond *p*) by designing the radial component of each projection (*r* – as a fraction of $k_{\max}$) to evolve according to Eq. [2-4]**,** adapted from (29).

$$\frac{dr}{d\tau} = \frac{p}{\Gamma\big(r(\tau)\big)r^2(\tau)} \qquad [2\text{-}4]$$

In this equation $\tau = \gamma Gt/k_{\max}$, the dimensionless fraction of the time required for a projection to reach the edge of k-space if it did not begin twisting (G is the gradient magnitude associated with the projection). When full Nyquist sampling is desired and the minimum number of cones and the minimum number of projections on each cone are to be used (as above), the following projection design constraints on $\Gamma(r)$ exist: $\Gamma(p) = 1/p$, and $\Gamma(r) \geq 1$. If these constraints are met the resulting sampling density will match $\Gamma(r)$ without 'Nyquist holes'. For a uniform sampling density shape, $\Gamma(r)$ must equal the constant 1/*p* for full Nyquist sampling, highlighting the 'global averaging' in uniform 3D-TPI.

2.2.3. Apodization Filter

A 'generalized Hamming' 3D radial filter (Eq. [2-5]) was developed for SDWA sodium imaging with 3D-TPI.

$$\Gamma(r) = s_1 - s_2\cos\big(\pi(1+r)\big) \qquad [2\text{-}5a]$$

$$s_2 = \frac{\left(\frac{1}{m} - n\right)}{1 - \cos\big(\pi(1+m)\big)} \qquad [2\text{-}5b]$$

$$s_1 = s_2 + n \qquad [2\text{-}5c]$$

This filter has a value of 1/*m* at *r* = *m*, and a value of *n* at *r* = 1 (when *m* = 0.08 and *n* = 1 this generalized filter reverts to the shape of the Hamming filter). The 3D-TPI design constraint for full k-space sampling described above is fulfilled

when $m = p$ and $n = 1$ (i.e. $\Gamma(p) = 1/p$, and $\Gamma(1) = 1$). For this filter, the greatest apodization characteristics are generated when m is small. However, the minimum value of p (projection design for $m = p$) will be constrained by the relative length of each projection.

2.3. Methods

Two different 3D-TPI projection sets were created for the comparison of UPFA and SDWA: one generating uniform k-space sampling density; and the other, the sampling density prescribed by Eq. [2-5] ($m = p = 0.16$). Both projection sets included the same number of projections (3700), each sampling the same number of k-space locations (225) to a very similar k-space extent (~156.4 1/m SDWA, and ~156.8 1/m UPFA). The sampling bandwidth (12500 Hz), and readout length (17.92 ms) were identical for both. To create projections of equivalent length, different twist parameters (p) were used to generate each projection set. When the sampling density shape of Eq. [2-5] is implemented with $m = p = 0.16$, the relative projection length is 4.48 times longer than if the projections did not begin twisting. For uniform sampling density, the same relative projection length was achieved with $p = 0.28$.

Both projection set designs were gridded with 'ones' to highlight sampling density using a Kaiser convolution kernel of width 4 and beta 5.8 (with no 'sub-sampling' of the k-space grid). The sampling densities for both the uniformly sampled, and sampling density weighted projection sets are highlighted in **Figure 2-2a** and **2-2b**. As each projection set acquires an equivalent number of points per projection (and an equivalent number of total points) the total sampling 'volume' (4D) is the same for each projection set. For both projection sets there are no locally under-sampled areas (or 'Nyquist holes') visible within the sampling density matrix generated. The uniform 3D-TPI projection set generates an over-sampling in the extents of k-space to a factor of 3.67 times. This is slightly greater than $1/p = 1/0.28 = 3.57$ as 3700 projections were implemented, while the minimum number of projections for full sampling was 3603. This 2.7% increase in projections is equivalent to the 2.7% increase in uniform sampling density. The SDWA projection set implemented generates a sampling density that is a scaled version of Eq. [2-5]. This global scaling results from the fact that the SDWA

projection set was implemented with 80% more projections (3700) than the minimum number required for full sampling (2059).

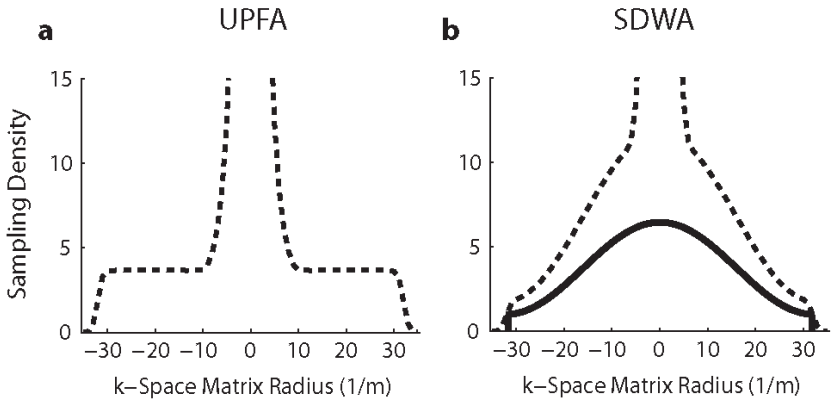

Figure 2-2: 1D profiles (dotted lines) through the three dimensional sampling density matrix are shown for both uniform sampling (**a**) and sampling density weighting (**b**) projection designs (minor deviations result for implementation with a gradient waveform memory limited system). In the SDWA case, the sampling points have been redistributed from the edges to the centre of k-space, creating the sampling density shape shown (note that this redistribution occurs in all three dimensions). The solid line in (**b**) is plotted directly from Eq. [2-5]; the sampling density weighting generated is a scaled version of this filter shape. Both the SDWA and the UPFA cases are over-sampled at the centre of k-space (an inherent quality of radial imaging). However, this local oversampling is the same for both filtering approaches presented and also relatively small in comparison to the total number of data samples collected (required compensation yields an ~ 5% reduction in SNR efficiency).

For image creation, over-sampling at the centre of k-space, along the z pole, and throughout the z = 0 plane (as a result of projection set implementation) was compensated for with an iterative approach (260). A Kaiser convolution kernel of width 4 and beta 6.5 (gridded k-space 'sub-sampled' at a rate of 1.2 (261)) was used for this compensation and subsequent k-space gridding for image construction.

Images were acquired from a spherical 50 mM [Na^+] saline phantom (with a long T_2* = 53 ms) and from the heads of three healthy volunteers for both apodization

approaches in only 3:10 minutes per scan (2 averages), with the intention (of the short scan time) to highlight image noise. For the UPFA case, k-space was post-acquisition filtered through the sampling density compensation process according to Eq. [2-5] (m = 0.16). For each image, SNR was measured in the identical ROI for both the SDWA and UPFA cases. For each volunteer this ROI consisted of many large regions throughout the brain including both gray and white matter. Noise variance was measured in the image background (using an ROI that consisted of 4 corner regions per slice on ~ 20 slices). High quality sodium images of the human brain were also generated in a practical scan time of 11.4 minutes for the SDWA approach. The minimum number of projections (3306, with rounding up on each cone) were used for this projection set (p = 0.16) covering an isotropic k-space volume to a maximum value 164.2 1/m.

All images were acquired on a 4.7 Tesla Varian Inova (Palo Alto, CA) scanner, using a home-made, single-tuned, birdcage RF head-coil. A steady-state sequence optimized under SAR constraint (42) was used to generate each image. This sequence consisted of a non-selective RF pulse of length 900 μs and flip angle 55^{o}, followed by either the UPFA or SDWA 3D-TPI readout, and subsequent gradient spoiling for a repetition time of 25 ms. It should be noted that the k-space acquisition comparison described is independent of RF pulse length, flip angle and TR.

2.4. Results

Images acquired from a saline phantom are shown for both SDWA and UPFA in **Figures 2-3a** and **2-3b**. Theory (Eq. [2-1]) suggests a relative SNR advantage of 17% for SDWA; an SNR increase of 16% was measured in this phantom (average over several scans). The noise colouring is also visibly different for both filtering methods, and the noise power spectral densities are plotted in **Figures 2-3c** and **2-3d** (from Eq. [2-2] and Eq. [2-3]). For the UPFA case the noise PSD at the centre of k-space is the same as when no post-acquisition filtering is performed. For the SDWA case, the noise PSD at the centre of k-space is reduced to 32%, or $K/\sum_K \mathrm{F}(k)$, of the UPFA case (from Eq. [2-2] and Eq. [2-3]).

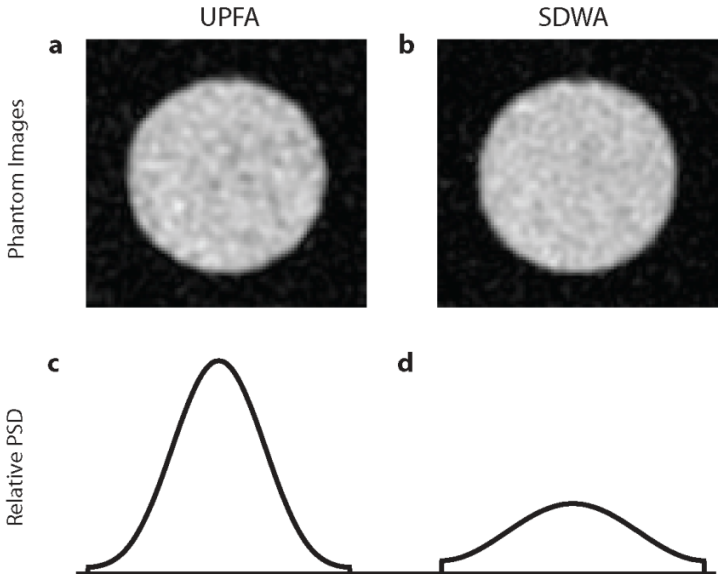

Figure 2-3: Images generated from a saline sphere are shown in (**a**) and (**b**). The SNR is clearly greater (16%) for SDWA over UPFA; there is also a visible difference in noise colouring (i.e. less low frequency and greater high frequency noise). In (**c**) and (**d**) 1D profiles of the relative noise power spectral density (PSD) are plotted from Eq. [2-2] and Eq. [2-3].

Representative human brain images acquired from a healthy volunteer in just over 3 minutes are shown in **Figure 2-4a** and **2-4b**. For both the UPFA and SDWA cases the effect of Gibbs' ringing has been reduced. When areas of the brain that are expected to be homogeneous are compared, the noise variance for the SDWA case is visibly less than for the UPFA case. A reduced 'speckle-size' is also apparent for the SDWA case. The measured relative SNR benefit of SDWA is plotted in **Figure 2-4c**, along with the SNR advantage calculated from Eq. [2-1], and for the three volunteers increases of 16%, 18%, and 16%, respectively, are in good agreement with theory (17%).

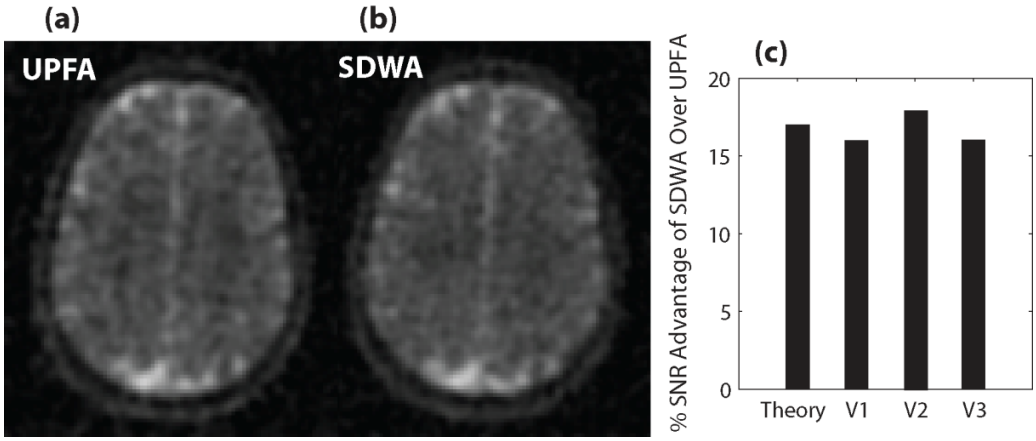

Figure 2-4: The relative SNR advantage of apodization by sampling density weighted filtering (SDWA) over uniform k-space acquisition with post-acquisition filtering (UPFA). This advantage is demonstrated with representative images from a healthy volunteer, and quantified over the whole brain for three volunteers (V1, V2, V3), which agrees well with theory.

In **Figure 2-5** multiple slices of a representative higher resolution image acquired from the brain of a healthy volunteer in ~ 11 minutes are displayed for the SDWA projection set described. This sodium image with isotropic voxels has an average SNR of 22 in brain tissue and does not display Gibbs' ringing.

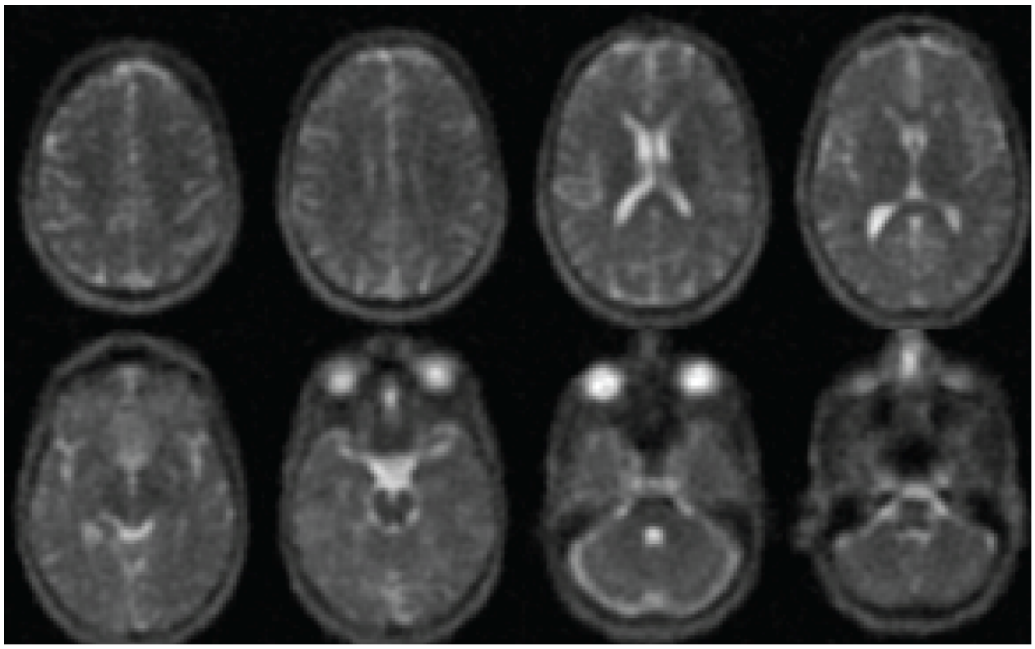

Figure 2-5: Multiple slices of a representative sodium image acquired from a healthy volunteer at 4.7 Tesla using the SDWA approach. This image was acquired in 11.4 minutes with a nominal isotropic resolution of 3.2 mm (given as $1/2 \cdot k_{\max}$). As can be seen there is no visible effect from Gibbs' ringing, and the image quality is excellent for a sodium scan. The average image SNR in brain tissue is ~ 22.

2.5. Discussion

In this paper a quantitative analysis of the SNR benefit associated with sampling density weighted apodization (SDWA) when compared to uniform sampling with post-acquisition filtering apodization (UPFA) is presented for sodium 3D-TPI by introducing a 'generalized Hamming' function that could be implemented by redistributing the inherent over-sampling (or global averaging) in uniform 3D-TPI without violating the Nyquist criterion. For this apodizing filter, a 17% SNR advantage associated with SDWA over UPFA was calculated from theory, and experimentally an average 17% benefit was measured with sodium imaging of the human head for three volunteers (**Figure 2-4**). It was also shown that SDWA apodization exhibits a substantial noise colouring benefit over UPFA (i.e. the noise variance reduction associated with SDWA over UPFA is predominantly in the low spatial frequencies) (**Figure 2-3**). The reduction in low frequency noise for SDWA yields images with smaller noise 'speckle-size'.

The SNR increase of 17% associated with the use of SDWA rather than UPFA is by no means insignificant. This increase can be exploited for a 27% decrease in imaging time (for the same SNR), which can be several minutes for sodium imaging. Conversely, this SNR advantage could be 'spent' to sample a greater k-space extent for increased image resolution. A reduction in noise 'speckle-size' associated with SDWA noise colouring may also help facilitate the quantitative analysis of small lesions, along with improving image appearance, as evident in **Figure 2-5**.

Although it may be expected that the rapid biexponential transverse magnetization decay exhibited by the sodium nuclear ensemble within cellular environments would provide adequate apodization to effectively minimize ringing, Gibbs' ringing still appears to be a problem when imaging structures like the human head (**Figure 2-1**). The problem when imaging the brain is that the transverse magnetization of sodium in CSF, which has ~3 times more sodium ions per

volume than tissue, decays much slower (T_2* = ~65 ms (25)). The apodization filter for this comparison effectively reduces Gibbs' ringing as is evident in **Figures 2-4** and **2-5** (compared to **Figure 2-1**).

The 'generalized Hamming' filter presented in this paper was developed to meet the 3D-TPI design constraint for full Nyquist encoding of 3D k-space. This constraint reflects the fact that when the minimum number of projections (a function of the twist parameter *p*) are implemented for 3D-TPI the sampling density at *p* will be 1/*p*, and a sampling density less than 1 will violate the Nyquist criterion at the edges of k-space. Locally under-sampling k-space results in the introduction of 'aliasing-noise' (262), which is undesirable for SNR starved sodium imaging. Because of these constraints not every filter shape is implementable. The maximum ratio between the value at the centre and at the edge of the filter is determined by *p* (i.e. smaller *p* values facilitate greater twisting and greater filtering characteristics).

Much more time is spent during each projection encoding the outer regions of k-space in the uniformly sampled case than in the SDWA case. This is an obvious requirement as many more points must be sampled in the outer regions of k-space if a uniform sampling density is to be achieved. For any given twist parameter (*p*) and maximum gradient strength, readout lengths can be shortened if sampling density weighting is implemented. This use of sampling density weighting, i.e. readout length reduction, with 3D-TPI has been previously considered for sodium imaging (29).

The SNR benefit of SDWA over UPFA can be calculated with Eq. [2-1] when an equivalent number of sampling points have been acquired for each case. In the theoretical development the final MTF for each case is equivalent. To demonstrate this benefit for 3D-TPI, two projection sets were generated that

sampled an equivalent number of points to the same (or very similar) k-space extent using the same number of projections and the same readout length. However, even though the readout lengths are the same for both projection sets, each set of projections takes a different route through k-space (with respect to the radial component of each trajectory). Because of this the experimental MTF for cellular tissue, which includes the effects of relaxation, will be slightly different for both cases, and the resolution of the images in **Figure 2-4** (although very similar) will not be exactly the same. The noise variance advantage predicted from theory and demonstrated with phantom and human brain imaging, however, is independent of relaxation effects and arises from the non-uniform, post-acquisition, numerical k-space weighting in the UPFA case.

In this paper the relative image noise variance advantage associated with the implementation of SDWA over UPFA was quantified both with theory and experiment. This was done for 3D-TPI sodium imaging with the generation of two directly comparable projection sets (each with full k-space sampling). SDWA may also be implemented (when Gibbs' ringing reduction is required) for other radial imaging techniques including 3D-Cones (263), with the same noise variance advantage (over UPFA). This direct quantification of the SDWA advantage (when a sampling density weighted shape can be smoothly generated without 'Nyquist holes') also applies to purely phase encode imaging techniques, where the utility of sampling density weighted apodization has been demonstrated (258) for the human heart in comparison to a gradient echo sequence.

It has been shown both with theory and experiment that sampling density weighted filtering provides a 17% SNR advantage for the 3D-TPI implementable filter proposed. However, not only does SDWA provide an SNR advantage, it also yields an improved noise power spectral density (when compared to UPFA). This paper demonstrates, in a directly quantitative manner, that whenever ringing is a problem for sodium imaging the most SNR efficient approach to reduce this

artifact is sampling density weighted apodization; this methodology is shown to yield excellent quality sodium images of the human brain in a reasonable scan time.

Chapter 3

k-Space Acquisition Comparison with Respect to Average Signal Measurement when Image Noise is Spatially Correlated

(unpublished)

3.1. Introduction

In many cases when MR images are to be analyzed average image intensities are measured within a region of interest (ROI). For sodium MRI studies this is a typical analysis method (6,12,41,66). It is well known that when image voxels are averaged the thermal noise variance (i.e. the random noise associated with image acquisition) in the measurement is reduced (54). If the image signal-to-noise ratio (SNR) is relatively low, signal averaging is a means to improve the confidence of the image intensity measurement. The purpose of this paper is to facilitate computation of the minimum ROI volume (in terms of number of voxels averaged) required to attain a desired measurement confidence with respect to noise, and to compare noise averaging characteristics of different radial k-space acquisition methods used for sodium imaging.

The computation of minimum ROI volume for desired measurement confidence involves consideration of how noise is averaged in an MR image. For non-zero-filled standard Cartesian imaging noise averaging is trivial; noise standard deviation is reduced as the square root of the number of voxels within the ROI. In this trivial case the noise power spectral density (PSD) is uniform across k-space, and its inverse Fourier transform, the autocorrelation function (R) (141), has a delta function shape. If the noise PSD is not uniform, image noise will be correlated and the calculation of noise averaging becomes much more complex. This paper will address this more complicated scenario, which is directly relevant to the radial k-space acquisition ‘commonly’ used for sodium imaging.

Because of its rapid biexponential T_2 decay, sodium imaging is often implemented with a short TE facilitating 3D radial imaging approach. However,

standard 3D projection imaging suffers from a $1/r^2$ sampling density dependence (where r is the radial fraction of the spherical extent of k-space sampled), which is far from an ideal transfer function for imaging applications. This sampling density dependence can be remedied with either post-acquisition weighting, or by using a k-space acquisition technique such as twisted projection imaging (TPI), in which a constant sampling density can be attained by altering radial projection evolution rate (30). Both radial k-space acquisition techniques will have non-uniform noise PSDs. While TPI produces images with greater SNR, a result of improved sampling efficiency (55), standard radial imaging involves greater k-space averaging at its centre with reduction of low-frequency noise. A comparison of these two radial techniques with respect to noise averaging in an ROI has never been considered.

The author is aware of only one other consideration of noise averaging when the noise PSD is non-uniform. This consideration involves the special case when the ROI volume is sufficiently large so as to contain the vast majority of the autocorrelation function (63). In the current paper, theory is presented for the computation of noise averaging within any ROI, given any noise PSD. This theory is verified through demonstration of the effect of zero-filling on noise averaging for standard, uniformly sampled, Cartesian imaging. As will be shown in the current paper, correlated noise averaging is dependent on ROI volume, and also dependent on ROI geometry.

The noise averaging computation presented is first used to compare standard radial imaging with TPI for minimum ROI volumes required to attain a given measurement confidence. This first comparison considers the case when a uniform transfer function (irrespective of relaxation) is desired (the seemingly ‘typical’ TPI implementation (6,12,30,36)). A second comparison considers the effect of k-space filtering by sampling density design on minimum ROI volumes for a given measurement confidence, acknowledging that k-space filtering is likely required for imaging the human brain (60). Finally, three methods of

generating the same k-space filter transfer function (irrespective of the T_2 relaxation) are compared: the first involves uniform TPI acquisition and post-acquisition weighting to produce the k-space filter, the second involves filtering by sampling density design, and the third involves standard radial acquisition and post-acquisition weighting k-space filter production.

3.2. Theory

3.2.1. Terms Used in this Paper

A term labelled the measurement-to-noise ratio (MNR) is introduced such that

$$\mathrm{MNR} = \mathrm{SNR}\sqrt{\mathrm{N_{eff}}}, \qquad [3\text{-}1]$$

where $\mathrm{N_{eff}}$ is the number of effectively uncorrelated noise volumes in a signal averaging measurement. Using the MNR term, the well known Gaussian relationship for a 95% relative confidence interval can be stated as

$$95\%\ \mathrm{CI}_{rel} = \pm 1.96 \cdot (1/\mathrm{MNR}). \qquad [3\text{-}2]$$

As an example, for an MNR of 80 the 95% relative confidence interval will be plus/minus 2.5% of the signal intensity in the SNR measurement. If small signal changes are expected in an MR study, high MNR ratios are required.

A second term labelled the correlation volume (CV) is at the heart of the noise averaging analysis of this paper. This term is defined according to Eq. [3-3] below

$$\mathrm{CV} = \frac{\mathrm{N_{ROI}}}{\mathrm{N_{eff}}}, \qquad [3\text{-}3]$$

where $\mathrm{N_{ROI}}$ is the total number of acquisition voxels (v_{acq}) within the ROI, and an acquisition voxel is defined as $v_{acq} = 1/(2k_{max})^3$. The CV term of Eq. [3-3] is analogous to the one-dimensional correlation distance of (63), but is expressed in this paper in terms of number of acquisition voxels. A third term labelled the processing gain (PG) of averaging is given below.

$$\mathrm{PG} = \sqrt{\mathrm{N_{eff}}} \qquad [3\text{-}4]$$

3.2.2. A Suggested Theory for Correlation Volume Computation

It is suggested in this paper that CV can be computed for a given ROI volume from convolution and sum of the 3D autocorrelation function within the defined ROI volume as:

$$\mathrm{CV} = \frac{\mathrm{A}^3}{\sum \mathrm{PSD} \cdot \sum_{v_{ZF} \in \mathrm{ROI}} \mathrm{Mask}_{\mathrm{ROI}}} \sum_{v_{ZF} \in \mathrm{ROI}} (\mathrm{Mask}_{\mathrm{ROI}} * \mathrm{R}), \qquad [3\text{-}5]$$

where $\mathrm{Mask}_{\mathrm{ROI}}$ is a mask of ones defined by the volume of the ROI, 'A' is the sampled dimensions of the k-space matrix, v_{ZF} is a zero-filled image voxel, PSD is the noise power spectral density, R is its Fourier transform (the autocorrelation function), and '$*$' denotes convolution. Alternatively, it is suggested that

$$\mathrm{CV} \cong \frac{\mathrm{A}^3}{\sum \mathrm{PSD} \cdot \sum_{v_{ZF} \in \mathrm{ROI}} \mathrm{Mask}_{\mathrm{ROI}}} \sum_{v_{ZF} \in \mathrm{ROI}} \mathcal{F}^{-1}(\mathcal{F}(\mathrm{Mask}_{\mathrm{ROI}}) \cdot \mathrm{PSD}) \qquad [3\text{-}6]$$

can be used for practical computation, where multiplication of the Fourier transformed ROI mask with a 'highly' zero-filled PSD excludes the extents of the Fourier transformed ROI mask where 'folding errors' associated with the discrete FT are expected to be the greatest (i.e. the approximation in Eq. [3-6] could effectively be removed).

3.2.3. The Power Spectral Density of Radial k-Space Acquisition

Power spectral density directly correlates with anti-aliasing filter bandwidth (BW), sampling density (SD), and the square of post-acquisition weighting (W)

$$\mathrm{PSD}(r \cdot k_{max}) \propto \mathrm{BW} \cdot \mathrm{SD} \cdot \mathrm{W}^2. \qquad [3\text{-}7]$$

The filter BW dependency is given below for k-space acquisition techniques such as TPI in which radial evolution is altered to attain a desired sampling density beyond the radial fraction *p* of the k-space sampling extent.

$$\mathrm{BW} \propto (k_{max} \cdot \tau_{Tot}/\mathrm{T}_{RO}) \qquad [3\text{-}8]$$

In Eq. [3-8] τ_{Tot} is a measure of projection 'length', or the relative time required for a projection to reach the edge of k-space when compared to the case where radial evolution does not slow to produce a desired sampling density (60). T_{RO} is the readout duration (which remains constant for the analysis of this paper).

The sampling density dependence is given in Eq. [3-9]

$$\begin{aligned} \mathrm{SD}(r \cdot k_{max}) &\propto (1/r^2) \cdot (1/k_{max}^2) \qquad (r < p) \\ \mathrm{SD}(r \cdot k_{max}) &\propto \Gamma(r) \cdot (1/k_{max}^2) \qquad (r \geq p), \end{aligned} \tag{3-9}$$

where $\Gamma(r)$ is the desired transfer function (see (29,60)), which has a requirement of

$$\Gamma(p) = (1/p^2), \tag{3-10}$$

for radial evolution altered sampling density design (29,60). Inclusion of k_{max}^2 in Eq. [3-9] accounts for global alteration of sampling density when the radial extent of sampled k-space is altered for a constant number of implemented projections (or excitations).

Post-acquisition weighting involved the production of $\Gamma(r)$ within p and any post-acquisition filtering $D(r)$ (where $D(r)$ has a value of 1 at $r = 0$).

$$\begin{aligned} \mathrm{W}(r \cdot k_{max}) &\propto \left(r^2 \cdot \Gamma(r) \cdot D(r)\right)/\mathrm{H}(0) \qquad (r < p) \\ \mathrm{W}(r \cdot k_{max}) &\propto D(r)/\mathrm{H}(0) \qquad (r \geq p) \end{aligned} \tag{3-11}$$

Division by the value at the centre of the modulation transfer function, $\mathrm{H}(0)$, produces a normalization of signal intensity within the image. The value at the centre of the modulation transfer function has the following dependency

$$\mathrm{H}(0) \propto \Gamma(0) \cdot (1/k_{max}^2), \tag{3-12}$$

where k_{max}^2 is included for the similar reason given above for sampling density.

Combining Eqs. [3-7 to 3-12] yields the following PSD dependence for a k-space acquisition techniques in which radial evolution has been altered to attain a desired sampling density:

$$\mathrm{PSD}(r \cdot k_{max}) \propto \left(\frac{k_{max}^3(\tau_{Tot}/\mathrm{T_{RO}})}{\Gamma^2(0)}\right) \cdot r^2 \cdot \Gamma^2(r) \cdot \mathrm{D}^2(r) \qquad (r < p) \qquad [3\text{-}13]$$

$$\mathrm{PSD}(r \cdot k_{max}) \propto \left(\frac{k_{max}^3(\tau_{Tot}/\mathrm{T}_{RO})}{\Gamma^2(0)}\right) \cdot \Gamma(r) \cdot \mathrm{D}^2(r) \qquad (r \geq p).$$

This equation is used in Eq. [3-6] to compare noise averaging characteristics within an ROI for each radial acquisition technique. Use of Eq. [3-13] for k-space acquisition comparison assumes a constant scan duration, or constant number of excitations.

It should be noted that the root 3D sum of values in the PSD is proportional to the standard deviation of noise in the image. Because a normalization by the value at the centre of the modulation transfer function is included in Eq. [3-13], the root 3D PSD sum of Eq. [3-13] also reflects image SNR. When all else remains constant, SNR is proportional to k_{max}^3 (acknowledging that the PSD volume of Eq. [3-13] also has a k_{max}^3 dependence) and inversely proportional to $\sqrt{\mathrm{T_{RO}}}$, as is well known.

3.3. Methods

3.3.1. Correlation Volume Verification using Zero-Filled Uniform k-Space

The correlation volume computation of Eq. [3-6] was experimentally verified by sampling computer generated noise at each Cartesian location on two different k-space matrices, one with a cubic (25 x 25 x 25) extent and the other a spherical (diameter = 25) extent. Each noise-filled k-space matrix was zero-filled to 128^3 and inverse Fourier transformed to produce a resultant noise image. The proportionately large zero-filling factor is used to facilitate measurement of correlation volume in a large number of ROI volumes (with spherical, cubic, and rectangular (1 x 1 x 2) geometries) within the range from 0 to 300 acquisition voxels. 50,000 images of noise were used to experimentally measure the correlation volume associated with each ROI.

On each of 100 images the standard deviation of (real) noise in the image was measured using a very large 3D ROI at the centre of the image, and the average (real) signal intensity measured in ROIs for the ROI geometrics and volume ranges above. The processing gain was measured as the relative (decreased) standard deviation of the 100 average signal intensity measurements from each ROI volume when compared to the average standard deviation of noise in each image. Correlation volume calculated as (from Eqs. [3-1, 3-3, and 3-4])

$$\mathrm{CV} = \frac{\mathrm{N_{ROI}}}{\mathrm{PG}^2}. \qquad [3\text{-}14]$$

This experiment was performed 500 times and the 95% confidence intervals computed for the mean correlation volumes. These correlation volumes, measured using 50,000 images of noise, were compared to correlation volumes computed from Eq. [3-6], using the exact sampling matrix dimensions, zero-filling, and ROI volumes.

3.3.2. Correlation Volume Calculation Validity with Radial Projections

The validity of the use of the radial k-space acquisition PSD dependence of Eq. [3-13] in combination with the correlation volume computation of Eq. [3-6] was tested for radial evolution altered projection sets designed to generated uniform sampling density beyond radial fraction *p* (the standard implementation of TPI). Four projection sets with values of p = 1.0, 0.5, 0.3, and 0.2 (p = 1.0 is the case of standard radial imaging) were created and made to sample computer generated noise over a k-space matrix diameter of 43. Each noise-sampled projection set was post-acquisition weighted to account for the oversampling at the centre of k-space and any minor sampling density deviation from uniform $\Gamma(r)$ design as the result of projection implementation, producing a uniform transfer function (irrespective of T_2 decay). The required weighting compensation of each sampling point was derived using an iterative approach (260). Each noise-sampled projection set was gridded using a Kaiser kernel (width 4, $\beta = 6.5$) on a 1.2x sub-sampled grid. k-Space was zero-filled to 256^3 (to an increased number of different ROI volumes for analysis) and noise images created from inverse Fourier transform.

For each projection set, processing gain was measured in cubic ROIs ranging in volume from ~ 0 – 200 acquisition voxels. This was done using 12 images with 8 cubic ROIs (toward the corners of the image) on each image (in the same manner described above). Each experiment of 12 images producing a PG measure was repeated 100 times and CV calculated from Eq. [3-14].

The measured correlation volumes were compared to those computed using Eqs. [3-6 and 3-13]. A somewhat larger matrix diameter of 51 was chosen to better reflect k-space sampling to a sphere. The spherical matrix for computation will be ‘quantized’ along its outer edge, while the implemented projection sets (which are non-Cartesian) will not exhibit this ‘quantization’.

3.3.3. Radial k-Space Acquisition Comparisons

Radial k-space acquisition was compared for the minimum ROI volume required to attain a desired MNR (and hence measurement confidence interval) using

$$N_{ROI} = \left(\frac{MNR}{SNR}\right)^2 CV. \quad [3\text{-}15]$$

For each projection set CV was calculated via Eqs. [3-6 and 3-13], and relative SNR calculated from the root 3D sum of Eq. [3-13]. Differences in SNR between compared projection sets were normalized to that of 'pure' uniform sampling to a spherical extent by adjusting the acquisition voxel volume (or k_{max}) accordingly. When SNR is normalized between projection sets minimum ROI volumes can be plotted for a range of ROI averaging processing gains that may be required for analysis (it should be noted that when SNR is normalized between projection sets, processing gain is directly proportional to measurement confidence, which can be calculated from Eqs. [3-2 and 3-4]).

To assess the value of TPI with respect to minimum required ROI volumes when a uniform transfer function is desired (irrespective of T_2 relaxation), the four projection sets with p = 1.0, 0.5, 0.3, and 0.2 described above were compared with 'pure' uniform sampling to a spherical extent (as presented for CV computation verification). For the given values of p, k_{max} was retracted from the case of 'pure' uniform sampling to a spherical extent by 0.91, 0.97, 0.99, and 1.00 respectively in order to maintain constant SNR.

To assess the effect of k-space filtering by sampling density design on minimum required ROI volumes, four projection designs were compared with Kaiser $\Gamma(r)$ shapes having β parameters of 0, 2, 3 and 4 (141). Note that the β = 0 case is that of uniform sampling density, and that filter roll-off increases with increase in β. Values of p = 0.200, 0.174, 0.157, and 0.142 respectively were used such that the centre of k-space was sampled in the same manner when the volume of k-space sampled was adjusted (k_{max} = 1.00, 1.16, 1.29, and 1.43 respectively). In this

design comparison the total number of sampling points acquired in each case was the same, along with the extent of post-acquisition weighting.

To compare methods of k-space filtering three cases were considered, each producing a Kaiser transfer function with β = 3. The first had uniform $\Gamma(r)$ and a Kaiser $D(r)$ (uniform TPI with post-acquisition filtering), the second a Kaiser $\Gamma(r)$ and a uniform $D(r)$ (sampling density designed filtering). Values of p = 0.226, and 0.157 respectively were used such that the centre of k-space was sampled in same manner when the volume of k-space sampled was adjusted for constant SNR (k_{max} = 1.26, 1.29 respectively). The third case was that of standard radial acquisition and post-acquisition weighting to produce the desired k-space filter. This is achieved with a Kaiser $\Gamma(r)$, a uniform $D(r)$, and a value of p = 1.0 (for use in Eq. [3-13]).

It should be noted that this paper includes the comparison of the production of transfer functions that do not include the effects of transverse relaxation (for example: uniform sampling density with 'standard' TPI). As such, readout duration is irrelevant to the results presented, but assumed equal for each technique for appropriate comparison (it is well known that noise variance is directly proportional to readout duration (54)). NMR sequence parameters such as flip-angle, TR and scan length are also irrelevant to this discussion.

3.4. Results

As shown in **Figure 3-1**, the correlation volumes computed with Eq. [3-13] are within the tight confidence intervals of the experimentally measured (with 50,000 images of noise) correlation volumes for both the uniformly sampled and zero-filled cubic and spherical k-space geometries, and for each ROI geometry.

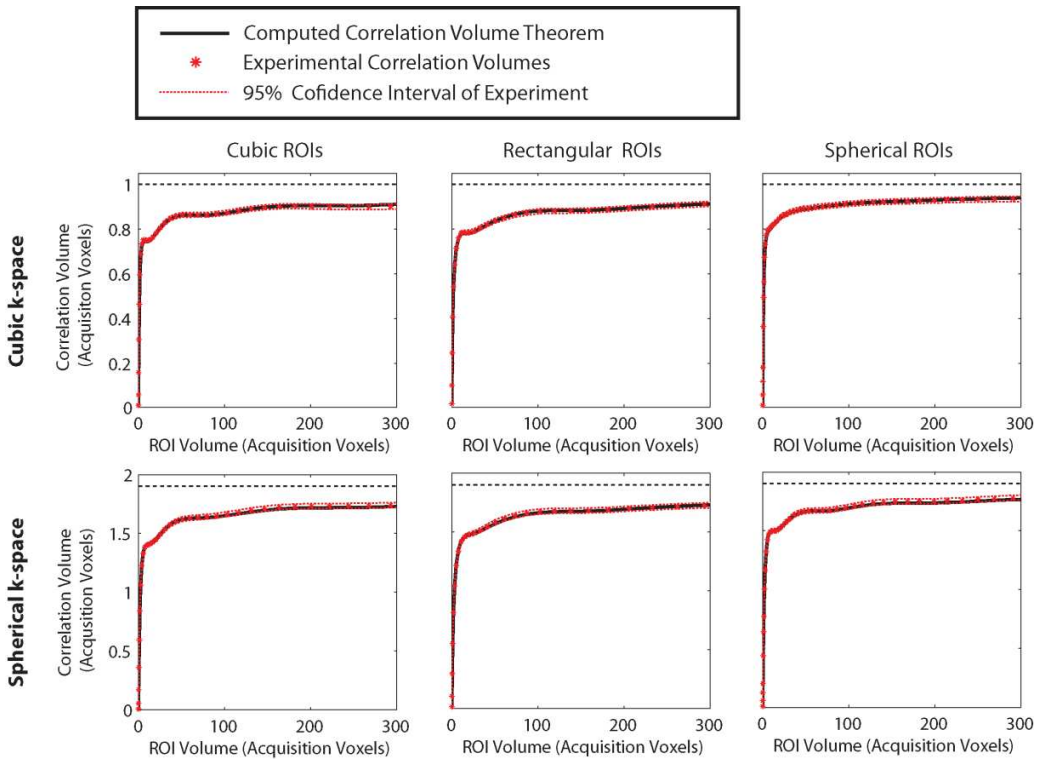

Figure 3-1: Verification of correlation volume computation. For both k-space sampled to a cubic extent and k-space sampled to a spherical extent (then zero-filled) the theoretically computed CV is within the tight 95% confidence intervals of experiment measured from 50,000 images of noise. Note the CV dependence on ROI volume and ROI geometry. The dashed line is the inverse of the 3D sampled k-space extent (1.91 acquisition voxels for k-space sampled to a sphere, the relevant case for radial imaging). The rectangular ROIs have the shape of 1 x 1 x 2.

When k-space is sampled to a cubic extent and not zero-filled the correlation volume will be equal to one acquisition voxel. However, when k-space is zero-filled beyond the sampled k-space extent the CV drops below this volume, but

approaches it within large ROIs. For k-space sampling to a spherical extent the dashed line in Figure 3-1 represents a theoretical voxel volume (defined as the inverse of the 3D sampled k-space extent) in terms of what have been defined as 'acquisition voxels' (or $v_{acq} = 1/(2k_{max})^3$). If it was possible to produce an image from 3D Fourier transform without zero-filling the corners of k-space in the process, the CV is expected to be equal to this theoretical voxel volume. When k-space is sampled to a spherical extent and zero-filled, the CV approaches this volume within large ROIs.

Correlation volumes measured from images generated with TPI projection sets are shown in **Figure 3-2**, and are in good agreement with those acquired from computation, highlighting the utility of the computation methodology to describe correlation volumes for non-Cartesian k-space acquisition.

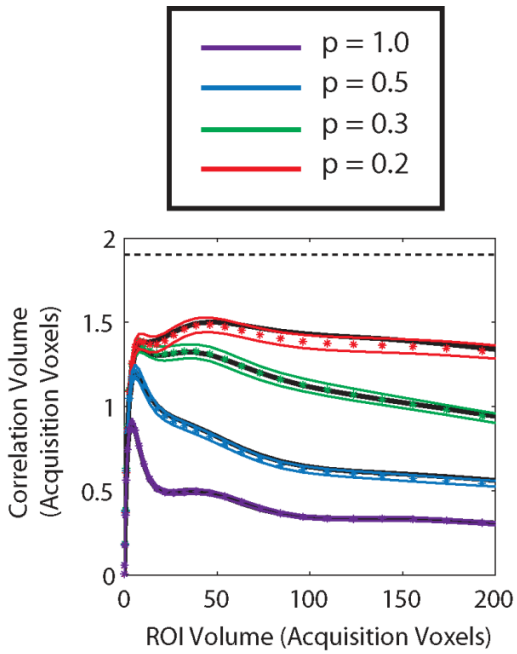

Figure 3-2: Validation of the use of the CV computation for radial k-space acquisition. The coloured stars are the correlation volumes measured from experiment with (1200) images generated by sampling noise with uniform TPI projection sets having the values of *p* as listed. The solid coloured lines are the 95% confidence intervals. The black lines are the computed correlation volumes from theory. The dashed line, as previous, is theoretical voxel volume for sampling k-space to a spherical extent (1.91 acquisition voxels).

The correlation volumes for standard radial imaging (p = 1) are substantially smaller than those of TPI (**Figure 3-3A**), even when increased voxel volume is taken into account to achieve the same SNR (**Figure 3-3B**) (as much as 3.5x smaller). It is interesting to note that the correlation volume actually begins to decrease for all values of p rather than approach the theoretical voxels volume associated with sampling k-space to a spherical extent (dashed line), but does so most rapidly and substantially for large values of p. This decrease is directly related to the reduction of noise power at low frequencies near the centre of k-space (**Figure 3-3C, 3-3D**). The total sum of values in the autocorrelation function is equal to the value at the centre of the PSD, and inclusion of larger proportions of the autocorrelation function for a greater number of voxels in the ROI reduces the correlation volume. In **Figure 3-3F** it can be seen that even when the acquisition voxel volumes of the standard radial approach are adjusted larger to offset the lower SNR of this method with respect to TPI, the minimum ROI volumes required for any given processing gain are lower for the standard radial approach than they are for TPI. For a processing gain of 2, a 9% smaller ROI is required for p = 1.0 than p = 0.2; for a PG of 4 a 39% smaller ROI is required; for a PG of 8 a 53% smaller ROI is required.

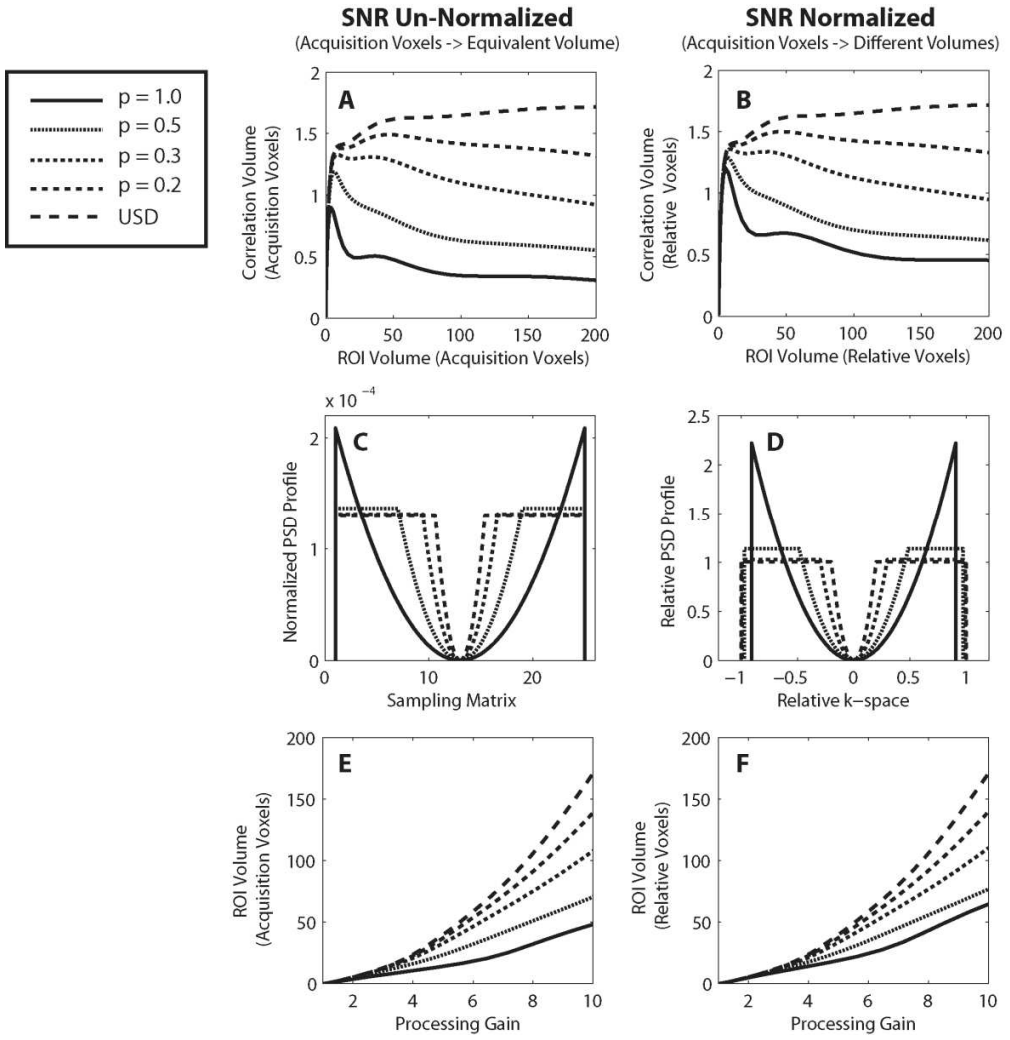

Figure 3-3: The noise averaging advantage associated with oversampling the centre of k-space when a uniform transfer function (irrespective of relaxation) is desired. Computed correlation volumes are given in (**A**) for various TPI projection sets with different values of p and uniform $\Gamma(r)$, along with 'pure' uniform Cartesian sampling to the same spherical k-space extent (labelled USD). The CVs are in general much smaller for standard projection imaging ($p = 1$) with post-acquisition compensation than they are for TPI . This is true even when voxel dimensions are adjusted to maintain constant SNR (**B**) (a relative voxel corresponds to the unadjusted acquisition voxel volume of 'pure' uniform sampling). The PSDs normalized according to their total sum of values are given in (**C**). The relative PSDs with altered k-space sampling extents and constant total sum values are given in (**D**). In (**E,** and **F**) the required ROI volumes for different ROI averaging processing gains are given. In **F** it can be seen that even when voxel volumes are adjusted for SNR, required ROI volumes for any processing gain are still considerably less for standard projection imaging than for TPI.

In terms of acquisition voxels, correlation volumes are substantially increased when greater k-space filtering by sampling density design is implemented (note again that $\beta = 0$ is the case of uniform sampling density) (**Figure 3-4A**). However, when the reduction of acquisition voxel volume associated with SNR normalization is taken into account, the correlation volumes associated with k-space filtering by sampling density design are actually less than those for uniform sampling (**Figure 3-4B**). This is a result of redistributing noise power away from the centre of k-space (**Figure 3-4D**). It is shown in **Figure 3-4F** that minimum ROI volumes to achieve a desired measurement confidence are actually reduced when the k-space filtering shape produced by sampling density design is made to roll-off toward the edges of k-space to a greater extent.

In **Figure 3-3** it was shown that oversampling the centre of k-space is advantageous in terms of minimum ROI volumes to achieve a given measurement confidence when the desired transfer function is uniform. In **Figure 3-5** it is shown that this is equally true when the desired transfer function has a filtering shape (a $\beta = 3$ Kaiser window in this case). The production of uniform sampling density with TPI followed by post-acquisition k-space filtering yields the greatest low-frequency noise power contributions, while low-frequency contributions are greatly reduced for standard radial imaging (**Figure 3-5D**). **Figure 3-5** also shows that while it is already known that filtering by sampling density design is more SNR efficient than acquiring k-space with uniform sampling density TPI (Chapter 2) (60), filtering by sampling density design also has a large advantage with respect to reduced correlation volume (**Figure 3-5a**). However, the combined value of filtering by sampling density design is still less than that of standard radial imaging with respect to the minimum ROI volume required to achieve a desired measurement confidence.

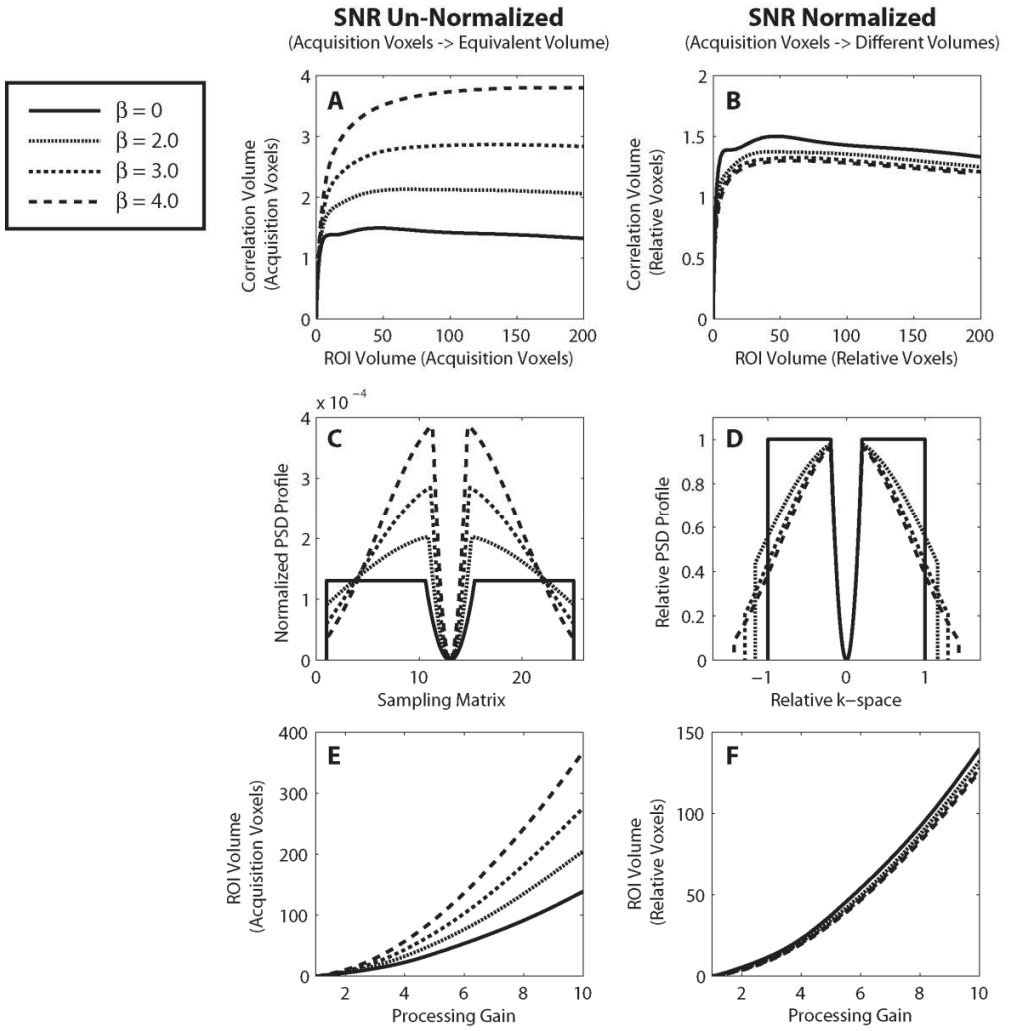

Figure 3-4: The noise averaging advantage associated with increasing k-space filtering by sampling density design. Computed correlation volumes are given in (**A**) for 'degrees' of k-space filtering. Although filtering by sampling density design increases the number of acquisition voxels in the CV, the reduction in acquisition voxel volume associated with SNR normalization more than offsets this increase (**B**). The PSDs normalized according to their total sum of values are given in (**C**). The relative PSDs with altered k-space sampling extents and constant total sum values are given in (**D**). Although more acquisition voxels are required in the ROI to achieve a desired processing gain (**E**), expansion of k-space to maintain constant SNR yields smaller ROI volumes for any desired PG when filtering by sampling density design is implemented (**F**).

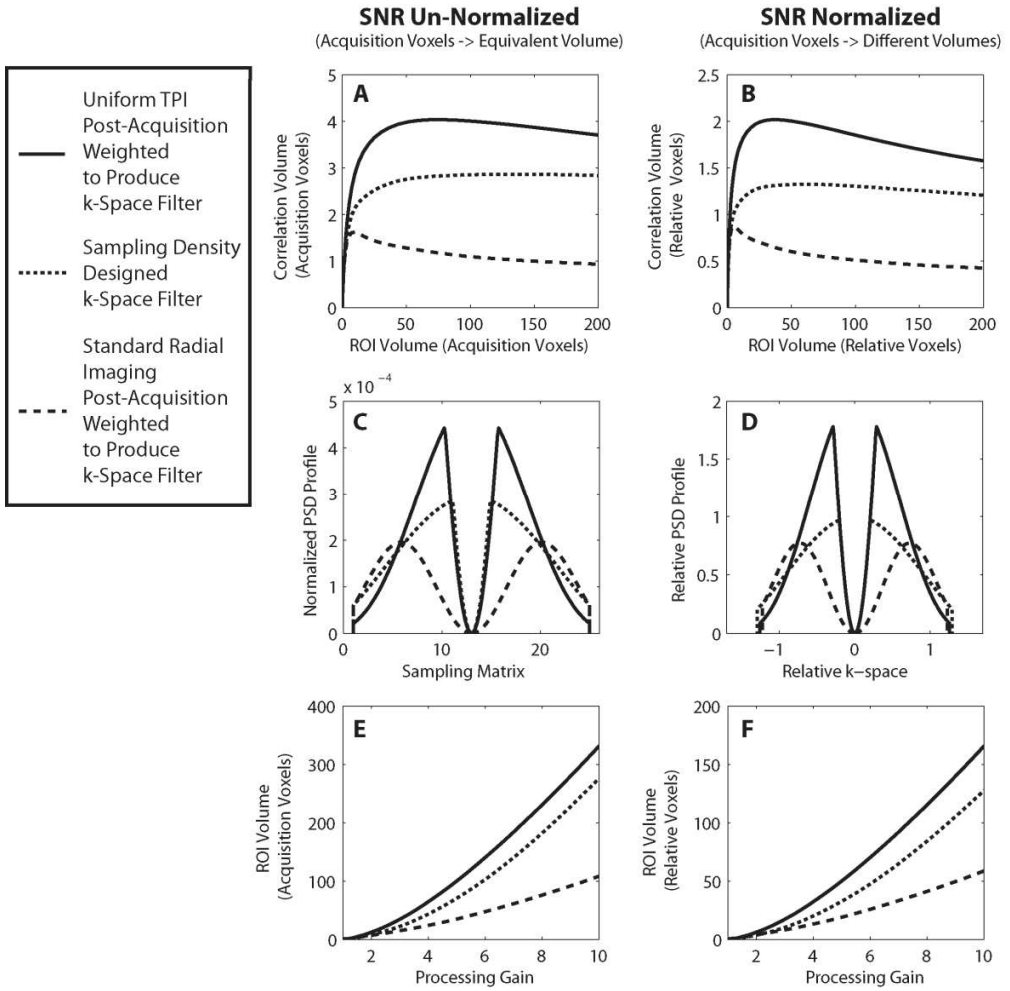

Figure 3-5: The noise averaging advantage associated with oversampling the centre of k-space when a k-space filtering shape (irrespective of relaxation) is desired. Computed correlation volumes are given in terms of acquisition voxels for three different methods of producing a k-space filter with radial acquisition in (**A**). Even when acquisition voxels volumes are normalized for SNR, the standard radial imaging approach yields smaller correlation volumes (**B**). The PSDs normalized according to their total sum of values are given in (**C**). The relative PSDs with altered k-space sampling extents and constant total sum values are given in (**D**). It is shown in (**F**) that for images with acquisition voxel volumes normalized for SNR, minimum ROI volumes to attain a desired measurement confidence are attained for the standard radial imaging approach.

3.5. Discussion

The correlation volume (CV) metric given in this paper directly specifies, together with SNR, the minimum ROI volume that must be used to attain a desired measurement confidence with respect to noise, assuming signal averaging within the ROI. While CV is equal to the acquisition voxel size for non-zero-filled standard Cartesian imaging sampling k-space to a cubic extent, that is not the case for radial imaging where image noise is correlated. In this paper theory for correlation volume computation was suggested and verified with experiment. This was done using zero-filled Cartesian matrices sampled to either a cubic or spherical extent with three different ROI geometries each. In each case the computed CV was within the tight 95% confidence interval of experiment measured from the processing gain associated with averaging on 50,000 images of noise (**Figure 3-1**). Following validation of correlation volume computation for radial imaging techniques (**Figure 3-2**), it was shown (using this computation) that standard radial imaging with its great oversampling at the centre of k-space and reduction of low frequency noise requires smaller ROI volumes for a desired measurement confidence than TPI (**Figure 3-3**). It was also shown that increased k-space filtering by sampling density design is advantageous in terms of minimum ROI volumes (**Figure 3-4**), but k-space filtering by sampling density design is not the most advantageous method in this regard, standard radial imaging also requires the smallest ROI volumes for a desired measurement confidence when k-space must be filtered (**Figure 3-5**).

Another consideration of correlation volume was concerned with the case where the ROI volume was ‘sufficiently large’ (63). When the correlation volume is sufficiently large Eq. [3-13] reduces to

$$\mathrm{CV} \cong \frac{\mathrm{A}^3 \cdot \mathrm{PSD}(0)}{\sum \mathrm{PSD}}. \qquad [3\text{-}15]$$

This dependence is essentially the same as that given in (63), however in (63) it is assumed that $\mathrm{PSD}(0) = 1$. The one-dimensional correlation distance is also given

in terms of physical distance yielding the $1/\sum \mathrm{PSD}$ relationship. Notwithstanding the fact that $\mathrm{PSD}(0)$ approaches zero for radial imaging, this simple relationship for very large ROI volumes does not account for the substantial CV variation with smaller ROI volumes. It should be noted that correlation distance is also (in other fields, including antennae theory) considered as the distance from the centre of the autocorrelation function to its first null location. However, the definition of correlation distance of (63) (or correlation volume in this paper) has direct meaning with respect to noise averaging.

A theory for computation of correlation volume is beneficial for the analysis and optimization of k-space acquisition techniques producing non-uniform noise power spectral densities. Given the involvement of convolution in the gridding process for non-Cartesian imaging approaches, the generation of an image can be a 'long' process. The production of *many* images to generate a high confidence CV measurement can yield a very long experiment. In this paper projection sets were made to sample computer generated noise. It is assumed that this noise is effectively equivalent to that which would be sampled within an MRI scanner. Computer generated noise was used, as the acquisition of 1200 noise images from the MRI scanner would have involved an exceptionally long process.

Although zero-filling does not improve resolution, it does improve noise averaging within an ROI. When k-space is not zero-filled and the PSD is uniform the autocorrelation function is a delta function, and one could consider the noise associated with each voxel as being contained within that voxel. However, when k-space is zero-filled, the magnitude at the centre of the autocorrelation function is reduced from 1 in proportion to the extent of zero-filling, and non-zero values are produced throughout the image, such that the total sum of values in the autocorrelation function remains constant. In this case one could consider the noise associated with each voxel as being spread throughout the image. In order to 'recapture' the effect of noise on CV one must perform averaging in an ROI large

enough that most of the autocorrelation function from most of the voxels is within the ROI.

Autocorrelation function contributions from voxels outside the ROI are also included in the ROI. When the ROI is a ‘point source’ the sum of autocorrelation function contributions from all the other voxels ensures that the noise power in a ‘points source’ image measurement is equal to the image noise power. However, because image noise power is attained in a volume much less than one acquisition voxel, CV is reduced toward zero.

In **Figure 3-1** it can be seen that ROI geometries with the greatest surface area to volume ratio produce the smallest correlation volumes, i.e. the greater the anisotropy of the voxel, the smaller it need be to produce a desired processing gain. Greater average distance between voxels within the ROI yields less correlation between voxels and greater processing gain. The ‘ripples’ in the shape of the CV increase with increase in ROI volume of **Figure 3-1** can be explained by observing the 3D autocorrelation function profiles, shown in **Figure 3-6** below for uniform k-space sampling to cubic and spherical extents. The ‘ripples’ in the CV dependence on ROI volume arise from inclusion of the negative lobes of the autocorrelation function as the ROI volumes are expanded.

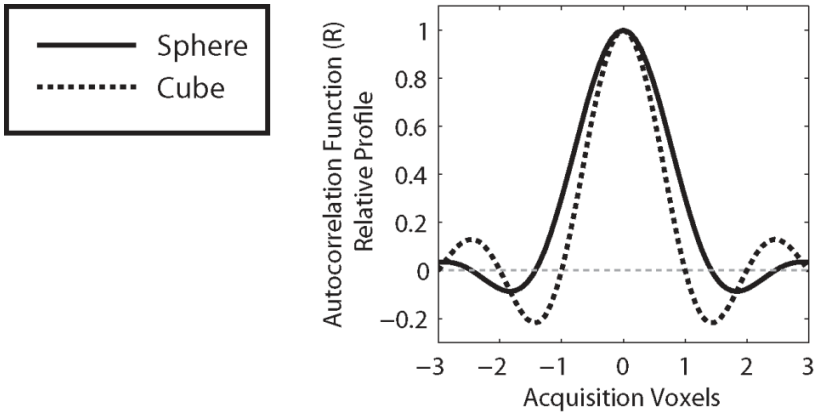

Figure 3-6: A profile through the 3D autocorrelation function for k-space sampled to spherical and cubic extents (as in **Figure 3-1**). Note that while the negative 'ringing' lobe is much deeper for k-space sampled to a cubic extent, for k-space sampled to a spherical extent the negative 'ringing' lobe is symmetric around the centre of k-space (as 3D ripples in a pond).

For standard radial imaging the centre of k-space is highly oversampled. This oversampling leads to sampling SNR inefficiency (55). It was to address this sampling SNR inefficiency of standard radial imaging that TPI was originally developed (30). Using the small value of $p = 0.2$ to produce a uniform sampling density, the sampling SNR efficiency can be improved from 0.75 to 0.99. However, it is the purpose of this paper to point out that when an average measurement is to be made within an ROI, SNR is not the only image metric that matters with respect to the confidence of that measurement, correlation volume must also be considered. When acquisition voxel volumes are adjusted such that SNR is normalized between the standard radial and TPI k-space acquisition techniques, the dramatic oversampling at the centre of k-space and reduction of low frequency noise power associated with standard radial imaging facilitates the use of smaller ROI volumes to achieve any desired processing gain, or measurement confidence. This is the case if a uniform transfer function (irrespective of T_2 decay) is required (**Figure 3-3**), or if a k-space filtering transfer function is required (**Figure 3-5**).

It has recently been noted that a uniform transfer function is perhaps not ideal for imaging the human brain. Ringing associated with the 3x sodium concentrated cerebral spinal fluid (with respect to brain tissue) can contaminate brain tissue measurements (Chapter 2) (60). It was shown that filtering by sampling density design was more SNR efficient than the use of 'standard' uniform TPI and post-acquisition filtering. It was also shown that the noise benefit is achieved primarily at low spatial frequencies. In the current paper the value of the noise colouring differences of the two k-space filtering techniques observed in (Chapter 2) (60) is quantified within the calculation of correlation volume. Smaller correlation volumes associated with filtering by sampling density design add to its advantage with respect to image noise. However, neither method facilitates measurement in ROI volumes as small as that of standard radial imaging for a given measurement confidence.

k-Space filtering by sampling density design has also been implemented for sodium imaging with other phase-encoding k-space acquisition techniques (256,258). While the constancy of SNR is well known when the same number of k-space samples are used to 'smear' an oversampled rectangular k-space shape into a filtering shape with increased sampled k-space boundaries (251), in the current paper an additional advantage of filtering by sampling density is presented other than Gibbs' ringing apodization. This advantage is the redistribution of noise power to higher spatial frequencies, the reduction of correlation volume, and the increase in measurement capability with respect to noise.

It should be noted that when k-space acquisition methods are normalized for SNR, the TPI approach will have smaller acquisition voxel volumes than standard radial imaging. While these smaller voxel volumes are not sufficient to facilitate smaller ROI volumes with respect to image noise and measurement confidence, they will improve image appearance. Smaller voxel volumes will also minimize 'partial volume' effects and the spatial extent of the point spread function which will include the effects of transverse magnetization decay during the readout.

Finally, it is again noted that the measurement confidence discussed in this paper is with respect to the underlying thermal noise in the image. While the signal intensities in an ROI may be heterogeneous for various reasons, including those related to inclusion of different tissue types and 'pathologic states', it is assumed that an average image intensity measure within an ROI is sufficient for analysis. As mentioned in the introduction, average ROI measurements are very common for quantitative image analysis. The alternative, voxel-by-voxel analysis, will suffer from either measurement uncertainty related to increased image noise or the implementation of large voxel volumes required to generate sufficient SNR.

The purpose of this paper was to compare radial k-space acquisition methods used for sodium imaging with respect to correlated image noise and the minimum ROI volume required for measurement confidence when an signal average measurement is made within an ROI. This required a method with which to compute the correlation volume, or the effective volume of 'statistically independent noise voxels.' A theory with which to compute correlation volume was presented and verified using images generated with the sampling of computer generated noise. It was shown that correlation volume is dependent on ROI volume and geometry; this is true for all zero-filled k-space acquisition. It was also shown that when a specific measurement confidence is desired, SNR efficiency should not be the only metric imparting value to a k-space acquisition method; the colouring of the noise (or the shape of the PSD) as a result of the acquisition method, as reflected in the correlation volume, should also be considered. It was shown in this paper that standard radial imaging, with its 'dramatic' oversampling of low spatial frequencies (and associated noise power reduction), facilitates measurement confidence with respect to image noise in smaller ROI volumes than the more SNR efficient TPI. Acquisition methods, such as filtering by sampling density design, that shift noise power from low to high spatial frequencies are also advantageous with respect to measurement confidence and minimum ROI volumes.

Chapter 4

Radial k-Space Sodium Acquisition Optimization for Object Quantification with Concern to the Human Head

(unpublished)

4.1. Introduction

The value of human brain sodium MRI lies in the potential that signal intensity, reflecting sodium concentration, may correlate with pathological status in many disorders including stroke (13,41,66), cancer (3,5-7) and Alzheimer's disease (23). In dense macromolecular environments such as cellular brain tissue, sodium nuclei exhibit very rapid biexponential T_2 relaxation with T_{2f} ~ 2.9 ms (60%) and T_{2s} ~ 29 ms (typical in-house human cellular brain tissue T_2* measurements at 4.7T, related T_{2s} values have been measured at other field strengths (25,37)). In order to capture the signal before it significantly decays, k-space acquisition methods with short delay between excitation and acquisition of the centre of k-space (TE) are required. To accomplish this task, radial (centre-out) k-space acquisition methodologies are commonly used (5-7,41,66). Because standard radial acquisition suffers from sampling inefficiency related to SNR (55), a technique in which radial evolution is altered to attain a uniform sampling density was developed (twisted projection imaging – TPI) (30). However, it was shown in Chapter 3 that although standard radial k-space acquisition is inefficient with respect to SNR, its excessive oversampling surrounding the centre of k-space and reduction of low-frequency noise is actually advantageous when average signal intensities are to be quantified within a region of interest (ROI). While the TPI technique may not be beneficial with respect to image noise, it has been shown very recently (2009) that the radial projection evolution alteration of TPI is advantageous to change the shape of T_2 decay across k-space (36). The purpose of the current paper is to assess the value of radial evolution altered k-space acquisition (of which TPI is a member) for imaging the human head in the context of both noise and signal blurring. This is accomplished through evaluation of

optimal readout duration and optimal image SNR, while acknowledging that k-space filtering is required to minimize the pervasion of brain tissue with 'ringing' from the 3x concentrated cerebral spinal fluid (CSF) signal (Chapter 2) (60).

It is well known that image noise variance will decrease in direct proportion to an increase in readout duration (T_{RO}), however, roll-off toward the edges of k-space will also increase resulting in a 'smearing' of the point spread function (PSF) and image blurring (54). It has been suggested that selection of T_{RO} to match the (monoexponential fit for sodium) T_2 decay parameter provides a reasonable compromise between noise and blurring effect (30). On the other hand, a theoretical optimal readout duration 50% of T_{2s} (when T_{2s} is 10x T_{2f}) has been suggested (36). For the case of T_{2f} = 2.9 ms and T_{2s} = 29 ms (measured cellular brain tissue relaxation at 4.7T) the readout duration of (30) is ~ 9 ms and the readout duration of (36) is ~ 15 ms. It should be noted, however, that beneficial reduction of T_{RO} to 4 ms (facilitated by altered sampling density design under hardware constraint in this case) has also been suggested (29). In many sodium radial k-space acquisition papers the T_{RO} parameter used is omitted (12,30,66). One sodium TPI paper of human brain used a $T_{RO} = 29\,\text{ms}$ (6). For sodium imaging performed at 4.7 Tesla (the field strength used in this chapter) ~ 17 ms readout durations have typically been used (Chapters 2, 5, and 6) (41,42,60).

Optimal T_{RO} is highly dependent on the optimized image metric. The image metric used by Nagel (36) is that of point-source SNR, and is the same metric previously used for optimization in the presence of rapid monoexponential proton T_2 decay (264). (It should be noted that no specific optimization metrics were given for Boada's T_{RO} suggestions (29,30)). It is contended in this chapter that because sodium imaging is primarily concerned with the signal intensity quantification, an image metric directly related to quantification capability is required. Given (as will be shown) that image intensity is modulated by object volume when object volumes are small with respect to the spatial extent of the

PSF, the image optimization metric presented in this chapter includes measurement accuracy related to PSF smearing.

The optimal SNR at which to perform radial sodium imaging of the human head has never before been considered. It is suggested in this chapter that while choosing a high SNR (i.e. large voxel volume) may facilitate a given measurement confidence (precision) with respect to image noise in a smaller ROI volume (assuming signal averaging within the ROI), the larger voxel volumes of high SNR will spatially stretch the shape of the PSF and increase the minimum object volume required to attain a desired measurement accuracy with respect to PSF smearing. Thus the radial k-space acquisition optimization presented in this chapter (which includes optimization for SNR) concerns the minimum object volume in which a precise (with respect to image noise) and accurate (with respect to PSF smearing) measurement can be attained.

Radial k-space acquisition optimization begins with presentation of a radial acquisition method in which the modulation transfer function (H – which includes T_2 decay) remains a constant Kaiser window shape in CSF across all readout durations by sampling density design. Because the sodium signal from 3x concentrated CSF (with respect to brain tissue) does not exhibit extremely rapid biexponential relaxation (~ 65 ms at 4.7T), and because k-space must be sampled to a finite extent, the side-lobes of the near sinc function when k-space is unfiltered will extend into the brain tissue (Chapter 2) (60), potentially affecting brain tissue signal measurement. In this paper it is acknowledged that the flexible Kaiser window trades step-response (at an object's edge) for side-lobe reduction in a near ideal fashion through its β parameter (141). Maintenance of a constant Kaiser modulation transfer function in CSF across readout duration facilitates analysis of T_{RO} for constant PSF shape in CSF and constant CSF side-lobe amplitude. An appropriate amount of k-space filtering required for imaging the human head is considered along with the effect of k-space filtering with respect to image acquisition optimization.

Three different approaches to radial k-space acquisition are compared in this chapter with respect to minimum object volume required for precise and accurate analysis. These approaches include: standard projection imaging with a $T_{RO} \sim 2$ ms similar to that of (5) (labelled SP), radial evolution altered imaging with a 'short' $T_{RO} = 4$ ms similar to that of (29) (labelled 'short readout' SR), and radial evolution altered imaging with a 'long' $T_{RO} = 17$ ms similar to that of (41,42,60) (labelled 'long-readout' LR). A constant Kaiser modulation transfer function in CSF was generated with post-acquisition weighting for the standard projection approach and sampling density design for the radial evolution altered approaches. For each k-space acquisition approach voxel volumes were adjusted to maintain constant SNR. Computation for radial acquisition relative SNR was verified using a large 5% agar phantom. Image intensity modulation with object volume was demonstrated in 5% agar spheres of various volumes (0.65 cm^3 – 10 cm^3), and compared with modulation computed from radial k-space evolution and measured T_2 decay. Given reasonable correspondence between measured and computed image intensity modulation with object volume in 5% agar, image intensity modulation computation with human brain relaxation parameters was used for radial k-space acquisition optimization. Each k-space acquisition approach is compared with respect to minimum object volume required for precise and accurate analysis, as are variations of each approach, and an optimum SNR range at which to perform quantitative sodium imaging is suggested. An additional image metric, the containment of CSF signal intensity within its bounds, is also considered and demonstrated with images acquired from healthy human brain and saline resolution phantoms. Finally, an ideal approach to radial k-space acquisition for quantitative sodium imaging in the human brain is proposed.

4.2. Theory

4.2.1. Relaxation Compensating Sampling Density k-Space Acquisition

Any 3D radial sampling density shape $\Gamma(r)$ (where r is a fraction of k_{max}) can be generated in the volume of k-space at and beyond p (also a radial fraction of k_{max}) by designing the radial component of each projection to evolve according to

$$\frac{dr}{d\tau} = \frac{1}{\Gamma\big(r(\tau)\big)r^2(\tau)}, \qquad [4\text{-}1]$$

where τ is a dimensionless fraction of the time required for a projection to reach the edge of k-space if its evolution were not altered to generate the desired sampling density. The term p is designated here as the 'fractional extent of unaltered sampling density.' Alternatively, this parameter has been designated 'trajectory twist' (30), but the twisting of projections (under the maintenance of a constant sampling speed) is not relevant to the optimization of this chapter. At the initiation of radial evolution alteration along each projection, i.e. at radial location p, τ has the value of zero $(r(0) = p)$. If the radial projection velocity slows to alter sampling density beyond p from its $1/r^2$ dependence, the relative projection length, $\tau_{tot} = \tau(r = 1) + p$, will be greater than 1.

Sampling density which takes monoexponential T_2 relaxation into account to produce a $\Psi(r)$ transfer function is given below.

$$\Gamma\big(\mathrm{r}(\tau)\big) = \Psi(r) \cdot \exp\left(\frac{\mathrm{s} \cdot \tau}{\mathrm{T}_{2(\mathrm{D})}}\right) \qquad [4\text{-}2]$$

The 'D' subscript identifies the transverse relaxation parameter in Eq. [4.2] as a design parameter (i.e. the actual T_2 relaxation in a given tissue may vary from $T_{2(D)}$). The variable s in Eq. [4-2] is defined as

$$s = \mathrm{T_{RO}}/\tau_{tot}, \qquad [4\text{-}3]$$

and produces a conversion to real time, where T_{RO} is the duration of the projection readout. At the radial location *p,* the acquired sampling density remains unaltered from the $1/r^2$ dependence and must have a value of $1/p^2$ for correct projection generation in Eq. [4-1]. The transfer function, $\Psi(r)$, must be correctly scaled to account for this (i.e. it must have a value of $1/p^2$ at $r = p$).

Solutions to Eqs. [4-1, 4-2 and 4-3], were achieved using an iterative process. The relative length of each projection, τ_{tot}, is initially unknown. The iteration process was initiated by solving Eq. [4-1] with a value of s = 1. The value of $\tau(r = 1)$ was attained from this solution, the variable *s* recalculated for the desired readout duration, and Eq. [4-1] resolved. This process was continued until the change in s was less that 0.01%.

When a critical number of projections are included in a projection set (i.e. $4\pi(\mathrm{FoV} \cdot k_{max})^2$ projections) the sampling density will be directly that of $\Gamma(r)$. The combination of $\Gamma(r)$ and the actual transverse magnetization decay across k-space, $M_{xy}(r)$, will produce the modulation transfer function $H(r)$.

$$H(r) = \Gamma(r) \cdot M_{xy}(r) \qquad [4\text{-}4]$$

For monoexponential transverse magnetization decay

$$M_{xy}(r(\tau)) = \exp\left(-\frac{(s \cdot (\tau + p) + TE)}{T_2}\right), \qquad [4\text{-}5]$$

and for biexponential transverse magnetization decay

$$M_{xy}(r(\tau)) = 0.6\exp\left(-\frac{(s \cdot (\tau + p) + TE)}{T_{2f}}\right) + 0.4\exp\left(-\frac{(s \cdot (\tau + p) + TE)}{T_{2s}}\right). \qquad [4\text{-}6]$$

It should be noted that because $\tau = 0$ at radial fraction p in the solution of radial projection evolution of Eq. [4-1], the dimensionless time fraction τ within p will be less than zero with dependence

$$\tau = r - p\,. \qquad [4\text{-}7]$$

If the actual transverse magnetization decay is monoexponential and T_2 matches $T_{2(D)}$, $H(r)$ will be a scaled version of $\Psi(r)$. Acquisition of more (or less, which is possible to the fraction of p without violating Nyquist when projection twisting is implemented) projections will produce a simple scaling of $\Gamma(r)$ and $H(r)$.

4.2.2. The Kaiser Function

The appropriately scaled $\Psi(r)$ (as discussed above) to generate a Kaiser modulation transfer function is given in Eq. [4-8]. In this equation I_0 is the zeroth-order modified Bessel function of the first kind, and the β parameter determines the extent of the main-lobe area for side-lobe reduction trade (note that when β = 0 the Kaiser function is a uniform or flat function) (141).

$$\Psi(r) = \left(\frac{1}{p^2}\right) \cdot \frac{I_0\left(\beta\sqrt{(1-r^2)}\right)}{I_0\left(\beta\sqrt{(1-p^2)}\right)} \qquad [4\text{-}8]$$

4.2.3. Post-Acquisition Compensation for Sampling Density Deviation from Desired Shape

For radial evolution altered k-space acquisition the central portion of k-space, until the initiation of evolution alteration at p, possesses a $1/r^2$ sampling density which must be compensated by post-acquisition weighting

$$W(r) = \begin{cases} \left(r^2 \cdot \Gamma(r)\right) & 0 \le r < p \\ 1 & p \le r \le 1 \end{cases} \qquad [4\text{-}9]$$

to produce the continued shape of $\Gamma\left(r(\tau)\right)$ within the radial fraction p and the final transfer function of $H(r)$ over the full k-space extent. The shape of $\Gamma(r)$ within the radial fraction p required to produce the $\Psi(r)$ function can be found from solution to Eq. [4-2] where $\tau = r - p$ (as mentioned above). In practice post-acquisition compensation was done using an iterative gridding process (260),

which also accounts for small local deviations in sampling density as a result of projection shape deviation from design in the implementation process.

4.2.4. Relative SNR for Radial k-Space Acquisition

The total signal contribution to the image of any object is un-modulated by PSF smearing, and is directly proportional to $\Gamma(0)$ (assuming $\mathrm{M_{xy}}(0)$ remains constant in Eq. [4-4]). Note that for small objects much of the total signal contribution to the image may be 'smeared out' beyond the object. In a sufficiently large object

$$\mathrm{SNR} \propto \Gamma(0)/\sigma. \qquad [4\text{-}10]$$

The dependence of the standard deviation of image noise (σ) is given below

$$\sigma \propto \sqrt{\mathrm{BW} \cdot \mathrm{S}}\,, \qquad [4\text{-}11]$$

where

$$\mathrm{S} \propto \int_{\tau=-p}^{\tau_{(r=1)}} \mathrm{W}\big(\mathrm{r}(\tau)\big)^2, \qquad [4\text{-}12]$$

and BW is the anti-aliasing filter bandwidth

$$\mathrm{BW} \propto (\tau_{tot}/\mathrm{T_{RO}}). \qquad [4\text{-}13]$$

Combining Eqs. [4-9 through 4-13] yields the radial acquisition SNR dependence below (assuming a constant number of implemented projections)

$$\mathrm{SNR} \propto \Gamma(0) \Big/ \sqrt{\left(\frac{\tau_{tot}}{\mathrm{T_{RO}}}\right) \cdot \left(\int_{\tau=-p}^{0} \Big(r^2(\tau) \cdot \Gamma\big(r(\tau)\big)\Big)^2 + \int_{\tau=0}^{\tau_{(r=1)}} 1 \right)}. \qquad [4\text{-}14]$$

The relative SNR of Eq. [4-14] is solved numerically in this chapter for the 'non-analytic' $\Gamma\big(r(\tau)\big)$ functions generated.

4.2.5. Assessment of Minimum Object Volumes Required for Measurement Accuracy and Precision

Measurement precision is defined in this paper as the confidence interval pertaining to image noise in a signal averaging measurement within an ROI

$$95\%\ \mathrm{CI} = \pm 1.96 \cdot (1/\mathrm{MNR})\,, \qquad [4\text{-}15]$$

where MNR is the measurement-to-noise ratio

$$\mathrm{MNR} = \mathrm{SNR}\sqrt{\mathrm{N_{eff}}}\,, \qquad [4\text{-}16]$$

and $\mathrm{N_{eff}}$ is the number of effectively uncorrelated noise volumes in the signal averaging measurement (Chapter 3). The 95% relative confidence interval is plus/minus a percent of the signal intensity in the SNR measurement. If SNR is measured in normal tissue, the 95% CI defines the minimum relative increases that will be statistically significant. An 'effectively uncorrelated noise volume' is labelled the correlation volume (CV) (63), such that

$$\mathrm{N_{eff}} = \frac{\mathrm{N_{ROI}}}{\mathrm{CV}}\,, \qquad [4\text{-}17]$$

where $\mathrm{N_{ROI}}$ is the total number of acquisition voxels (v_{acq}) within the ROI, and an acquisition voxel is defined as $v_{acq} = 1/(2k_{max})^3$. Calculation of correlation volume, which is also dependent on $\mathrm{N_{ROI}}$, is given in Chapter 3. From Eqs. [4-16 and 4-17] it is apparent that the minimum number of acquisition voxels required within an ROI volume to attain a given measurement confidence with respect to image noise is:

$$\mathrm{N_{ROI}} = \mathrm{CV}(\mathrm{MNR}^2/\mathrm{SNR})\,. \qquad [4\text{-}18]$$

Measurement (in)accuracy in this paper concerns errant evaluation of signal intensity produced by a uniform object (or an object producing uniform signal) as a result of PSF smearing. PSF convolution with an object-mask of 'ones' yields image intensity dependence within an object as a result of PSF shape. If the object

volume is sufficiently large, the object image intensity will approach full-value at and surrounding the object centre. For a range of ROI volumes that may be required for measurement precision, required object volumes can be found such that the average image intensity in the ROI volume is a given fraction of full value. This fraction of full value is defined as the measurement accuracy.

When SNR and v_{acq} are adjusted in an offsetting manner in Eq. [4-18] the required object volumes for a given measurement accuracy and precision will be altered and an optimal SNR can be determined along with a minimum required object volume.

4.3. Methods

4.3.1. Sodium Imaging Aspects

All sodium MRI was performed on a 4.7T Varian Inova scanner, using an in-house manufactured single-tuned RF birdcage head coil. In the spirit of sodium quantification, a minimally relaxation weighted sequence was used for radial k-space acquisition comparison. This sequence consisted of a 30^o rectangular RF pulse of length 0.27 ms (producing a TE of 0.194 ms) and a repetition time (TR) of 50 ms, allowing 'full' T_1 recovery. Although not required for the comparisons presented, projections were implemented to twist through 3D k-space on concentric sets of cones. For each comparison a constant number of projections were 'played-out' for constant scan duration.

4.3.2. Sodium Phantoms Used for Analysis

SNR was measured experimentally in a 2L, 50 mM [^{23}Na], spherical, 5% agar phantom with scans 5 minutes in duration. Two resolution phantoms were also scanned: a 50 mM, 5% agar phantom having transverse relaxation of T_{2f} = 2.7 ms (60%) and T_{2s} = 23 ms (40%); and a 150 mM saline resolution phantom with monoexponential transverse relaxation of T_2 = 53 ms. These two resolution phantoms were intended to represent the sodium environments of brain tissue and CSF respectively. A set of 2M [^{23}Na], 5% agar spheres ranging in size from 0.65 cc to 10 cc were used to demonstrate image intensity modulation with object volume for different projection sets (as described below). A high sodium concentration was chosen to facilitate the effective removal of noise from the images. Transverse relaxation for these agar spheres was measured as T_{2f} = 2.8 ms (60%) and T_{2s} = 22 ms (40%).

4.3.3. k-Space Filter Comparison for Imaging the Human Brain

Three projection sets producing β = 2, 3, and 4 modulation transfer functions in the presence of CSF relaxation (T_2 = 65 ms) were implemented to assess k-space filtering required for imaging the human brain. Each projection set was designed

with very similar readout duration, and in such a manner that SNR and gradient magnitude (G_{max}) remained constant (~5 mT/m in this case) (**Table 4-1**). Constant G_{max} implies equivalent radial sampling rate around the centre of k-space for each projection set. It should be noted that

$$G_{max} \propto (\tau_{tot}/T_{RO}) \cdot \sqrt[3]{rSNR}, \quad [4\text{-}19]$$

when acquisition voxel volumes are to be adjusted to maintain a constant SNR. The term rSNR in Eq. [4-19] is the relative SNR associated with each projection set calculated from Eq. [4-14]. The value of p was altered to achieve a constant G_{max}, as τ_{tot} is dependent on the value of p.

β	p	G_{max}	T_{RO}	voxel volume
2	0.17	4.9 mT/m	17.1 ms	0.089 cm^3
3	0.15	4.9 mT/m	17.2 ms	0.064 cm^3
4	0.14	4.9 mT/m	17.2 ms	0.047 cm^3

Table 4-1: Projection set parameters used for k-space filtering comparison with p and voxel volume adjusted for the same G_{max} and SNR respectively

Weighted (for oversampling at the centre of k-space) and gridded sampling points of each projection set are presented to highlight sampling density shape, $\Gamma(r)$. Each sampling point is also weighted according to T_2 relaxation during each projection readout and the associated modulation transfer function shown. The SNR of each projection set was measured in the spherical agar phantom, and images of both agar and saline resolution phantoms were acquired along with images from human brain.

4.3.4. Image Intensity Modulation with Object Volume

The three approaches to radial k-space acquisition of primary concern to this paper are given in **Table 4-2**. In each case a β = 3 Kaiser k-space filter in CSF space is generated, and in each case voxel volumes are adjusted to attain constant

SNR. For the standard projection (SP) approach $\Gamma(r)$ is generated entirely by post acquisition weighting. Both the short readout (SR) and long readout (LR) radial evolution altered approaches were designed for a G_{max} of ~5 mT/m. The SP approach had a G_{max} of ~4 mT /m, which for standard radial imaging is solely dependent on readout duration selection.

	p	G_{max}	T_{RO}	voxel volume
SP	1.0	4.2 mT/m	1.8 ms	0.208 cm^3
SR	0.29	5.1 mT/m	4.0 ms	0.124 cm^3
LR	0.15	4.9 mT/m	17.2 ms	0.064 cm^3

Table 4-2: Relevant projection set parameters of the three radial k-space acquisition approaches compared in this chapter. For each case voxel volume was adjusted to achieve the same SNR. For the SR and LR approaches p was adjusted to attain G_{max} ~ 5 mT/m.

To demonstrate image intensity modulation with object volume the 5% agar spheres ranging in size from 0.65 cc to 10 cc were each individually scanned using the three projection sets. Each sphere was placed in the same location at the centre of the RF coil within a loading shell devoid of sodium. Given small object volumes, additional coil loading was expected to have very little effect on acquired signal intensity. Individual object scanning at the same location in the RF coil eliminates PSF contribution between objects and signal dependence on B_1 field variation. For each projection set constant SNR was verified with measurement in the large 50 mM, 5% agar phantom.

Scaled image intensity values measured at the centre of each object were compared with that generated from effective PSF convolution with a uniform object-mask of ones. A zero-filled spherical $H(r)$, constructed from Eq. [4-4] using the relevant projection set parameters of **Table 4-2** and the measured T_2 of 5% agar, was multiplied with the Fourier transformed object-mask and inverse Fourier transformed to compute effective PSF convolution.

4.3.5. Comparing Approaches to Radial k-Space Acquisition for Minimum Required Object Volume

For each of the SP, SR and LR projection sets above the associated zero-filled noise correlation volume was computed as described in Chapter 3. Spherical objects (and spherical ROIs) were first considered. For each approach the minimum number of v_{acq} required in a ROI (N_{ROI}) was plotted from Eq. [4-18] for a range of SNR values from 5 to 80 and a desired MNR of 40 (~ $\pm$ 5% precision) and 80 (~ $\pm$ 2.5% precision). The required number of v_{acq} in an ROI volume is also given for a constant correlation volume of 1.91 acquisition voxels, the case for a hypothetical, non-zero-filled, uniform, spherical noise power spectral density.

For a range of spherical object volumes the maximum ROI volume in which an 80% and 90% accuracy can be attained in a signal averaging measurement (both in terms of v_{acq}) was found from the object image intensities generated with the effective PSF – object-mask convolution described above. For each object volume the maximum ROI volume producing a given average measurement accuracy was found from simple analysis of sequentially larger ROIs. A high 'level' of zero-filling (H(r) was generated to a spherical diameter of 25 and zero-filled to 256^3 – the same zero-filling was used for the agar comparison above) was used to facilitate analysis of ~ 350 effectively spherical object volumes from 8 to 800 acquisition voxels. A high 'level' of zero-filling also facilitates small 'spacing' between sequentially larger ROIs used to determine maximum ROI volumes for a given accuracy. The same 'level' of zero-filling was also used for correlation volume computation. The use of PSF convolution computation to assess object intensities with respect to PSF smearing allowed analysis for brain tissue relaxation parameters, and followed from correlation of image intensity computation with experiment in agar phantoms (above).

To determine minimum object volumes for analysis the number of v_{acq} required in an ROI for measurement precision (N_{ROI}) was associated with the number of v_{acq} required in an object, such that N_{ROI} was the maximum number of v_{acq} allowed in the ROI for measurement accuracy in that object. Physical object volumes required for each radial k-space acquisition approach were found from their SNR – v_{acq} relationships. For each projection set the voxel volume of **Table 4-2** was assigned an SNR of 15, similar to that obtained from each projection set in both **Tables 4-1** and **4-2** for a 10 minute scan of healthy human brain. For this optimization, when SNR is adjusted away from the value of 15, the acquisition voxel volume is also adjusted in proportion to maintain the same ratio. If the SNR – v_{acq} relationship was to be altered by 'external' means (i.e. increased scan duration, or change in NMR sequence parameters, etc…), the required object volumes would be scaled by this alteration.

Because the optimization of this paper is primarily concerned with the best radial k-space acquisition approach to quantify brain lesions, which are unlikely to be spherical, an anisotropic object geometry of (1 x 1 x 2) was selected for subsequent projection set comparison. Optimization for an even greater degree of anisotropy will 'intensify' the result as explained in the discussion.

Alterations from the SP, SR and LR radial acquisition approaches were also compared for minimum required object volume. Each alteration was designed for the same constant SNR. In the first consideration readout durations increased from that of the SP approach were considered for standard projection imaging.

	p	β	T_{RO}	voxel volume
(SP)	1.0	3	1.8 ms	0.208 cm^3
2	1.0	3	2.6 ms	0.175 cm^3
3	1.0	3	3.2 ms	0.157 cm^3
4	1.0	3	4.6 ms	0.134 cm^3

Table 4-3: Relevant projection set parameters for standard projection imaging analysis of readout duration longer than that of the SP approach.

In the second consideration two additional readout durations were considered for radial evolution altered k-space acquisition. The value of p was selected to maintain constant gradient magnitude.

	p	β	T_{RO}	voxel volume
2	0.19	3	11 ms	0.076 cm^3
(LR)	0.15	3	17 ms	0.064 cm^3
3	0.14	3	24 ms	0.057 cm^3

Table 4-4: Relevant projection set parameters for radial evolution altered k-space acquisition analysis of readout duration shorter and longer than that of the LR approach.

In the third consideration the value of p was adjusted from that of the LR approach. For case 1 the gradient magnitude is 2x that of LR; for case 2 the gradient magnitude is 1.5x that of LR; for case 4 the gradient magnitude is 0.5x that of LR.

	p	β	T_{RO}	voxel volume
1	0.11	3	17 ms	0.064 cm^3
2	0.13	3	17 ms	0.064 cm^3
(LR)	0.15	3	17 ms	0.064 cm^3
4	0.22	3	17 ms	0.065 cm^3

Table 4-5: Relevant projection set parameters for radial evolution altered k-space acquisition analysis of p value other than that of the LR approach.

In the final consideration differences in k-space filtering by sampling density design are compared. The projection sets of **Table 4-1** are used along with a $\beta = 0$ (uniform sampling density) projection set with $p = 0.2$, $T_{RO} = 17$ ms and voxel volume = 0.139 cm^3.

4.3.6. Comparing Radial k-Space Acquisition in Resolution Phantoms and Human Brain

Image from saline and 5% agar resolution phantoms were acquired for each of the SP, SR and LR radial k-space acquisition approaches. Finally, images acquired from healthy human brain are also presented for comparison.

4.4. Results

4.4.1. k-Space Filter Comparison for Imaging the Human Brain

Images generated from projection sets producing β = 2.0, 3.0 and 4.0 Kaiser modulation transfer functions in CSF are displayed in **Figure 4-1**. Each projection set had the same T_{RO} and gradient magnitude, and was designed for constant SNR. Sampled k-space radius expansion associated with increased β to maintain a constant SNR is highlighted in **Figures 4-1A – 4-1C**, and constant SNR demonstrated in the 5% agar phantom images of **Figures 4-1D – 4-1F**. Detrimental ringing artifacts can be observed with projection design for a β = 2.0 modulation transfer function in CSF (**Figures 4-1G, 4-1J**); these artifacts are reduced in the β = 3.0 case (**Figures 4-1H, 4-1K**), and further reduced for β = 4.0 (**Figures 4-1I, 4-1L**).

While the total sum of values within the normalized modulation transfer function, and hence the magnitude at the centre of the PSF, remains constant for each β in both brain tissue and CSF (a logical requirement given the same T_{RO}, gradient magnitude, and equivalent number of projections implemented for each projection set), the shapes of the PSF are slightly different for each β. A (very) slight decrease in the width of the PSF at half its maximum value is evident for both the CSF and brain tissue type environments **Figures 4-2A – 4-2B**, and **4-2F – 4-2G**. The effect of this slight narrowing of the main lobe of the PSF can be somewhat observed with respect to distinguishing resolution elements in the saline resolution phantom (**Figures 4-2C – 4-2E**).

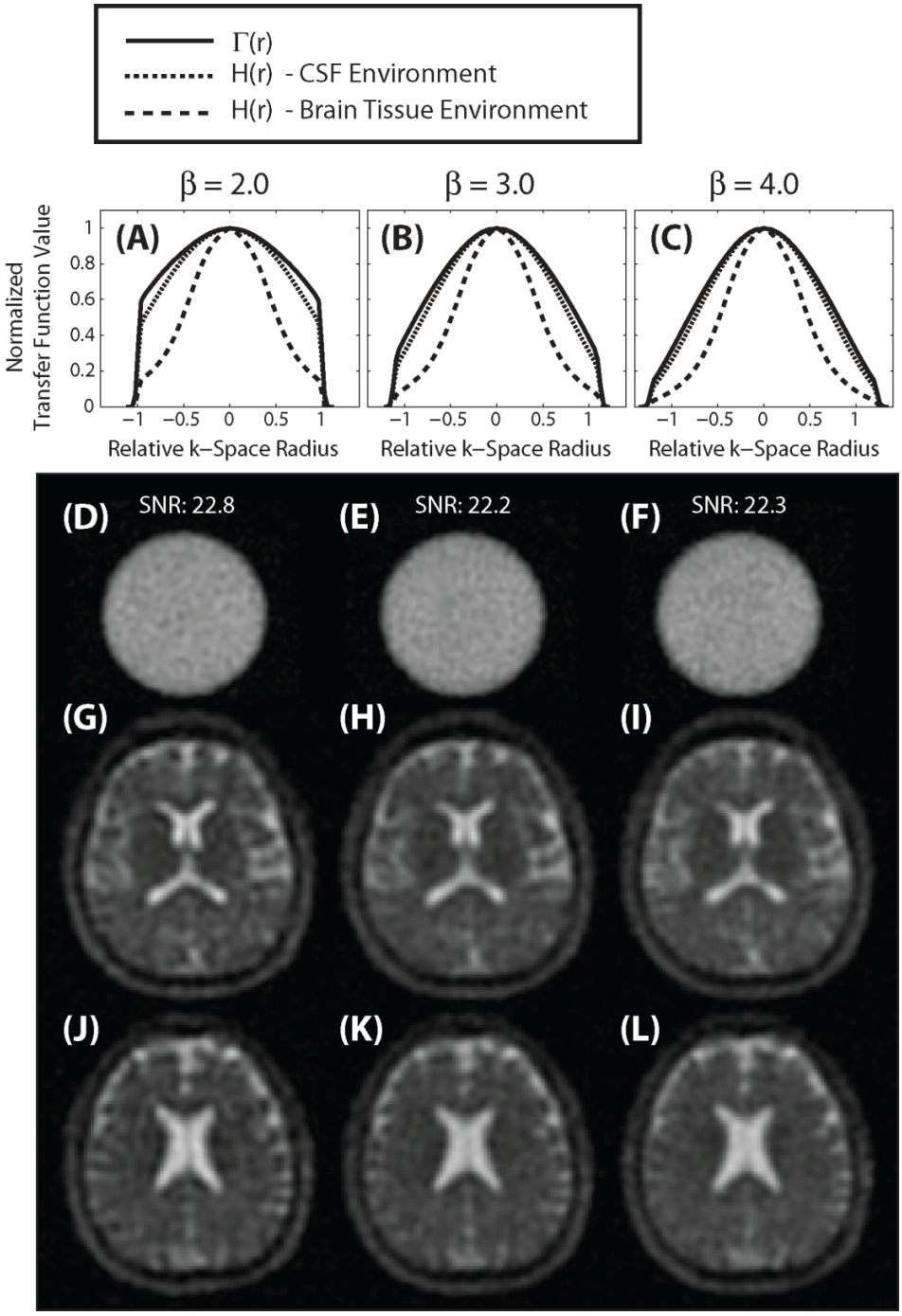

Figure 4-1: CSF ringing artifact dependence on Kaiser β design parameter. As β is increased the extents of k-space sampled are expanded (**A** – **C**) to maintain constant SNR (**D** – **F**). Detrimental ringing artifacts surrounding the CSF structures for β = 2.0 (**G**, **J**), which also superimpose to create a noisy image appearance, are reduced for β = 3.0 (**H**, **K**) and further reduced for β = 4.0 (**I**, **L**). It should be noted that images generated with uniform sampling density exhibit considerably more artifact than all of the images shown above.

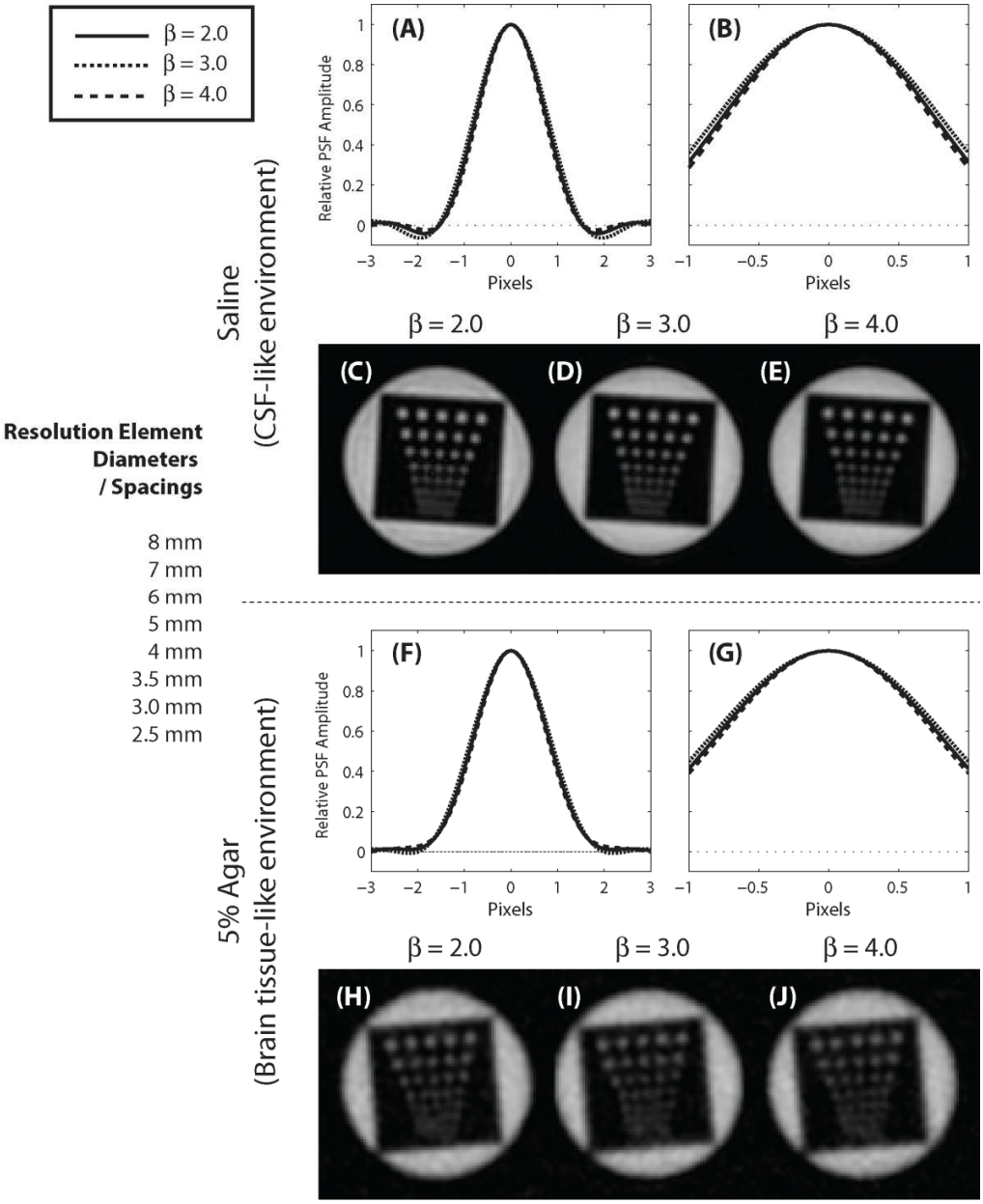

Figure 4-2: PSF shape and resolution phantom image dependence on Kaiser β parameter. While the total sum of values within the PSF and its centre magnitude remain constant for different β, the shape of the PSF changes. The proportional volume of the main lobe is slightly decreased along with its width at half max (**A** – **B**, **F** – **G**). As a result of this slight decrease, object distinction is slightly improved for increased β (somewhat observable in the fluid case (**E**)). The effect of proportional main lobe decrease on image intensity modulation with object volume will be discussed below. It should be noted that PSF shape dependence occurs in all three dimensions. It should also be noted that while the magnitude at the centre of the PSF remains the same within the separate environments for each β implementation, the magnitude at the centre of the PSF for the brain tissue environment is considerably less than that for the CSF environment.

4.4.2. Image Intensity Modulation with Object Volume

Image intensity modulation with object volume is displayed in **Figure 4-3** for the three different approaches to radial k-space acquisition designed for constant SNR. For each projection set, image intensity modulation with object volume closely matches that of effective PSF – object-mask convolution computation. Image intensity modulation appears roughly similar between acquisition approaches even though the v_{acq} volumes are very different. The LR approach with the greatest k-space roll-off related to T_2 decay in combination with k-space filter design exhibits the least ringing superposition effect for the larger object volumes.

In **Figure 4-4** image intensity modulation is displayed from effective PSF – object-mask convolution computation for the T_2* decay parameters of healthy human cellular brain tissue at 4.7T. As can be seen, image intensity modulation is quite similar for the two different radial evolution altered approaches (SR and LR) over small object volumes, but image intensity increase with object volume for the LR approach slows beyond 80% relative signal intensity. Both the SR and LR approaches exhibit more rapid image intensity increase with object volume in general than that of the standard projection approach.

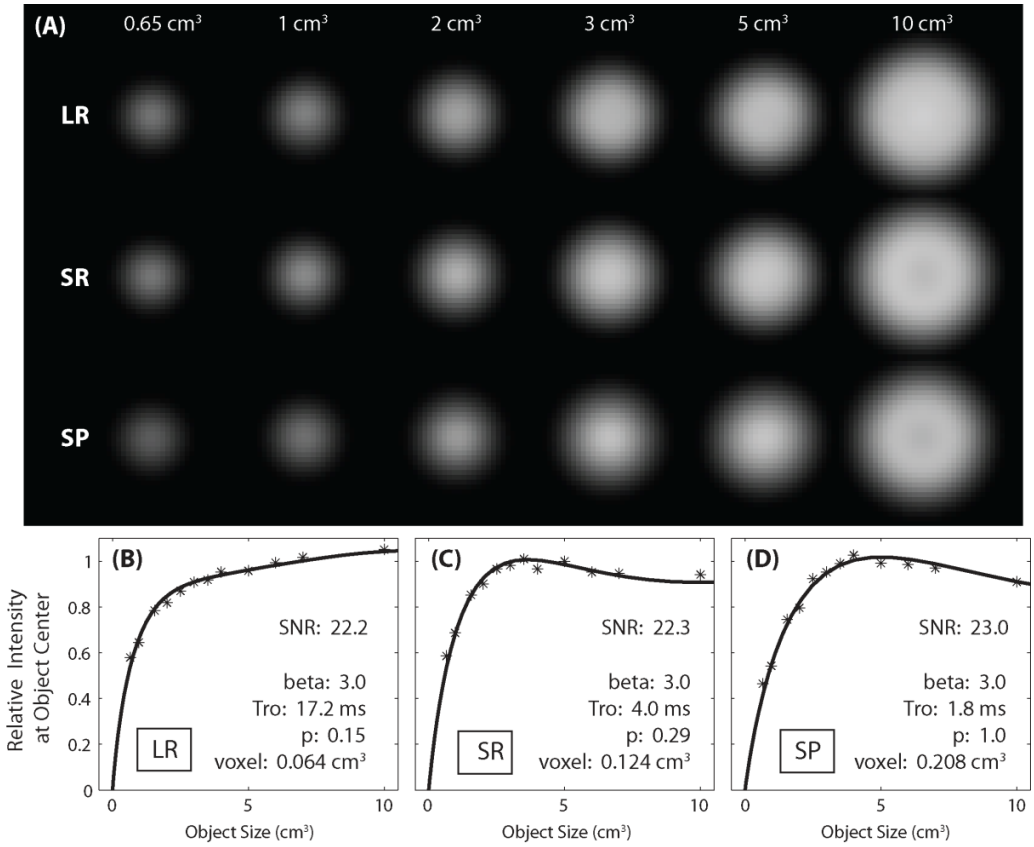

Figure 4-3: Image intensity modulation with object volume (given at the top of each column in cm^3) in spherical 5% agar phantoms for the LR, SR and SP radial k-space acquisition approaches, each designed for constant SNR. Although the acquisition voxel volumes are quite different, image intensity modulation with object value is similar for the three approaches. In each case the shape of image intensity increase with object volume at the object centre (stars) (**B** – **D**) matches that computed with effective PSF – object-mask convolution. For the short readout duration approaches (SR and SP) ringing superposition is evident in the large objects (visible as hypointensity at centre of image in 10 cm^3 case).

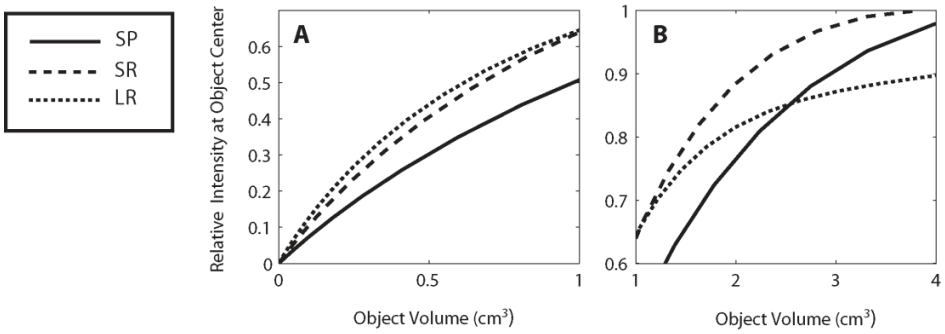

Figure 4-4: Image intensity modulation with spherical object volume computed at object centre for cellular brain tissue relaxation using effective PSF – object-mask convolution. 'A' highlights intensity for small objects, and 'B' intensity for larger objects (split for easier observation of differences). The LR approach has the greatest initial rate of image intensity increase, but tapers off before approaching 90% of full value; the SR approach continues with rapid rise through 90% of full value. The SP approach exhibits a much slower initial image intensity increase than either LR or SR, but approaches 90% of full value in a smaller object than the LR approach.

4.4.3. Comparing Approaches to Radial k-Space Acquisition for Minimum Required Object Volume

In **Figure 4-5** the required spherical object volumes for a given measurement precision and accuracy are computed for the SP, SR and LR approaches to radial k-space acquisition. The SP approach with its large reduction of low frequency noise requires the fewest number of v_{acq} in an ROI (N_{ROI}) to achieve a desired measurement precision (**Figure 4-5A**). At an SNR 1/4 the desired MNR, the minimum N_{ROI} required for the SP approach is ~ 60% that required for the other two approaches. It should be noted that when SNR is equal to the desired MNR only one zero-filled image voxel is required for measurement precision. Given the high 'level' of zero-filling, the required ROI volumes for SNR = MNR are a small fraction of one v_{acq}.

In **Figure 4-5B** it can be seen that for the SP and SR approaches PSF smearing across k-space has a similar effect on the maximum number of v_{acq} allowed within an ROI for any given number of v_{acq} within an object. For the LR approach the minimum number of v_{acq} required in an object to attain a 90% accurate measurement in a very small ROI is roughly 4x larger than the SP

approach, however, a very small increase in v_{acq} within the object from its minimum number facilitates a very large increase in maximum allowable N_{ROI}. For all three radial k-space acquisition methods the maximum allowable N_{ROI} to achieve a desired accuracy approaches the number of v_{acq} within the object when this number is large.

Combining the minimum number of v_{acq} required in an object for a given SNR (from **Figure 4-5A** and **4-5B**, as demonstrated with the gray, arrowed line) with the v_{acq} – SNR relationship (**Figure 4-5C**) yields the physical required object volume (**Figures 4-5D** and **4-5E**). For 90% accuracy the minimum required object volume for the LR approach is similar to that of the SR approach, and for 80% accuracy the minimum required object volume for the LR approach is smaller. Although the LR approach possess larger correlation volumes than the SP approach (as reflected in **Figure 4-5A**), and greater PSF smearing effect than both the SP and SR approaches (as reflected in **Figure 4-5B**), its much smaller v_{acq} – SNR relationship facilitates minimum required object volumes comparable or less than the other two approaches.

It should be noted that in **Figures 4-5A**, **4-5D** and **4-5E** the curves for 2.5% and 5% precision have the exact same shape when SNR is plotted as a fraction of MNR. For this reason only the case of 2.5% precision (MNR = 80) will be given in the following comparisons. The optimum SNR for any other precision (or MNR) can be found from this relationship, i.e.

$$\mathrm{SNR} = \frac{\mathrm{MNR}}{80}\mathrm{SNR}_{\mathrm{MNR}=80}\,, \qquad [4\text{-}21]$$

at which the minimum required object volume (MROV) is

$$\mathrm{MROV} = \frac{\mathrm{MNR}}{80}\mathrm{MROV}_{\mathrm{MNR}=80}\,. \qquad [4\text{-}22]$$

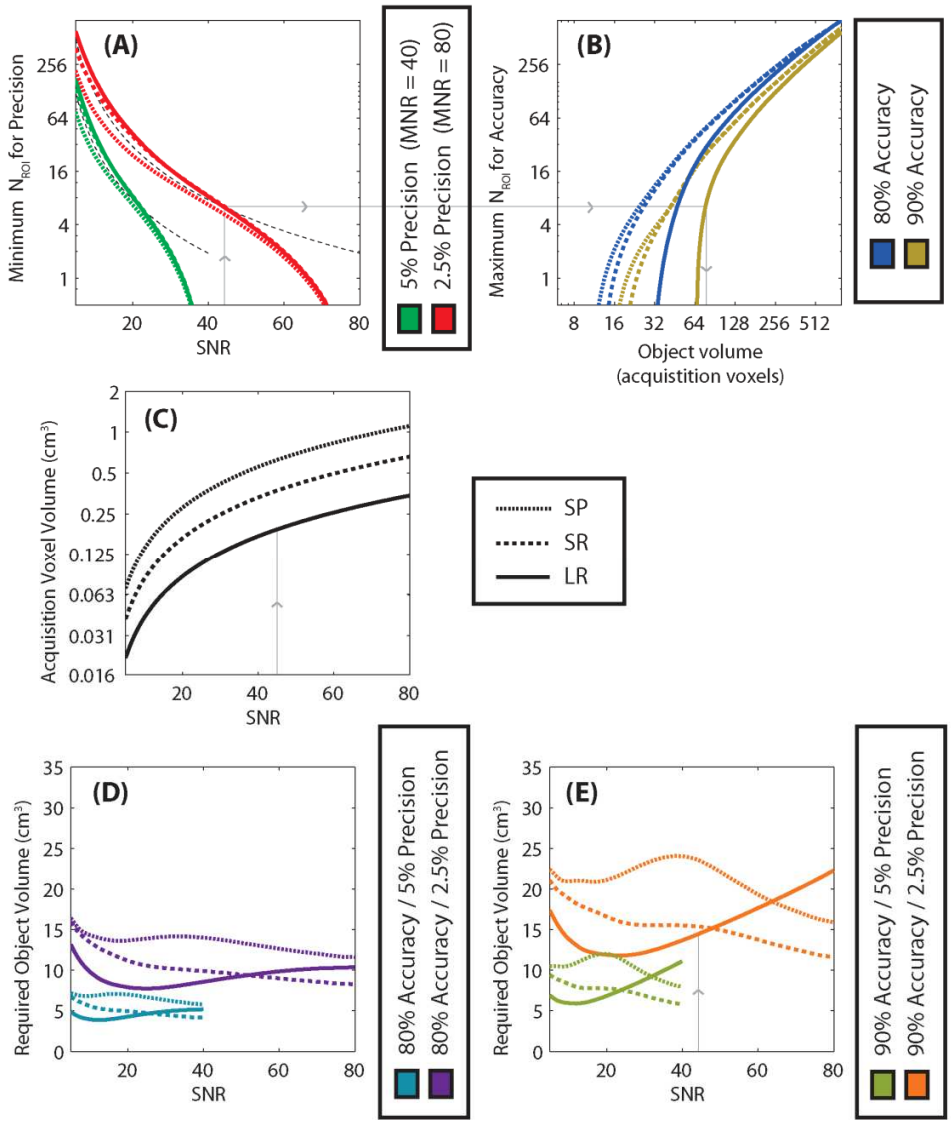

Figure 4-5: Optimization for minimum *spherical* object volume required to achieve a given measurement accuracy and precision. The number of voxels required in the ROI to attain the MNR associated with 5% and 2.5% precision is given in (**A**) (the thin dashed lines highlight the hypothetical case of constant CV = 1.91 acquisition voxels – i.e. the hypothetical case for a non-zero-filled, uniform, spherical noise power spectral density). For each ROI volume required to attain a desired precision, a required object volume to attain a desired accuracy can be found from (**B**). Using the SNR – voxel volume relationship of (**C**) the physical required object volumes can be plotted for each projection set with respect to SNR (**D** and **E**). The gray arrowed lines highlight a calculation example for the LR approach at an SNR of 44, a precision of 2.5%, and an accuracy of 90%. For *spherical* objects the minimum required object volume for the SR and LR approaches are similar, however, the optimum SNR for the LR approach is ~ 1/4 that of the desired MNR.

SNR optimization for the SP, SR and LR projection sets when objects have a geometry of (1 x 1 x 2) is shown in **Figure 4-6**. While the required N_{ROI} is reduced from the case of spherical voxels for measurement precision (**Figures 4-6A** vs. **4-5A**), the effects of PSF smearing have greater impact, especially on the minimum number of v_{acq} required within an object to obtain a given accuracy (Note that the minimum number of object v_{acq} to attain a desired accuracy will produce that accuracy in a very small region at the centre of the object – bottoms of **Figures 4-6B** vs. **4-5B**). The result is increased required object volumes across SNR for each acquisition approach, but most substantially for implementations in which SNR approaches the desired MNR. The optimum SNR value is shifted lower for each acquisition approach, most noticeably for SP and SR. The LR approach facilitates precise and accurate measurement in minimum ROI volumes ~ 25% smaller than SR and ~ 40% smaller than SP, and does so at an SNR < ¼ the desired MNR.

Readout duration increase from that of the SP approach is considered in **Figure 4-7** for standard radial imaging. Note that in general T_{RO} would have zero impact on correlation volume in terms of v_{acq}. For this optimization, because the effect of relaxation is considered in the production of a constant Kaiser function within CSF, post-acquisition weighting is slightly altered with T_{RO} change. The result is a very small dependence on correlation volume in terms of v_{acq} (**Figure 4-7A**). It is shown that although the PSF is smeared over a greater number of v_{acq} when T_{RO} is increased (with affect given in **Figure 4-7B**), this increased smearing is offset by facilitated voxel volume reduction (**Figure 4-7C**). As a result, the same minimum required object volumes are facilitated for 90% accuracy with a T_{RO} increase to 3.2 ms, however, the implementation of small v_{acq} (sacrificing SNR) is critical to maintaining minimum object volumes for analysis. For 80% accuracy the minimum required object volume can be slightly reduced with increased T_{RO}.

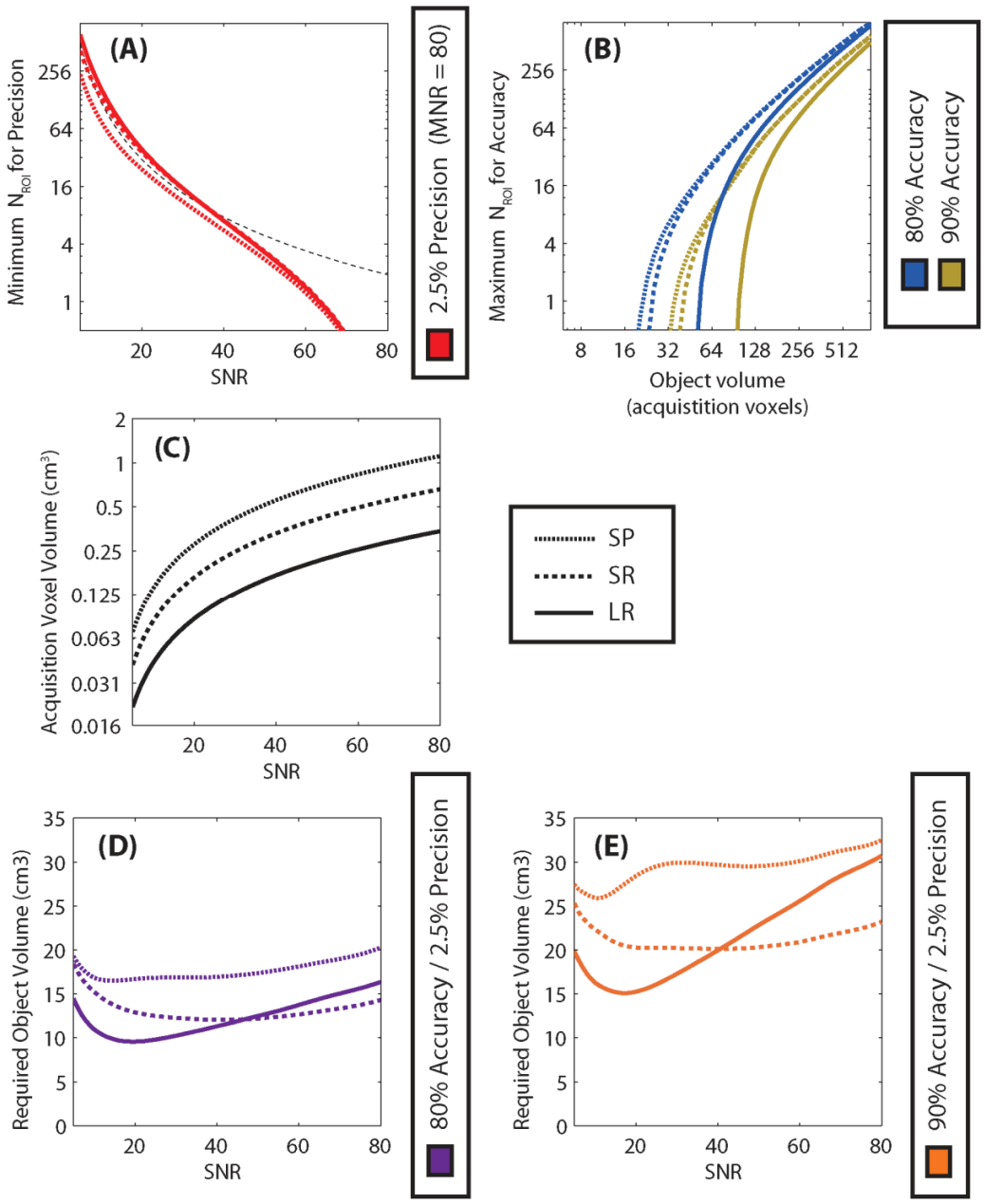

Figure 4-6: Optimization for minimum *anisotropic* (1 x 1 x 2 rectangular geometry) object volume required to achieve a given measurement accuracy and precision. For anisotropic objects the required number of v_{acq} in an ROI to attain the desired MNR is reduced (**A**) from that for spherical objects (Figure 4-5A). However, the maximum v_{acq} allowed in an ROI to attain a desired accuracy is decreased (from Figure 4-5B) for any given number of v_{acq} in the object (**B**), especially for small objects. The v_{acq} – SNR relationship of (**C**) is the same as that of Figure 4-5C. The physical object volumes required for measurement precision and confidence (**D** and **E**) are increased from the case of spherical objects (Figures 4-5D and 4-5E), particularly for implementation of SNR = MNR. Optimum SNR values are shifted to 1/8 – 1/4 of desired MNR for each approach. The LR approach clearly facilitates the smallest required object volumes.

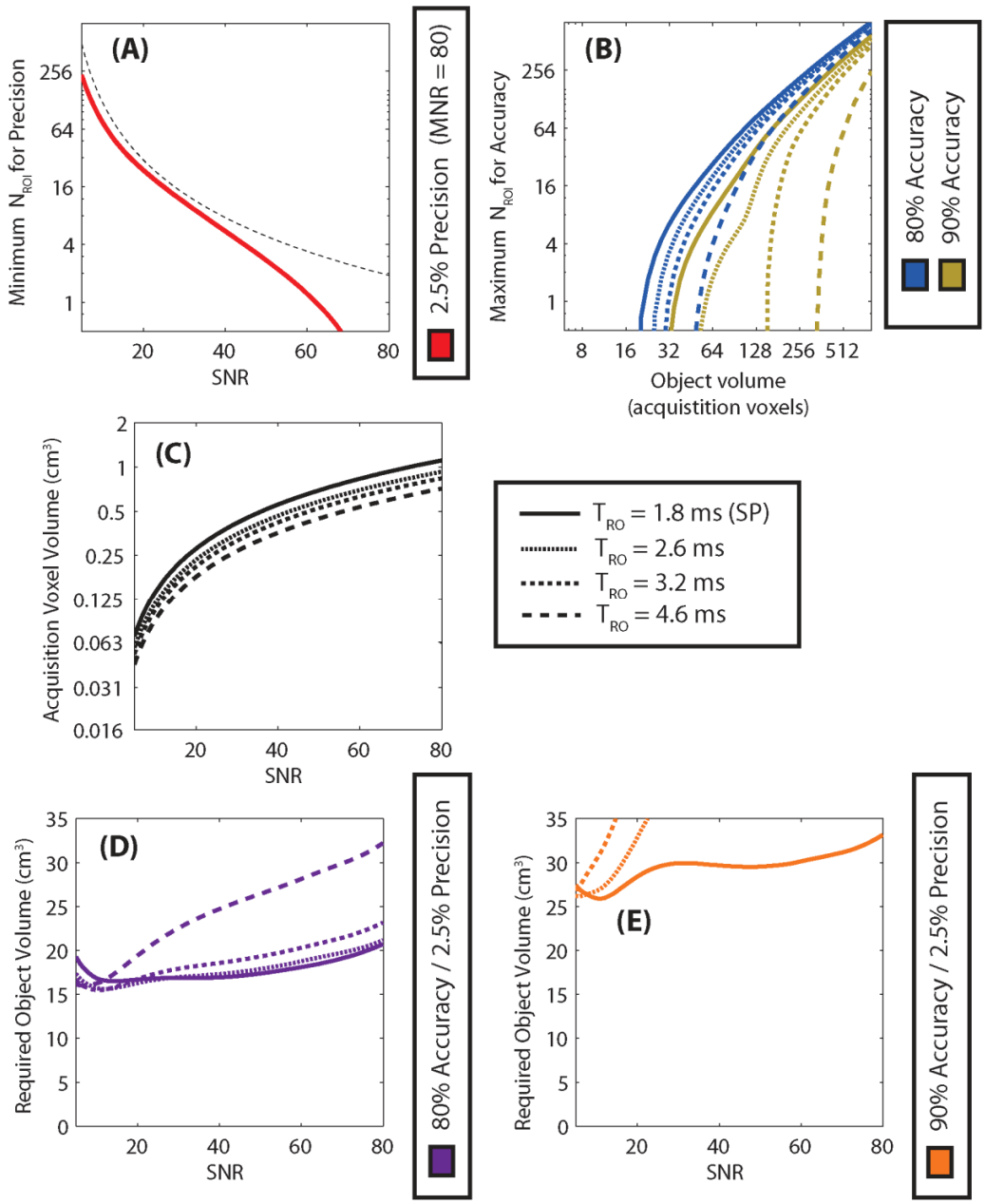

Figure 4-7: Limited effect of readout duration increase on minimum required object volumes for analysis when T_{RO} is increased beyond that of the SP approach for standard radial imaging. The effect of smearing the PSF over a greater number of v_{acq} with increased T_{RO} is most observable in the minimum number of v_{acq} required within an object to achieve a given accuracy (bottom of **B**). However, for objects containing large numbers of v_{acq}, maximum allowable N_{ROI} values are not greatly decreased with increase in T_{RO} to 3.2 ms. Because T_{RO} increase facilitates v_{acq} volume reduction (**C**), offsetting PSF smearing effect, a minor decrease in object volume required to attained 80% accuracy can be attained (**D**). For 90% accuracy the same minimum required object volumes are facilitated by T_{RO} increase to 3.2 ms, but small voxel volume implementations are critical (**E**).

Figure 4-8 highlights SNR optimization for 2 additional radial evolution altered cases with readout durations of 11 ms and 24 ms. Even though PSF smearing is increased for longer T_{RO}, acquisition voxel volumes are reduced. A slight advantage to increasing the readout duration beyond that of the LR approach is suggested. This advantage is achieved with further reduction in optimal SNR.

The necessity of reduced p to facilitate the minimum required object volume advantage of long readout duration is demonstrated in **Figure 4-9**. The value of p between 0.11 and 0.22 has effectively no impact on the v_{acq} – SNR relationship (**Figure 4-9C**). This is because the SNR sampling efficiency is very near one for each case. However, an increase in p beyond that of the LR approach to 0.22 has a large impact on PSF smearing, as can be seen in its effect on **Figure 4-9B**. Increasing p from that of the LR approach is quite detrimental; decreasing p below that of the LR approach offers diminishing return, but requires increased G_{max} (1.5x for p = 0.13, 2x for p = 0.11) beyond the 5 mT/m used in this paper.

The effect of k-space filtering by sampling density design on minimum required object volumes is demonstrated in **Figure 4-10**. If k-space filtering could be eliminated minimum required object volumes could be reduced. However, when k-space filtering is required, as it is for sodium imaging of the human brain, increased roll-off from that of the LR approach has marginal effect.

When the SP, SR and LR radial k-space acquisition approaches are implemented to achieve the same SNR, their v_{acq} volumes are very different (**Table 4-2** – **Figures 4-5C** and **4-6C**). In the fluid space of CSF the PSF directly scales with voxel volume between projection sets by design. This is directly apparent in the saline resolution phantom images of **Figure 4-11**. Resolution increase is also apparent for the 5% agar phantoms, but not to the same extent. Resolution differences between the acquisition approaches can also be observed in the human brain slices of **Figure 4-12**, particularly with respect to CSF signal containment within its bounds.

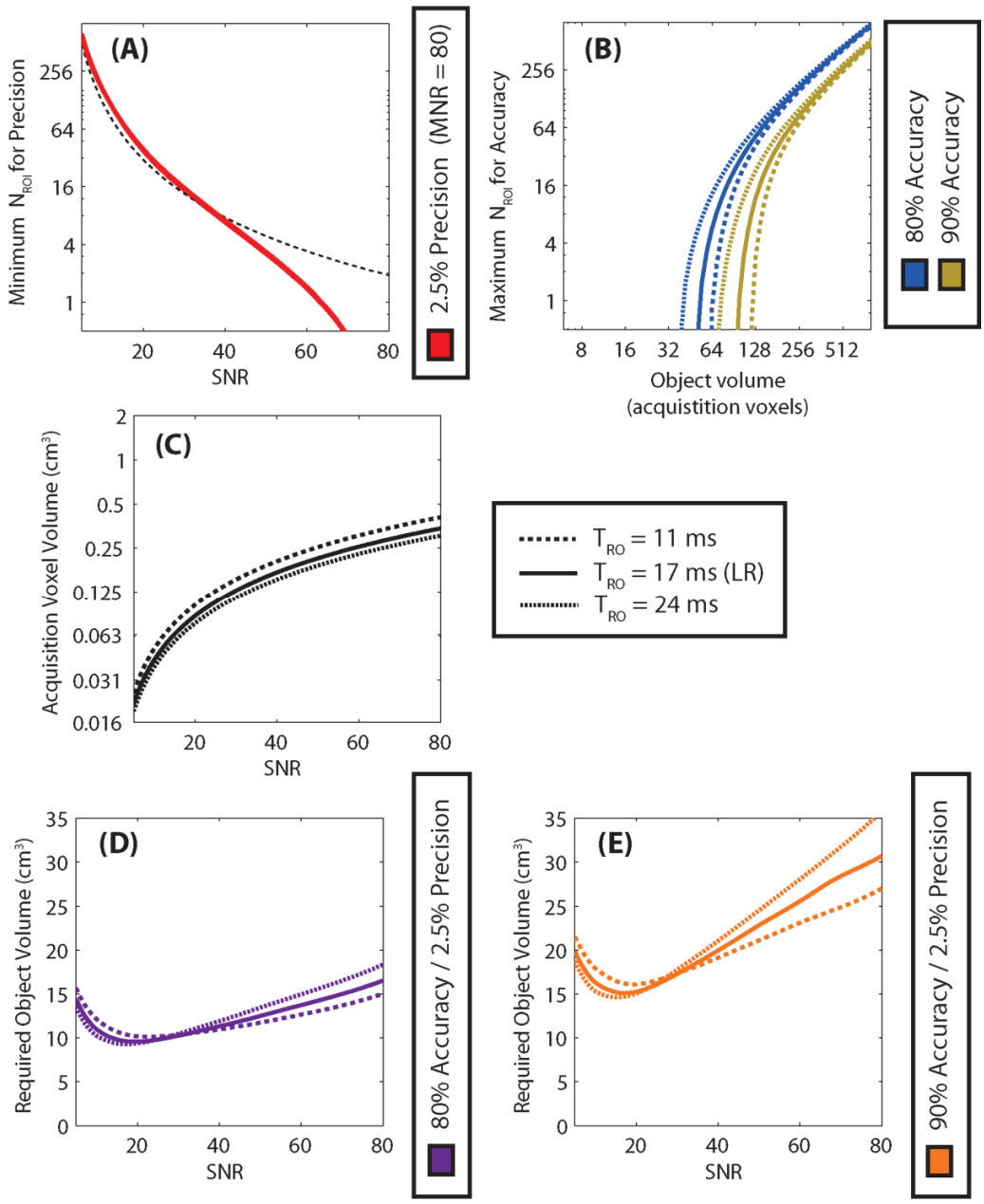

Figure 4-8: Small advantage of readout duration increase beyond that of the LR approach. Although the PSF is smeared over a greater number of v_{acq} when T_{RO} is increased, this increased smearing has limited effect on the maximum N_{ROI} allowed for accuracy when objects contain large numbers of v_{acq} (**B**). Reduced voxel volumes with T_{RO} increase (**C**) facilitate small reductions in minimum required ROI volume for both 80% and 90% accuracy (**D** and **E**). T_{RO} reduction from the LR approach to 11 ms is slightly disadvantageous.

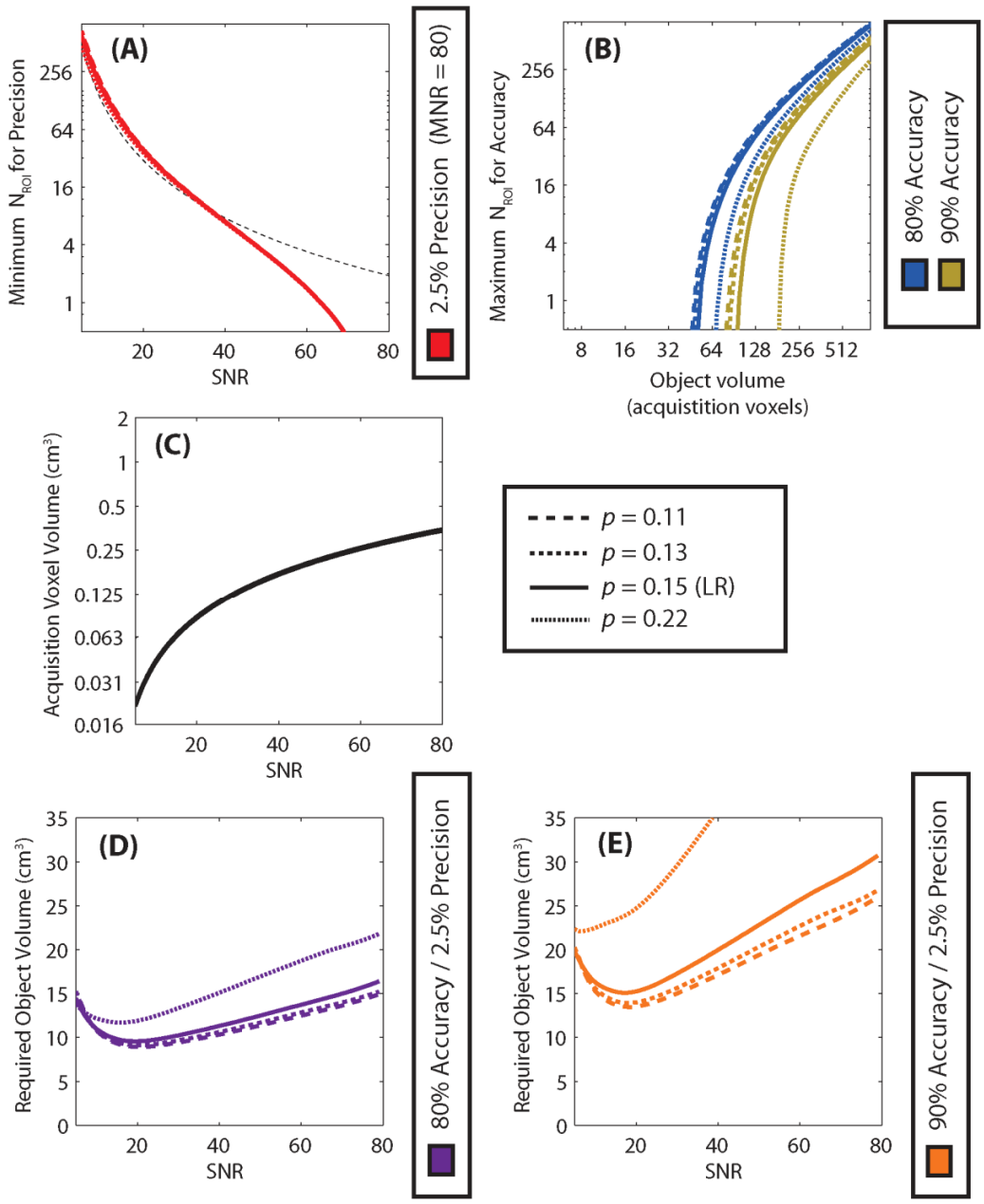

Figure 4-9: The critical requirement of small p value for minimum required object volume reduction when readout duration is long (that of the LR approach – 17 ms). Alteration of p between 0.11 and 0.22 in the generation a β = 3 Kaiser function in CSF with sampling density has little effect on correlation volume (**A**), and very little effect on the v_{acq} – SNR relationship (**C**). However, increase in p from 0.15 (that of the LR approach) to 0.22 has an obviously large effect on PSF smearing (as reflected in **B**). This increase in p results in much larger minimum required object volumes for analysis (**D** and **E**). Further reduction of p beyond that of the LR approach is slightly advantageous, especially when high accuracy is desired, but comes at the cost of increased G_{max}.

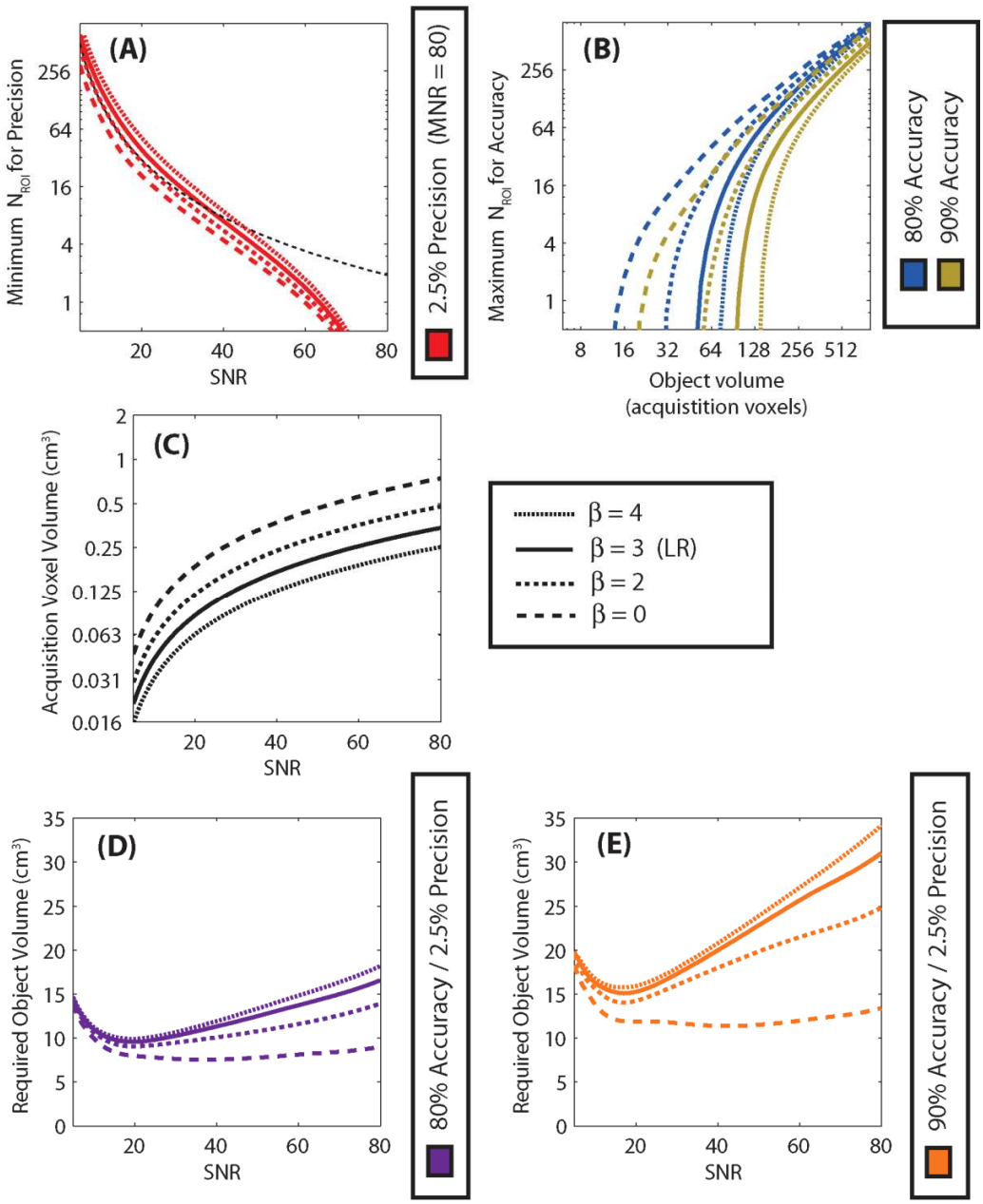

Figure 4-10: The marginal effect of increased k-space filtering by sampling density design from that of the LR approach. An increase in the β filter shape parameter results in larger correlation volumes (as reflected in **A**), but reduced voxel volumes (**C**). Increased k-space filtering also results in greater PSF smearing (as reflected in **B**). The combined result is a minor increase in minimum required object volume if k-space filtering by sampling density design is increased beyond that of the LR approach. No k-space filtering would facilitate somewhat smaller minimum required object volumes.

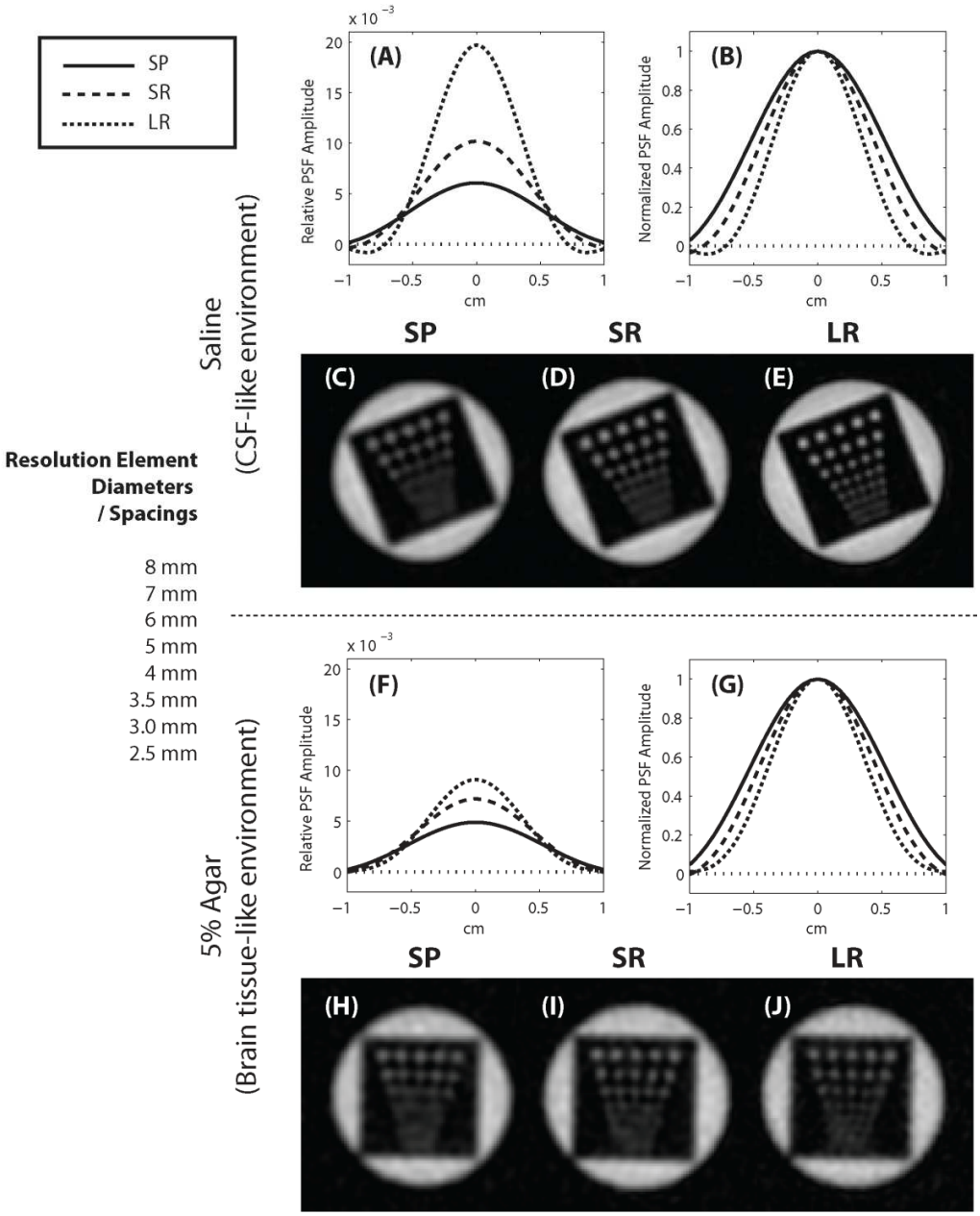

Figure 4-11: Radial k-space acquisition approach PSF and resolution phantom image comparison. The 3.3x increase in extent of k-space sampled for the LR approach, compared with SP, results in a 3.3x increase at the centre of the PSF within CSF (**A**), and reduction of main lobe width (**B**). PSF differences are easily observable in saline resolution phantoms (**C** – **E**). As a result of T_2 decay the total sum of values in the modulation transfer function for the LR approach (as reflected at the centre of the PSF) is less than 3.3x greater than the SP approach for brain tissue (**F**). While image intensity modulation with object volume is similar for the three approaches, the shape of the PSF enables enhanced distinction of smaller resolution elements for the LR approach as can be observed in the 5% agar resolution phantoms (**H** – **J**).

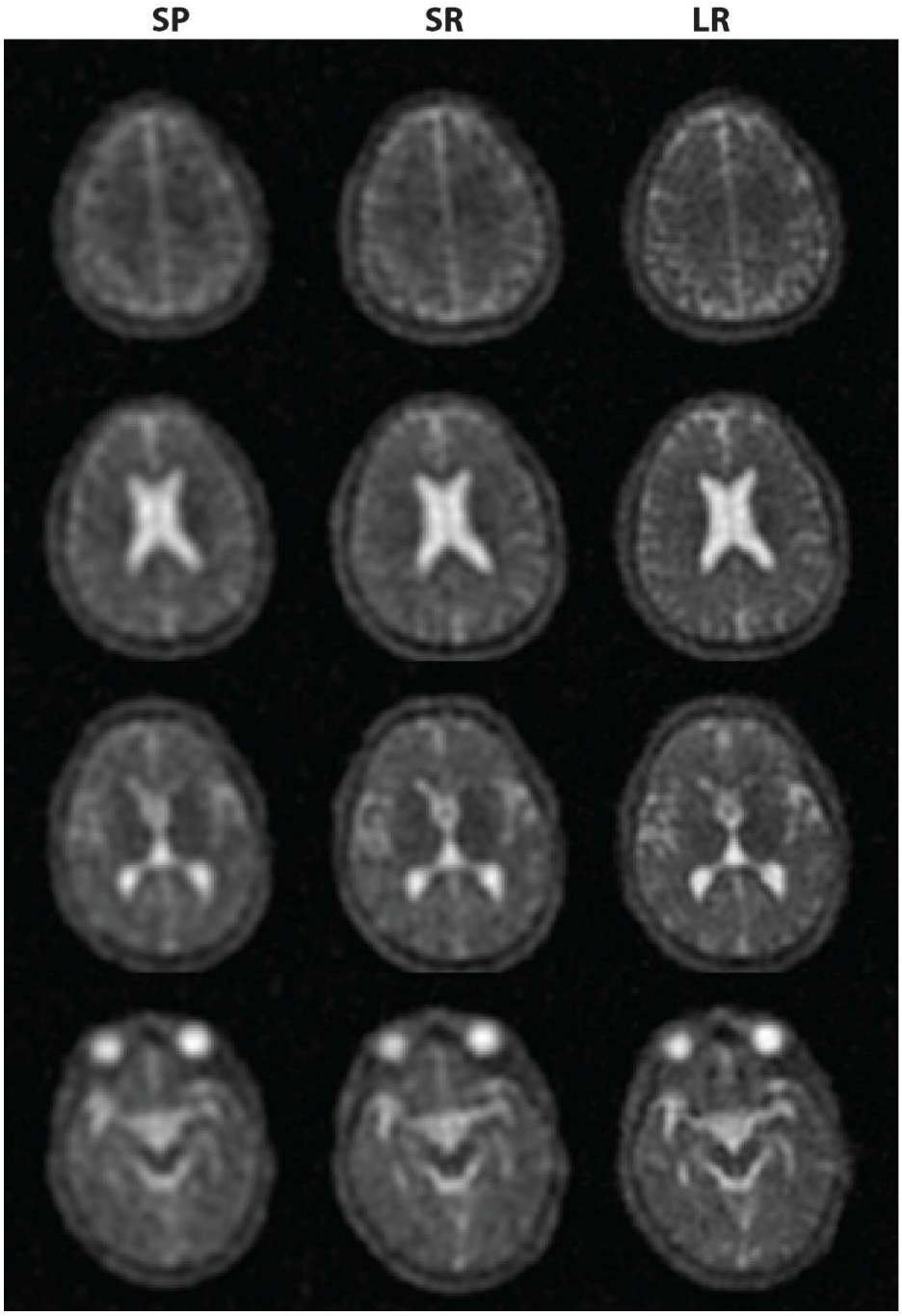

Figure 4-12: Slices of healthy human brain acquired using the SP, SR and LR approaches to radial k-space acquisition. While image quality cannot be directly assessed for brain tissue, image quality with respect to CSF is easily ascertained. The shape of the modulation transfer function, and hence the PSF, is constant for each approach in CSF by design (β = 3.0). As a result CSF signal intensity containment within its bounds is directly proportional to the voxel volume of each approach. The LR approach exhibits the least 'smearing-out' of CSF signal intensity beyond its bounds.

4.5. Discussion

In this paper three radial sodium k-space acquisition approaches were compared with respect to quantitative imaging for the human head. The first (SP) involved standard projection imaging with a short readout duration ~ 2 ms (similar to that of (5)); the second (SR) involved readout evolution altered k-space acquisition to produce a k-space filtering sampling density with short readout duration of 4 ms (similar to that of (29)); the third also involved readout evolution altered k-space acquisition but had a long readout duration of 17 ms (similar to that of Chapters 2, 5, and 6 (41,42,60)). A β = 3 Kaiser modulation transfer function, in which the effect of transverse relaxation in CSF was included, was selected (**Figure 4-1**) to reduce CSF ringing image contamination and was implemented for each acquisition approach in the comparison. For the standard projection (SP) approach the Kaiser transfer function was generated with post-acquisition weighting, for the other two it was generated with sampling density design using the methodology presented. Each projection set was designed for constant image SNR (in a sufficiently large object) using an equation presented for radial k-space acquisition, and constant SNR was verified in a large 5% agar phantom. Design for constant SNR required voxels volumes with ratios 3.3: 1.9: 1.0 (SP: SR: LR), however, although the voxel volumes were much different, image intensity modulation with object volume was 'similar' for each approach (**Figures 4-3** and **4-4**). When measurement precision (with respect to image noise) and accuracy (with respect to image intensity modulation with object volume) are considered for an average measurement within an ROI, the LR approach facilitates analysis in the smallest object volumes for brain tissue relaxation, this is especially true for anisotropic objects (~25% smaller than SR, and ~40% smaller than SP for 90% accuracy in **Figures 4-6**). It is suggested that optimum SNR for each approach at which to generate sodium images is roughly 1/8 to 1/4 the measurement-to-noise ratio (MNR) required for the desired measurement confidence. However, not only is the LR approach advantageous with respect to signal intensity measurement in cellular tissue, its much smaller voxel volumes facilitate much better containment of CSF signal intensity within its bounds (**Figures 4-11** and **4-12**). Minor

improvements may be possible for the LR approach with further increased readout duration and reduction of the value of *p* (**Figures 4-8** and **4-9**); increased k-space filtering to further minimize CSF ringing is not detrimental (**Figure 4-10**). It is suggested that radial evolution altered k-space acquisition with sampling density designed k-space filtering, a small value of *p*, and long readout duration (similar to LR) is an ideal approach for radial sodium MRI of the human head.

While shortening T_{RO} so as to reduce rapid T_2 signal attenuation across k-space has been 'fundamentally accepted' as appropriate for radial sodium k-space acquisition (5,29), this chapter suggests the opposite. Although for standard projection imaging **Figure 4-7** suggests that increasing T_{RO} beyond the ~ 2 ms of the SP approach (T_{RO} similar to (5)) is not necessarily beneficial in terms of minimum required object volumes for analysis, the reduced voxel volumes associated with noise variance reduction of increased T_{RO} (**Figure 4-7C**) to achieve optimum implementation SNR (**Figures 4-7D** and **4-7E**) will facilitate improved CSF containment for imaging the human head. Nielles-Vallespin, et. al. (5) suggest a T_{RO} decrease to improve their images. In this chapter it is suggested that a ~50% T_{RO} *increase* would improve the sodium images, assuming sufficiently small v_{acq} volumes were implemented such that SNR in the tissue of interest was ~ 1/8 the desired MNR for analysis precision.

For radial evolution altered k-space acquisition this chapter suggests that *substantial* readout duration increase from that of T_{RO} = 4 ms (the T_{RO} suggested in (29)) is beneficial. While reduced noise variance is outweighed by increased T_2 decay across k-space for *large* T_{RO} increase with standard projection imaging, that is not the case for radial evolution altered imaging. The reason for this was very recently given by Nagel (36), and was described as: "the k-space position (for radial evolution altered acquisition) is always ahead in time compared to conventional radial sampling." The sampling density produced with readout evolution altered k-space acquisition will be scaled by $1/p^2$ (for proper implementation of Eq. [4-1**]**). To achieve this sampling density the relative

projection length (τ_{tot}) will be increased when p is reduced, and an increase in τ_{tot} for the same T_{RO} yields much more rapid sampling at the centre of k-space and slower sampling toward the edges. This effect, which is strongly dependent on the value of p implemented, could also be described as 'bending time' across k-space and is shown in **Figure 4-13A** below. As a result of this effect, the shape of the modulation transfer function for the same T_{RO} will be beneficially altered (**Figure 4-13B**). The greater total sum of values within $H(r)$ will increase the value at the centre of PSF in proportion (**Figure 4-13C**). The value at the centre of the PSF was of concern in the readout optimization considered by Nagel (36), however, the total volume within the three-dimensional main lobe of the PSF is increased to an even greater relative extent than the value at the centre of the PSF. Object-mask convolution with a PSF having a much larger main lobe yields 'dramatically' reduced image intensity modulation with object volume (**Figures 4-13D** and **4-13E**). More of the signal intensity associated with the object remains within the object rather than being 'smeared' outside its bounds. It is because of the 'time bending' effect across k-space that the image intensity modulation with object volume is similar for the three acquisition approaches compared in this chapter (**Figures 4-3** and **4-4**). The requirement of small p to facilitate long T_{RO} is demonstrated in **Figure 4-9**.

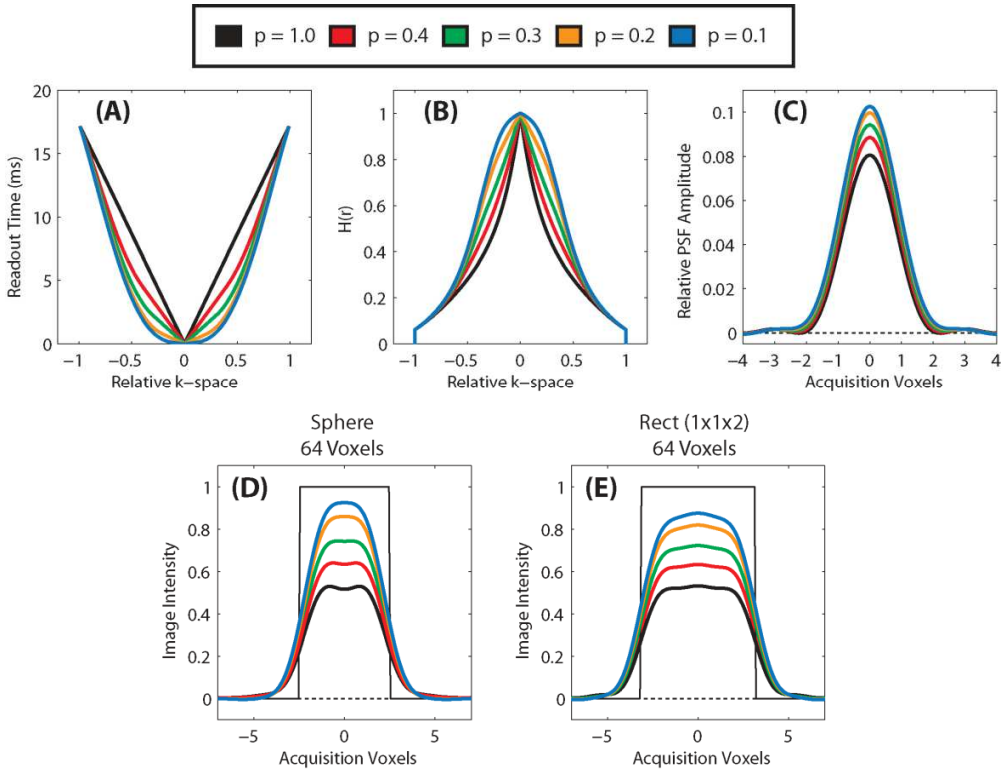

Figure 4-13: The k-space 'time-bending' advantage of radial evolution altered acquisition. When the value of p is reduced from 1.0 the centre of k-space is sampled much more rapidly than its outer aspects (**A**), and the shape of H(r) is altered from that of biexponential decay (**B**). The result is not only an increase in the magnitude at the centre of the PSF, but a large increase in main lobe volume, with a smaller percentage of values spread into the periphery (**C**). When the PSFs of (C) are convolved with 'small' (64 v_{acq}) object volumes it can be seen that the reduction of p has 'dramatic' effect to facilitate image intensities approaching full value (**D** and **E**).

It is also suggested in **Figure 4-8** that an increase in T_{RO} beyond that of the LR approach may be slightly beneficial. Although an increase in readout duration will 'amplify' image artifacts related to local field inhomogeneities, it should be noted that the gyromagnetic ratio of sodium is ~ ¼ that of proton. Field inhomogeneity effects for sodium at 4.7T will be less than that for proton at 1.5T. It should also be noted that 'bending time' across k-space also mitigates local off-resonance effects (36). For the LR approach presented in this chapter there are no visibly detrimental field inhomogeneity artifacts even in the 'extreme' resolution phantom case (**Figure 4-11**).

It should be noted that when images are implemented such that SNR equals desired MNR the minimum required ROI volume is one zero-filled voxel (i.e. no averaging is necessary), and the image intensity in one zero-filled voxel approaches 90% accuracy for the smallest surrounding spherical object volume when the *SR* approach is implemented (**Figure 4-4** and the right edge of **Figure 4-5F**). While the centre of the PSF has greatest magnitude for the LR approach to a radius of ~ 0.4 cm, the SR PSF has greater magnitude through the remainder of the main lobe which includes a much larger 3D volume (**Figure 4-11F**). Note that the image intensity at the centre of a uniform object is proportional to the total sum of values within the PSF encompassed by that object. Image intensity is elevated most rapidly in small objects for the LR approach, but as object volumes increase beyond ~ 1 cm^3, further inclusion of the PSF does not continue the image intensity rise to full value as it does for the SR approach (**Figure 4-4**). An image intensity 90% of full value is achieved in an object almost 2x larger for LR when compared to SR in this figure, despite the fact that the LR voxels are half that of SR. For the LR approach a greater proportion of the PSF is spread into its periphery creating a PSF 'tail' (or a large region of the PSF with very small values). Because a large portion of this 'tail' must be included to produce 90% accuracy at the object centre the required number of voxels in the object will be large, but the image intensity surrounding the centre of the object will also be very near 90% accuracy (as can be seen in **Figure 4-13C** and **4-13D**). Large increases in maximum allowable N_{ROI} while maintaining an average measurement accuracy of 90% can be achieved with very little increase in object volume. This can be seen in **Figure 4-5B**, where for a large number of voxels within an ROI, the required number of voxels in a spherical object becomes similar for the SR and LR approaches. When SNR is lowered through v_{acq} volume reduction (**Figure 4-5C**) and a large number of voxels are used to attain measurement precision (**Figure 4-5A**), the impact of PSF smearing to achieve a desired average measurement accuracy is dramatically reduced for the LR approach (**Figure 4-5B**), facilitating its advantage with respect to image analysis.

The twisted projection imaging (TPI) technique was initially presented for the reduction of SNR sampling inefficiency inherent to standard projection imaging (30). However, it was shown in Chapter 3 that standard projection imaging with its great oversampling at the centre of k-space and reduction of low-frequency noise yields much smaller correlation volumes. As a result much fewer voxels are required within an ROI to attain the desired measurement confidence, as is apparent in **Figures 4-5A** and **4-6A**. For an SNR 1/4 and 1/8th the desired MNR the required ROI volumes must contain ~70% and ~80% more voxels for the LR approach than the SP approach. As such, the advantage of readout evolution altered k-space acquisition (of which TPI is a member) does not lie in its characteristics with respect to image noise (as originally presented in (30)), but in 'bending time' across k-space (**Figure 4-13**) to mitigate T_2 decay and facilitate long T_{RO} with reduced v_{acq} volume.

The optimization of Nagel (36) concerns optimization for the magnitude at the centre of the PSF while maintaining constant noise variance. Although this optimization for the 'tiny' image intensity present in very small (point-source) objects may be of minimal direct relevance to signal quantification, the optimization of Nagel produced a similar result to that presented in the current paper. In **Figure 4-11F** it is obvious that the LR approach has the greatest value at the centre of its PSF, and in **Figure 4-4** it can be seen that for very small objects the image intensity produced by the LR approach is the greatest. However, although the optimization of Nagel also suggests a radial evolution altered approach with long T_{RO} as an ideal sodium imaging methodology, the optimization of Nagel fails to identify that the advantage of long T_{RO} for quantification is only attained for 'low SNR' (small acquisition voxel) implementations. The optimization of Nagel also fails to identify the reduction in the value of p as critical for long T_{RO} implementation, as highlighted in **Figure 4-9** and **Figure 4-13**.

To the author's knowledge, optimization for the ideal SNR with respect to image quantification has not been considered in the literature (at least not for sodium imaging). It is suggested the optimum implementation SNR for the analysis of anisotropic objects is 1/4 – 1/8 the desired MNR (i.e. for a desired precision of $\pm 2.5\%$ the required MNR is 80, and the optimal SNR between 10 – 20). Another large advantage of 'low SNR' (i.e. small voxel volume) implementation for sodium imaging of the human head is the containment of the 3x concentrated CSF within its bounds. Spatial PSF smearing for sodium nuclei in CSF directly correlates with voxel volume. Enhanced CSF containment within its bounds (at an optimal SNR implementation) is another substantial advantage of the LR approach over the other two. This is demonstrated in Figures **4-11A** – **4-11E**, and is easily apparent in the human brain images of **Figure 4-12**.

It is reasonable to assume that when brain lesions are to be evaluated the majority of these 'objects' will not have a spherical shape. For this reason a 'mildly' anisotropic object geometry (1 x 1 x 2) was chosen for the comparisons in **Figures 4-6** – **4-10**. Although correlation volumes are slightly decreased with object anisotropy (Chapter 3, as reflected in **Figure 4-6A** vs. **4-5A**), the effect of PSF smearing in objects containing only a few voxels is greatly 'intensified' (bottoms of **Figure 4-6B** vs. **4-5B**). Convolution of the smeared PSF with voxels spaced on average further from the centre of the object produces a smaller sum at the centre of the object from values on average further into the periphery of the smeared PSF. As a result, the minimum required object volumes are greatly increased when no ROI averaging is to be done (i.e. SNR=MNR – right sides of **Figures 4-6E** vs. **4-5E**). However, the effect of object anisotropy on average measurement accuracy is not as great when ROI volumes are large (tops of **Figure 4-6B** vs. **4-5B**, and right sides of **Figure 4-6E** vs. **4-5E**). For the assessment of anisotropic objects the use of smaller voxel volumes (and hence lower SNR) is of increased importance to the spatial reduction of PSF smearing. For anisotropic objects the LR approach is clearly the best approach. If object anisotropy is increased from that of (1 x 1 x 2) the value of the LR approach

becomes greater, and the use of small acquisition voxel volumes even more important.

For the optimization of T_{RO} in this chapter the T_2 relaxation in CSF was compensated to produce a Kaiser modulation transfer function. This was done because for long T_{RO} increased T_2 roll-off across k-space 'intensifies' filtering. Relaxation compensation facilitates constant filtering of CSF signal across T_{RO} for rigorous comparison between long and short readout methodologies. However, the effect of CSF T_2 compensation on minimum object volume optimization is actually quite small. Without relaxation compensation for long T_{RO} the Kaiser filter in CSF is effectively increased from $\beta = 3.0$ to $\beta = 3.5$. If the LR approach was designed for $\beta = 3.5$ (i.e. essentially equivalent to design for $\beta = 3.0$ with no relaxation compensation) the effect on optimization and minimum object volumes would be mostly negligible (**Figure 4-10**). While CSF T_2 relaxation compensation was used in this chapter for T_{RO} comparison it is not required for 'ideal' radial k-space acquisition implementation. If CSF was absent from the human head, compensation of brain tissue relaxation with sampling density may be possible (compensation of brain tissue relaxation in the presence of CSF would dramatically over-compensate the CSF signal, producing an excessive ringing problem). In this case, the minimum required object volumes for analysis could be further reduced from that of the LR approach (data not shown). It is hypothesized that this k-space acquisition approach could have value for CSF-nulled human brain sodium imaging applications (Chapter 7 - (44)).

A $\beta = 3$ Kaiser transfer function in CSF was selected for comparison between radial k-space acquisition approaches. However, as increased k-space filtering is of minor consequence to minimum required object volumes (**Figure 4-10**), there is little reason not to use an increased k-space filter of $\beta = 4$ to further reduce CSF ringing artifact (**Figure 4-1**). The $\beta = 4$ Kaiser window approaches the limit of a sampling density shape that can be implemented without critically under-sampling the edges of the sampled k-space extent (Chapter 2) (60). A previous

paper implemented a 'Hamming-like' k-space filter to demonstrate the SNR advantage of filtering by sampling density design (Chapter 2) (60). This filter facilitates even greater side-lobe reduction than a β = 4 Kaiser window. Although the 'Hamming-like' filter is not ideal (in terms of maximizing signal energy around the centre of k-space (141)) the minimum object volume required for analysis with this filter is suggested to be only marginally increased from the β = 4 Kaiser window in **Figure 4-10**. An additional 'advantage' of increased k-space filtering (besides PSF side-lobe reduction) is the improvement of image appearance. Slight reduction in volume of the main PSF lobe with increased filtering (which produces the small negative effect on quantification) is associated with a marginally narrower main lobe width at half max, slightly improving distinction of objects in a resolution phantom (**Figure 4-6**).

Other radial k-space acquisition papers have considered different sampling densities and k-space weightings. Combined with his implementation of short T_{RO} similar to the SR approach of this paper, Boada (29) effectively implemented a sampling density shape similar to the β = 2.0 Kaiser window (**Figure 4-1**). Although the advantage of long T_{RO} was shown for a β = 3.0 Kaiser window in this chapter, the same long T_{RO} value exists for the 'under-filtering' β = 2.0 Kaiser window. Neilles-Vallespin (5) in her implementation of standard radial imaging with T_{RO} similar to the SP approach of this paper, implemented a filtering shape with post-acquisition weighting having a flat portion to a radial distance of 25% k_{max} and a $1/r^2$ dependence following that. This filter which deviates from the ideal Kaiser shape was selected with respect to the minimization of error when less projections than that required by Nyquist were implemented in accordance with (262).

The 'accuracy' considered in this chapter concerns *average* image intensity deviation from full value in an ROI with respect to PSF smearing. A more stringent definition of accuracy may require all image voxels within the ROI to be a given percent of full value. For such a definition the minimum required object

volumes for analysis will be expanded, however, the LR approach remains the most beneficial at similar implementation SNR. If ROIs are drawn to include the full object volume, the average intensity in the measurement for each approach will be considerably modulated by object volume for objects less than ~ 10 cm^3 – 20 cm^3 (at which point average measurement accuracy approaches 70% of full value). If ROIs that include the full object volume are used, image intensity will approach full value in a similar manner for the SR and LR approaches (with LR being slightly more beneficial); both will be considerably better than the SP approach.

Obviously, lesions within the human brain are not stand-alone objects. However, when lesion relaxation characteristics remain unchanged from the surrounding cellular brain tissue, a lesion can be considered as a 3D step function 'on top of' a uniform background, with the average measurement accuracy with respect to PSF smearing being a percent of the signal intensity increase. If relaxation in the lesion is known to be considerably longer than that of brain tissue (i.e. a very old stroke), requirements on minimum ROI volumes for accuracy and precision can be relaxed. In this case the advantage of the LR approach will be directly related to voxel volume. However, if relaxation in a lesion is unknown or possibly even more rapid than in normal brain tissue (as may be the case in hyper-acute stroke (65)), minimum object volumes may be required to avoid errors related to PSF smearing and noise. It should be noted that the measurement accuracy and precision of this chapter does not concern signal intensity heterogeneity that may exist within a real lesion.

The optimization for object analysis of this chapter is concerned with how one 'draws' an ROI within a small object, and the desire for either confidence or accuracy will offset each other. For any small object an increased ROI volume within the object will increase precision, while a decreased ROI volume will increase accuracy. If an application involves the statistically significant measure of small relative increases, a sufficiently tight confidence interval is required; if

the application involves a measure of large relative increases across a range of lesion volumes, high accuracy may be desired to minimize object volume dependent 'contrast'. If both precision and accuracy are desired, small objects may have to be discarded. It should be noted that if calibration phantoms with relaxation characteristics similar to that of brain tissue are to be used for absolute concentration quantification (6), they should be sufficiently large and evaluated in a sufficient manner so as to avoid an image intensity dependence on their volume. The result of PSF smearing in small calibration phantoms could yield globally elevated concentration measurements in the brain.

Finally, concern must be given to the fact that the minimum required object volume for 90% accuracy and a 2.5% confidence interval, as presented in **Figure 4-6B**, is very large at ~ 15 cm^3 for the optimal LR approach. It should be remembered, however, that object volumes of **Figures 4-5E** & **4-5F – 4-10E** & **4-10F** will be scaled by the v_{acq} – SNR relationship. The v_{acq} – SNR relationship of these figures is based on a 10 minute scan. The required object volumes can be reduced by 30% if the scan length is doubled to 20 minutes. The v_{acq} – SNR relationship used is also based on an ultra-short TE (0.19 ms) 'non-relaxation weighted' sequence. If a steady-state sequence similar to that of chapter 5 (42) is used, required object volumes can be reduced by an additional ~ 38%. The value of 'long' scan length and NMR sequence optimization for SNR are readily apparent if one desires high measurement accuracy and precision for signal analysis. In addition, further static magnetic field increase and hardware optimization may also aid analysis of small objects.

4.6. Conclusion

When sodium signal intensity in an object having T_2 relaxation characteristics like that of human cellular brain tissue is to be quantified with a given precision (with respect to image noise) and a given accuracy (with respect to PSF smearing) the optimum radial k-space acquisition approach is suggested to be one in which radial projection evolution is altered to produce a sampling density designed k-space filter with a small value of *p* and a long readout duration. This approach facilitates both the minimum object volumes required for analysis and a greatly enhanced containment of CSF within its bounds. A sufficiently high 'degree' of k-space filtering to minimize CSF related ringing artifact is suggested, having marginal impact on quantification capability. It is also suggested that small acquisition voxels be selected for radial sodium imaging such that SNR is roughly 1/8 – 1/4 the desired measurement-to-noise ratio required for analysis precision.

Chapter 5

Sodium Imaging Optimization Under Specific Absorption Rate Constraint

A version of this thesis has been published
(R.S. Stobbe, C. Beaulieu, Magn Reson Med, 59, 345-355, 2008)

5.1. Introduction

Since the first in-vivo sodium images were created in 1983 (265) continued effort has been applied to bring this tool with burgeoning potential into the main-stream of the MRI community. Many human disorders involve disrupted or altered regulation of sodium concentrations and several studies have been conducted in patient populations to assess the value of sodium imaging and its potential to elucidate and diagnose pathology. These include studies of: acute stroke and the time-course of tissue sodium increase following ischemic onset (12,66,110); the time-course of tissue sodium following myocardial infarction (15,16,266); tissue sodium in relation to tumour grade (5,6); renal sodium concentrations (267,268); proteoglycan loss in relation to sodium content in cartilage (19,269); exercise, and sodium channelopathies in muscle (17,270).

Despite these promising clinical applications, and potentially others, the proliferation of sodium imaging has been hampered by technical limitations. Apart from the multinuclear capability requirement, the most significant drawback of sodium MRI is the low concentration in-vivo (approximately 50 mM in brain tissue). When NMR sensitivity is taken into account, tissue signal-to-noise ratio (SNR) for an ideal pulse-acquire acquisition would be ~ 0.02% that of proton in-vivo. Low tissue SNR must be offset by low resolution imaging. Although the goal of sodium imaging is to provide physiological data otherwise not attainable with proton imaging, sufficient image resolution is required to extend its utility beyond large pathology and to minimize partial volume effects with neighbouring tissues that have very different sodium concentrations. Clearly, there are two approaches, beyond hardware optimization, to maximize image

SNR (and hence image resolution): static magnetic field increase, and pulse sequence optimization.

The sodium nuclear ensemble (spin 3/2) experiences very rapid biexponential transverse relaxation in dense macro-molecular environments like those that exist in cellular tissue (with a ratio of 0.6 fast and 0.4 slow). In the human brain a fast component (T_{2f}) of approximately 1.7 ms (4T and 4.7T) (25,45), and a slow component of approximately 17 ms (T_{2s}* at 4T) (25) have been fit from regression for a one compartment relaxation model of brain tissue in subcortical gray matter. The sodium nuclear ensemble also experiences rapid (biexponential with a ratio of 0.2 fast and 0.8 slow) longitudinal relaxation due to the dense macro-molecular environments. For a one compartment model of human brain tissue, longitudinal relaxation has been measured using a monoexponential fit (often used since biexponential T_1 is difficult to separate, especially when compared to the biexponential T_2) as 36 ms (4.7T) (45).

An important aspect of pulse sequence optimization for SNR is to make TE as short as possible minimizing T_2* signal loss (which is essentially T_2 loss, as this loss is primarily dependent on T_{2fast}). This can be accomplished by sampling k-space with a 3D radial acquisition approach, where the centre of k-space is acquired following a hard, non-selective excitation pulse. With this acquisition approach, TE directly depends on the length of the RF pulse. However, most times this acquisition approach has been implemented the concern has been tissue sodium concentration (TSC) measurement, which requires relaxation weighting to be minimized; to minimize relaxation weighting repetition times must be sufficiently long to avoid T_1 saturation (6,12,66,110,270). Another method of sodium image optimization for SNR involves the implementation of a spoiled steady-state pulse sequence with shortened TR values that facilitate increased averaging within a constant scan duration. However, most times spoiled steady-state RF pulse sequences have been implemented, 3D gradient-echo k-space

acquisition has also been used which generates less than ideal echo times (15,16,19,266-269).

This dichotomy that has persisted in sodium imaging (i.e. 'fully relaxed' TSC sequences with radial acquisition vs. steady-state sequences with gradient echo acquisition) was recently transcended with the implementation of a steady-state sequence employing radial acquisition (5,18) which benefits (with respect to SNR) from both short TE and short TR. This approach was implemented at 1.5T. However, there seems to be a considerable advantage associated with the use of higher magnetic field strengths for sodium MRI, and substantial work has been done at 3T (12,30,64,267), 4T (19,25,39,269), 4.7T (44), and even higher fields (271,272).

Especially at high fields, sequence design must take RF power deposition or the specific absorption rate (SAR) into account (maximum 3 Watts/kg averaged over 10 minutes for the human head) (273). RF pulse length, TR and flip angle cannot necessarily be adjusted in isolation from one another. Decreased TR may require an increase in RF pulse length (and hence TE), and/or a reduction in flip angle to satisfy SAR regulations (Eq. [5-1]) (57).

$$\mathrm{SAR} \propto \frac{\mathrm{B}_0^2 \cdot \theta^2}{\mathrm{TR} \cdot \tau_{\mathrm{RF}}}. \qquad [5\text{-}1]$$

At 1.5T a spoiled steady-state implementation of ultra-short TE imaging using radial acquisition with 300 μs RF pulses and repetition times as short as 4 ms was possible (5). However, at 4.7T this is not the case. SAR limitations necessitate either increased TR or pulse length (and by corollary, TE), or reduced flip angle. In our study, quantum mechanical simulations were performed to assess transverse magnetization, as well as relaxation weighting and relative SNR, for various RF pulse parameter sets (which include RF pulse length, flip angle, and TR) from steady-state to 'fully relaxed' sequences, given SAR constraints. The

RF pulse parameter analysis under SAR constraint presented is unique to sodium imaging as the T_2 decay of sodium in-vivo is extremely rapid and lengthened TE as a result of increased RF pulse length reduces the available signal at the centre of k-space.

The purpose of this work was to assess the SNR value of a spoiled steady-state sequence implemented with radial k-space acquisition for sodium imaging of the human brain at 4.7T given SAR limitations. This sequence (implemented with an advantageous set of RF pulse parameters gathered from simulation) is referred to as Na-PASS, or projection acquisition in the steady-state for sodium imaging. It was compared to a commonly implemented TSC imaging approach, which also uses radial k-space acquisition along with 90^o flip angles and longer TR values that facilitate ultra short echo times (to minimize relaxation weighting) (6,12,66,110,270). A substantial SNR advantage associated with the Na-PASS sequence was confirmed with in-vivo experiments of the human brain.

5.2. Methods

5.2.1. Simulation

The quantum mechanical (spin 3/2) simulation performed was based on the sets of differential equations that describe the evolution of the density operator under the quadrupolar Hamiltonian (71,145,146), and facilitated a consideration of relaxation during each RF pulse. The sequence simulated consisted of a rectangular (non-selective) RF pulse followed by a 128 μs delay (to account for system delays before acquisition), a 2 ms gradient spoiling pulse, and an appropriate delay yielding TR. Gradient spoiling was accomplished by averaging the total sequence spin-response for a set of appropriate gradient frequency shifts (in the location of the gradient pulse) which produced transverse magnetization dephasing. The simulation tracked the evolution of the density operator over 9 consecutive RF pulses (and subsequent delays). It was determined empirically that a steady-state was obtained with 9 consecutive sequence 'play-outs.' A final steady-state transverse magnetization value (relative to the total available magnetization, M_o), acquired following the system delay at what would be the centre of k-space in the acquisition scheme (or at TE), was recorded from simulation and used for subsequent relaxation weighting and relative SNR calculations.

A one compartment relaxation model of subcortical human brain tissue at 4.7T with spectral density parameters $J_0(0)$ = 558 Hz, $J_1(\omega_o)$ = 32 Hz, and $J_2(2\omega_o)$ = 12 Hz was used for this simulation. This model yields a T_{2fast} of 1.7 ms, and a T_{2slow} of 23 ms (**Figure 5-1a**), as well as a T_{1fast} of 16 ms and a T_{1slow} of 42 ms (**Figure 5-1b**). $J_1(\omega_o)$ and $J_2(2\omega_o)$ were set to generate a T_{2slow} relaxation parameter similar to the T_{2slow}* value measured in-vivo (25) (but somewhat longer as T_{2slow} will be longer than T_{2slow}*, and this T_{2slow}* parameter was measured at 4T) and a best fit to the monoexponential T_1 simplification measured in-vivo (45). No residual quadrupole interaction was assumed. It should be noted that the fast component of transverse relaxation and the monoexponential longitudinal relaxation fit are of

primary importance to the relative SNR analysis presented in this paper, and altering the distribution of $J_1(\omega_o)$ and $J_2(2\omega_o)$ has marginal effect on relative SNR.

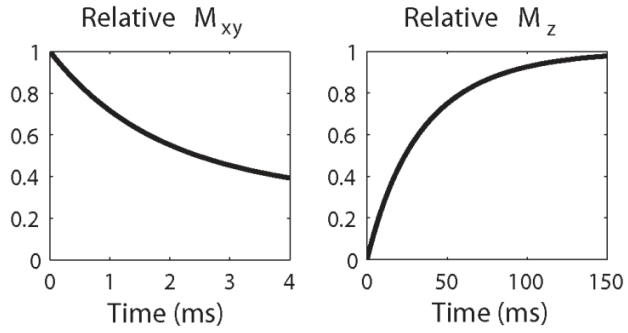

Figure 5-1: Sodium magnetization relaxation curves plotted from the one compartment relaxation model of subcortical gray matter in the human brain used for simulation. Relaxation curves are plotted over the relevant periods of interest.

For each simulation experiment presented, TR was varied from 10 ms to 150 ms, and the RF pulse length (τ_{RF}) varied from 0.1 ms to 4.0 ms. For each TR and RF pulse length pair, the flip angle (θ) required to generate a constant SAR was calculated from Eq. [5-2]. In this equation θ_o, τ_{RFo}, and TR_o are a reference set of RF pulse parameters known to dissipate the desired RF power for the constant SAR experiment. A constant SAR of approximately 1.5 W/kg dissipated over the human head at 4.7T was chosen for simulation and experiment. This SAR value is relatively conservative for short imaging protocols. However, this value was chosen as sodium imaging protocols typically involve lengthier imaging durations. In this study the imaging duration was 20 minutes (i.e. two 10 minute scans).

$$\theta = \theta_0 \sqrt{\frac{\tau_{\mathrm{RF}} \cdot \mathrm{TR}}{\tau_{\mathrm{RF}_0} \cdot \mathrm{TR}_0}} \qquad [5\text{-}2]$$

Relaxation weighting (RW) was calculated as the percent loss in transverse magnetization at each acquisition as a result of relaxation (Eq. [5-3]). Without the effects of relaxation (i.e. TR is long enough for full T_1 relaxation, and the RF pulse length and TE are infinitesimally short) $M_0 sin(\theta)$ yields the ideal transverse magnetization available. M_{xy} in this equation is the transverse magnetization (relative to M_0) recorded at TE from simulation for each RF pulse parameter set.

$$\mathrm{RW} = \left[1 - \frac{\mathrm{M_{xy}}}{\sin(\theta)}\right] \cdot 100\% \qquad [5\text{-}3]$$

The percent loss of transverse magnetization as a direct consequence of SAR was determined by considering a case where SAR could be ignored and the RF pulse length made short enough (i.e. the RF power dramatically increased) that relaxation had essentially no effect during the RF pulse. For each flip-angle, RF pulse length, and TR combination calculated from Eq. [5-2], the transverse magnetization was re-simulated with the RF pulse length set to 100 ns. 'SAR loss' is given in this paper as the percent signal loss when the SAR constrained case is compared to the non-constrained case.

Relative SNR (rSNR, as the percent difference from the reference implementation) was calculated from the magnitude of the simulated transverse magnetization at TE (or what would be the centre of k-space) and the repetition time (which takes into account the noise variance decrease associated with an increased number of acquisitions during a given scan time) (Eq. [5-4]).

$$\mathrm{rSNR} = \left[\frac{\mathrm{M_{xy}}}{\mathrm{M_{xy_0}}}\sqrt{\frac{\mathrm{TR_0}}{\mathrm{TR}}}\right] \cdot 100\% \qquad [5\text{-}4]$$

This calculation assumes that k-space acquisition (i.e. readout duration, filter bandwidth and resolution) remains constant for each set of RF pulse parameters implemented. In this equation M_{xy0} is the simulated transverse magnetization

generated from the reference RF pulse parameters θ_o, τ_{RFo}, and TR_0 (with actual values given in the next paragraph).

A sodium imaging pulse sequence with RF pulse parameters of flip angle = 90^o and TR = 150 ms, was used as the reference for this paper (referred to as the TSC imaging approach). A 90^o flip angle was implemented for this reference as it is common to previous TSC sodium imaging implementations (6,12,270,271), and the 150 ms TR was implemented to minimize T_1 saturation. With these parameters an RF pulse length of 0.45 ms dissipated an SAR approximately of 1.5 W/kg over the human head at 4.7T (measured using the system RF power monitor and the assumption that human head is ~ 3 kg). Very short echo times are required for TSC imaging (to minimize relaxation weighting), and with an RF pulse length of 0.45 ms a TE of 0.353 ms was achieved.

Since many other groups have human MRI scanners at field strengths other than 4.7T, simulations were carried out to consider the effects of SAR constraints at 3T, 7T, and 9.4T. From Eq. [5-1] it can be seen that SAR varies according to B_o^2. To simulate the tightened SAR constraint on the sequence parameters at higher fields, RF pulse parameter sets of TR, RF pulse length, and flip angle were calculated according to a constant SAR of approximately 1.5 W/kg dissipated over the human head at 4.7T adjusted by the relative difference in magnetic field squared. For simulation at each magnetic field strength the 4.7T brain tissue relaxation model (above) was used as an approximation. Signal loss at TE, which is dominated by the spectral density at 0 Hz, is expected to be very similar at all magnetic field strengths (209). Small differences in T_1 relaxation times at each field strength are expected (i.e. the higher field strengths are expected to exhibit slightly longer T_1 values (209)). These differences in T_1 relaxation will slightly over-estimate the SNR advantage of the spoiled steady-state sodium imaging sequence at higher magnetic field strengths (7T and 9.4T), and under-estimate the steady-state advantage at lower field strengths (3T). Finally, the optimal flip

angles for greatest signal at any given TR were presented from analysis of the simulated transverse magnetization data sets.

5.2.2. Experiment

The spoiled steady-state sequence implemented with 3D radial k-space acquisition consisted of a non-selective rectangular RF pulse followed by a 128 μs system delay, 3D centre-out twisted projection acquisition (30,56), and gradient spoiling. The RF pulse parameter optimization presented in this paper is independent of the radial trajectory from the centre of k-space (i.e. straight or twisting); however, prudent trajectory selection has SNR merit of its own. 3D twisted projection acquisition is a particularly advantageous centre-out trajectory as noise variance increases related to sampling density compensation of non-uniformly sampled k-space are minimized (55).

In-vivo images of the head were acquired on a 4.7T Varian Inova scanner (Palo Alto, CA) from four healthy volunteers (ages 24 to 27, who gave informed consent to be part of this study) using an in-house designed and manufactured single-tuned RF birdcage coil. This sodium imaging project at 4.7T was approved by the Heath Research Ethics Board at the University of Alberta. Two RF pulse sequence imaging experiments were conducted with each volunteer. Each had an equivalent SAR (based on the physical relationship described by Eq. [5-1]) of approximately 1.5 W/kg (again measured using the system RF power monitor, and the assumption that human head is ~ 3 kg). and a scan duration of 10 minutes for a total experiment length of 20 minutes.

SNR was calculated as the average signal measured in a brain tissue region of interest (ROI) divided by the standard deviation of noise measured over a large volume outside the head. SNR in ‘deep gray matter’ was measured in an ROI drawn to contain primarily the caudate, the putamen, the globus palidus and the

thalamus (as best identified on each sodium image). SNR in 'white matter' was measured in an ROI drawn to contain primarily the centrum semiovale. Care was taken to avoid the inclusion of obvious CSF in each ROI.

For each imaging experiment k-space acquisition was the same and consisted of 3996 projections fully covering 3D k-space (volume 0.019 $1/mm^3$) with a twist of 0.25 and readout length of 19.4 ms. The transverse magnetization was subsequently rewound and spoiled with a gradient pulse (2 ms) consisting of the negative of the integrated area under the readout gradient summed with a constant value.

The first pulse sequence imaging experiment consisted of a TR of 150 ms, a flip angle of 90^o and an RF pulse length of 0.45 ms (TE = 0.353 ms). Only 1 average was acquired yielding a scan duration of 10 minutes. Based on the results of simulation, the second experiment consisted of a TR of 25 ms, a flip angle of 55^o, and an RF pulse length of 1 ms (TE = 0.628 ms). In this experiment 6 averages also yielded a scan duration of 10 minutes.

5.3. Results

Figure 5-2a displays the flip angle required for each RF pulse length, TR combination in order to maintain a constant SAR (in this case approximately 1.5 W/kg @ 4.7T). These flip angle values were calculated directly from Eq. [5-2] and the maximum flip angle simulated was 90^{o}. The spoiled steady-state spin response was simulated for each combination to determine the value of transverse magnetization at TE. These values are displayed in **Figure 5-2b** as a percent of total available magnetization.

Relaxation weighting is displayed in **Figure 5-2c**, and is a consequence of both longitudinal and transverse relaxation. Changes along the horizontal axis are the result of longitudinal relaxation. Changes along the vertical axis are the result of both transverse relaxation and longitudinal relaxation. Increased RF pulse lengths (and TE) generate increased T_2 losses, while increased flip angles (**Figure 5-2a**) generate greater T_1 saturation. For the TSC reference RF pulse parameter implementation ('O' on the plot, TE = 0.353 ms) the relaxation weighting is 14%. At a TR of 150 ms this relaxation weighting is primarily caused by T_2 decay. For the Na-PASS RF pulse parameter implementation ('X' on the plot, TE = 0.628 ms) the relaxation weighting is 41%, the result of T_2 decay over TE and T_1 saturation in roughly equal proportion.

Signal loss (or transverse magnetization loss at TE) as a direct consequence of the SAR constraint is given in **Figure 5-2d** as 'SAR loss'. This relative loss for each RF pulse parameter set in **Figure 5-2d** is a result of the 'non infinitesimally short' RF pulse length included in each set, but cannot be completely explained as 'increased T_2 loss during longer TE', especially for longer RF pulses (see discussion). For the Na-PASS RF pulse parameter implementation ('X' on the plot, TE = 0.628 ms) an 'SAR loss' of 15.7% is expected from a simple 'T_2 loss during TE' calculation when compared to the unconstrained case (TE = 0.128

ms); the simulated loss is only 14.7%. For a pulse sequence implemented with a 3 ms RF pulse (TE = 1.628 ms), an 'SAR loss' of 40% is expected from a 'T_2 loss during TE' calculation, however, the 'SAR loss' presented in this figure from simulation is only ~25%.

Relative SNR for each SAR equivalent RF pulse parameter set of **Figure 5-2a** is shown in **Figure 5-2e**, as calculated from Eq. [5-4] and the transverse magnetization at TE acquired from quantum mechanical simulation (**Figure 5-2b)**. It is readily apparent that an SNR advantage is associated with the implementation of shorter TR values. This is the result of substantially reduced noise variance associated with an increased number of acquisitions in a given scan time. As can be seen, RF pulse lengths on the order of 1 ms (or more) are required to implement short TR values with an appropriate flip angle under SAR constraint. Although longer RF pulse lengths increase T_2 signal loss, a 37% SNR increase is suggested from simulation when the Na-PASS approach to sodium imaging is implemented instead of the TSC reference approach.

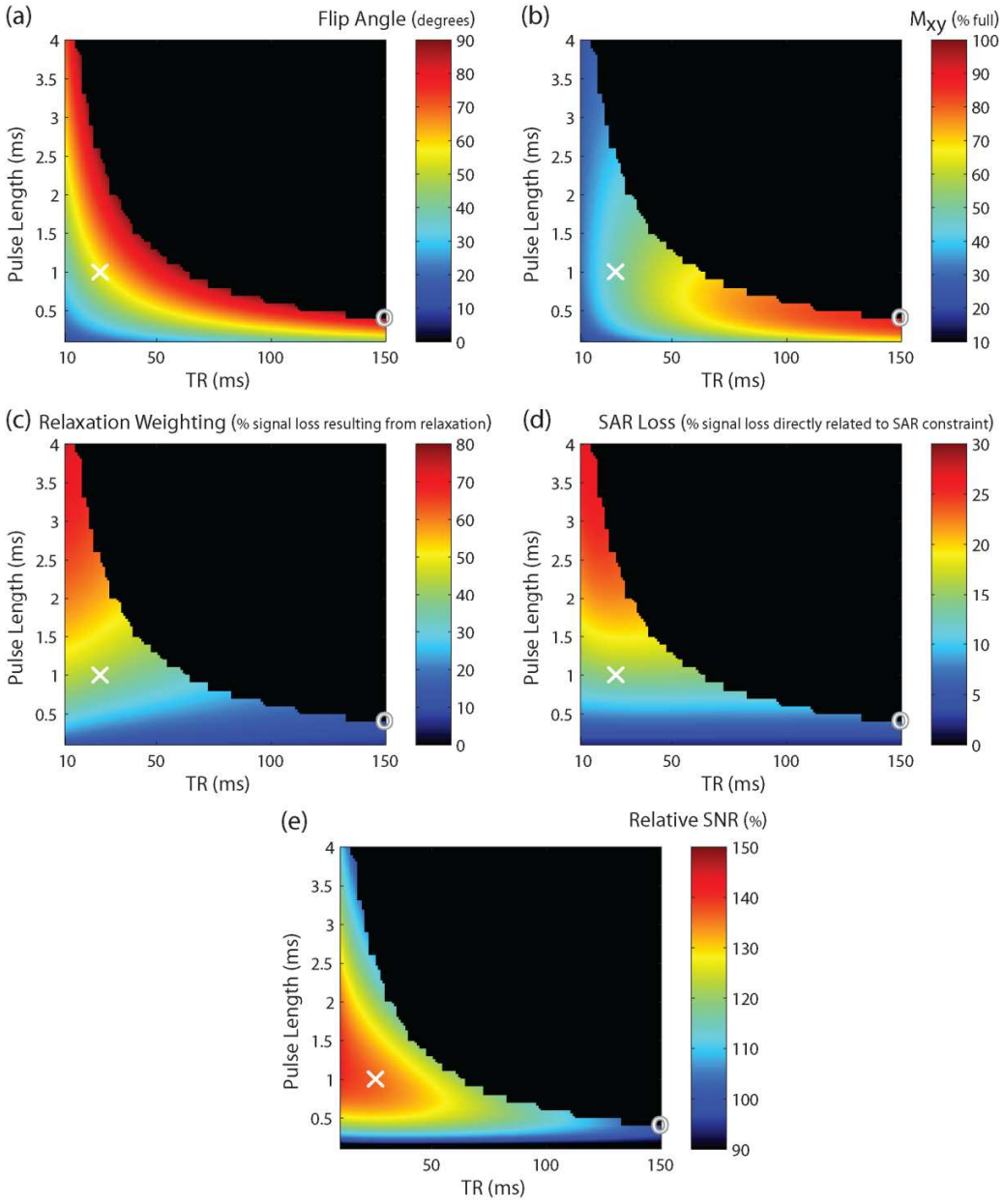

Figure 5-2: Simulated steady-state sodium sequence analysis under SAR constraints (approximately 1.5 W/kg @ 4.7 Tesla). In **(a)** the flip angles calculated from **Eq. [5-2]** are given for each RF pulse length and TR pair. Each flip angle, pulse length, TR combination yields the equivalent SAR above. The maximum flip angle was chosen to be 90°, and the top right dark region of each chart which prescribes flip angles greater than 90° was not simulated. In **(b)** the transverse magnetization acquired from simulation is presented for each RF pulse length, TR and flip angle combination of **(a)**. Transverse magnetization is given as a percent of the fully relaxed longitudinal magnetization. Image **(c)** displays relaxation weighting (calculated from the simulated transverse magnetization) given as the percent of signal lost as a result of relaxation. Image **(d)** displays signal loss as a direct result of the SAR constraint. This loss (for each RF pulse parameter combination) is given relative to the case where SAR can be ignored and the

RF pulse length made short enough that relaxation has no effect over the pulse. In **(e)** the SNR advantage (calculated from the simulated transverse magnetization) of a spoiled steady-state RF pulse sequence is shown. This SNR advantage exists in spite of longer RF pulses required to realize this benefit under SAR constraint. The white 'X' identifies the location of the RF pulse parameters used to generate the human brain images in **Figure 5-3b** and **Figure 5-4** (Na-PASS approach). The gray 'O' identifies the location of the RF pulse parameters used to generate the human brain images in **Figure 5-3a** (TSC approach).

Representative images from one volunteer are shown in **Figure 5-3**. Each image was acquired with an equivalent scan duration of 10 minutes and an equivalent SAR of approximately 1.5 W/kg at 4.7T. Image **(b)**, acquired using the Na-PASS spoiled steady-state approach, has 39% greater SNR, measured in deep gray matter, than image **(a),** acquired with the TSC imaging approach. In **(c),** the measured relative SNR advantage of the spoiled steady-state approach is given for each volunteer. Measured relative increases are in good agreement with the value predicted from simulation for all four volunteers. Simulation predicts a 37% SNR increase, while an average SNR increase of 38.5% +/- 1.3% was measured in deep gray matter and an average SNR increase of 38.3% +/- 2.8% was measured in white matter for the four volunteers.

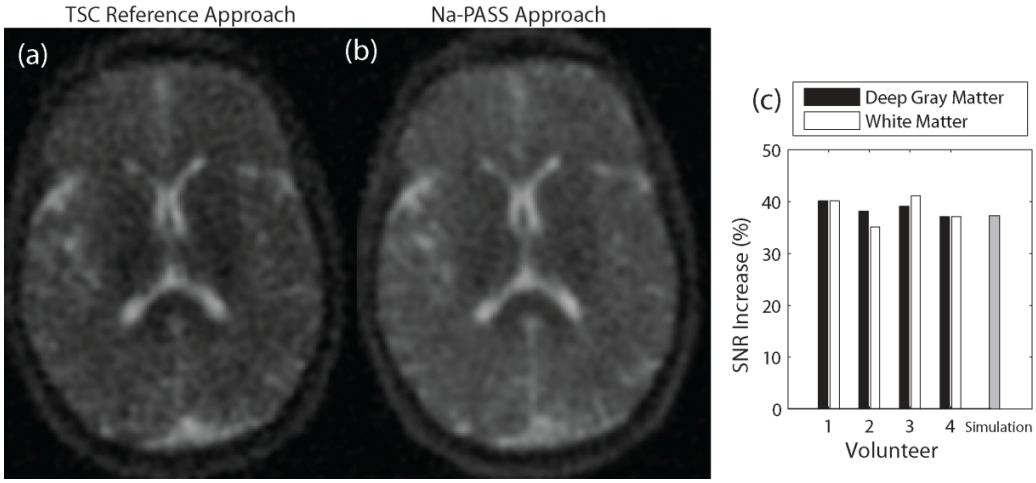

Figure 5-3: The SNR advantage of a spoiled steady-state approach to sodium imaging with radial acquisition implemented under SAR constraints (approximately 1.5 W/kg at 4.7 Tesla) demonstrated in a healthy volunteer. For each image, k-space was sampled with the identical twisted projection acquisition scheme and each had a scan duration of 10 minutes. The pulse sequence used to generate image **(a)** had a TR of 150 ms, a flip angle of 90^{o}, and an RF pulse length of 0.45 ms (TE = 0.353 ms). One average was acquired to generate this image. The RF pulse sequence used to generate image **(b)** had a TR of 25 ms, a flip angle of 55^{o}, and a pulse length of 1 ms (TE = 0.628 ms). Six averages were acquired to generate this image. In **(c)** the SNR advantage of the Na-PASS pulse sequence **(b)** over the reference TSC pulse sequence **(a)** is shown for each of four volunteers, which agrees reasonably well with simulation.

Figure 5-4 displays slices of a 3D image acquired from a healthy volunteer covering the extent of the brain. The nominal voxel size for this image is 52.8 mm^3 (given as 1 / k-space volume). Average SNR in deep gray matter is 14.1 +/- 1.5 and 14.3 +/- 1.3 in white matter over all four volunteers.

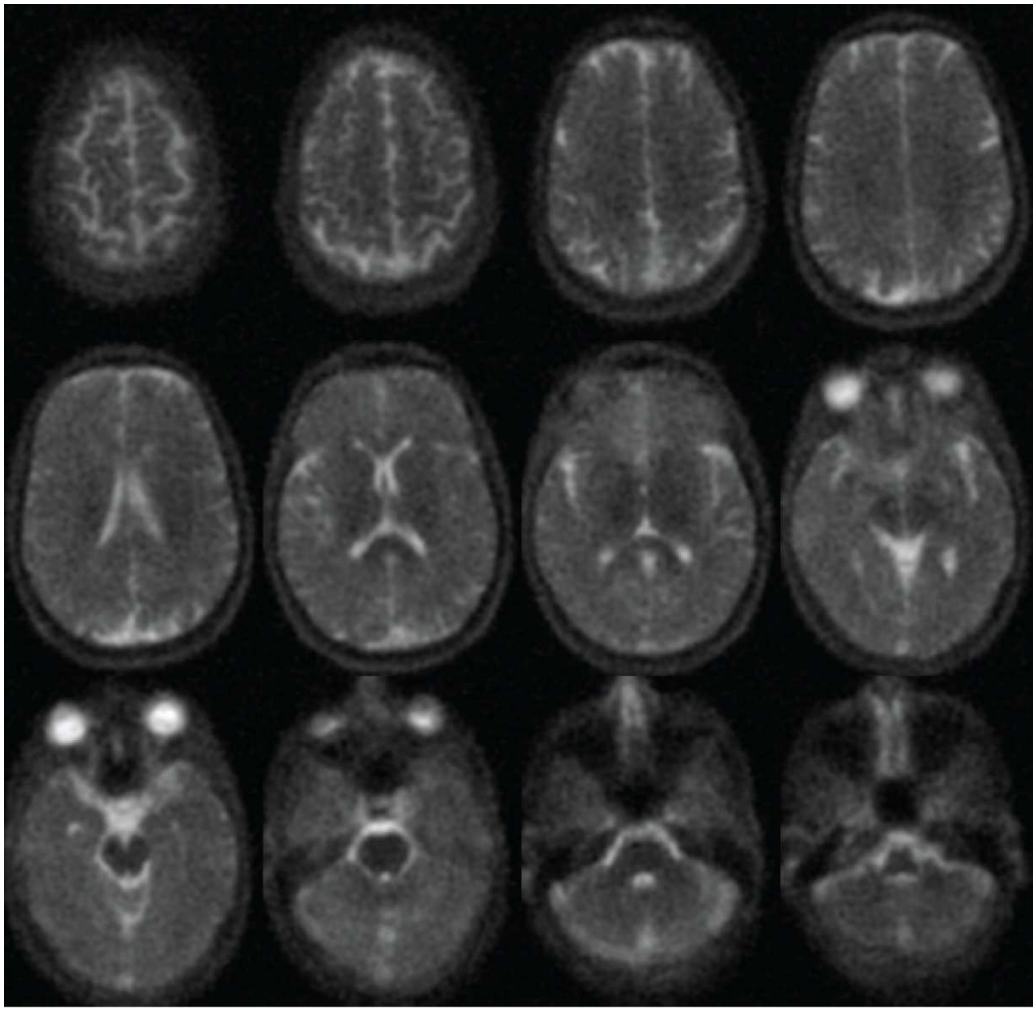

Figure 5-4: A representative sodium image acquired from a healthy volunteer at 4.7 Tesla using the Na-PASS pulse sequence (parameters the same as **Figure 5-3b**) and 3D twisted projection acquisition. The nominal voxel size (given as 1 / k-space volume sampled) is 52.8 mm^3. The in-plane resolution (measured as holes distinguishable in a saline resolution phantom) is 2.5 mm. The out-of-plane resolution is (by design) twice the in-plane resolution. The SNR measured in white matter is 15, the SNR in deep gray matter is also 15. This image was acquired in 10 minutes.

5.4. Discussion and Conclusions

In this paper optimization of the sodium imaging RF pulse parameters for SNR was considered under SAR constraint. It was suggested using quantum mechanical simulation (and a one compartment relaxation model of the human brain) that a spoiled steady-state approach to sodium imaging with radial acquisition (Na-PASS) generates a substantial SNR advantage when compared to the reference TSC sodium imaging approach implemented with ultra-short TE, even when the SAR constraint at 4.7T is taken into account. This SNR advantage was demonstrated experimentally for the human brain (**Figure 5-3)**.

To realize the SNR advantage of spoiled steady-state radial imaging at 4.7T, RF pulse lengths must be increased for SAR to remain within approved limits; this results in the signal loss labelled 'SAR loss' (**Figure 5-2d)**. However, the rapid T_1 recovery of the sodium spin ensemble and the use of shorter repetition times (i.e. increased averaging for a given scan duration) more than compensates for this signal loss, facilitating a noise variance reduction and an overall increase in SNR. **Figure 5-2e** suggests that under SAR constraint implementation of a sequence with the shortest possible RF pulse length (and by corollary TE) does not yield an image with the greatest image SNR for a given scan duration.

The SNR advantage of Na-PASS imaging may be particularly useful, as this SNR may be 'spent' to generate images with smaller voxel sizes. As sodium images have inherently large voxel sizes (when compared to proton), all attempts to improve these images should be considered. The generation of images with smaller voxel sizes may be particularly important for the detection of smaller lesions or for the analysis of lesions in the cortex of the brain where partial volume averaging with CSF space (which has approximately 3 times more sodium than brain tissue) must be a major concern. Images with smaller voxel sizes may also enable more accurate selective analysis of gray and white matter. The measured SNR increase of approximately 38% associated with steady-state

optimization under SAR constraint presented here is almost equivalent to the theoretical signal increase associated with a magnetic field strength upgrade from 4.7T to 7.0T. Conversely this SNR advantage may be 'spent' to decrease sodium scan duration, which is of particular value when patient populations are to be studied.

The Na-PASS sequence implemented to generate the sodium images in **Figure 5-4** is a relaxation weighted sequence. This is readily apparent from **Figure 5-2c**. While TSC sodium imaging is concerned with the acquisition of a tissue sodium concentration number [mM], relaxation weighted imaging is generally used for relative signal intensity comparisons between lesions and the contralateral tissue. Although TSC measurement (which requires relaxation weighting to be minimized) is one goal of sodium imaging, many important findings have been demonstrated with relaxation weighted sodium imaging, and relative signal intensity comparisons. These include a linear sodium signal intensity increase with time after stoke (65), correlation between sodium signal intensity and tumour grade (5), and the ability to predict and monitor response to chemotherapy (274) to name a few. The extent to which the Na-PASS sodium imaging approach (and the reference TSC imaging approach presented in this paper for that matter, which maintains some residual relaxation weighting) reflects actual tissue sodium concentration increases in a lesion will depend on the nature and degree of any relaxation changes within that lesion. It may be that the unique origin of sodium relaxation (an interaction between the electric quadrupole moment of the sodium nucleus and the environmental electric field gradient – a derivative of macromolecular structure, density, and order) provides valuable information in addition to and complementing tissue sodium concentration.

A one compartment relaxation model of human brain tissue was used for the quantum mechanical simulation of each RF pulse parameter set. Use of this model assumes for simulation that all sodium nuclei within the tissue exhibit the same

relaxation characteristics. However, it is most likely that the sodium spin ensemble within intracellular space exhibits more rapid biexponential transverse relaxation than the sodium spin ensemble within interstitial space (also biexponential) (28,75,109,275). Although it seems intuitive that this should be the case in the human brain (given shift-reagent aided studies in other tissue (46,49,223), diffusion studies in brain (229), and the existence of volume transmission through the interstitial space) compartmental relaxation parameters in the human brain (or any intact brain) are unknown. The interstitial space also contains an abundance of macromolecules (attached to cell membranes) and is bordered by the cell membranes themselves, both of which can effect long-range electric field gradients and a rapid fast component of T_2 relaxation. Compartmental relaxation measurement typically requires the administration of shift-reagents which are toxic and do not pass the blood-brain-barrier. A technique has been proposed to measure relaxation parameters for a two compartment model of the human brain (45), however this work is ongoing. For this reason the simulation presented in this paper was limited to a one compartment relaxation model of human brain tissue.

It may be thought that if the intracellular space exhibits more rapid biexponenential T_2 decay, any T_2 relaxation weighting will unequally weight each voxel toward the slower relaxing interstitial space which is of lesser consequence than the intracellular space. However, the (most likely) longer T_1 of the extracellular space will generate greater T_1 saturation losses. It is possible (based on preliminary attempts to selectively measure the relaxation parameter of intracellular and extracellular space (45)) that the Na-PASS RF pulse parameters used in the generation of **Figure 5-4** actually slightly weight each voxel toward the intracellular space, although this is purely speculative at this point.

It was suggested that the 'SAR loss' presented in **Figure 5-2d** cannot be completely explained as 'increased T_2 loss during longer TE.' If this was the case

this relative loss should remain constant (across TR) for every RF pulse length, and should match simple 'T_2 loss during TE' calculations. This is not the case for the 'SAR loss' presented in **Figure 5-2d**, especially for longer RF pulse lengths. This occurs in part because rapid relaxation during a soft RF pulse alters the magnetization evolution during that RF pulse (44); longitudinal magnetization is decreased less for a given flip angle, thus modifying the steady-state response. The simulated transverse magnetization at TE is also somewhat altered by the generation of rank three single quantum coherence during the RF pulse (included in the quantum mechanical simulation).

Concerning the simulation performed in this paper a few items should be mentioned. First, an SAR value of approximately 1.5 W/kg at 4.7T was chosen for this study because sodium experiment durations can be quite lengthy (in this case 20 minutes). This SAR value may be slightly overestimated, as power losses in coil were not considered. If SAR was allowed to double, simulation suggests that SNR could be increased by ~8 % at a steady-state TR of 25 ms. This increase is associated with the facilitated implementation of shorter RF pulse lengths. Second, the system delay (i.e. the delay between the end of the RF pulse and acquisition of the first data point) was 128 μs for simulation and the images presented. This delay was related to system gradient delays and the transient response of the anti-aliasing filter. A shortened system delay will generate a small benefit for the Na-PASS sequence (however, the length of the system delay is more important when a maximum relaxation weighting is to be attained for TSC imaging, as described below). Third, the simulation outcome will differ (slightly) with the implementation of a different relaxation model (i.e. for refined relaxation measurements in the brain, relaxation measurements in other tissue, or relaxation measured at field strengths other than 4.7T). Fourth, although the quantum mechanical simulation presented provides a more complete analysis of the evolution of the sodium spin magnetization, a classical calculation, which models the RF pulse as an impulse (Eq. [5-5] with parameters described previously, d = system delay), is adequate but only when the implemented RF pulse is sufficiently

short. This classical model will suffice for the RF pulse length used to generate the sodium images in Figure 3; however, this is not the case for the range of longer RF pulses simulated in this paper.

$$\mathrm{M_{xy}} = \mathrm{M_0}\sin\left(\theta_0\sqrt{\frac{\tau_{\mathrm{RF}}\cdot\mathrm{TR}}{\tau_{\mathrm{RF}_0}\cdot\mathrm{TR}_0}}\right) \cdot \frac{1-\left(0.8\cdot e^{\frac{-\mathrm{TR}}{\mathrm{T_{1slow}}}}+0.2\cdot e^{\frac{-\mathrm{TR}}{\mathrm{T_{1fast}}}}\right)}{1-\left(0.8\cdot e^{\frac{-\mathrm{TR}}{\mathrm{T_{1slow}}}}+0.2\cdot e^{\frac{-\mathrm{TR}}{\mathrm{T_{1fast}}}}\right)\cos\left(\theta_0\sqrt{\frac{\tau_{\mathrm{RF}}\cdot\mathrm{TR}}{\tau_{\mathrm{RF}_0}\cdot\mathrm{TR}_0}}\right)} \cdot \left(0.6\cdot e^{\frac{-(\tau_{\mathrm{RF}}/2+d)}{\mathrm{T_{2fast}}}}+0.4\cdot e^{\frac{-(\tau_{\mathrm{RF}}/2+d)}{\mathrm{T_{2slow}}}}\right) \quad [5\text{-}5]$$

Because of the proliferation of high-field MRI systems, simulations were performed to assess the SNR advantages of higher field strengths for both Na-PASS and TSC sodium imaging. Notice that as the static magnetic field strength increases the RF pulse length must increase to generate a given flip angle at a given TR for a constant SAR (**Figure 5-5a**). For the TSC reference described in this paper, the effect of this RF pulse length increase is greater relaxation weighting, as depicted in **Figure 5-5b**. To decrease the RF pulse length and minimize the relaxation weighting (which is the goal of TSC imaging), either TR must be increased or the flip angle reduced; observation of **Figure 5-5c** (which depicts relative SNR) suggests the second approach may have a greater SNR benefit. At each field strength there is an SNR advantage associated with steady-state imaging, despite the considerable (and growing with field strength) RF pulse length (TE) increase required to realize this SNR advantage at high fields.

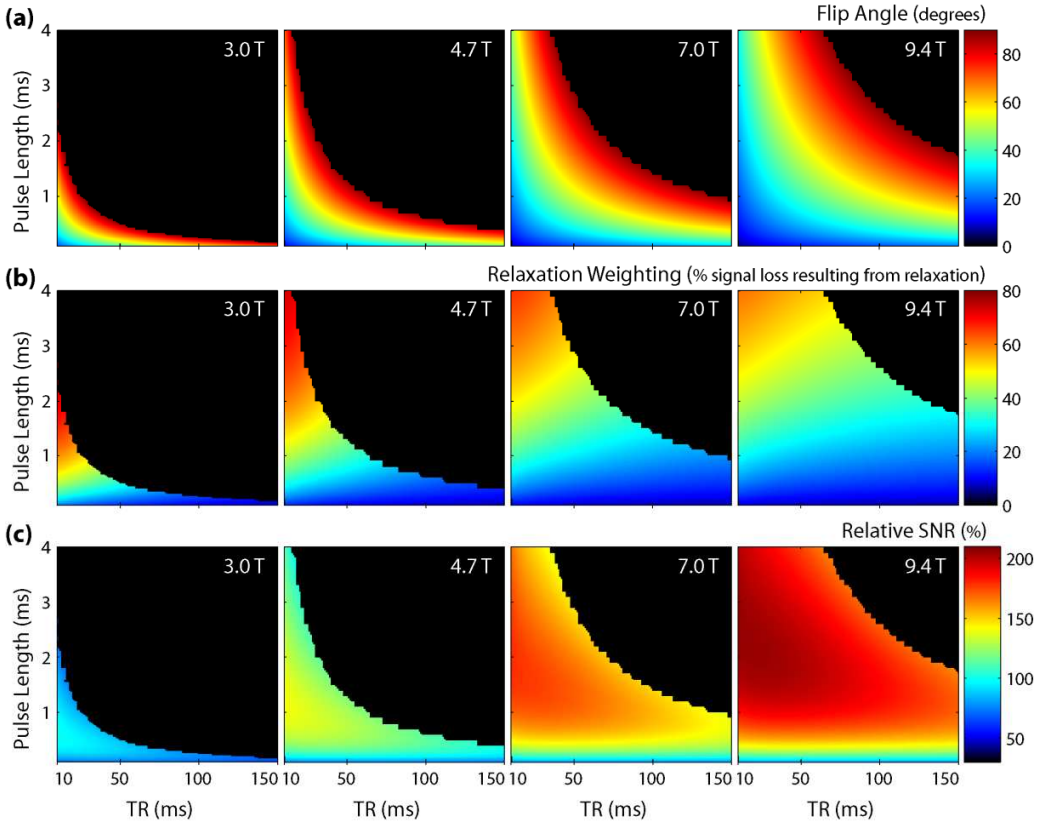

Figure 5-5: Simulated sequence analysis when SAR constraints at field strengths other than 4.7 Tesla are considered. In Figure **(a)** the flip angles required to generate a constant SAR (equal to that generated in this paper) are given for each RF pulse length and TR combination. Relaxation weightings for each field strength are given in Figure **(b)**. Figure **(c)** displays the relative SNR advantage associated with imaging at higher fields. For each magnetic field strength displayed there is an SNR advantage associated with steady-state imaging. This advantage exists in spite of long, and increasing, RF pulse lengths (and TE) required to realize this advantage at higher fields.

In **Figure 5-6** the optimal flip angles (for greatest signal) at each TR are gathered from this quantum mechanical simulation. It is interesting to note that for large magnetic field strengths the optimal flip angle is considerably less than the Ernst angle. This is primarily due to the SAR constraint as smaller flip angles facilitate shorter RF pulses which reduce T_2 losses.

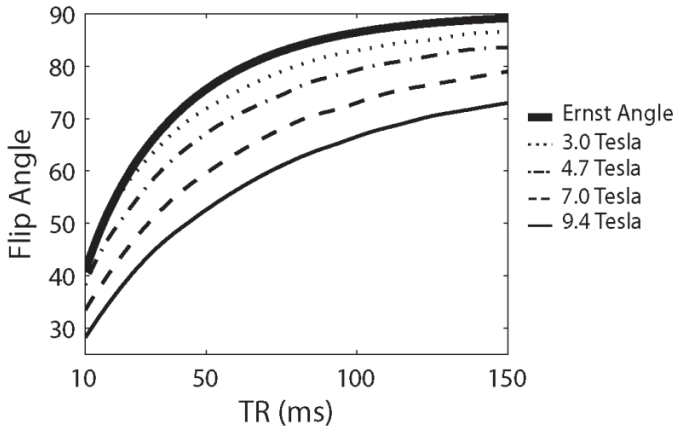

Figure 5-6: The optimal (for SNR) sodium imaging steady-state flip angles gathered from the simulations presented in **Figure 5-5**. As the magnetic field strength increases, either the RF pulse length must increase or the flip angle decrease to meet SAR requirements for a given TR. RF pulse length increases will lead to greater T_2 signal loss. As a result the optimal flip angles are considerably less than the theoretical Ernst Angle (shown for a T_1 of 36 ms).

Relative SNR is displayed in **Figure 5-7** for three (implementable) sodium imaging approaches, calculated from simulation with the RF pulse parameters in **Table 5-1**. Considering the reference TSC imaging approach (which uses 90^o flip angles) implemented for 10% relaxation weighting (assumed to be a maximum case), simulation suggests that the SAR constraint significantly diminishes SNR gains expected at higher fields. For this approach, some of the expected SNR advantage of high field imaging can be recovered if the system delay (between excitation and acquisition) can be decreased. This allows RF pulse lengths to be longer and TR reduced while maintaining SAR and a 10% relaxation weighting. Simulation also suggests that under tightened SAR constraint smaller flip angles can generate significantly greater SNR for TSC imaging (labelled the 'modified TSC approach'). Finally, it is suggested that as the SAR constraint tightens, the SNR advantage of the Na-PASS sodium imaging approach increases (with respect to TSC imaging).

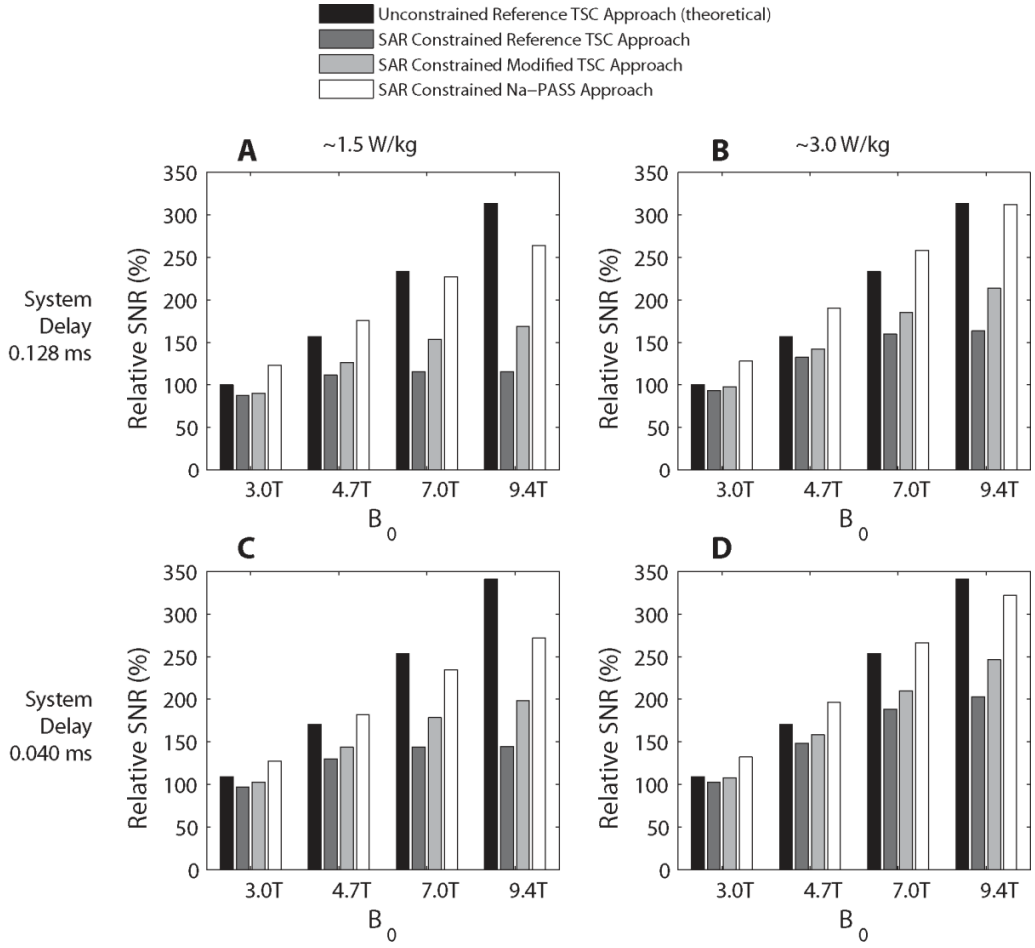

Figure 5-7: Relative SNR from simulation for three different approaches to sodium imaging (in relation to the *theoretical* unconstrained reference TSC approach simulated with a system delay of 0.128 ms). The RF pulse parameters for each simulated approach are given in **Table 5-1** for each magnetic field strength. For this constant SAR analysis, simulation suggests that SNR increases expected at higher magnetic field strengths are mitigated by SAR. This can be seen in the relative SNR difference between the SAR constrained and unconstrained reference TSC approach (which uses 90^{o} flip angles). It can also be seen that the modified TSC approach (which uses flip angles other than 90^{o}) generates an SNR advantage for the same relaxation weighting as the reference TSC approach, especially at higher fields. Finally, the Na-PASS sequence is associated with a relative SNR advantage over TSC imaging that increases as the SAR constraint tightens. **A** and **C** display relative SNR for the same SAR used in this paper; in **B** and **D** allowable SAR is doubled. **A** and **B** are generated with the system delay associated with the images generated in this paper (0.128 ms); in **C** and **D** the simulated system delay is reduced to 0.040 ms.

Table 5-1

The SAR Constrained RF Pulse Parameters Used in Simulation to Generate the Relative SNR Charts in Figure 5-7 [a,b]

		System Delay: 0.128 ms			System Delay 0.040 ms		
	B_0	**θ**	**τ_{RF} ms**	**TR ms**	**θ**	**τ_{RF} ms**	**TR ms**
Unconstrained Reference TSC Approach [c]	3.0T	90 (90)	0.0001 (0.0001)	110 (110)	90 (90)	0.0001 (0.0001)	93 (93)
	4.7T	90 (90)	0.0001 (0.0001)	110 (110)	90 (90)	0.0001 (0.0001)	93 (93)
	7.0T	90 (90)	0.0001 (0.0001)	110 (110)	90 (90)	0.0001 (0.0001)	93 (93)
	9.4T	90 (90)	0.0001 (0.0001)	110 (110)	90 (90)	0.0001 (0.0001)	93 (93)
SAR Constrained Reference TSC Approach [d]	3.0T	90 (90)	0.19 (0.11)	144 (126)	90 (90)	0.23 (0.13)	117 (104)
	4.7T	90 (90)	0.31 (0.22)	217 (154)	90 (90)	0.42 (0.27)	160 (123)
	7.0T	90 (90)	0.33 (0.32)	448 (235)	90 (90)	0.51 (0.44)	289 (169)
	9.4T	90 (90)	0.33 (0.33)	807 (404)	90 (90)	0.52 (0.51)	516 (262)
SAR Constrained Modified TSC Approach [e]	3.0T	71 (75)	0.16 (0.09)	114 (106)	69 (71)	0.18 (0.10)	89 (84)
	4.7T	64 (70)	0.26 (0.17)	134 (116)	65 (67)	0.33 (0.20)	106 (90)
	7.0T	50 (62)	0.31 (0.26)	145 (135)	52 (62)	0.43 (0.34)	116 (105)
	9.4T	41 (53)	0.34 (0.31)	162 (151)	43 (55)	0.48 (0.42)	127 (118)
SAR Constrained Na-PASS Approach [f]	3.0T	58 (61)	0.45 (0.25)	25 (25)	58 (60)	0.45 (0.24)	25 (25)
	4.7T	53 (58)	0.93 (0.55)	25 (25)	53 (57)	0.93 (0.54)	25 (25)
	7.0T	46 (52)	1.55 (0.99)	25 (25)	46 (52)	1.55 (0.99)	25 (25)
	9.4T	40 (47)	2.11 (1.46)	25 (25)	40 (47)	2.11 (1.46)	25 (25)

(a) Values in brackets are given for an SAR double that implemented in this paper.

(b) RF pulse parameters are given for system delays of 0.128 ms and 0.040 ms.

(c) For this *theoretical* approach the RF pulse length is made exceptionally short (i.e. SAR is ignored); a 10% relaxation weighting is maintained.

(d) Flip angles are maintained at 90^o and the TR and RF pulse length combinations that generate the greatest SNR for a relaxation weighting of only 10% are used for simulation.

(e) Flip angles are not maintained at 90^o and the RF pulse parameter combinations that yield the greatest SNR for a relaxation weighting of 10% are used for simulation.

(f) The RF pulse parameters that yield the greatest SNR at a TR of 25 ms are used for simulation.

The SNR optimized Na-PASS sequence presented in this paper was considered within the context of imaging the human brain. However, this steady-state imaging approach should also have an SNR advantage for imaging other tissues such as muscle and cartilage. For these cases the optimal RF pulse parameters will depend on the local SAR constraint and sodium relaxation characteristics in the tissue of interest.

Chapter 6

Sodium Imaging Intensity Increases with Time after Human Ischemic Stroke

M.S. Hussain*, R.W. Stobbe*, Y.A. Bhagat, D. Emery, K.S. Butcher, D. Manawadu, N. Rizvi, P. Maheshwari, J. Scozzafava, A. Shuaib, C. Beaulieu, Ann Neurol, 66, 55-62, 2009
(* co-first authors)

6.1. Introduction

Advanced brain imaging methods play an important role in the assessment of the acute stroke patient (276). For example, perfusion (PWI) and diffusion (DWI) weighted magnetic resonance imaging have been proposed as an individual-based framework to help identify patients with a more probable improvement in outcome following thrombolysis (99,100,277). However, even with image-based patient selection, time of ischemic stroke onset is a critical determinant of the effectiveness of acute stroke treatment (88,89). Approximately one-third of stroke patients present with an uncertain time of onset, often making them ineligible for thrombolytic therapy (101) since the onset time is assumed to be the time last seen well which is usually beyond the narrow eligible time window (3 h currently for intra-venous tissue plasminogen activator). These include patients who wake with stroke symptoms and those who are unable to convey their stroke onset time due to acute neurological deficits. However, some of these wake-up patients, for example, may have had their stroke shortly before awakening yet are currently denied acute stroke therapy. A non-invasive imaging method that could estimate onset time in such patients with unknown onset time could make them eligible for thrombolytic therapy.

Diffusion-perfusion MRI cannot estimate the time of stroke onset in the acute time period. While diffusion weighted imaging (DWI) identifies areas of cerebral ischemia within minutes of onset (90-92), apparent diffusion coefficient (ADC) values of water remain low within the infarcted area until one week post onset when they begin to pseudonormalize (98,278). Metabolites and ions may yield more specific changes than water as they are intimately related to the ischemic

cascade. Due to energy failure in acute stroke, the sodium–potassium ATPase, which maintains ionic gradients, fails and sodium shifts intra-cellularly (95,115). The newly established concentration gradient between the sodium ion depleted extracellular space of the ischemic core and the intravascular space drives the transfer of sodium ions from the blood to the brain lesion across the blood brain barrier (BBB), either early in stroke through a secondary active process or later through 'free passage' if the BBB is injured (130,135). In fact, direct, non-imaging measurements of sodium concentration in experimental models of ischemic stroke have shown time dependant increases in brain tissue sodium concentrations (68,102,106,112).

Tissue sodium levels can be studied non-invasively utilizing MRI (40,265,279-281). Animal models indicate that signal intensity within ischemic brain lesions on sodium MR images increases in a linear fashion after stroke onset (12,64-67). In ischemic stroke patients, an earlier study found sodium MRI intensity increases only at late time points (> 36 hours after onset), but was limited by low-resolution images and few patients scanned at < 24 hours (13). Sodium MRI of human ischemic stroke has also been studied to find thresholds for irreversible injury (12) and although increases in sodium intensity were found, a specific temporal relationship was not shown. Thus, an evolution of sodium signal intensity with time in human ischemic stroke has not been demonstrated.

In this study, we tested the hypothesis that sodium signal intensity within the ischemic lesion, measured with sodium MRI, is related to time after symptom onset in human stroke patients with known onset time.

6.2. Methods

6.2.1. Patient Selection

This study was conducted at the University of Alberta Hospital, a tertiary care hospital in Edmonton, Alberta, Canada. The local human research ethics board approved study protocols and written informed consent was obtained from all patients or their next of kin. Ischemic stroke patients with definite known time of onset and no contraindications to high field MRI scanning were eligible. All patients received standard care, including intravenous tissue plasminogen activator (IV tPA) if indicated. Patients showing imaging signs of hemorrhage, small lesions (< 1.5 cm^3), or severe white matter hyper-intensities were excluded.

A total of 21 stroke patients (12 males, 9 females, mean age = 63±15 years) were included, yielding 32 time points. Patient clinical and scanning characteristics are given in **Table 6-1**. Ten patients received IV tPA before scanning. Two patients were enrolled in the Albumin In Acute Stroke (ALIAS) trial(282). One patient was enrolled in the Multiple Interventions for Neuroprotection Utilizing Thermal-regulation in the Emergent Treatment of Stroke (MINUTES) trial, a local neuroprotective study in which stroke patients in the treatment arm received magnesium, albumin, atorvastatin, minocycline, and hypothermia. The National Institutes of Health Stroke Scale (NIHSS) score ranged from 1-19. Time of onset was established clinically, based on patient and family reports. Initial imaging times ranged from 4-104 hours (symptom onset to completion of the sodium scan), and repeat scans were performed in 10 patients (one patient had two follow-up scans), ranging from 23-161 hours after onset, to yield 32 time points. Five patients also returned for repeat scans 3-7 months later (patient 1 – 212 days, patient 2 – 133 days, patient 5 – 91 days, patient 6 – 88 days, patient 8 – 227 days).

Table 6-1: Clinical and imaging characteristics of the 21 stroke patients.

Pat. No.	Age	Sex	Co-morbidity	Acute Stroke Treatment	Localization	Time of Initial/Serial MRI scans (hr)	Initial /Follow-up NIHSS score	DWI Lesion volume (cm^3)	Relative Sodium Increase (%) Over Contra-lateral
1	69	M	HTN, ↑chol, DM	IV tPA	Right striatocapsular	17.5/161	12/12	2.9/6.3	23/62
2	52	M	Smoker	None	Left MCA	14/36	12/10	63.9/90.6	35/48
3	56	M	Smoker	None	Left MCA	6.25/25.5	13/7	27.7/39.9	9/35
4	58	F	HTN, ↑chol, DM	ALIAS	Left PCA	29	11	37.2	49
5	46	M	Afib	IV tPA /ALIAS	Left MCA	4/25.5	7/7	50.6/74	-2/45
6	84	M	HTN, ↑chol	IV tPA /MINUTES	Right striatocapsular	23	6	10.2	56
7	48	M	Past MI	IV tPA	Right PCA	5.25/22.5	4/3	3.2/15.7	3/31
8	54	M	None	IV tPA	Left MCA	6.75/28	7/5	26.1/36.8	3/13
9	22	M	None	None	Left MCA	6/52	1/1	5.8/17.3	6/34
10	78	F	HTN, ↑chol, DM	None	Left MCA	45	1	4.4	53
11	82	F	HTN, ↑chol, afib	None	Right striatocapsular	36	6	6.6	88
12	55	F	None	IV tPA	Left striatocapsular	47	7	14.1	96
13	54	M	HTN, past cardiac arrest	None	Right MCA	13/37/61	10/10/10	4.7/4.7/5.7	25/62/58
14	55	F	↑chol	None	Right striatocapsular	38/58	6/6	1.7/1.7	50/65
15	61	M	None	None	Right SCA	18.5	7	7.8	59
16	72	F	HTN	IV tPA	Right MCA	9.33/80	19/19	147.7/216.5	24/110
17	66	M	HTN, ↑chol, MI	IV tPA	Left striatocapsular	29.5	5	11.8	75
18	81	F	HTN, ↑chol, CHF	IV tPA	Left MCA	104	8	33.5	46
19	74	F	HTN, ↑chol	None	Right striatocapsular	21.5	12	15.3	38
20	73	M	Afib	None	Left MCA	50	5	57.1	62
21	73	F	HTN, Smoker	IV tPA	Right MCA	98	17	65.5	96

HTN - hypertension, chol - cholesterol, DM - diabetes mellitus, afib - atrial fibrillation, MI - myocardial infarction, CHF – congestive heart failure, ALIAS - Albumin in Acute Stroke trial, MINUTES - Multiple Interventions for Neuroprotection Utilizing Thermal-regulation in the Emergent Treatment of Stroke, IV tPA – intravenous tissue plasminogen activator, MCA - middle cerebral artery, PCA - posterior cerebral artery, PICA - posterior inferior cerebellar artery, SCA - superior cerebellar artery

6.2.2. MRI acquisition and post-processing

After informed consent, patients underwent scanning in a 1.5 Tesla (T) Sonata scanner (Siemens Medical Systems, Erlangen, Germany). The scanning protocol included turbo spin echo T2 (repetition time (TR) = 5800 ms, echo time (TE) = 99 ms), fluid attenuated inversion recovery (FLAIR) (TR = 7950 ms, TE = 94 ms, inversion time (TI) = 2400 ms), gradient recalled echo, and DWI (b = 1000 s/mm^2). These images were used to identify the lesion, appropriate contralateral tissue, and the presence of hemorrhage. Five patients also underwent gadolinium based perfusion-weighted imaging (patients: 3,5,7,8,17). Total scanning time was 16 minutes for the complete proton MRI protocol.

Patients were then transferred immediately to the high field 4.7T Varian (Palo Alto, CA, USA) MRI scanner for sodium imaging, performed with an in-house designed and manufactured single-tuned 53-MHz quadrature birdcage head coil. A new sodium MRI technique named "Sodium Projection Acquisition in the Steady State" (Na-PASS) was used together with sampling density weighted apodization, allowing for the generation of high quality sodium images of the complete human brain in a clinically feasible scan time of 10 minutes(42,60). The sequence parameters were: TE = 0.6 ms, TR = 25 ms, excitation flip angle = 55^o, and 6 averages. Images generated had a nominal voxel size of 2.4x2.4x4.8 mm^3.

6.2.3. Region of Interest Analysis

The sodium and DW images (along with ADC map) were co-registered with the high-resolution proton T_2-weighted and FLAIR images from the same imaging session using SPM5 (Wellcome Cognitive Institute of Neurology). For images within 7 days of onset, the lesion was defined manually as voxels with visibly increased intensity on the DWI. Each region of interest (ROI) drawn on the DWI was subsequently transferred to the high resolution T_2-weighted image and ROI areas containing visible cerebrospinal fluid (CSF) were removed. The resulting

ROIs were transferred to the sodium image and an average intensity measured from within the complete ROI volume. This average lesion sodium signal value was compared with average sodium signal intensity in the normal homologous volume on the contralateral side. For images acquired after 7 days of onset, the lesion was identified and the ROIs were drawn on the T_2–weighted image. The sodium signal change was defined as (Signal Intensity $(Na)_{ipsi}$ − Signal Intensity $(Na)_{contra}$) / Signal Intensity $(Na)_{contra}$). In all cases, the same ROIs used for sodium image analysis were also used to measure relative signal intensity increases on T_2-weighted and FLAIR images as well as ADC decrease in the lesion.

6.2.4. Statistical analysis

A 'best fit' line, based on weighted non-linear least squares regression, was fit to the 32 relative sodium signal intensity change data points collected over the first week post stroke onset. The non-linear model selected for this regression was required to have a relative signal change of zero at time zero, a logical requirement for healthy tissue. A second requirement of the non-linear model was that it approach an upper asymptote at later times past onset, taking into account the fact that signal increases do not continue indefinitely. From these requirements, an asymmetric sigmoid model (a modified Morgan, Mercer, Flodin model(283)) was selected to 'best fit' the data points. The thirteen data points acquired within the first 24 hours were also binned into 3 groups with average time after onset of 5.7h (N=5), 13.3h (N=4), and 21.4h (N=4) for the sodium, T2-weighted, and FLAIR images. Relative signal intensity increases of the later over the earlier time after onset bins were tested for significance using a one-sided t-test that did not assume equal variance between groups.

6.3. Results

Representative sodium images from 6 different patients scanned between 7 to 52 hours are shown in **Figure 6-1** along with the corresponding DW, T_2-Weighted, and FLAIR images. Each 10 minute Na-PASS sodium scan has sufficient resolution and signal-to-noise ratio (SNR, 16±3 in normal brain tissue) to visualize the lesions and facilitate the identification of small sulcal spaces, aiding image co-registration and analysis. It is evident in the cross-sectional data that the sodium signal intensity within the lesion is increasing with time after stroke onset. This is also observed in serial data from the same patient where sodium intensity in the lesion progresses over time (**Figure 6-2**).

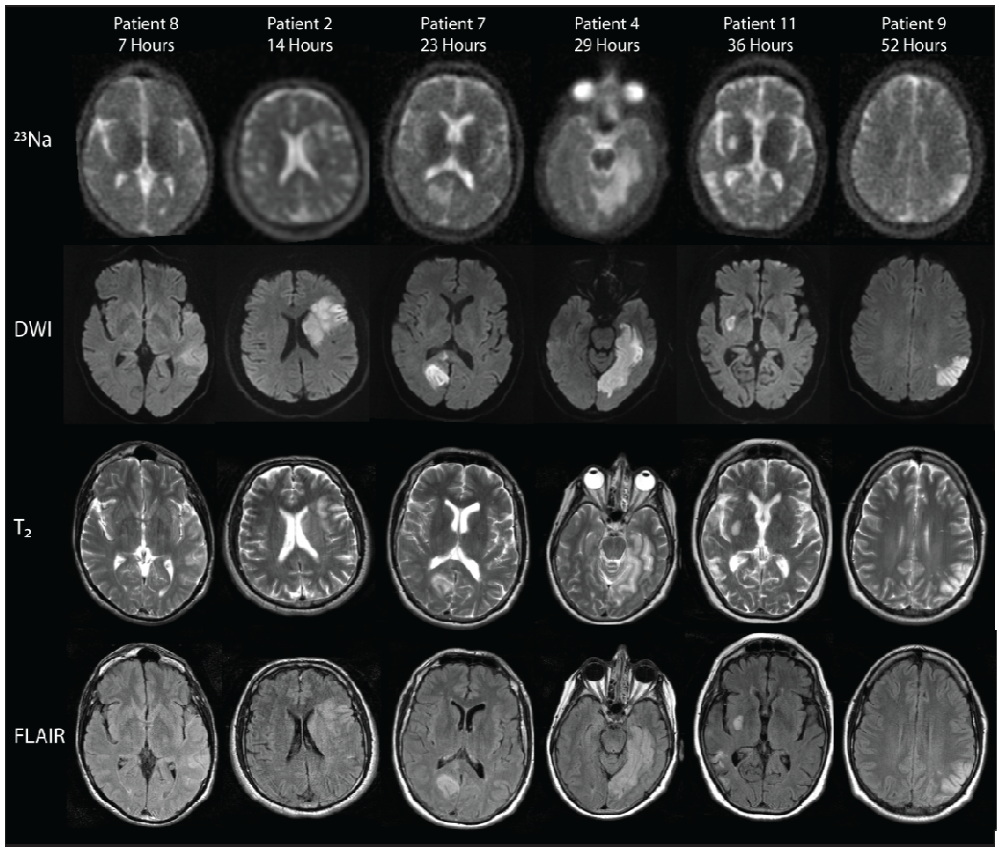

Figure 6-1: Representative sodium (^{23}Na), DWI, T_2-Weighted and FLAIR images from patients who were 7 – 52 hours post ischemic stroke onset. Areas of sodium signal intensity increase correspond to the lesions identified on DWI. The sodium signal intensity in the areas of ischemia qualitatively increases with time.

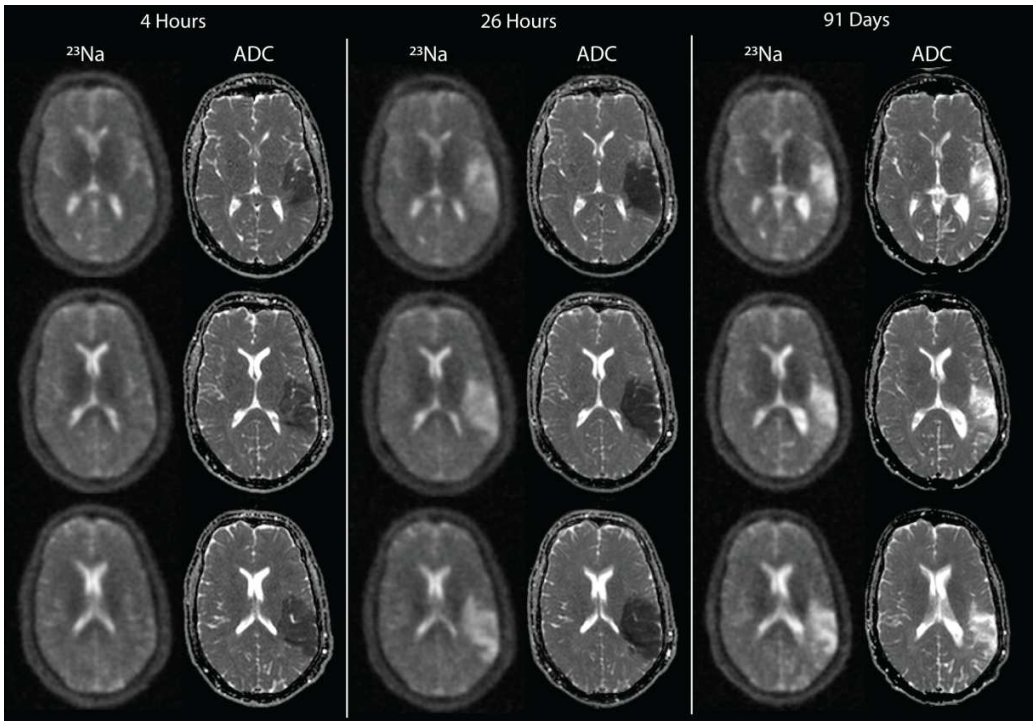

Figure 6-2: Representative sodium (^{23}Na) images and water apparent diffusion coefficient (ADC) maps from a single patient (patient 5) scanned at 4 hours, 26 hours, and 91 days. There is a dramatic increase in sodium signal intensity between the acute time point of 4 hours (no change over contralateral side) and the time point 22 hours later (45% increase over contralateral side). At 91 days, the sodium signal intensity increase persists (75% relative increase).

Quantitative lesion analysis over all 32 time points from 4 to 161 hours shows a non-linear increase of sodium intensity (**Figure 6-3**). Initially, sodium signal intensity rose at a slow rate up to 5-6 hours, followed by a more rapid increase to 18-20 hours. There is an eventual leveling to an upper asymptote of 69±18% (error reflects 95% confidence interval) relative increase in signal intensity compared to the normal contralateral hemisphere (80% of maximum reached by ~ 31 hours post-onset). At later time points (88-227 days) the sodium signal intensity in the infarct was elevated by 76±20%.

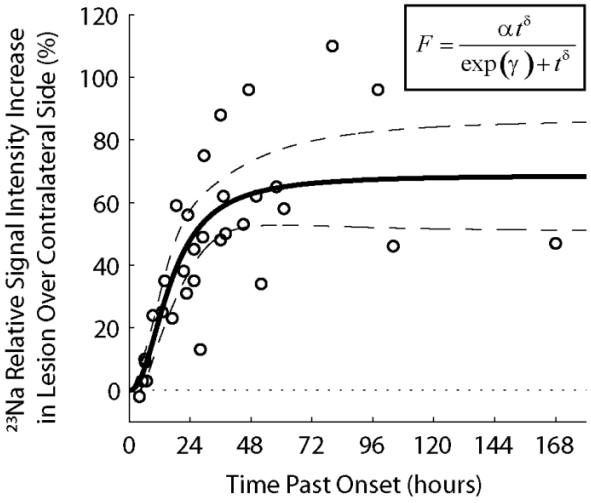

Figure 6-3: Sodium MRI signal intensity increases non-linearly versus time over the first week after stroke onset and reaches an asymptote of 69% ± 18% (n=32, R^2 = 0.56, parameters of fit: α = 69 ± 18, δ = 2.2 ± 1.0, γ = 6.1 ± 2.3). Dashed lines represent 95% confidence interval of fit.

Early increases in sodium intensity within the first 40 hours are demonstrated in **Figure 6-4A**. Each sodium image acquired within 7 hours (n = 5) had a relative signal intensity increase within the lesion of ≤ 10%, while each image acquired beyond 9 hours, with the exception of one image collected at 28 hours, had a relative signal intensity increase ≥23%. Relative ADC values over the same time span were decreased by 15-44% (**Figure 6-4B**), and no useful temporal information could be extrapolated from ADC values within 40 hours after stroke onset.

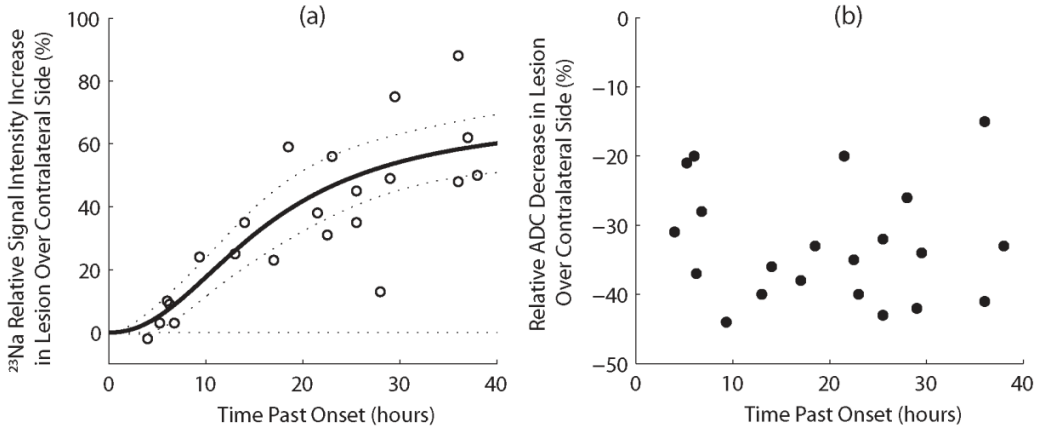

Figure 6-4: (**A**) Relative sodium intensity increase shows a clear progression over time during the first 40 hours post stroke onset. Images acquired within 7 hours (n = 5) had a relative signal intensity increase within the lesion of < 10%, while each image acquired beyond 9 hours, with the exception of one image collected at 28 hours, had a relative signal intensity increase > 23%. Dotted lines represent 95% confidence interval of the fit (**B**) On the other hand, as expected, the relative average decrease in water ADC shows no temporal evolution over this time

T2-weighted and FLAIR images also demonstrate relative signal intensity increases with onset time within the DWI-defined lesion in the first 24 hours, although the evolution differs from sodium. First, there is a lag in the rise of the sodium intensity with more marked increases only occurring at later time points >7 hours, whereas the T2-weighted and FLAIR intensities are elevated throughout (**Figure 6-5A**). Second, the rate of signal intensity increase between the binned onset time groupings of 4-6.75 hours to 9.3-17 hours, and 9.3-17 hours to 18.5-23 hours, is greater for sodium (2.9%/hour, and 2.4%/hour) than for either T2-weighted (1.9%/hour and 1.3%/hour) or FLAIR (1.2%/hour and 0.7%/hour) (**Figure 6-5B**). Thus the sodium images discriminate onset time better than either the T2-weighted or FLAIR proton images.

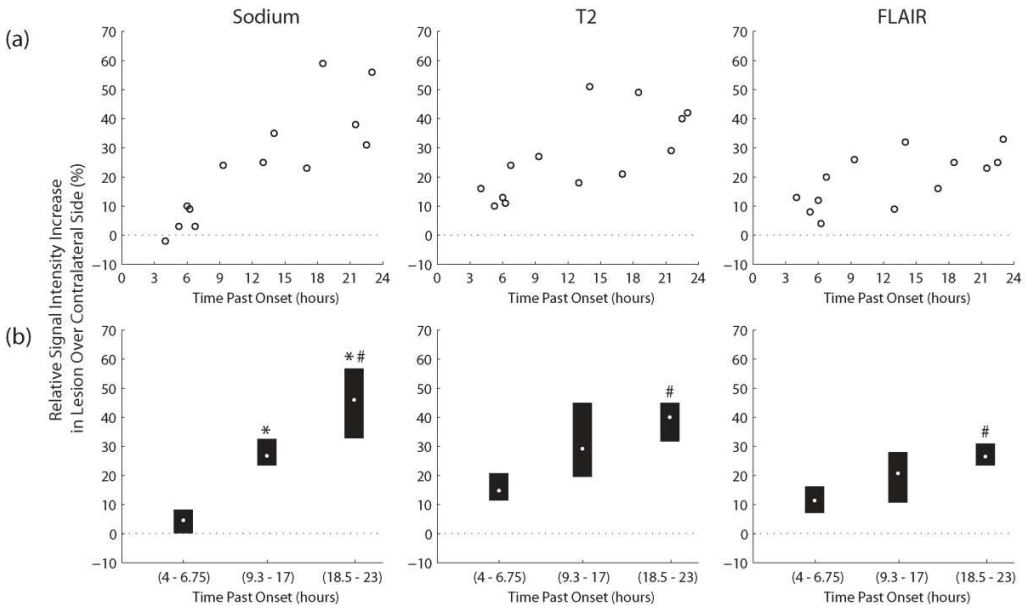

Figure 6-5: (**A**) Signal intensity within the DWI defined lesion increases in a different manner on sodium images than it does on T_2-Weighted and FLAIR images. Relative signal intensity increases on the sodium images are initially delayed when compared to the proton methods. This initial delay, and steeper changes of sodium at later time points, result in a substantial difference between early and more subacute time-points as is highlighted in the binned analysis (**B**). The mean values of each bin are plotted along with the bias-corrected, bootstrapped confidence intervals. The * indicates statistical difference from the (4 – 6.75 hour group) at $p < 0.05$, and the # indicates statistical difference from the (9.3 – 17 hours group) at $p < 0.05$.

6.4. Discussion

We demonstrated that sodium signal intensity, measured with Na-PASS MRI, increases in a time-dependent fashion during human acute ischemic stroke, whereas water ADC did not yield any useful temporal information. Based on the present sodium MRI data, patients with a < 10% relative sodium signal intensity increase are closer to their stroke onset and are likely to be within commonly accepted therapeutic time windows (≤3 hours IV tPA and ≤6 hours for experimental intra-arterial therapies), whereas larger increases would be suggestive of older strokes. While signal intensities on both T_2-Weighted and FLAIR images also increase with time past onset, the signal intensity on the sodium images does so in a substantially different manner. Signal intensity within the DWI-defined lesion on sodium MRI appears, from regression analysis, to lag until about 4-6 hours post onset at which time it begins a much more rapid ascent (**Figure 6-4A**). It is this lag and subsequent rapid ascent which distinguishes early onset times from later ones that may provide utility for sodium imaging over T_2-Weighted and FLAIR imaging (**Figure 6-5**). While identification of the putative penumbra with diffusion-perfusion MRI is being studied as an approach to identify suitable individuals for aggressive therapy(99,100,277), time from onset remains an inclusion criterion in these studies, and may still be a predictor for beneficial outcome(88,89). In some cases of unknown stroke onset, sodium MRI may be able to show that a stroke is likely within a specified therapeutic window, thus making an otherwise ineligible patient now eligible for thrombolytic therapy.

Neither of the two published studies of sodium MRI in human ischemic stroke has confirmed a temporal relationship between sodium intensity and symptom duration within the first week after onset(12,13). In the 1993 study, there were no sodium signal changes before 13 hours (n=3), but signal increase was observed at 38-82 hours (n=4)(13), unlike our study where sodium intensity evolution was observed even within the first 13h. They were hampered by poor spatial resolution and low SNR due to the sequence used, lower field strength of 1.5T,

and a very long spin echo time (TE) of 13 ms. A more recent study in 1999 investigated stroke patients with a focus on linking elevated tissue sodium concentration (TSC) with infarcted tissue(12). In their study, all 26 patients showed minimum TSC increases of 25% within the lesion, and there was no evidence of a temporal relationship between TSC and time-after-onset over the time window from 4h to 7 days post-onset. An average relative increase of ~45% with respect to the contralateral side can be estimated from their three patients within 8 hours; however, our 5 subjects within 7 hours had much smaller average relative increase of ~5%. Although both studies employed twisted projection acquisition to generate a short TE (0.4 ms versus 0.6 ms in our study), they used a longer TR (100 ms) for 'full' longitudinal magnetization recovery, while we used a signal enhancing steady-state approach (TR = 25 ms)(42). It is possible that the difference in early signal intensity increase on the sodium images is due to the sequence parameters.

In agreement with our human stroke sodium data, a non-imaging study of middle cerebral artery occlusion in rats demonstrated a non-linear increase of sodium where there was a lack of sodium increases at 3 and 6 hours post onset followed by significant changes at 12 hours and beyond(68). Interestingly, they showed a significant increase in tissue water concentration at the early time points when sodium was not elevated. This is similar to our observation that T2-weighted and FLAIR signal intensity increases, presumably reflecting elevated water content, precede increases of sodium signal intensity. It has been suggested that sodium ions are not the sole source of osmoles that drive early tissue water increases; other contributors likely arise from increased catabolic activity(68,102). The non-linear progression of sodium has also been observed with MRI where little sodium increase was observed within the first 2 hours followed by more rapid and linear sodium increases in both rabbit(65) and primate(12) stroke models. A rat model showed linear increases of sodium from 3.5–7h but did not have data at earlier time points(64). The transition from slow to more rapid signal intensity increase may reflect initiation of BBB break-down(106).

Time-dependent sodium MRI signal intensity increases in human stroke, as measured in this paper, are slower and lower in magnitude than those shown in rat(64), rabbit(65), and primate(12) stroke models where sodium signal intensity increases were as great as 25%/hour, 11%/hour and 11%/hour, respectively, in the acute period. In the current patient study, the maximum rate of sodium intensity increase was 2.8%/hour. These differences most likely reflect the uniqueness of human and animal brain anatomy as well as differences in the nature of stroke in humans versus the usual complete cessation of blood flow used in animal models.

There are several limitations to our study. In low resolution images (sodium MRI is 5000x less sensitive than proton MRI), differences of partial volume averaging over a range of lesion sizes is a concern. However, lesion volumes were well distributed over time of onset (**Table 6-1**) and thus are unlikely to have significant bearing on the sodium regression (**Figures 6-3 and 6-4A)**. Ischemic stroke patients vary considerably and some data scatter could be due to lesion location, gray/white matter tissue distribution (as we summed up all the voxels over the entire lesion), and the degree of perfusion deficit or reperfusion (spontaneous or tPA induced). Perfusion-weighted images were only acquired in 5 subjects and thus we cannot assess the perfusion status at the time of sodium MRI. In future, it would be interesting to assess whether sodium changes in the PWI-DWI defined mismatch region. Also, longitudinal scans at later time points would be required in order to assess the role of sodium MRI in delineating potentially salvageable tissue. The effect of gadolinium on sodium MRI intensity is unknown, although those subjects (patients 3,5,7,8,17) were in line with the others. Although we demonstrated a significant trend in sodium evolution with 21 patients scanned at 32 time points, future studies with larger numbers of subjects, particularly at the hyper-acute time points, will be required to confirm our findings. Research and clinical application of sodium MRI requires broadband transmitters/receivers, specialized radiofrequency coils, and specific optimized pulse sequences. However, as more centres gain these capabilities and clinical MRI scanner field

strengths continue to increase, we believe that sodium MRI will provide valuable information for the assessment of the acute stroke patient.

Chapter 7

In-vivo Sodium Magnetic Resonance Imaging of the Human Brain
Using Soft Inversion Recovery Fluid Attenuation (SIRFLA)

(R.S. Stobbe, C. Beaulieu, Magn Reson Med, 54, 1305-1310, 2005)

7.1. Introduction

The ability to assess intracellular sodium concentrations [Na_{in}] may greatly facilitate the diagnosis of diseased tissue in the human brain. [Na_{in}] appears to directly correlate with the rate of cell proliferation (218) and monitoring [Na_{in}] may be useful in the analysis of neoplasms and their response to chemotherapy (284). The ability to assess [Na_{in}] may also be useful in the setting of acute stroke, as dramatically increased [Na_{in}] levels, associated with anoxic depolarization (and the subsequent, relatively slow, diffusion of sodium ions from other parts of the brain into the ischemic core), appear to be directly linked to cell damage during ischemia (95). Although valuable information pertaining to the diseased state of tissue can be obtained with sodium MRI techniques that facilitate quantification of bulk tissue sodium concentrations (6,12), strongly intracellular weighted imaging techniques that limit the signal contribution from the more highly concentrated extracellular space (ECS) (140 mM vs. 10-15 mM intracellular) may provide an improved means to characterize [Na_{in}] in some cases.

Three approaches have been considered to isolate the NMR signal from intracellular sodium. The first concerns the use of shift-reagents (50). Unfortunately, toxicity and passage through the blood brain barrier remain a problem for *in-vivo* experiments. The second approach concerns the use of multiple-quantum filtering techniques (28,275). However, the signal intensity following a multiple-quantum spin sequence is a small fraction of the signal intensity following a single, ideal, 90^o excitation pulse (10% has been given as a

typical *in-vivo* value) (28). The third approach concerns the use of an inversion recovery (IR) technique and has been considered for mouse tumours (284).

If considerable T_1 relaxation differences exist between two environments, IR can be used to eliminate the signal contribution from either environment (285). Although it is well understood that the ECS in the brain contains many different types of proteoglycans, most attached to cell membranes, little is known about the density of these molecules. It has been suggested that the density of this extracellular matrix is quite sparse, allowing volume transmission through the ECS (229). Because T_1 measurements have been shown to correlate with matrix density (209), sodium T_1 relaxation in the ECS may be significantly longer than in the intracellular space (ICS). Shift reagent aided experiments using an implanted gliosarcoma in rats (50) also suggest this to be the case. Minimal sodium exchange is expected between the ICS and ECS on the relevant sodium NMR timescale (284). If the sodium T_1 in the ECS is significantly longer than in the ICS, an IR sequence may be used to eliminate the ECS signal contribution from a sodium image.

Unfortunately, sodium IR imaging of the human brain *in-vivo* is complicated by tissue heating or specific absorption rate (SAR) limitations. Because sodium T_1 relaxation is quite rapid *in-vivo* (<50 ms) 3D acquisition schemes with hard, nonselective, rectangular pulses are typically implemented, and repetition times (TR) may be as short as 30 ms in a steady-state approach (26). The addition of a 180^o inversion pulse to a sequence originally containing only one $<90^o$ excitation pulse dramatically increases the power dissipated by the sequence (a 180^o pulse dissipates 4x more power than a 90^o pulse if the pulse lengths are the same). This power increase can be mitigated by significantly increasing TR, but increasing TR has an adverse effect on image signal to noise ratio (SNR), by limiting the number of averages in a given scan time.

However, the average power dissipated by an MRI sequence is also inversely proportional to the length of the RF pulses in the sequence. But, due to the spin 3/2 nature of the sodium nucleus and its rapid biexponential T_2 relaxation *in-vivo* (the fast component has been measured as short as <1.0 ms (286)), it is important to limit echo time (TE) (29). For this reason sodium MRI sequences have typically been implemented with very short excitation pulses (as short as 0.2 ms (26)). However, the inversion pulse length in a sodium IR experiment is not limited by a short TE requirement. The great increase in sequence power dissipation associated with a 180^o pulse can be significantly reduced by dramatically increasing the inversion pulse length.

When the relaxation constants T_1 and T_2 are much longer than an RF pulse the effects of relaxation during the pulse can essentially be ignored. The calculation of flip angle is simple and is directly related to pulse power and length. While this is usually the case for the uncoupled ^1H nuclide, this is not the case for the quadrupolar sodium nucleus. In this paper the effect of relaxation during long (or soft) inversion pulses is explored. An IR technique labelled 'Soft Inversion Recovery Fluid Attenuation' (SIRFLA) is proposed for sodium imaging of *in-vivo* human brain and the efficacy of this technique is demonstrated through the minimization of sodium signal from the cerebrospinal fluid (CSF) in brain images acquired at a static magnetic field strength of 4.7 Tesla.

7.2. Methods

NMR Experiments were conducted using a 4.7T Varian (Palo Alto, CA) whole body MRI scanner. The maximum gradient strength was 35 mT/m, with a slew rate of 117 T/m*s. The spectrometer was fit with a 4 kW RF amplifier. All experiments were conducted using an in-house designed and manufactured single-tuned 53MHz quadrature birdcage head-coil.

To explore the sodium spin response during a long RF inversion pulse, quantum-mechanical sodium spin simulation software was designed. This software is based on the differential equations that describe the evolution of the density operator (using irreducible tensors) under the combined influence of relaxation and RF irradiation (71,145,146). The simulation results presented in this paper assume isotropic environments. The T_{00} spin operator (unity), omitted from the set of differential equations described in the previous references, was added so that the equilibrium value of longitudinal magnetization (I_z) could be included in the differential equation matrix solution. This enables M_z to relax towards M_0. The response of longitudinal and transverse magnetization to rectangular inversion pulses ranging from 0.5 ms to 10 ms was simulated, and spin-response benefits associated with longer inversion pulses were investigated.

The effects of relaxation during long inversion pulses were examined using spectroscopic experiments with spherical phantoms: a 20% agar gel phantom with 100 mM [Na^+] (tissue model) and a 500mM [Na^+] saline phantom (CSF model). To simulate the effects of relaxation in the spin simulation software, the spectral density parameters [$J_0(0)$, $J_1(\omega_0)$, and $J_2(2\omega_0)$] must be known (145). The high-frequency spectral densities for each phantom, $J_1(\omega_0)$ and $J_2(2\omega_0)$, were determined using an iterative inversion-recovery experiment. The low-frequency spectral density parameter, $J_0(0)$, the predominant component of fast transverse relaxation, was extrapolated from a pulse-acquire experiment. The following values were determined for the saline phantom [$J_0(0)$ = 10.64 +/- 0.01 Hz; $J_1(\omega_0)$

= 9.24 +/- 0.003 Hz; $J_2(2\omega_0)$ = 9.24 +/- 0.003 Hz], and the 20% agar phantom [$J_0(0)$ = 625 +/- 8 Hz; $J_1(\omega_0)$ = 50.8 +/- 1.9 Hz; $J_2(2\omega_0)$ = 30.4 +/- 0.2 Hz]. Because of the rapid molecular motion in the saline environment (i.e. the correlation time constant is very short < 10 ps) all three spectral density parameters in the saline phantom are expected to be equal. Although the effects of magnet inhomogeneity in the pulse-acquire experiment were taken into account in the regression (i.e. the inclusion of a dephasing envelope), errors may be larger than these values which represent the 95% confidence intervals of the least-squares fitting algorithm and indicate the quality of the fit.

To explore the combined effects of power deposition and spin-response on the SNR of an IR imaging sequence when long inversion pulses are used, a constant SAR experiment was conducted. Ten IR sequences with inversion pulse lengths ranging from 1 ms to 10 ms were implemented with appropriate TR values to achieve the same average power deposition in each sequence. The excitation pulse length was maintained at 1 ms. The inversion recovery delay (TI) for each sequence implementation was determined empirically using simulation and NMR experiments to minimize the signal acquired from the saline phantom (with very similar results). A spoiling gradient was added following the inversion pulse to eliminate residual transverse magnetization remaining at the end of the pulse. The height of the FID was measured at what would be the centre of k-space in the imaging experiments presented (TE of 2.3 ms). To determine the SNR benefits of long inversion pulses in an IR imaging experiment, the signal acquired from the non-nulled (agar) environment was multiplied by $\sqrt{TR_1/TR_k}$, where TR_1 is the length of TR when a 1 ms inversion pulse was implemented, and TR_k is the length of TR associated with each consecutively longer inversion pulse length. The calculation accounts for the fact that more averages can be acquired when a shorter TR is used in an imaging experiment of set total duration.

The time-averaged RF output power from the system was maintained below 6 Watts (the actual power absorbed *in-vivo* will be less due to cabling and coil losses) for each *in-vivo* imaging scan. SAR was calculated using the assumption that the average human head is 3 kg (SAR < 2 W/kg). The resonance frequency of sodium at 4.7 Tesla (53 MHz) is approximately 10 MHz less than the ^{1}H resonance frequency at 1.5 Tesla, and internal 'hot spots', problematic at the high resonance frequencies associated with large magnetic fields, are not expected. For each image, iterative asymmetric reconstruction was performed with k-space (Hamming) filtering in each dimension before Fourier transform. Shimming was performed manually by optimizing the sodium signal acquired over the entire head. Both SIRFLA and 3D-FLASH images were acquired, with a 5 minute delay between each scan, from 5 healthy volunteers.

The SIRFLA sequence was implemented by adding a 10 ms nonselective, rectangular, inversion pulse in front of a standard 3D gradient echo (TI = 21 ms, TR = 93 ms, excitation pulse = 1 ms, 90^{o}, nonselective, rectangular). Using the shortest excitation pulse length possible limits loss of transverse magnetization during the excitation pulse. However, SAR, and by corollary the minimum sequence TR, is also limited by the 90^{o} excitation pulse (especially for sequences using long inversion pulse lengths). From simulation results (data not shown), a 1 ms excitation pulse was chosen as a good compromise between the loss of transverse magnetization during the RF excitation pulse and minimum TR. The voxel dimensions were 5 mm x 5 mm x 10 mm and the imaging matrix was 128 following asymmetric reconstruction (anterior/posterior – read) x 60 (left/right – phase encode 1) x 30 (superior/inferior – phase encode 2). 60% asymmetric acquisition was used with an acquisition bandwidth of 12.8 kHz, yielding a TE of 2.36 ms. Four averages were acquired and the total scan length was 11.1 minutes.

3D-FLASH images were acquired for anatomical comparison with voxel dimensions of 3 mm x 3 mm x 7.5 mm, and an imaging matrix of 128 x 100 x 50.

A 0.75 ms nonselective, rectangular RF excitation pulse was used with a flip angle of 63^{o} and a TR of 30 ms. 60% asymmetric acquisition with an acquisition bandwidth of 12.8 kHz was used yielding a TE of 2.42 ms. Four averages were acquired and the total scan length was 10.0 minutes.

7.3. Results

Using the spectral density values listed in the methods, initial simulations investigating the effect of relaxation during RF inversion pulses are shown in **Figure 7-1**. During longer RF pulses (e.g. 10 ms) the differences in relaxation between saline (CSF model) and 20% agar (tissue model) significantly separate the values of longitudinal magnetization in these two environments.

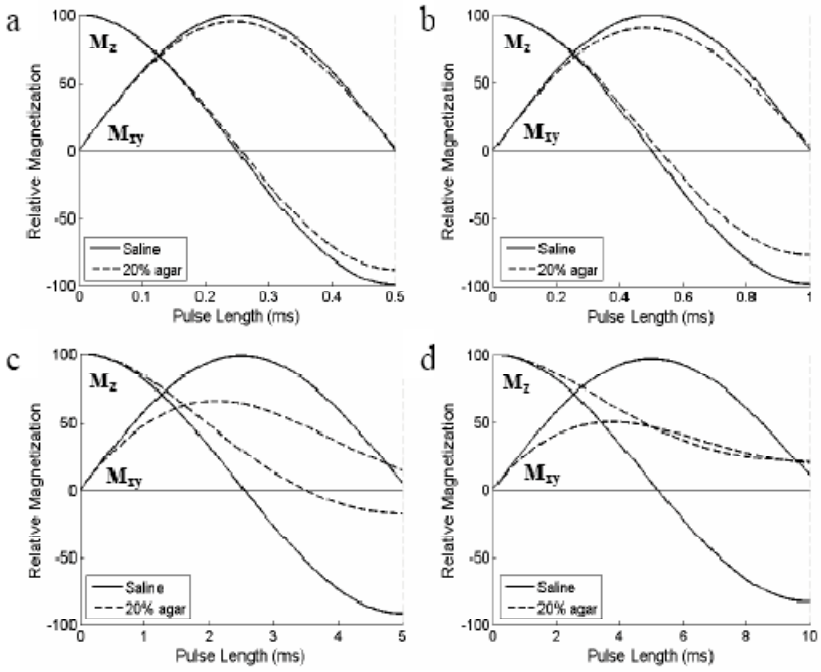

Figure 7-1 : The effect of relaxation on the longitudinal and transverse magnetization generated in both saline and 20% agar during RF inversion pulses of length: **a)** 0.5 ms; **b)** 1.0 ms; **c)** 5.0 ms; **d)** 10.0 ms. As the RF inversion pulse length increases, the 'depth' of inversion significantly decreases in the 20% agar phantom. Since the saline inversion does not vary greatly with inversion pulse length, a significant difference in M_z magnetization exists between agar (i.e. brain tissue model) and saline (i.e. tissue model) at the end of a long inversion pulse.

The benefits of increasing the inversion pulse length in an IR experiment are twofold. Increasing the inversion pulse length allows TR to be shortened while maintaining acceptable SAR. This permits more averages to be acquired in an imaging experiment for a given scan length. Increasing the inversion pulse length

also significantly increases the value of M_z in the agar phantom following the delay period TI required to null the signal in the saline phantom (a direct result of the reduced inversion in the agar phantom). In **Figure 7-2** the combined benefits of long inversion pulses are displayed. In the 20% agar phantom an approximately 85% signal increase could be achieved by switching from a 1 ms inversion pulse to a 10 ms inversion pulse in an IR imaging experiment with the same SAR and scan length. Of this 85% increase, 20% is directly associated with relaxation during the RF pulse.

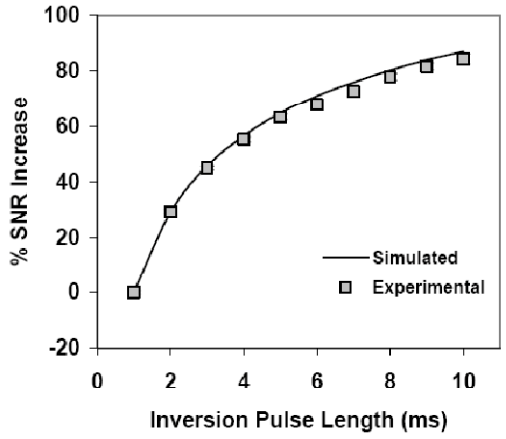

Figure 7-2 : The beneficial effects of soft inversion pulses (measured in 20% agar) on relative SNR of an imaging experiment for constant SAR and a constant acquisition period. For each simulated and experimental data point, TI has been appropriately adjusted to null the signal from a saline phantom. Residual transverse magnetization was sufficiently spoiled following the inversion pulse. The relative SNR of each data point was calculated from the simulated, or acquired signal, and the $\sqrt{N_{ave}}$ SNR increase associated with reduced TR in a constant length experiment.

In-vivo images of the human brain generated using 3D-FLASH and SIRFLA are shown in **Figure 7-3**. For the 5 volunteers the SNR in the 3D-FLASH image was measured to be 16 +/- 2 and 45 +/- 3 in brain tissue and CSF, respectively. In contrast, the SNR of brain tissue in the SIRFLA image was measured to be 17 +/- 1.5, whereas the SNR was only 4 +/- 2 in CSF. Note that the sodium acquisition voxel size of the CSF-suppressed SIRFLA images (0.25 cm^3) is 3.7 times greater than that in the standard 3D-FLASH images (0.0675 cm^3). The sodium signal

from CSF is approximately 2.8x the signal from brain tissue in the 3D-FLASH image, while in the SIRFLA image the signal from CSF is approximately 0.23x the signal from brain tissue.

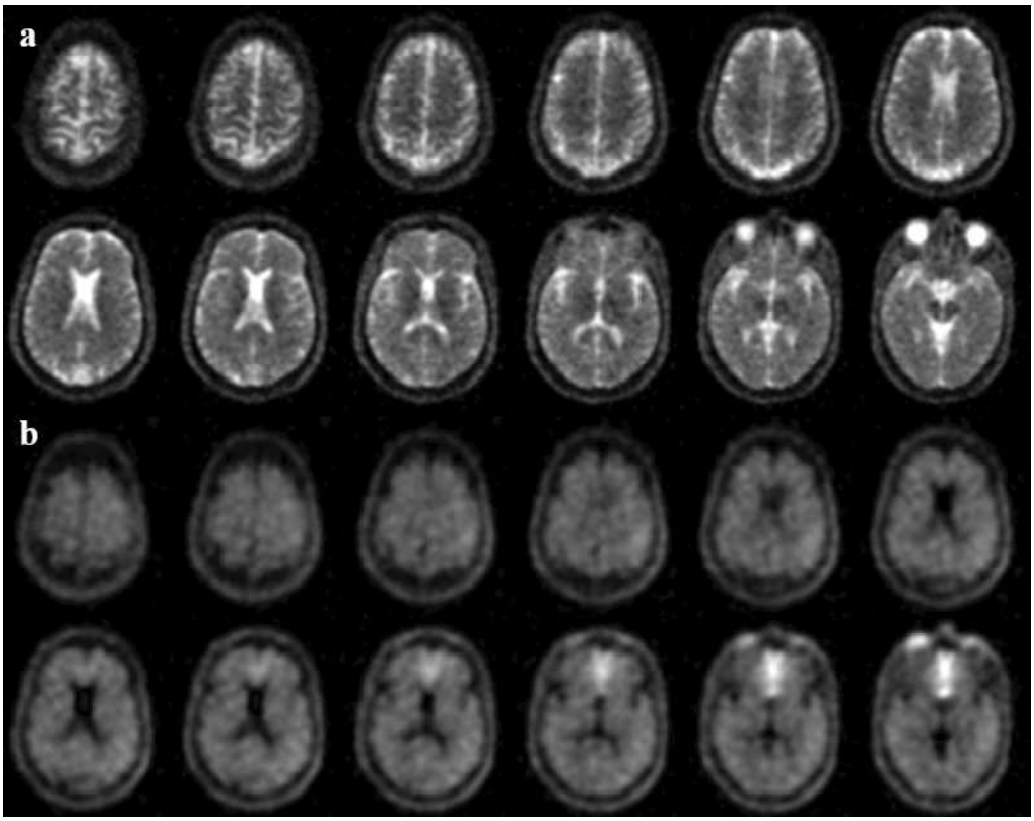

Figure 7-3 : Sodium images acquired from the same healthy volunteer at 4.7T. **a)** 3D-FLASH images acquired in 10 minutes with a voxel size of 0.0675 cm^3. SNR in the CSF is 46; SNR in the brain tissue is 15. **b)** CSF-suppressed SIRFLA images acquired with an inversion pulse length of 10 ms and a TR of 93 ms from a healthy volunteer in 11.1 minutes with a voxel size of 0.25 cm^3. SNR in the CSF is 3.3; SNR in the brain tissue is 18.

7.4. Discussion

The effectiveness of soft inversion pulses to separate sodium longitudinal magnetization in different environments has been shown **(Figure 7-1)** along with the resultant benefit in the SIRFLA sequence **(Figure 7-2)**. This separation is the direct result of the large quadrupole interaction experienced by the sodium nucleus and is not possible in conventional ^{1}H NMR. It is because the inversion pulse length has a dramatic impact on signal acquired from the non-nulled environment that this IR sequence implemented with long RF inversion pulses has been given the new designation 'Soft Inversion Recovery Fluid Attenuation' – SIRFLA. An IR image was also acquired with an inversion pulse of 1 ms and TR of 334 ms (for equivalent SAR – **Figure 7-4b**). Using two averages and a reduced imaging matrix (with the same voxel size) this image was acquired in a scan time of 10.7 minutes. Image SNR was only 10 in the brain tissue when the short 1 ms inversion pulse was used whereas the brain tissue SNR was 17 when the long 10 ms inversion pulse was used in the SIRFLA sequence.

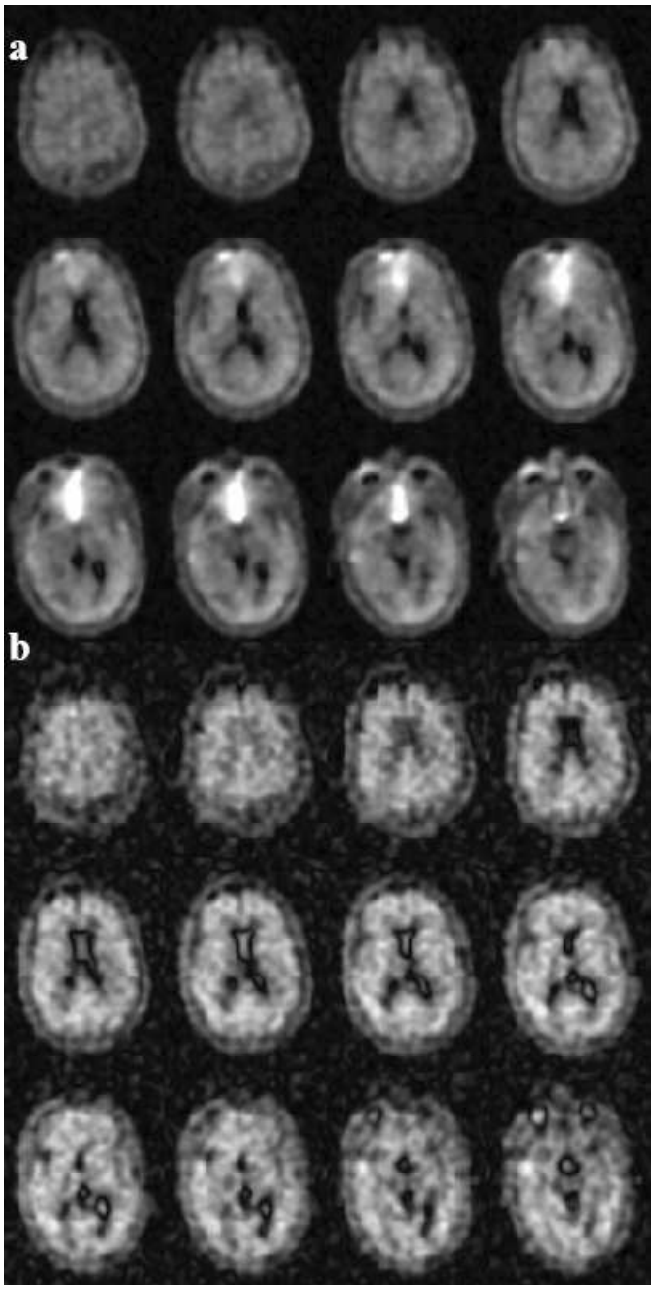

Figure 7-4: **a)** SIRFLA images acquired in another healthy volunteer with image parameters the same as in **Figure 7-3b** (inversion pulse length of 10 ms). SNR in the CSF is 4 and SNR in the brain tissue is 17. **b)** Sodium IR images acquired with a much shorter inversion pulse length of 1 ms and a TR of 334 ms. SAR and voxel size are equivalent to **(a)** and the image duration was 10.7 minutes (or ~ 25 seconds shorter than **(a)**). SNR in the CSF is 2.5 and SNR in the brain tissue is 10. Notice that the SNR is 70% greater in **(a)** with the longer inversion pulse than in **(b)**. One disadvantage of the longer inversion pulse is its narrow bandwidth which results in an artifactual hyperintensity in the known areas of susceptibility **(a)** that is not seen in **(b)**. The images in **(a)** and **(b)** are not globally scaled.

In this paper CSF-suppressed SIRFLA sodium images of the human brain have been presented. These images have an acquisition time of 11.1 minutes, a matrix voxel size of 0.25 cc and an SNR of 17, and are comparable to those acquired at 1.5T for patient studies (6,12,30). Although removing partial volume averaging from CSF is one benefit, the main advantage of the SIRFLA sequence most likely lies in the potential of IR to generate strongly intracellular weighted images (as proposed by Kline et al. (284) and described in the introduction). For this reason, an appropriate comparison of image quality should be made with other techniques that consider intracellular weighted imaging (28). A 3D gradient recalled echo (3DGRE) acquisition was used to acquire the SIRFLA images, but this k-space acquisition technique has rather long echo times (for sodium), because of phase-encode and readout 'rewind' gradients. The implementation of 3D projection acquisition (3DPA) would eliminate the need for preparatory gradients and, as acquisition begins at the centre of k-space, would significantly reduce echo times. 3DGRE is sufficient to demonstrate SIRFLA as a technique, however switching to an optimal form of 3DPA (30) should significantly improve SNR and image quality.

The TI used in the SIRFLA images presented was chosen to null signal from CSF, demonstrating the ability to null signal in slower relaxing environments. Admittedly sodium relaxation in the extracellular space (ECS) is presumably quicker than in CSF. Considering the intracellular space (ICS) and ECS sodium relaxation times (ICS: T_1 = 24 ms, T_{2fast} = 2.0 ms, T_{2slow} = 13.9 ms. ECS: T_1 = 46 ms, T_{2fast} = 3.4 ms, T_{2slow} = 30.1 ms) measured in a gliosarcoma implanted in a rat (50), the optimal TI to minimize the ECS signal contribution would be ~ 7 ms (from simulation). This shortened TI, relative to the 19 ms TI used for CSF, results from the fact that the ECS will also experience only 'partial inversion' during the long inversion pulse, because of rapid T_{2fast} decay. The M_z value of the ICS after the inversion time TI of 7 ms would be ~36% of its fully relaxed value (from simulation). Considering these relaxation parameters the SIRFLA sequence may offer an SNR benefit over TQF for intracellular imaging (287). The TQF

sequence is also limited by SAR, as three hard 90^o RF pulses are required and increasing the RF pulse length decreases acquired signal intensity (71). A TQF sequence with three 1 ms 90^o RF pulses and the same TR presented for the SIRFLA sequence would dissipate twice the power of the SIRFLA sequence. The SIRFLA sequence can also theoretically facilitate 'full elimination' of the ECS signal contribution. *In-vivo* TQF studies suggest a 40% residual contribution from the ECS (49).

Several marked artifactual hyperintensities can be seen in **Figures 7-3b** and **7-4a** that are not apparent in **Figure 7-4b**. The most significant begins above the sphenoid sinus and extends into the frontal lobe. Two other less pronounced artifacts exist on the outer edges of the parietal lobes. Susceptibility induced B_0 inhomogeneities are well known to exist in these areas, a product of the surrounding sinuses and bone. Artifacts caused by these B_0 inhomogeneities are apparent in other imaging modalities such as single-shot EPI. These artifacts (**Figures 7-3b** and **7-4a**) are the result of the narrow bandwidth associated with the long inversion pulse and are minimized by the wider bandwidth of the short inversion pulse in **Figure 7-4b**. Improved shimming may help reduce these artifacts.

This paper demonstrates the first application of inversion recovery to sodium imaging in humans. The benefits of soft inversion pulses in the SIRFLA sequence were demonstrated through simulation and comparison with pseudo-biological environments. The application of the SIRFLA sequence to disease and its benefit to *in-vivo* sodium brain imaging remains to be evaluated.

Chapter 8

Discussion and Conclusion

8.1. Thesis Summary

This thesis concerns the analysis and optimization of sodium MRI for imaging the human head. Using the 'high quality' images facilitated by this work, a study of acute stroke was conducted and time dependent intensity increase on sodium images following stroke onset was conclusively demonstrated in humans for the first time.

Chapter 2 highlights that k-space filtering should be a requirement for human brain sodium imaging, minimizing contamination of brain tissue measurements with ringing from the 3x concentrated cerebral spinal fluid (CSF) space which does not exhibit rapid signal decay. A k-space filter shape is proposed for twisted projection imaging (TPI) implementation and used to quantify the signal-to-noise ratio (SNR) advantage of filtering by sampling density design as opposed to filtering by post-acquisition weighting. Chapter 2 also demonstrates a 'noise colouring' advantage associated with filtering by sampling density design.

Chapter 3 concerns quantification of the 'noise colouring' discussed in Chapter 2. This quantification involves measurement of correlation volume, or the volume of effective 'statistical independence' and is of value to determine the number of voxels required within a region of interest (ROI) to attain a desired measurement precision. A theory for the computation of correlation volume is proposed for any noise power spectral density and ROI volume. Chapter 3 highlights that standard radial imaging with its excessive oversampling at the centre of k-space and low-frequency noise reduction facilitates measurement precision in smaller ROIs than the TPI technique even though TPI is more efficient with respect to SNR.

While TPI may not be beneficial with respect to image noise (ironically, the context in which it was originally proposed), a different advantage of this technique with respect to T_2 decay is highlighted in Chapter 4. This chapter concerns optimization for the minimum object volume required to attain a given measurement precision (with respect to image noise) and accuracy (with respect to PSF smearing and image intensity modulation with object volume). It is suggested that radial evolution altered k-space acquisition (of which TPI is a member) with sampling density designed k-space filtering, a small (as possible) value of *p* and 'long' readout duration is an optimal radial approach to sodium imaging of the human brain, given small voxel volume implementation such that image SNR is ~ 1/8 – 1/4 that required for the desired measurement precision. This radial k-space acquisition approach is used in Chapters 5 and 6.

Chapter 5 diverges from consideration of k-space acquisition to discuss NMR sequence optimization. A steady-state approach to sodium MRI is proposed in combination with TPI to achieve a greatly increased SNR/voxel-volume relationship when compared with typical TPI implementation using full T_1 recovery. This advantage exists despite TE increase (related to RF pulse length increase) required to facilitate steady-state imaging under power deposition constraint at high field.

In Chapter 6 a time-dependent intensity trend on 'high quality' sodium images following time after stroke onset is demonstrated for acute human stroke. This trend follows the shape of an asymmetric sigmoid curve, and exhibits initial delay up to < 6 hours at which point rapid increase begins. This period of increase is followed by asymptotic levelling at roughly a day after stroke onset. The time-line for intensity on the sodium images appears to be somewhat different than that on standard proton MR images, which likely reflect tissue water concentration changes.

While Chapters 2 – 6 are concerned with 'bulk tissue' sodium imaging, or the analysis of all the sodium within tissue, Chapter 7 concerns the other aspect of sodium imaging that has garnered a particular amount of interest in the literature, the potential for selective imaging of intracellular sodium. An inversion recovery based sequence is presented in which sodium nuclei with different relaxation times are separated both by fast T_2 differences during a soft inversion pulse, and slow T_2 differences during inversion recovery. The 'softness' of the inversion pulse also mitigates the power deposition associated with the inversion pulse. This technique was demonstrated through the minimization of signal from the potentially problematic CSF space in human brain.

This thesis has attempted to provide improved methodology to each (current) major aspect of sodium imaging as it pertains to the human brain: k-space acquisition; bulk tissue NMR sequence optimization; and relaxation selective NMR sequence optimization. Further discussion specifically related to each of these is given below, along with some discussion of an additional characteristic of sodium NMR that should be addressed. The possible role of sodium MRI in the setting of acute stroke is discussed, and other potential applications of sodium MRI are proposed.

8.2. Discussing Aspects Related to this Thesis

8.2.1. Concerning Other k-Space Acquisition Methods for Human Brain Sodium MRI

Two other k-space acquisition methodologies have been used for sodium imaging of the human brain: they include the (asymmetric) gradient echo (GRE) (3,23) and single point imaging (SPI) (39) techniques. The former, suffers from longer minimum TE values (the primary result of correlation between TE and readout duration), and problematic partial k-space reconstruction (unless fully asymmetric acquisition is used – i.e. each half of k-space is acquired separately). In the case of fully asymmetric k-space acquisition the use of long readout duration to reduce

noise variance, facilitating voxel volume reduction, will result in extensive one-dimensional PSF smearing. The gradient echo technique presents no way to achieve T_2 decay reshaping across k-space, or smooth sampling density related k-space filtering (within the confines of Cartesian acquisition). However, GRE Cartesian acquisition does facilitate much simpler image production, i.e. a gridding process (Appendix 2) is not required, and MR scanners do not need to be reprogrammed.

The pure-phase-encode SPI technique does not exhibit any modulation across k-space related to T_2 decay, however, readout durations are inherently *very* short as only one k-space location is acquired per excitation. As a result, voxel volumes must be very large to achieve sufficient SNR. The downside of very large voxels is the inability to contain CSF within its space for analysis of brain tissue, particularly along the cortex. The SPI technique also suffers from the requirement of *many* more excitations to fill k-space than the GRE or TPI techniques. As a result, SNR inefficient NMR pulse sequences with very small flip angles and very short TR values are required. Images copied from the .pdf documents in which the GRE and SPI techniques have been used to image the human brain are given below (Chapter section 8.3).

8.2.2. Concerning Anisotropic k-Space Acquisition

Centre-out radial acquisition generally implies a sampling of k-space to a spherical extent. However, that need not be the case. The oblate spheroidal k-space acquisition used in Chapters 5 and 6 was presented at the non-Cartesian workshop in Sedona, Arizona (288). It's development is very straight forward and simply involves a scaling of the z-axis gradient values of each projection during design (maintaining sampling density shape). The SNR increase associated with the global sampling density increase (which can also be described in terms of voxel volume increase) can be use to decrease in-plane voxel dimensions.

Anisotropic voxels are acquired for the vast majority of standard proton scans. Most often this is done out of necessity when 'full' brain coverage is desired for two-dimensional imaging and scan time must be limited (i.e. slices are made thick). There are two reasons to implement anisotropic voxels for sodium imaging. The first, and perhaps most compelling, is to match the voxel shape with the shape of the object to be assessed. In this manner a maximum number of voxels can be fit within the object, and equal numbers of voxels fit across the length and breadth of the object. As highlighted in Chapter 4, image intensity modulation with object volume for isotropic k-space acquisition is exacerbated in anisotropic objects. This is intuitive for a 'narrow' object as PSF smearing will have greater effect across the narrow width. Spatial scaling of the PSF in proportion to the shape of an object will minimize this effect. Oblate spheroidal k-space acquisition may be of particular value to evaluate sodium within the hippocampus, with its 'cylindrical-like' shape. Oblate spheroidal k-space acquisition may also be useful to evaluate sodium within long directional white matter fibres. Higher in-place resolution facilitates improved 'selective imaging,' or less partial volume averaging with neighbouring fibres.

The second reason to implement anisotropic voxels for sodium imaging concerns the 'matching' of sodium images to standard proton images. In the human stroke study of Chapter 6, sodium images were co-registered and re-sliced according to the diffusion weighted proton images (DWI), on which the boundaries of the stroke were identified. The DWI images were highly anisotropic, having a slice thickness of 5 mm with a 1.5 mm gap and 0.65 mm in-plane voxel dimensions (i.e. effective 3D voxels of 10:1:1). Anisotropic sodium voxels were acquired to somewhat match the out-of-plane dimensions of the sodium and DWI voxels (the sodium acquisition voxel dimensions were 4.8 mm out-of-plane and 2.4 mm in plane). Seeking greater out-of-plane resolution for sodium imaging only to lose it in the re-slicing process was considered to be SNR inefficient. However, as sodium imaging contains considerable PSF blurring which can modulate image

intensity within the lesion (Chapter 4), implementing anisotropic voxels to assess lesions with no particular known anisotropy may not be beneficial.

8.2.3. Concerning Projection Twisting

The advantage of altering the radial evolution of each projection to reshape T_2 decay across k-space is unrelated to projection twisting (Chapter 4) (36). However, this does not mean that maintaining a constant sampling speed while radial evolution slows is not unuseful for sodium imaging (see also Appendix 1). When filtering by sampling density design is implemented the extent of sampled k-space can be expanded. For a k-space sampling to a discrete matrix diameter of 80 (the case for 3.2 mm cubic acquisition voxels and a field of view of 256 mm), ~ 20,000 straight radial projections would be required to fill k-space. Assuming 'full' T_1 recovery following a 90^o excitation pulse is desired (with TR = 150 ms), the minimum scan time would be 50 minutes for complete Nyquist k-space coverage. Under-sampling k-space with a reduced number of projections will generate noise-like error in the image (262). This problem is exacerbated if anisotropic k-space acquisition is used as described above. For this implementation, which maintains sampling density shape, the minimum number of projections required to critically fill k-space is given by the discrete matrix diameter of the expanded 'high-resolution' dimensions (i.e. the z-dimension scaling of each projection will not improve projection spacing around the z-poles). For 2.4 mm in-place acquisition voxels (and a field of view of 256 mm), ~ 35,000 straight radial projections would be required. For twisted projection imaging, the number of projections required can be reduced in proportion to p (30,56). It should be noted, however, that minimum scan time can also be reduced by a factor of 6 if the steady-state PASS approach is used instead of a full T_1 recovery sequence (Chapter 5); for PASS implementation projection twisting may not be necessary.

8.2.4. Concerning Sodium Relaxation Characterization in Brain Tissue

Although three papers have been written concerning the measurement of bulk tissue T_2 (or T_2*) in the human brain (25,37) the fast T_2 component, which accounts for 60% of the biexponential decay, remains to be confidently defined. The first paper in 1989 (48) does not measure biexponential relaxation, and the subsequent papers in 2004 (25) and 2009 (37) are concerned with the slow component of T_2* relaxation. Although a value for the fast T_2* component is suggested in (25) (1.7 ms), this value is associated with a large confidence interval. Minimum echo times shorter than 12 ms (gradient-echo) (37), 3.8 ms (gradient echo) (25), and 2.5 ms (spin-echo) (48) are likely required to evaluate the fast T_2* component of sodium relaxation.

To the author's knowledge only one paper has measured T_1 values for bulk human brain tissue (6). However, the T_1 value measured for CSF (20 ms) is much less than expected from measurements of the slow component of T_2* for CSF (> 47 ms) (25,37,48). In fluid environments T_1 is expected to be equal to T_2 which will be monoexponential (160). This result casts doubt on the T_1 measurements made in both white and gray matter.

It is suggested that a comprehensive analysis of sodium relaxation in the human brain is in order. A study including 7 healthy volunteers has been initiated to this end. It is proposed that with the radial k-space acquisition methodology of this paper and a minimum TE of 0.4 ms (and a total of 7 different TE values), the fast component of 'bulk tissue' T_2* can be identified with high confidence in the regression (typically $\pm$15% for both short and long). The T_2* values used in Chapter 4 for radial k-space acquisition optimization come from average 'general subcortical tissue' T_2* measurements in 5 healthy volunteers. It is also proposed that using the SIRFLA technique with 6 different inversion times a monoexponential T_1 approximation can be measured with high confidence in the regression (initial analysis suggests a 'general subcortical tissue' measure of ~37

ms). These methods have been validated for their consistency in agar phantoms. Segmented tissue analysis remains to be conducted.

It is also suggested that a comprehensive analysis of sodium relaxation in the human brain include some consideration of environmental compartmentalization. It is proposed that differences in 'bulk tissue' T_2 measured with relaxometry conducted using either a triple quantum approach or an approach based on the SIRFLA technique with a fluid-nulling inversion delay may reflect some form of environmental compartmentalization. Early triple quantum regression using simulation based spectral density regression (presented at ISMRM Seattle, Stobbe, Beaulieu, 2006 (45)) suggests more rapid T_2 decay when fluid signal is eliminated.

8.2.5. Concerning Residual Quadrupole Effect in Brain Tissue

Sodium nuclei possess a spin 3/2 related NMR contrast mechanism which has essentially been ignored for sodium imaging of the human brain. The existence of this contrast mechanism is of particular importance if absolute tissue sodium concentration measurements are to be made. For measurements of this sort the signal attained must solely depend on sodium concentration, i.e. all NMR related weighting must be eliminated. To attain concentration measurements of sodium nuclei in the human brain minimization of *relaxation* weighting has been the primary concern (234). However, in 'ordered' environments the transverse magnetization of spin 3/2 sodium is affected by more than rapid biexponential relaxation – the spectrum of transverse magnetization is split into three components (a central peak and two satellites, see Chapters 1.5 and 1.6). There are several problems associated with spectral splitting including: partial signal position shifts in the image, and partial signal dephasing in large voxels with inhomogeneous 'order' (the partial signal effects are associated with the satellite components of the split signal). Another, perhaps greater problem involves 'selective spectrum excitation.' If the bandwidth of the RF excitation pulse is not

sufficiently wider than the extent of the split spectrum, less than 100% of the available longitudinal magnetization can be 'flipped' into the transverse plane; in the extreme case of a very narrow bandwidth RF pulse the maximum transverse magnetization possible is only 20% of the available longitudinal magnetization (247).

The notion that sodium signal loss may arise from spectral splitting is quite old, and has been described in terms of 'invisibility' (246), however, this signal loss mechanism has essentially been ignored in the context of imaging the brain since 1987. In 1987 it was reported that sodium was 100% visible with respect to spectral splitting in (cat) brain (236). An experiment similar to that of (236) was recently conducted in healthy human brain, yielding evidence of a significant spectral splitting related signal loss effect. This result, presented at ISMRM Hawaii (Stobbe, Beaulieu, 2009) (164), has impact for absolute sodium concentration measurement, and is exacerbated at high field where maximum RF bandwidths are increasingly constrained by RF power deposition. A method for minimizing this residual quadrupole dependent contrast would be beneficial. Alternatively, it is suggested that this NMR contrast mechanism which is highly dependent on tissue order may be interesting to explore in cases where tissue order is pathologically altered.

8.2.6. Concerning the PASS Sequence and its Use in the Stroke Study

The steady-state sequence optimization of Chapter 5, used a fast T_2 (or T_2*) value suggested by (25) (which was corroborated by relaxation measurements made using a novel approach to fast T_2 relaxation that measured T_2 effect during a soft inversion pulse (45)). More recently, fast T_2 measurements using a more robust 'standard' multiple TE approach in healthy human brain (as mentioned above) suggest longer values of fast T_2 (i.e. an increase from 1.7 ms to 2.9 ms). If this longer value of fast T_2 would have been used in the optimization of Chapter 5,

slightly greater benefit associated with the PASS sequence would have been expected (from 38% to 41%).

It is suggested in this thesis that the large SNR benefit associated with the use of a steady-state approach to sodium imaging is worth the addition of relaxation contrast to the images. As suggested in Chapter 4, the minimum object volumes (with brain tissue relaxation parameters) required for precise and accurate analysis can be quite large. If physically small pathologies are to be assessed, the SNR/voxel-volume relationship must be increased. Increasing scan duration is one approach. However, implementing a steady-state approach yields roughly the same advantage as doubling scan duration, and as Chapter 4 suggests, may be required in addition to long scan duration.

The T_2 weighting at an increased TE of 0.6 ms associated with PASS implementation (when compared to 0.3 - 0.4 ms of other full T_1 recovery TPI implementations (66)) is still quite small, yielding a transverse magnetization loss of only ~ 12% as a result of this delay (compared with 7% at a TE of 0.3 ms). Large changes in tissue T_2 decay would be required to substantially affect signal intensity. However, relatively large T_1 weighting is introduced by the PASS sequence. In the setting of hyper-acute stroke it could be hypothesized that both T_2 and T_1 relaxation may become more rapid given the intracellular compartmental shift of anoxic depolarization (and the supposed increased macromolecular density of the intracellular space). While T_2 related signal loss would increase, this loss would be offset by more rapid T_1 recovery in a steady-state sequence. Any differences between the steady-state PASS and non-relaxation weighted TPI sequences in the setting of hyper-acute stroke remain to be determined, but are expected to be minimal. In the sub-acute setting of stroke (the period of days post-onset), as tissue structure begins to disintegrate sodium T_1 times may lengthen toward that of fluid. In this case, measured lesion intensities are expected to be reduced by increased T_1 saturation effect.

In the past others have been concerned with answering the specific question of sodium concentration in tissue (6,12,66). The scientific merit of quantitative [^{23}Na] MRI is unquestioned. The potential to evaluate a real and directly relevant component of physiology sets sodium MRI (and proton spectroscopy for that matter) apart from standard proton MRI, whose links to real physiological components are indirect. However, in a medical diagnostic context image correlation with pathology is of greatest concern. Although the exact nature of any given contrast may be complex and involve many real physiological processes, this contrast can have great diagnostic value if it robustly predicts pathophysiologic tissue state. This premise is used extensively for standard proton MRI.

While tissue sodium concentration measurement in acute stroke may provide knowledge of a real physiological variable, any direct correlation between tissue [^{23}Na] and stroke patient pathophysiologic status with respect to treatment consideration remains unknown. It has been suggested that a specific tissue [^{23}Na] level predicts irreversible tissue damage, however, this study (which involved 1 treated and 1 non-treated non-human primate) (12), could just as easily have been conducted using the PASS sequence and the same correlation made with '[^{23}Na] plus relaxation' image intensity.

Finally, it's again noted, if one wants to argue that the value for sodium imaging lies solely in absolute concentration measurement, attaining an accurate concentration measurement may be complicated by more than rapid relaxation. As discussed above, signal loss related to spin 3/2 residual quadrupole interaction may also be present in human brain tissue. For any sodium MRI sequence, image intensity may only be a reflection of sodium concentration.

8.2.7. Concerning the Enhancement of Sodium NMR Dependent Contrast

Further sodium MRI consideration beyond the 'quantitative [^{23}Na] box' may yield other interesting image correlation with pathology. The relaxation mechanism of sodium (i.e. the quadrupole interaction – see Chapters 1.5 and 1.6) is different than that of protons in water, and relaxation differences as great as 50x may exist between sodium T_{2f} in cellular environments and that in fluid spaces. The purpose of a novel sequence (labelled Projection Acquisition with Coherent MAgNetization – PACMAN) recently presented at ISMRM Toronto (Stobbe, Beaulieu, 2008 (249)) is to enhance the unique relaxation contrast of sodium in an 'additive' manner. This is accomplished through steady-state imaging with transverse magnetization refocusing, increasing signal from sodium nuclei in environments with longer T_2 relaxation constants. It is proposed that the PACMAN sequence also enhances quadrupole splitting dependent contrast, and as such provides a strong link to long range tissue order. The contrast of this sequence may be interesting to study in demyelination disorders such as multiple sclerosis.

8.2.8. Concerning the SIRFLA Sequence

The purpose of the SIRFLA sequence presented in Chapter 7 was to null signal contribution from fluid environments. Assuming the interstitial space in the human brain is more fluid-like than the intracellular space (which remains unknown, but likely – see Chapter 1.6), it may be possible to selectively acquire signal from intracellular sodium ions. The same assumption concerning these compartmental relaxation differences is the basis for the substantial work that has gone into developing multiple quantum filtering techniques (see Chapters 1.5 and 1.6). 'High quality' triple quantum filtered images of the human brain were recently presented by our lab at ISMRM Toronto (Tsang, Stobbe, Beaulieu, 2008 (289)). However, even 'optimized' multiple quantum filtering suffers from very low yield. It is proposed that the SIRFLA sequence can produce images with as much as 5x – 10x the SNR/voxel-volume relationship of triple quantum images. It

is suggested that presentation of a direct comparison between SIRFLA and triple quantum filtered imaging is in order. A quick visual inspection is offered below for a 10 minute SIRFLA image, and the 11 minute TQF image presented in the ISMRM abstract of Tsang (289).

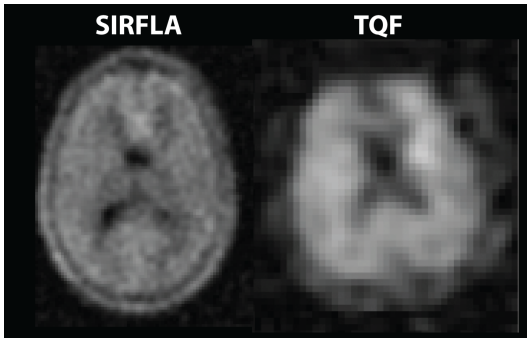

Figure 8-1: SIRFLA and TQF images of healthy human brain, both generated at 4.7T in approximately 10 minutes.

It is also proposed that the SIRFLA sequence can 'completely' null signal contribution from the interstitial space if it is known, even if it still exhibits mild bi-exponential relaxation. Triple quantum filtering will only 'completely' null signal contribution from fully fluid environments exhibiting monoexponential relaxation. However, a SIRFLA image with its soft inversion pulse suffers to a greater extent from susceptibility related artifacts.

It is suggested that the value of intracellular sodium imaging (given its possibility) lies in the analysis of compartmental sodium redistribution without tissue sodium concentration change. This is the case expected very acutely in ischemic stroke (see Chapter 1.2). Interestingly, triple quantum filtered signal has 'mirrored' this early expected sodium redistribution in an animal stroke model (111). SIRFLA images collected from most of the stroke patients in Chapter 6 also highlight a different image intensity trend than the bulk tissue images. This data remains to be presented.

Intracellular sodium concentrations may also be increased in correlation to tumour grade (or rate of cellular proliferation) (218,219), and sodium influx is involved in

apoptotic or 'programmed' cell death (290) and the toxic effects of chemotherapy (284). Although comparison of intracellular sodium signal (again assuming its acquisition possibility) from tumour with normal tissue may be intriguing, an evaluation of this sort will be confounded by large cell packing changes in tumour tissue (235). While intracellular sodium concentrations may be increased, this increase will be offset by a smaller fraction of space being occupied by the oncotic cells. It is suggested that bulk sodium tumour analysis, as recently conducted by Bartha (3), in which the effects of cellular packing and intracellular sodium increase combine (rather than offset) may be of more practical value. However, intracellular sodium imaging may be of value for the assessment of early tumour apoptotic response to chemotherapy (284). Assuming the total sodium concentration remains constant before and directly following the administration of chemotherapy (i.e. before expected cellular disintegration) intracellular sodium influx may reflect initiation of cellular apoptosis – the design goal of chemotherapeutic approaches.

The SIRFLA images of Chapter 7 were acquired using gradient echo imaging (before TPI was developed during PhD thesis). It is suggested that these images can be improved with the radial k-space acquisition method used in Chapters 5 and 6 of this thesis (this method is used for both the SIRFLA and TQF images in **Figure 8-1** above). In Chapter 4 it is also proposed that compensating brain tissue relaxation with sampling density may be advantageous for fluid-nulled sodium imaging. This has yet to be evaluated.

8.2.9. Concerning Sodium MRI in Stroke

Although an intensity increase on sodium images with time after onset was demonstrated for acute stroke (Chapter 6), this curve has considerable scatter. If sodium imaging is to be predictive for time after onset, this scatter will need to be minimized. It is suggested that one of the greatest sources of this scatter is stroke location and the inclusion of different percentages of gray and white matter. With

an increased number of patients scanned, the segmentation of signal intensity increase for different tissue types may aid in the reduction of this scatter.

The sodium images of Chapter 6 were analyzed using ROIs drawn on the DWI images, and as such each ROI included the full volume of the lesion. Analysis that redefines the ROIs within the lesion according to desired measurement accuracy and precision (as per Chapter 4) would remove any intensity modulation with lesion volume. However, given varying lesion sizes throughout the study time-line and the large degree of unrelated scatter, the shape of the intensity increase with time after onset is not expected to be significantly altered with redone ROI analysis as per Chapter 4. Redone ROI analysis may, however, slightly reduce the scatter in this trend.

An alternative to the use of sodium images in acute stroke for 'timing' related purposes may be the use of standard T_2-weighted, FLAIR, or proton density images. The timelines of tissue water and sodium accumulation may be significantly different during the hyperacute period of stroke (68) and differences in the 'predictive capability' of each technique remain to be determined. In this thesis the timelines of signal intensity increase on T_2-weighted and FLAIR images were compared with sodium, however, signal intensity increases on proton density images, more directly reflecting water concentration increase, were not considered.

While considerable effort has been focussed on the imaging based identification of patients with under-perfused, at risk tissue that may benefit from thrombolysis with rtPA (100,291), recent thought has also been given to the imaging based identification of patients who may be at greater risk of thrombolytic harm from symptomatic intracranial haemorrhage (292). Early ischemic changes on CT (293,294), the size of the DWI lesion (295-297), as well as the presence of leukoaraiosis (or white matter T_2 hyperintensity), a radiological marker of chronic ischemic damage of the cerebral microcirculation (298), have all been correlated

with symptomatic intracranial haemorrhage following rtPA. If the decision to treat could be based solely on the risk and benefit identified for each patient with medical history (293) and imaging, a treatment option may be opened to those beyond current time window constraints.

It has been suggested that blood brain barrier damage secondary to prolonged ischemia may be an important mechanism for intracranial haemorrhage (130,292,299), and several studies have investigated imaging methods of measuring the permeability of the blood brain barrier in this regard (300-302). It is hypothesized that the rate of sodium increase within the lesion core may also reflect the permeability of the blood brain barrier, with delayed rapid increase reflecting the delayed fenestrated opening of the microvasculature associated with transformation to the period of vasogenic edema (130).

8.2.10. Concerning Other Proposed Sodium Imaging Uses

It has been proposed through modelling that intracellular sodium concentrations may be substantially increased (by as much as 50%) for sustained brain activation (303). If this is indeed the case, intracellular sodium imaging may be able to detect this increase. If the interstitial fluid space remains buffered through transcapillary ion flux, tissue sodium concentrations may also be elevated in the case of sustained brain activation. Although numerous attempts were made to identify intensity change on sodium MRI correlating with sustained brain activation (concerning observation of a flashing checkerboard) using both the PASS and SIRFLA sequences, each attempt proved futile. It must be acknowledged that neurons, in which intracellular increase is assumed, occupy only a fraction of the brain tissue volume (304). Assuming (for argument) that extracellular space occupies 20% of the volume, intracellular neuron space – 48%, and other intracellular space (neuroglia, erythrocytes, etc...) – 32%, and that sodium concentrations remain constant in all spaces except the intracellular neuronal space, a 50% neuronal sodium increase would amount to only a 10%

tissue sodium increase. However, a 10% tissue sodium increase should be detectable. A large reason attempted sodium functional MRI failed may have been 'partial voluming' of a localized effect for low 'resolution' sodium images. Another hypothesis for failure (among many) may be that interstitial sodium concentrations are not fully buffered during transient sustained activation (< 2 minutes was typically considered). This hypothesis is supported by the lack of tissue sodium increase measured in the early stages of acute stroke (Chapter 6) in spite of the large intracellular sodium shift of anoxic depolarization. This hypothesis may also be supported by DWI detection of neuronal activation (305) which is assumed dependent on compartmental ion differential change to redistribute tissue water. Assuming intracellular sodium increases are associated with elevated neuronal activity, it is thus hypothesized that small brain tissue sodium increases may exist following 'chronic' neuronal activity elevation. A simple suggested experiment may be the comparison of morning and afternoon sodium scans.

A potentially interesting, but yet to be assessed, application of sodium MRI concerns the possibility that elevated intracellular sodium concentration may play a part in the underlying pathophysiology of abnormal moods in bipolar disorder (306,307). It has recently been shown that administration of lithium normalized intracellular sodium concentrations (308); this action is suggested to be important to the efficacy of this treatment for bipolar disorder (309). A proposed study may include a sodium imaging comparison between manic and/or depressed bipolar volunteers and matched normal controls. Alternatively, or in conjunction, a study may include comparison between bipolar volunteers experiencing mania or depression and those same volunteers experiencing a time of euthymia (or normal mood), given expected sodium concentration differences between mood states (306).

8.3. Final Discussion and Conclusion

Sodium MRI remains in its 'infancy' when compared to proton MRI. A quick search of "MRI" yields >100,000 hits on the Web of Knowledge (http://apps.isiknowledge.com). There are now 32 studies total (including the 4 in this thesis) of sodium MRI in human brain. It is suggested that this paucity of research is *not* related to lack of possible application, given the sodium ion's intimate role in cellular metabolism. While the move to higher field has been a boon for sodium imaging (especially given its gyromagnetic ratio ~ ¼ that of proton), perhaps the greatest advancement came in 1997 when Boada introduced TPI for sodium imaging. Although the advantage of the short TE of radial imaging is directly evident, the merit of TPI has been questioned especially given its 'complicated' implementation, and it has remained unimplemented by others unrelated to the original developers. This thesis highlights a pathway of optimal TPI implementation for sodium imaging of the human brain. It is suggested that selection of appropriate sampling density shape, readout duration, value of *p*, and implementation SNR provides the substantive step that completes the 1997 introduction of TPI for human brain sodium imaging and facilitates its great advantage. It is also suggested that use of TPI acquisition in a steady-state sequence has an SNR/voxel-volume advantage that can't be ignored for a signal starved application. Combining radial k-space acquisition and NMR sequence optimization with the high field of 4.7T, this thesis hopes to nudge sodium imaging into a realm of excitement within the greater MRI community such that its mostly untapped potential may be explored.

To put the work of this thesis in perspective, other sodium images acquired from the human head must be considered. In **Figure 8-2** below 'current' images of the SPI approach (2006 (39) - **A**), the GRE approach (2008 (3) - **B**), the standard projection imaging approach (2007 (5) - **C**), and the TPI approach (2003 (6) - **D** and 1999 (12) - **E**) are given, copied from their respective .pdf documents. More recent TPI human brain images (2005 (66)) are in a journal with poor .pdf quality. The images (1997 (30) - **F** and 1997 (29) - **G**) are from the original sodium TPI

papers. Optimized images produced from the ideal approach suggested in this thesis are given in (**H**). Multiple axial, sagittal, and coronal slices associated with the image in (**H**) are shown in **Figure 8-3**, **8-4** and **8-5** respectively.

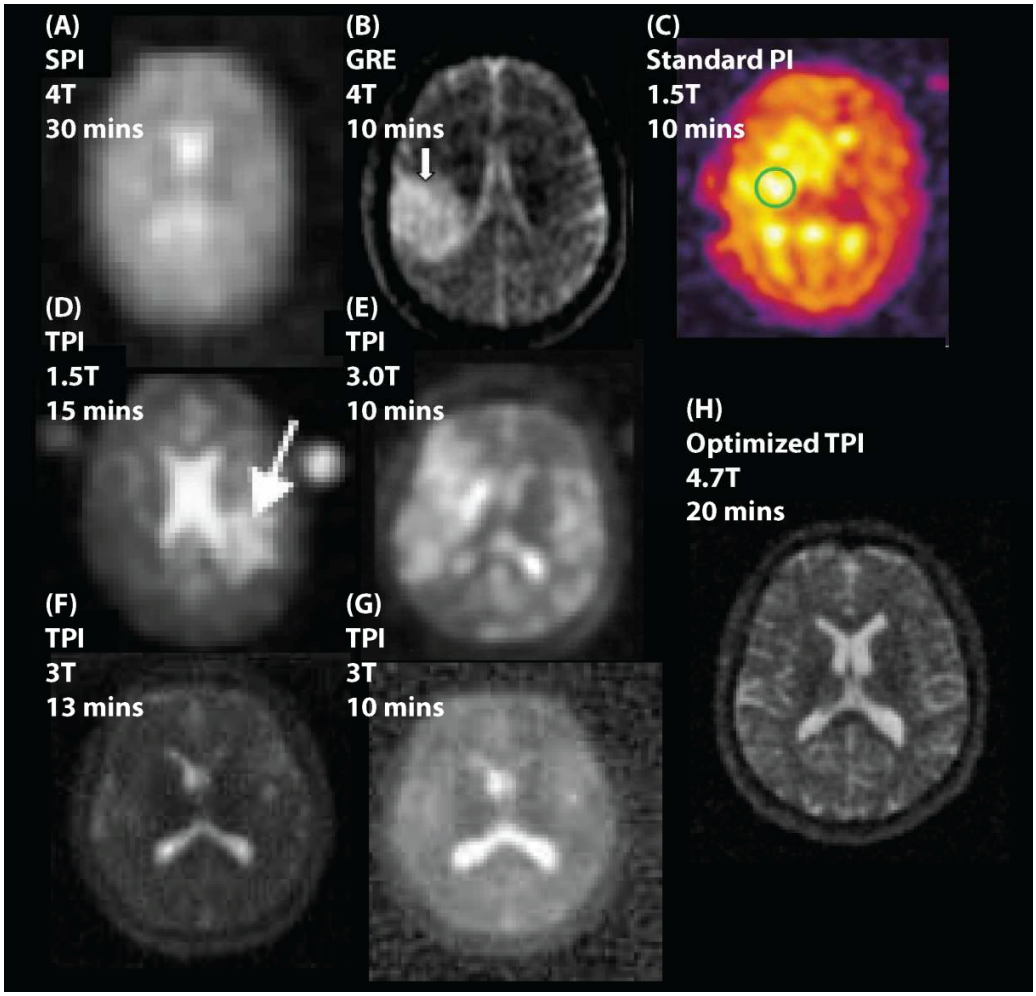

Figure 8-2: Comparative sodium images of the human brain. A - (39), B - (3), C - (5), D - (6), E - (12), F - (30), G - (29), H – images acquired from the optimization suggested in this thesis (note that voxel dimensions for this image are isotropic). Images A – G are copied from their respective pdf documents.

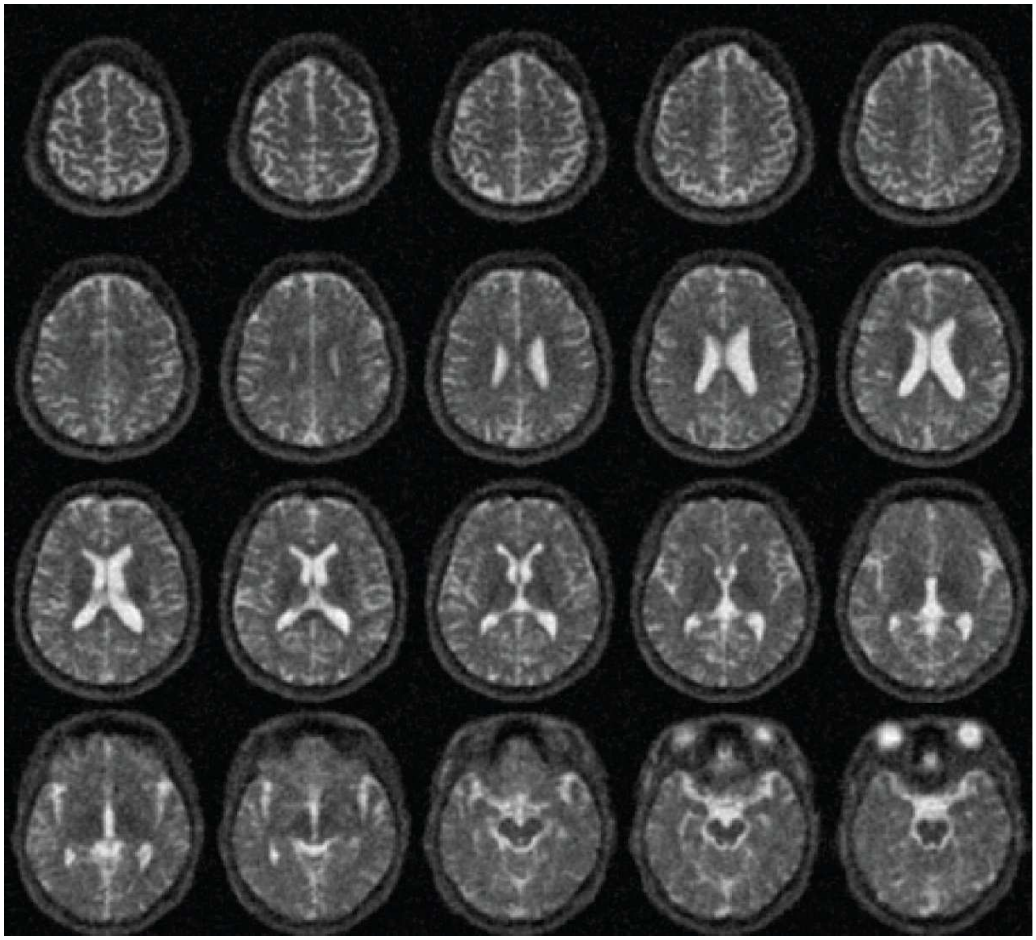

Figure 8-3: Multiple axial slices of the **Figure 8-2H** image acquired using the optimal approach to sodium imaging suggested in this thesis. These images are of a healthy volunteer and were acquired in 20 minutes at 4.7T (note that voxel dimensions are isotropic).

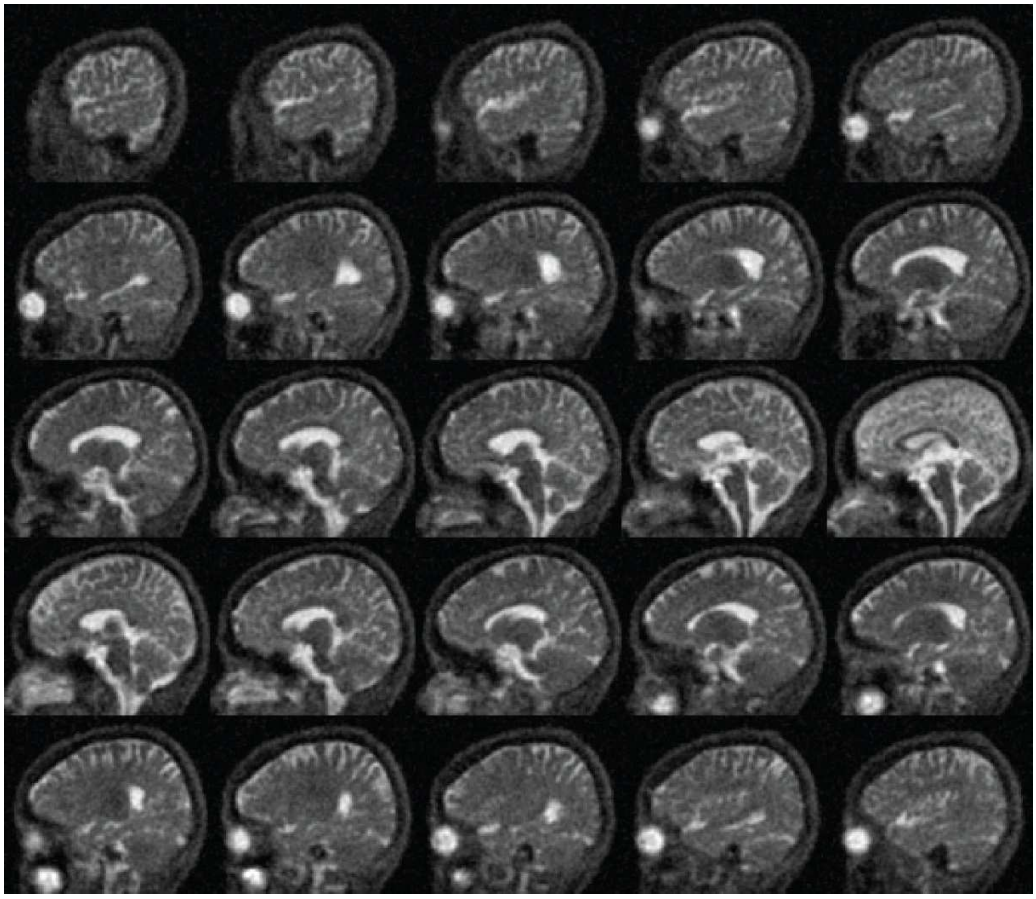

Figure 8-4: Multiple sagittal slices of the **Figure 8-2H** image acquired using the optimal approach to sodium imaging suggested in this thesis. These images are of a healthy volunteer and were acquired in 20 minutes at 4.7T (note that voxel dimensions are isotropic).

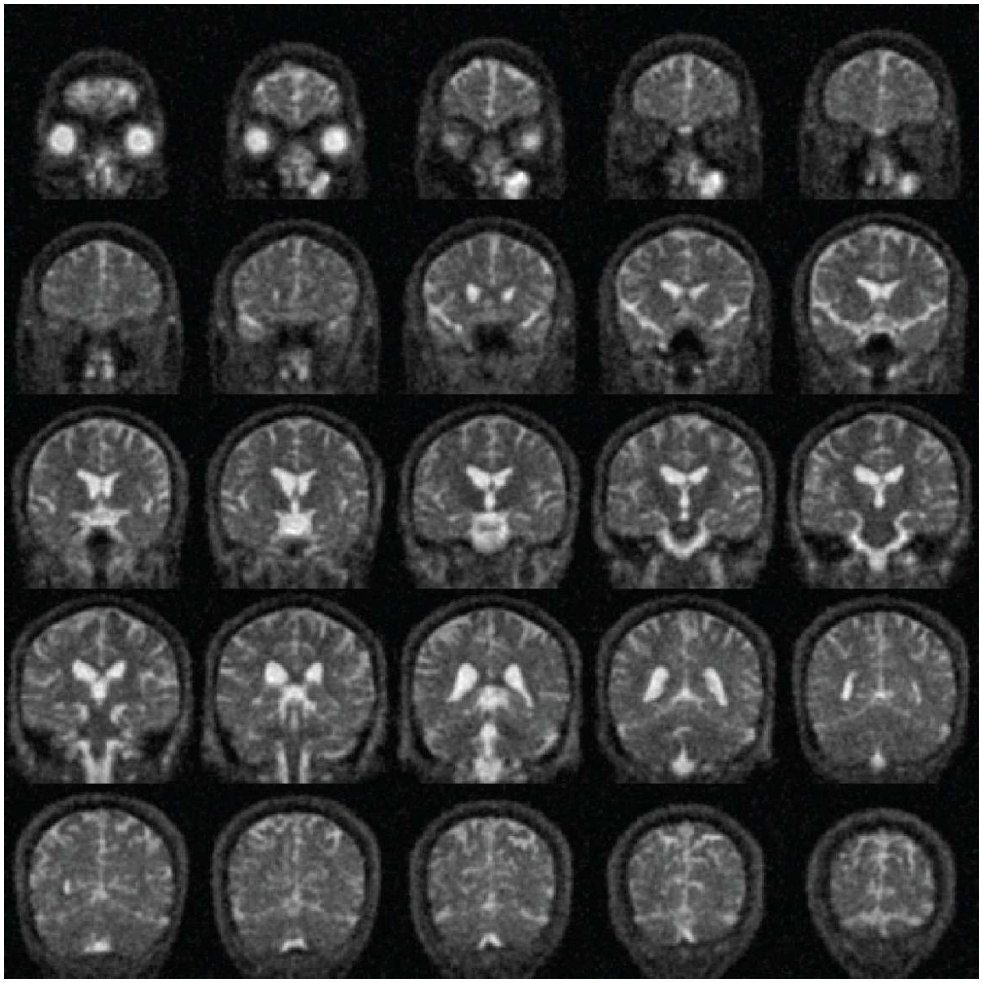

Figure 8-5: Multiple coronal slices of the **Figure 8-2H** image acquired using the optimal approach to sodium imaging suggested in this thesis. These images are of a healthy volunteer and were acquired in 20 minutes at 4.7T (note that voxel dimensions are isotropic).

The question, "why do your images look so good?" has been asked. The answer is that long readout duration, with its associated noise variance reduction, facilitates reduced voxel volumes and the containment of the 3x concentrated non-rapidly decaying CSF. It is the CSF that directly affects the visual appearance of a human brain sodium image. The Northern Pikes have a song on their 1990 "Snow in June" album with lyrics, "she ain't pretty she just looks that way." An intention of this thesis has been to highlight that this is *not* the case for the acquisition approach presented and now extensively used for sodium imaging in Edmonton.

Through evaluation of previously unconsidered and directly relevant image metrics including correlation volume and PSF-smearing-related image intensity modulation with object volume, an attempt has been made to evince additional image 'beauty' beyond that of CSF containment (which is very substantial and valuable in itself) for sampling density filtering TPI with long readout, small value of *p*, and small voxel volumes. Perhaps the best visual example of its 'beauty' beyond CSF containment concerns its presentation of acute stroke, shown in **Figure 8-6** below from Chapter 6.

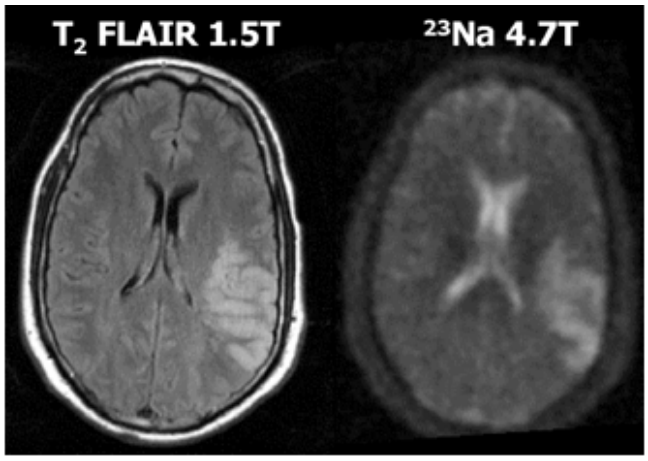

Figure 8-6: Proton and sodium imaging acquired from an acute stroke patient at 25 hour post symptom onset (from Chapter 6). This image is shown to highlight visualization of the stroke lesion on 'optimal' TPI sodium images at 4.7T.

Much interesting research remains to be done in the field of human brain sodium MRI, as mentioned above. The research involves: comprehensive analysis of the sodium NMR environment in brain tissue, i.e. the full measurement and characterization of relaxation and residual quadrupole splitting; assessment of sodium intracellular imaging possibility and sodium NMR sequence comparison; and last, but far from least, further exploration of the role of the (critical to cellular function) Na^+ ion in various disorders. The 10 studies of human brain pathology with sodium MRI since 1990 suggest that further research is warranted in the setting of acute stroke, cancer and Alzheimer's disease. It is likely that other currently unexplored disorders may also benefit from sodium MRI research.

Appendix 1

Implementing TPI on the Varian Inova

Although it is suggested that the advantages of TPI are primarily associated with altering radial evolution, rather than projection twisting, there is a practical advantage to projection twisting for radial evolution altered k-space acquisition implementation on the Varian Inova system.

The Varian Inova is limited by a gradient waveform memory of 64k specification words (per x, y, z channel). This memory is allocated to the entire experiment and must be used to specify all gradients waveforms within that experiment. All waveform memory for a given experiment is loaded at the start of the experiment which can be a somewhat time consuming process, depending on the number of projections specified. Although one may think that for standard radial k-space acquisition only one gradient waveform need be specified, and this waveform specified at different angles throughout 3D k-space, the Varian Inova system does not seem capable of performing this operation 'on the fly.' Instead, the orthogonal x, y and z gradient waveforms for each projection are pre-calculated for each projection and individually written to waveform memory. In this case the number of projection savings of TPI (as much as 80% for values of $p = 0.20$, a typical implementation value) allows each waveform to be specified with many more words.

As discussed previously 3D-TPI is typically implemented on sets of cones. It can however, also be implemented in different manners, as 3D-TPI is really a two dimensionally twisting technique in that only two of the spherical dimensions are altered with time during the readout. If the azimuthal angle is held constant rather than the polar angle (for implementation on cones) projection evolution is prescribed along a disc (30,310). Sets of discs can be rotated throughout 3D k-space, but this will create an oversampling of the polar ('z') axis. Implementation

on sets of discs requires π more projections than implementation with cones. Oversampling along and around the pole, which must be post-acquisition compensated, will also reduce sampling efficiency. There is also a gradient word advantage to implementation on sets of cones, the projections sampling the top and bottom haves of the k-space sphere can be reflections of each other. In this manner only projections defining one half of the projections sampling the k-space sphere need be specified with waveform memory, the other half can be produced with negative values (something the Varian Inova system can do 'on the fly'). If more gradient words are required, a scan can be split into two experiments and projections loaded twice, however that has not been necessary for imaging the human brain in this thesis, as will be discussed below.

While the gradient waveform memory limitation may seem detrimental, it has lead to an effective method of implementing TPI, which pertains to 'implementation beyond the gradient slew rate'. Twisted projection implementation has, in the past been constrained by gradient slew (30). There are three 'locations' where the acceleration of 3D-TPI projections are likely to exceed gradient slew limitations. As discussed previously 3D-TPI projections are typically implemented on sets of cones. Assuming the first 'cone' is a linear sampling of the polar ('z') axis, i.e. no twisting, the second cone will have a polar angle of $\phi = 2/(\mathrm{M}-1)$. Centripetal acceleration (a) as the radial evolution slows beyond *p* could approach that of Eq. [A1-1] (if radial evolution slowed very rapidly at *p*) (30).

$$a = \frac{\left(\frac{\mathrm{d}r}{\mathrm{d}\tau}\right)^2}{p \cdot \sin(\phi)} \qquad \text{[A1-1]}$$

For large k-space matrix dimensions and small values of *p*, centripetal acceleration on this second cone could have a value hundreds of times larger than the sampling speed. Sampling speed is directly proportional to the gradient magnitude and the required slew rate can be far from practical (implemented gradient magnitudes in this thesis are typically around 5 mT/m, and the current

gradient slew rate under which effective function possible is ~ 120 mT/(m*ms) – although this value will be discussed below)

The second 'location' where the acceleration of 3D-TPI projections exceeds gradient slew limitations is at the initiation of twisting, or at relative radial location *p*. At this location there is a discontinuity in projection sampling velocity as each projection abruptly changes direction from sampling along a straight radial trajectory to sampling along a twisting trajectory (56). The third 'location' where the acceleration of 3D-TPI projections exceeds gradient slew limitations is at the initiation of each trajectory. Infinite gradient slew rate is required to begin each trajectory at the gradient magnitude required for desired sampling speed.

The 3D-TPI implementation used in this thesis involves a sampling of the k-space projection design at intervals specified by the number of gradient words afforded each projection (one word is used to define the initial straight component, and the rest the twisting component). The gradient values associated with each word are calculated from the previous sampled location along the k-space trajectory and the constant gradient integral value required to attain the next k-space location. For this implementation the transition at trajectory initiation is ignored (i.e. full magnitude is specified at initiation), the transition at *p* is 'smeared', and the rapid acceleration of the narrow cones 'sub-quantized' (i.e. quantized below 2x the frequency of gradient evolution of the 'x' and 'y' axes specified by projection design).

While this quantized gradient waveform may sound problematic, it is quantized in such a manner such that each interval is sufficiently long for each gradient to reach its full specified value; implementation cannot be beyond gradient slew rate. To be more precise, each interval is made sufficiently long for each gradient *field* within the bore of the magnet to reach its full specified value, which includes the effects of eddy-currents. In the 'continuous' implementation case potentially unknown errors are generated when the gradients fields produced within the bore

of the magnet for each 'infinitesimal' step are not the specified value at instant the next value is specified. Although a 'continuously' implemented projection design may be within specified gradient amplifier slew rate limitations, imperfectly compensated eddy-currents can create 'complex' k-space location errors.

For the quantized gradient waveform implementation in this thesis the Varian Inova's gradient slew rate limiter is used to smooth each gradient step to within the limits of the gradient amplifier. For current image generation the slew rate limiter is set to 120 mT/(m*ms). To determine the 'actual' k-space locations sampled the quantized gradient steps are replaced with measured gradient field transition shapes for each associated step size. The 'actual' k-space locations sampled are then calculated from the integral of the gradient waveforms that include the measured field transition shapes.

An advantage of the 'quantized' gradient waveform technique developed for this thesis is that compensation for eddy-currents with short time constants need not be perfect for reasonable implementation; it is sufficient that they are known. However, this method does not take into account the generation of any short eddy-current cross terms; it was assumed these were minimal. It was also assumed that short eddy-current B_0 shifts were minimal, and that long eddy-current time constants are sufficiently compensated.

As might be expected the actual sampling density of the quantized waveform will slightly deviate from that prescribed by projection design (this will also be true for the 'continuous' implementation which must be altered from projection design). However, as described previously (Chapter 2), k-space is oversampled to a factor of $1/p$ for TPI at relative radial location p and typically oversampled throughout sampled k-space depending on the sampling density design implemented. As a result, gradient waveform quantization typically (for the scans presented) does not lead to critically under-sampled locations in k-space. Minor sampling density deviations from that prescribed by projection design are post-

acquisition compensated along with the oversampling at the centre of k-space, and local over-samplings associated with the quantization of the number of projections implemented on each cone. For each scan presented the desired $\Gamma(r)$ function is effectively re-produced with sampling efficiency (which is reduced for post-acquisition weighting) 94% - 98% (which includes the post-acquisition compensation for oversampling at the centre of k-space).

A quantized TPI projection (taken from the 'long readout' projection set of Chapter 4) is shown in **Figure A1-1** below. The gradient steps of the quantized waveform are shown in (**A**), along with the inclusion of the measured gradient field responses. The trajectory of this projection through k-space is given in (**B**) and (**C**).

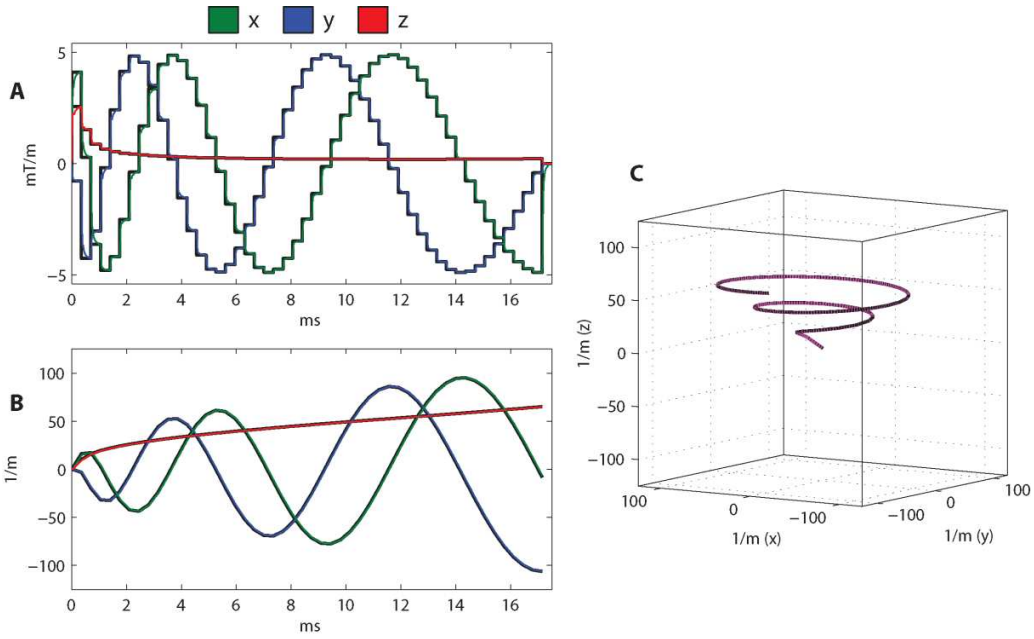

Figure A1-1: A TPI projection (from the long readout technique of Chapter 4) demonstrating gradient quantization and the addition of the gradient field response (A). Images (B) and (C) depict projection trajectory through k-space.

The gradient field step response for different step sizes was measured in the magnet using a small proton coil surrounding an NMR tube filled with Gadolinium doped water (set-up courtesy Chris Bowen, University of Dalhousie, N.S., Canada). For each orthogonal direction within the magnet the accumulation of phase was sampled at two locations (+/- ~ 5 cm along the orthogonal direction) for a set of gradient steps ranging from 0.5 mT to 8.5 mT in 0.125 mT steps. The relative evolution of phase difference between each location (used to exclude any background B_0 effect) was differentiated to produce the relative gradient field step response. In **Figure A1-2** the relative gradient field step response for the 'x' gradient is shown normalized to its value at 0.5 ms and multiplied with the corresponding gradient step producing this transition. The gradient field step responses of **Figure A1-2** include the effects of Varian Inova 'slewing', physical eddy currents, and eddy current compensation.

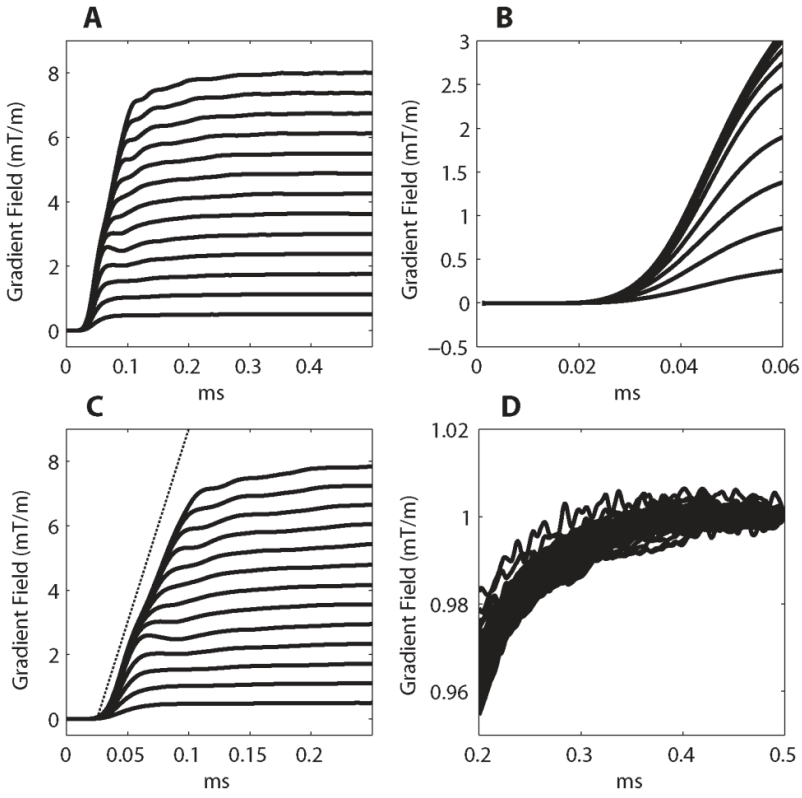

Figure A1-2: Measured gradient field step responses for various gradient field step sizes up to 8 mT/m. 'Oscillations' (manifest as over-shoot and undershoot for different step sizes) are related to gradient amplifier instability. Images (B, C and D) show zoomed-in regions of (A). In (B) it can be seen that the gradient field response follows a delay of ~ 25 μs, and that for gradient steps below 3 mT/m the rate of gradient increase is considerably less than the rate of gradient increase beyond 3mT/m. (C) highlights that the average rate of gradient field increase is less than the 120 mT/(m*ms) specified by the Varian Inova for these transitions. Also of note is the inverse exponential rise to maximum following the linear transition, suggesting the presence of uncompensated eddy currents. In (D) full gradient value can be seen to be attained ~ 350 μs.

In **Figure A1-2A** it can be seen that there are 'ripples' in the gradient field step responses. These ripples are related to instability of the gradient amplifier for small step sizes. These ripples can also be seen with the oscilloscope on the output of the gradient amplifier (they are considerably more pronounced for the 'z' gradient). The Varian Inova was set to produce a slew rate of 120 mT/(m*ms) for the measurements of **Figure A1-2** and the images generated using this

methodology. While the current gradient system (Gradient shim set: HFC-10, Tesla Engineering, West Sussex, England. Gradient amplifier: QDCM1400, PCI, Montgomeryville, Pennsylvania, USA) used in our 4.7T scanner can generate much faster step responses, up to ~220 mT/(m*ms), for more rapid slew rates the gradient amplifier oscillations are exacerbated (this problem is currently in the process of being resolved by the manufacturer). It should be noted that Chapters 2, 3, 6 and 7 were performed before a gradient upgrade (Gradient shim set: HFC-1, Tesla Engineering, West Sussex, England. Gradient amplifier: QDCM700, PCI, Montgomeryville, Pennsylvania, USA. Slew-rate: 110 mT/(m*ms)). The effective doubling of the gradient step response rate with the upgraded gradient system may be particularly useful for potential proton TPI applications where desired high-resolution may require larger gradient magnitudes than the < 8 mT/m (**Figure 8-3**) used for sodium imaging in this thesis.

For this gradient field step response measurement, sampling of phase accumulation begins at the same time that the gradient step command is issued. A delay of 25 μs before the initiation of gradient transition was extrapolated from **Figure A1-2B**. This delay following issue of the gradient waveform command was implemented before beginning TPI k-space acquisition. The gradient field step response following this delay was used to recalculate each k-space location.

In **Figure A1-2C** the gradient step responses are shown alongside the prescribed linear slew rate of 120 mT/(m*ms). The initial slow response for each gradient step and the reduced rate of increase for gradient steps less than 3 mT/m (most visible in **Figure A1-2B**) are the result of the Varian Inova's 'slewing.' The 'linear' portion of the gradient field step response for the large gradient steps shown deviates somewhat from the prescribed 120 mT/(m*ms), and is ~95 mT/(m*ms). This deviation during the linear portion of the gradient increase and the subsequent 'exponential' shaped rise to full value point to residual uncompensated eddy-currents within the bore of the magnet. While the short time-constant eddy current compensation could be improved, its imperfection

highlights the utility of this gradient waveform quantization and k-space location recalculation method. Perfect eddy-current compensation is not required; all that is required is knowledge of the gradient field step response.

At 200 μs past initiation the gradient fields are ~96.75% of their value at 500 μs, at 250 μs ~98.5%, at 300 μs ~99.25%, and at 350 μs ~99.75% (**Figure A1-2D**). For the images generated using this gradient field measurement, full gradient value is said to be attained at 250 μs, and the relative gradient step response is made proportional to this value. The small error associated with ending the gradient step response at 250 μs, and making it relative to the value at 250 μs, will be discussed below. For implementation of the quantized gradient waveform, the minimum step durations will be constrained by the gradient rise to full value time. The gradient waveform step response is implemented for k-space location recalculation in 4 μs steps, where each step is defined by the measured gradient step response at the centre of that step.

While the effect of the gradient step response of the k-space trajectory is difficult to see when observing the entire k-space trajectory (**Figure A1-1**), that is not the case is one zooms in on an initial trajectory segment (**Figure A1-3**). For large steps the sampled k-space locations are as much as 2 1/m less than that prescribed by the quantized step. The effect of not taking into account the gradient step response to recalculate the sampled k-space locations is readily apparent in **Figures A1-3C** and **A1-3D**. If the gradient step response is not taken into account to recalculate the sampled k-space locations, at the point in time in which the second sample of the trajectory is acquired all the spins within the object will have accumulated less phase than specified by the k-space location to which they are assigned. The effect could be simplistically described as erroneously elevated acquired signal intensity around the centre of k-space, producing an associated non-zero background effect in the image. Images from the 150 mM saline resolution phantom which was built using a piece of rectangular acrylic with holes drilled in it were used to assess the validity of k-space location re-calculation.

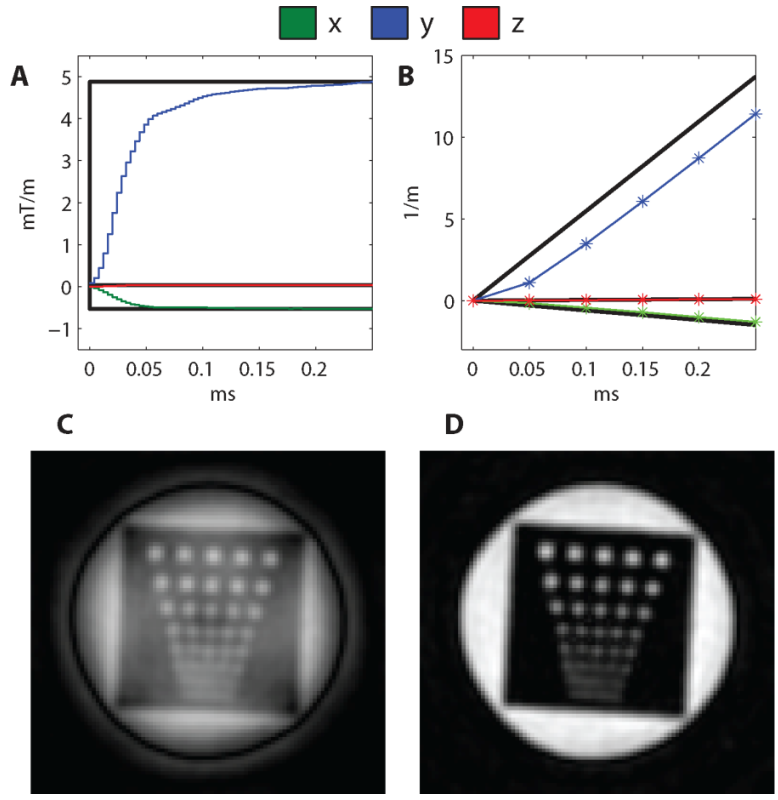

Figure A1-3: The effect of the gradient field step response (A) on the sampled k-space locations (B), and the effect on the image of not recalculating the sampled k-space locations (C). In (C) the k-space locations using the gridding process are those directly associated with the quantized gradient waveform. The image in (D) was created from k-space location recalculation using the measure gradient field step response.

Images generated using linear gradient responses to recalculate k-space locations are shown in **Figure A1-4**. By delaying the linear rise in the k-space location recalculation model beyond the gradient step, the first sampled points beyond the centre of k-space can be 'said' to have accumulated smaller gradient-time integrals and as such can be said to have k-space location closer to the centre. Reducing the recalculation slew rate produces similar effect. If the gradient-time integrals said to be associated with the first sampled points are too large, a non-zero background artifact is present in the centre of the image. If the said gradient-time integrals are too small a non-zero background artifact in the centre of the

image is accompanied with edge enhancement effects. Different slew rates and delays can be used to 'match' the measured gradient field response and minimize image artifacts, but the most artifact free image is still that produced by the measured gradient field response (**Figure A1-3**).

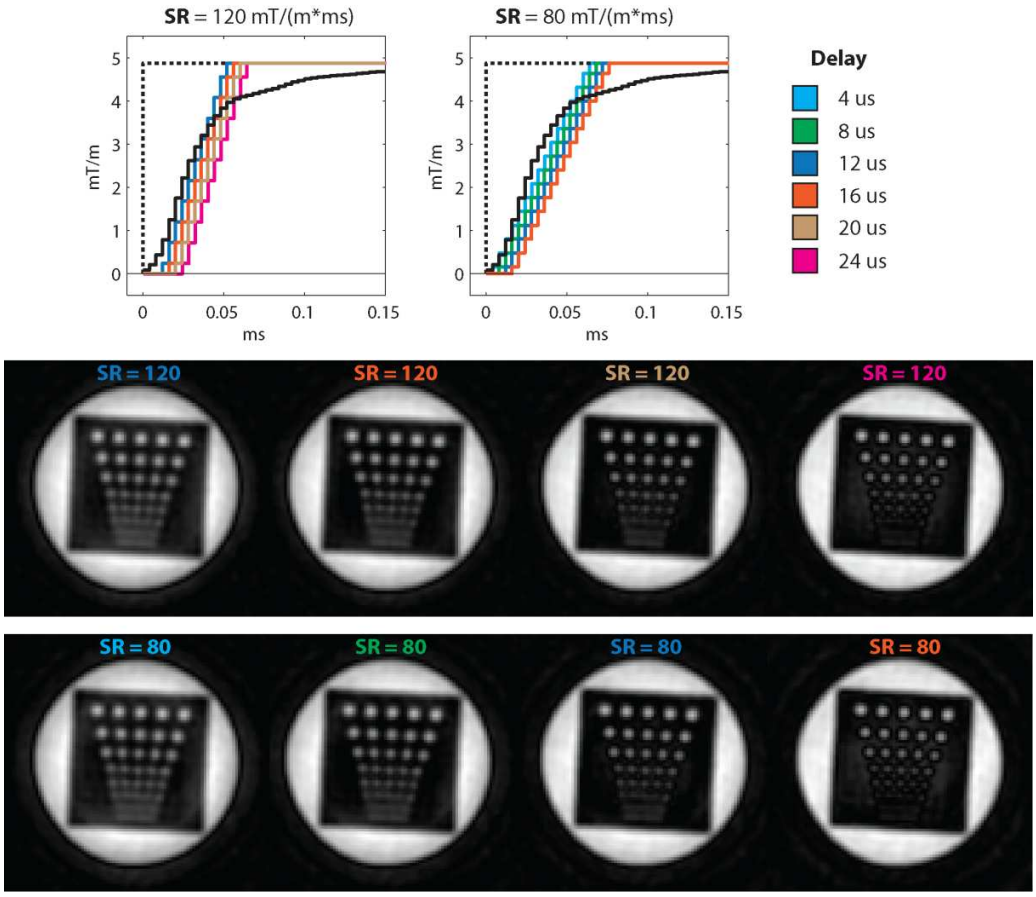

Figure A1-4: Saline resolution phantom images generated using linear slew rate models of 120 and 80 mT/(m*ms) to recalculate the k-space locations sampled in the quantized gradient waveform. Both linear rates of rise are implemented for k-space location with four different delays following the quantized gradient step. If the actual gradient-time integral at the first sampled point(s) beyond the centre of k-space is less than specified by the linear slew model in the k-space location recalculation, the image contains a circular background artifact. For the opposite case, a background artifact is also present along with an edge effect in the centre of the image. Although a linear model with appropriate 'delay' can be used to minimize artifacts in the image, none of the images above are as visibly free from artifact as the image generated using the measured field response (black line) (**Figure A1-3**).

The images of Chapters 2, 5 and 6, produced before the gradient upgrade, used a linear gradient response to recalculate k-space locations. This method also included accommodation for reduction in step response for small gradient step sizes associated with the Varian Inova's 'slewing (as described above). Smaller gradient magnitudes used in these chapters (< 3.5 mT/m), making the absolute accuracy of the gradient transition of less relevance, in association with expected better (although not measured) short eddy-current compensation facilitated effective image generation. A saline resolution phantom image produced before the gradient upgrade is shown below in **Figure A1-5**.

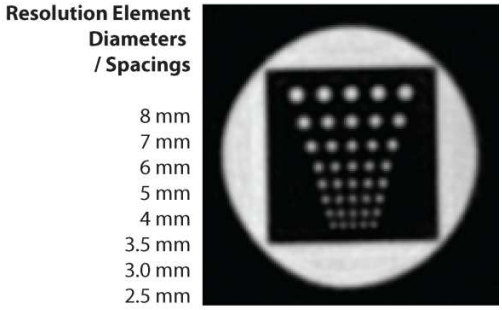

Figure A1-5: A saline resolution phantom image produced before the gradient upgrade with a projection set used in the stroke study. A linear gradient response was used to recalculate the sampled k-space locations to produce this image.

The method used in this thesis of gradient waveform quantization and sampled k-space location recalculation using the measured gradient field step response is demonstrated here to be effective in the presence of slow, and 'trailing-off', gradient field step responses. Improved eddy-current compensation and the use of increased Varian Inova defined slew rate would minimize the error of less accurate knowledge concerning the gradient field step response (i.e. a smaller proportion of the gradient integral associated with the first one or two sampled values along the trajectory would be associated with the step response). An improved gradient field step response would also facilitate the use of smaller gradient quantization step durations. While the gradient field step response

limitation is of little concern for the projection designs presented in general, it does constrain the minimum duration of the initial straight segment of the TPI trajectory and hence has impact on the minimum values of 'twist' (p) that can be effectively implemented; the initial straight segment of the TPI trajectory used in the figures of this appendix is 0.35 ms (the long readout projection set from Chapter 4). However, as discussed in Chapter 4, reduction of p beyond that implemented in the long readout projection set shown (p = 0.15) has some additional value.

It is assumed for this method of gradient waveform quantization and sampled k-space location recalculation that the eddy-currents manifest within the bore of the magnet can be expressed as gradient field alterations. This same assumption is also required for eddy-current compensation. It is also assumed for this method that the long time-constant eddy-currents, as well as short time-constant B_0 shift producing eddy-currents are properly compensated, and that cross-generated eddy-currents (i.e. the production of transient gradient fields in the directions orthogonal to the direction of an applied gradient field) are minimal. Any invalidity of these assumptions will introduce minor error into the images produced.

It is perhaps also interesting to note that because the sodium gyro-magnetic ratio is roughly ¼ that of proton, the gradient waveforms presented above would sample k-space to 500 1/m rather than the 125 1/m for sodium. However, if trajectories similar to that presented above were to be used to produce $1/(2*k_{max})$ = 1 mm acquisition proton voxels, 64x more projections would be required to fully fill k-space (2000 were implemented for the trajectory presented). In this case further reduction of p may be desirable to reduce the number of projections required. A technique facilitating order p^2 projection reduction, as was presented at the non-Cartesian workshop in Sedona, Arizona (Stobbe, Beaulieu, 2007) (144). Reduction of p and any reduction of the readout duration to alleviate susceptibility problems (protons exhibit 4x greater phase accumulation than

sodium in areas of local magnetic field variation) will require improved gradient field step response if TPI is to be used to produce high resolution proton images on the 4.7T Varian Inova system.

In retrospect the proton test setup could have been used to completely define the gradient field in the magnet for each waveform. However, this is not a desirable method of determining the actual k-space locations sampled for each projection set implemented, as it is a time consuming process. The method described above requires only one initial measurement of gradient field step response, from which sampled k-space locations can be recalculated for any given projections set implemented.

It is also important to note that beyond the shape and timing of the gradient field response the group delay of the anti-aliasing filter must also be known. For this thesis the analog filter fitted in the Varian Inova was used which has a group delay of 0.776 / FB (filter bandwidth). This lag must precede the acquisition of sampling points along each projection.

Appendix 2

Non-Cartesian Image Creation

10.1.1. General Convolution Based Gridding

Convolution based gridding (260,261,311,312) was used to generate images from non-Cartesian k-space sampling. This process essentially consists of weighting each sampled point according to the required compensation, convolving each point with a three dimensional kernel, sampling the result at the Cartesian matrix locations, inverse Fourier transform, and compensation for image space roll-off associated with k-space convolution. This is described mathematically below for both k-space and image space (Eqs. [A2-1, A2-2]), following Pipe (260). $\mathrm{M}(k)$ is the continuous intensity in k-space; S is the non-Cartesian sampling function associated with the projection set; W is the SDC weighting applied to each sampled point; C is the convolution kernel; and R is a Cartesian sampling function (lower case letters represent the Fourier transforms of the upper-case letters).

$$\mathrm{M}[n] = \Big(\big((\mathrm{M}(k) \cdot \mathrm{S} \cdot \mathrm{W}) * \mathrm{C}\big) \cdot \mathrm{R}\Big) *^{-1} \mathrm{C} \qquad \text{[A2-1]}$$

$$\mathrm{m}[n] = \frac{\Big(\big((\mathrm{m}(k) * \mathrm{s} * \mathrm{w}) \cdot \mathrm{c}\big) * \mathrm{r}\Big)}{\mathrm{c}} \qquad \text{[A2-2]}$$

10.1.2. Sampling Density Compensation

Successful design criteria for sampling density compensation is stated below (where Γ is the desired transfer function and γ its Fourier transform).

If

$$\Big(\big((S \cdot W) * C\big) \cdot R\Big) = \big((\Gamma * C) \cdot R\big) \qquad \text{[A2-3]}$$

then

$$(S \cdot W) = \Gamma \qquad \text{[A2-4]}$$

within a desired FoV
if there is no replication contribution to the FoV.

There are two ways to ensure that there is no replication contribution to the FoV. The first is to sample the convolution on an infinitely fine grid. In this case the Cartesian sampling function (R) can be removed from Eq. [A2-1] along with its replication generating Fourier transform (r) in Eq. [A2-2]. However, computation of a continuous Fourier transform, or even the DFT of an ultra finely sampled grid is practically impossible. The second way to ensure there is no replication contribution to the FoV is to use a convolution kernel whose Fourier transform is zero outside the FoV bound. This is also practically impossible as it requires a spatially infinite convolution kernel.

As it is impossible to completely eliminate replication contribution to the FoV, the intention is to ensure its minimization as possible within computing constraints. In this thesis the convolution is typically sampled 1.2x more finely than the matrix required for a given FoV; this expands the 'replication window' 1.2x beyond the FoV (261). A Kaiser convolution kernel was selected because it allows simple control of side-lobe amplitude in its Fourier transform through its β parameter; the width of the kernel in k-space can be used to control the width of its profile in image space (141). A convolution kernel width of 4 (1.2x sub-sampled) matrix locations was generally used together with a β parameter of 6.5 in this thesis. This places the first null crossing of the neighbouring replication at

the edge of the FoV. A cubic 3D kernel was constructed from orthogonal multiplication of the 1D kernel. 3D kernel selection will be discussed further below.

The goal in the generation of the sampling density compensating weighting coefficients is to seek the equality of Eq. [A2-3]. This is done iteratively following Pipe (Eq. [A2-5]) (260).

$$(S \cdot W_{i+1}) = \frac{\big((\Gamma * C) \cdot S\big)}{\Big(\big((S \cdot W_i) * C\big) \cdot S\Big)} \cdot (S \cdot W_i) \qquad [A2\text{-}5]$$

While Pipe is concerned with production of a uniform transfer function, here the concern is with the generation of an arbitrary transfer function – in particular one that is a k-space filtering shape. At any given sampled k-space location if the convolved sampled weighting function is less than or greater than the convolved desired transfer function the weighting at that location will be scaled accordingly. However, one iteration is not sufficient to achieve an acceptable weighting function; the subsequent convolution of altered weighting at each sampling location will not produce the shape of the convolved desired transfer function. This is because the value of the weighted and convolved sampling locations at any particular sampling location is also dependent on the altered weightings surrounding this location. The iterative process of sampling density compensation starts with a weighting function $W_0 = 1$ across k-space.

This iterative convolution-based sampling density compensation process was implemented in Matlab. The sampled convolution $\big((\Gamma * C) \cdot S\big)$ only needs to be solved once and can be done at the initiation of compensation, however, the sampled convolution $\Big(\big((S \cdot W_i) * C\big) \cdot S\Big)$ is very time consuming. Each sampled k-space location must be convolved onto its neighbouring locations within the volume of the convolution kernel. This requires knowledge of the all the sampling points and their locations located within the neighbourhood of each sampled k-

space location. This is an $O(N^2)$ process, where N is the number of sampled k-space locations. Although some of the geometry of projection design could be used to speed this search, with an N of 1e6 (for a typical scan) many operations are required. In theory this search need only be done once and the locations of neighbouring points for each sampling point recorded in a matrix for subsequent use. However, such a matrix would be very large especially for 3D projection imaging; typically thousands of sampling points surrounding the centre of k-space would each be associated with thousands of neighbours.

Instead of directly solving $\left(\left((S \cdot W_i) * C\right) \cdot S\right)$ the much simpler operation $\left(\left((S \cdot W_i) * C\right) \cdot R\right)$ is solved. This again follows in the path of Pipe (260). However, rather than perform a two step convolution as Pipe, the values following convolution at each sampling point are simply estimated through tri-linear interpolation. The tri-linear interpolation estimation method is effective for smoothly and slowly varying Γ because as the iterative process produces $\left(\left((S \cdot W_i) * C\right) \cdot R\right)$ closer to that of $\left((\Gamma * C) \cdot R\right)$ this interpolation becomes more and more accurate. This method has proven effective for the projection sets presented in this thesis.

Sampling density compensation is very mildly 'complicated' at the extents of sampled k-space. The Γ function is sampled on a Cartesian grid prior to convolution, and this sampling cannot reflect a 'perfect' spherical k-space sampling extent. At the edge of the sampled k-space extent the convolved Γ and sampling functions roll-off. If the effective radii are not the same, rolling-off values along the sampled extent of k-space will differ and compensation will be based on radius of k-space sampled rather than sampling density. For this reason the sampling points located beyond a radius $R_{max} - C_{wid}/2$ (where R_{max} is the radius of the sampled k-space sphere and C_{wid} is the width of the convolution kernel, both in sub-sampled voxels) are assigned the compensation value at $R_{max} - C_{wid}/2$ (with the same azimuthal and polar angles) throughout the SDC generation

process. In this manner compensation is not based on the convolution roll-off at the edge of the sampled k-space extent. Because for radial evolution altered k-space acquisition the sampling density beyond the radial fraction *p* is designed to match Γ, the required compensation should (ideally) be uniform beyond *p*.

The greatest difficulty of sampling density compensation for 3D projection imaging is the generation of appropriate weighting at the centre of k-space, where the sampling density is extreme and rapidly varying. An image produced using this sampling density compensation methodology and one iteration is shown in **Figure A2-1**. Notice that with only one iteration the 'incomplete' compensation of the sampling density at the centre yields a non-zero mean background intensity. For the projection set used in **Figure A2-1** one iteration produces an error at the centre of k-space of 50%, and an average error throughout k-space (to the initiation of convolution roll-off at the edges of k-space) of 1.5%. Ten iterations reduces the error at the centre of k-space to 9% and the average error throughout k-space to 0.31%. One hundred iterations reduces the error at the centre of k-space to 0.47% and the average error throughout k-space to 0.07%.

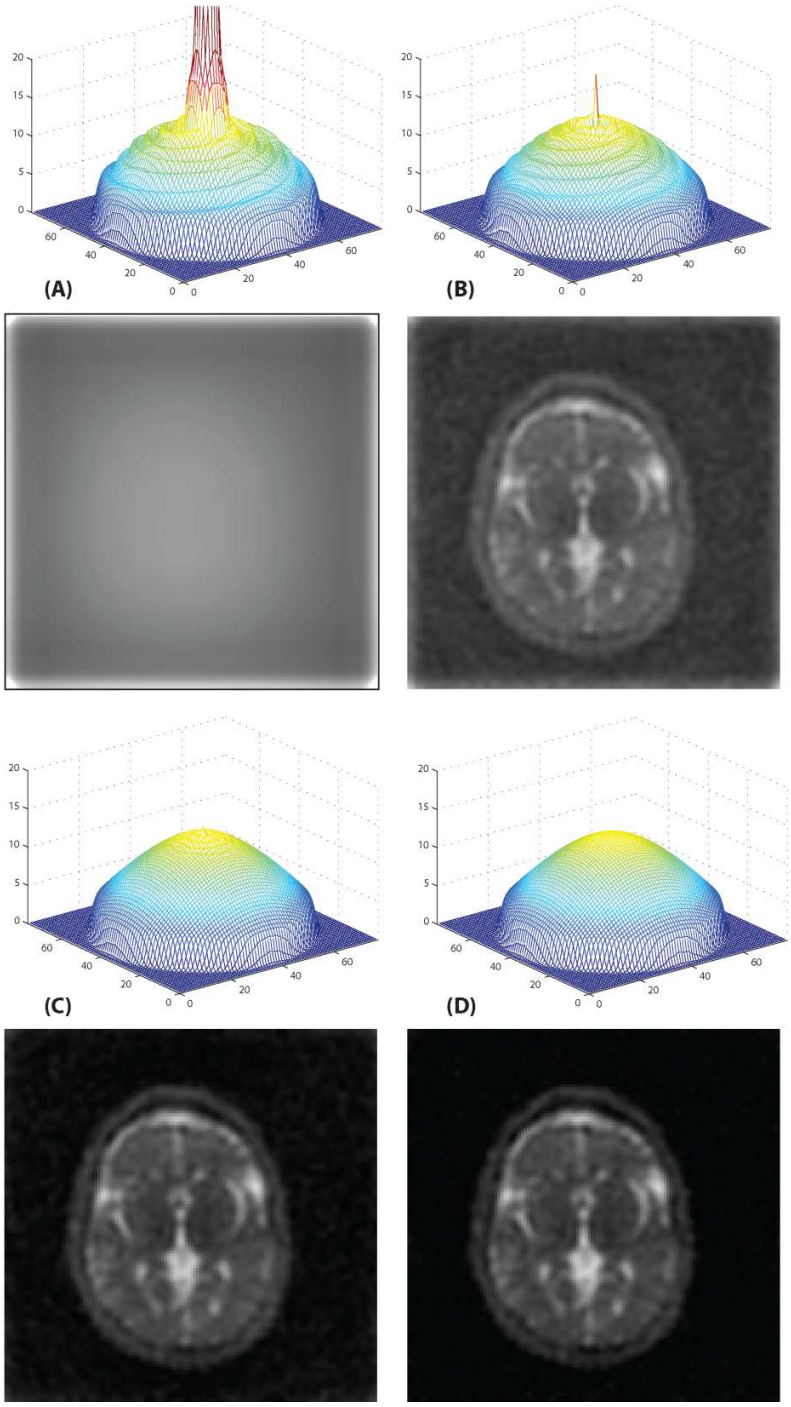

Figure A2-1: Effect of increased number of sampling density compensation generation iterations on the resultant image (images from a healthy volunteer created used long readout approach of Chapter 4). Also shown are the weighted and convolved sampling functions for each number of iterations. A) no sampling density compensation; B) one iteration; C) 10 iterations; D) 100 iterations.

A relatively large number of iterations are required to remove the uniform background intensity from the images. To further speed convergence to minimal error throughout k-space it was found that the iteration process could be accelerated according to Eq. [A2-6] below. These values were found from empirical testing to yield accelerated convergence for each projection set generated. It is more than likely this acceleration could be improved.

$$(S \cdot W_{i+1}) = \left[\frac{\big((\Gamma * C) \cdot S\big)}{\Big(\big((S \cdot W_i) * C\big) \cdot S\Big)}\right]^{A_i} \cdot (S \cdot W_i) \qquad [A2\text{-}6]$$

$$A_i = 1.1 \ \ (i \leq 3)$$
$$A_i = 1.8 \ \ (i > 3)$$

Plots of the accelerated convergence are given in **Figure A2-2**. As can be seen the relative k-space average and centre errors for the accelerated SDC approach are attained with approximately ½ the iterations of the non-accelerated approach. Plots of profiles through $\Big(\big((S \cdot W_i) * C\big) \cdot R\Big)$ and $\big((\Gamma * C) \cdot R\big)$ are given in **Figure A2-3** for W_{100} generated with the non-accelerated sampling density compensation and W_{50} produced with accelerated sampling density compensation. These plots are essentially the same. The noise variance inefficiency associated with post-acquisition weighting is the same for both cases – 2%.

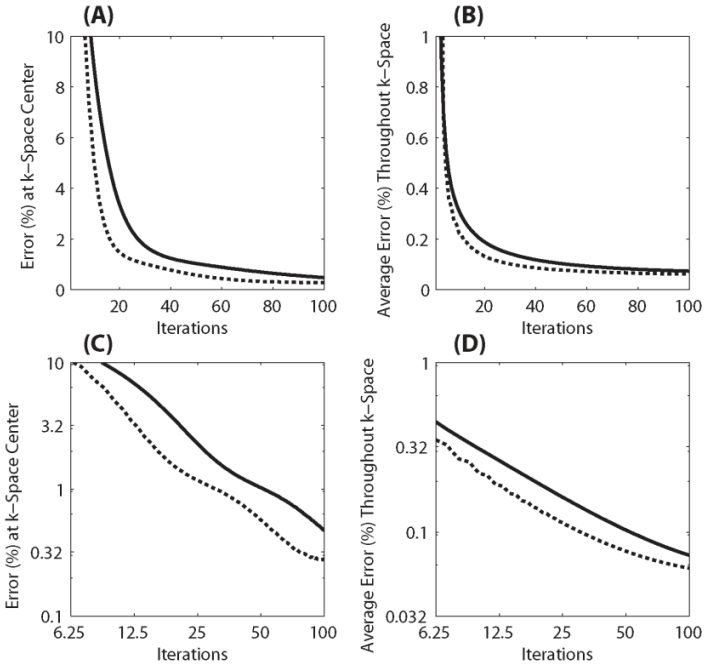

Figure A2-2: The reduction of deviation (error) of the weighted convolved sampling function from the convolved design function with increasing number of sampling density compensation iterations for both the accelerated (dotted line) and non-accelerated (solid line) methods. When plotted in a log-log fashion (C, D) it can be seen that roughly half the number of iterations are required for the accelerated method to produce the same errors at the centre and throughout k-space.

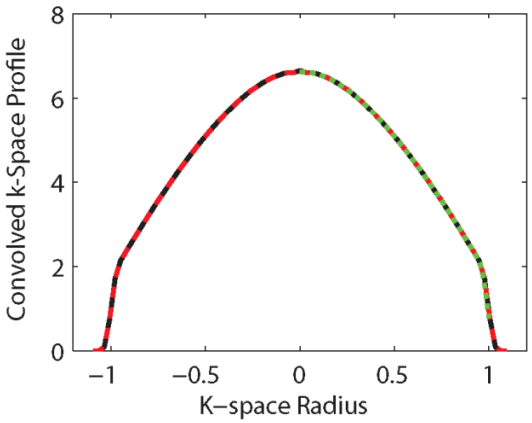

Figure A2-3: Profiles through the weighted and convolved sampling functions for both the non-accelerated case with 100 iterations (black), and the non-accelerated case with 50 iterations (red). One half of the convolved design function is also shown (green).

To save processing time the convolution kernel (C) is calculated before-hand and sampled in the convolution process. Due to computer memory limitations at the time of implementation it was quantized at a rate of 0.05 sub-sampled (1.2x) grid points. In the current implementation it is quantized to a rate of 0.01 sub-sampled grid points. However, the differences in the images produced as a result of the differences in quantization are infinitesimal (**Figure A2-4**).

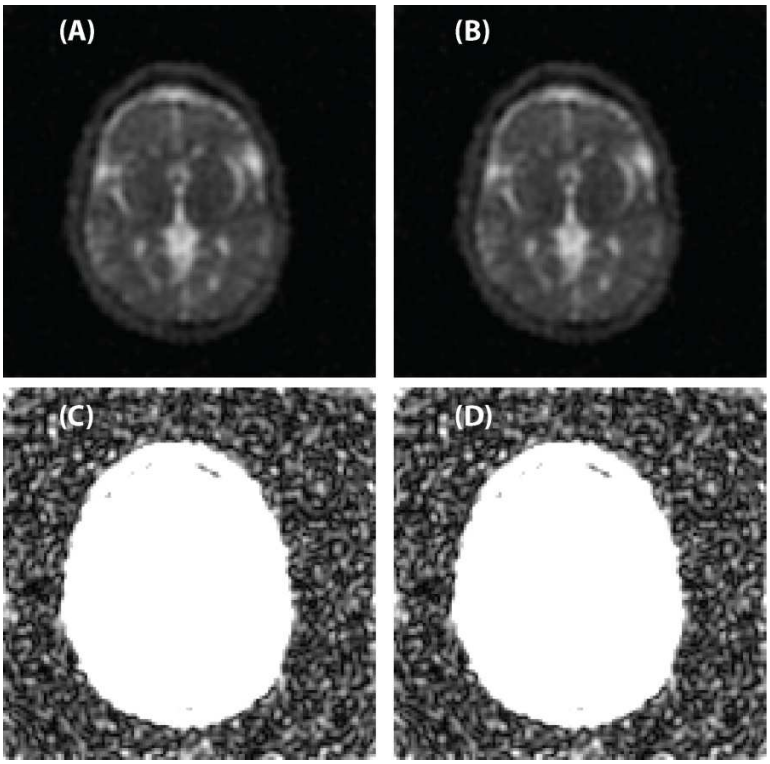

Figure A2-4: Convolution kernel quantization to the rate of 0.05 sub-sampled grid points (A, C) and 0.01 sub-sampled grid points (B, D). The impact of these kernel quantization differences are undetectable, even when windowed to search in the noise floor (C, D).

Production of a sampling density compensation matrix with 50 iterations for the projection set (from Chapter 4) demonstrated in the Figures above (~690000 sampled k-space locations) takes roughly 18 minutes (Dell XPS 420). Fortunately the SDC matrix does not need to be generated on the fly, but can be generated beforehand and recalled for image production. It is certain that more efficient

coding (ideally outside of Matlab) could improve this generation time. This remains to be completed.

10.1.3. Image Generation

Directly following Fourier transform the resultant image will exhibit signal intensity roll-off toward the edges of the image as a result of the k-space gridding convolution. The resultant image must be multiplied by the inverse of the Fourier transform of the convolution kernel. This 'inverse filter' (as it is labelled here) is calculated before-hand for different zero-filled k-space dimensions and imported into software at the moment of image generation.

While for sampling density compensation the shape of the kernel is used to ensure minimal replication contribution to the FoV space and the validity of the compensation, the shape of the kernel is also important in the image generation process. In the image generation process replication contributions to the FoV will be amplified, especially at the edges of the image, by the 'inverse filter.' A worst-case scenario is one where acquired k-space is simply a delta function at the centre. The image error associated with this case is described below.

$$\mathrm{M}[n] = (\mathrm{C} \cdot \mathrm{R}) *^{-1} \mathrm{C} \qquad \text{[A2-7]}$$

$$\mathrm{m}[n] = \frac{(\mathrm{c} * \mathrm{r})}{\mathrm{c}} \qquad \text{[A2-8]}$$

In this case the Fourier transform of the convolution itself will be replicated throughout the entirety of image space providing contributions to the image space within the FoV; the inverse filter will amplify these contributions.

Replication contributions to the FoV space associated with Fourier transform of the sub-sampled (1.2x) convolution kernel are shown in **Figure A2-5A** for both the width 4 and β = 6.5 kernel and a width 6 and β = 10.5 kernel (1D case – both empirically selected). Replication-amplification is shown in **Figure A2-5B** for

both kernels. As can be seen the error within the FoV is as great as 2.5% for the width 4 case. For a wider convolution kernel the β parameter can be made larger, and larger β is associated with side-lobe reduction. Amplified replication-based error can be seen (around the edges) above in **Figure A2-1A** when a non 'FoV-limited' image is produced from image generation without sampling density compensation; it is also slightly apparent for the case when sampling density compensation is generated with 1 iteration, and very slightly apparent (in the corners) for the case of 10 iterations. Each image shown in **Figure A2-1** is shown to its full 1.2x FoV extent.

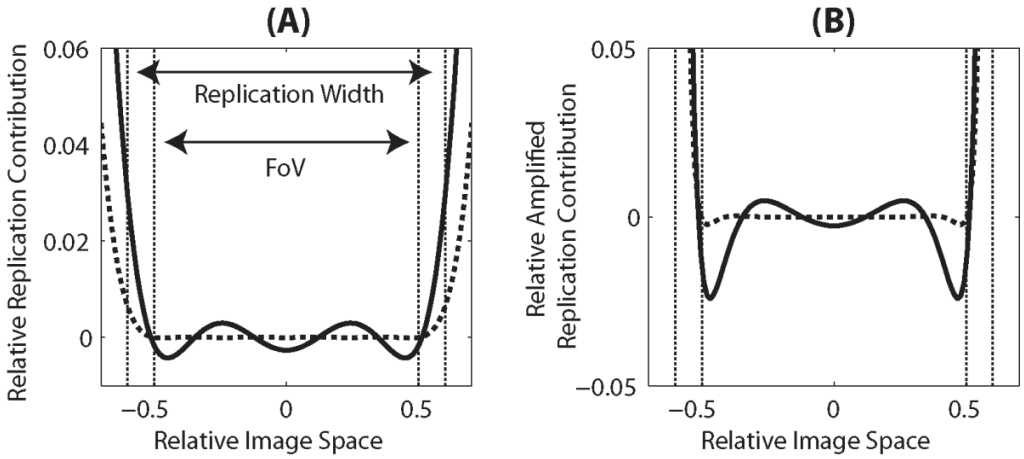

Figure A2-5: The relative replication contribution to the FoV associated with Fourier transform of the sampled (to 1.2x) convolution kernel (A) and the amplification of this contribution as a result of inverse filtering (B). This replication effect is shown for Kaiser kernels with width 4 and $\beta = 6.5$ (solid line) and width 6 and $\beta = 10.5$ (dotted line).

Although the width 6 kernel is associated with a much smaller amplified replication-based error than the width 4 kernel when the Fourier transform of the sampled kernel itself is considered, it should be remembered that the Fourier transform of the sampled kernel itself is a worst-case scenario in terms of replication contribution to the FoV (equivalent to convolution gridding a delta function, i.e. a uniform image throughout the entirety of image space). If an image

is perfectly constrained within its FoV, replication-amplification based error will be non-existent (independent of the convolution kernel selected), but because images are acquired in k-space, and because k-space is discretely sampled, all MRI images produced will not be entirely constrained within their FoV. However, replication contributions from the signal producing objects themselves, when these objects are contained within the prescribed FoV, are generally *very* small. When appropriate sampling density compensation is implemented for image generation such that the 'delta-error' at the centre of k-space is 'eliminated' the replication-amplification based error is essentially non-existent (**Figure A2-1D**). While the signal intensity associated with the signal producing object may be effectively 'FoV-limited,' the noise acquired in an MRI scan is not 'FoV-limited.' Replication-amplification based errors can be seen toward the corners of the images of **Figure A2-6** when one zooms in on the noise. However, this error is again small. As can be seen in **Figure A2-6** the effect on the image associated with convolution gridding using a width 4 kernel is negligible when compared to the use of a width 6 kernel. Increased kernel width requires a width cubed increase in convolution computations, and for this reason a width 4 kernel was selected.

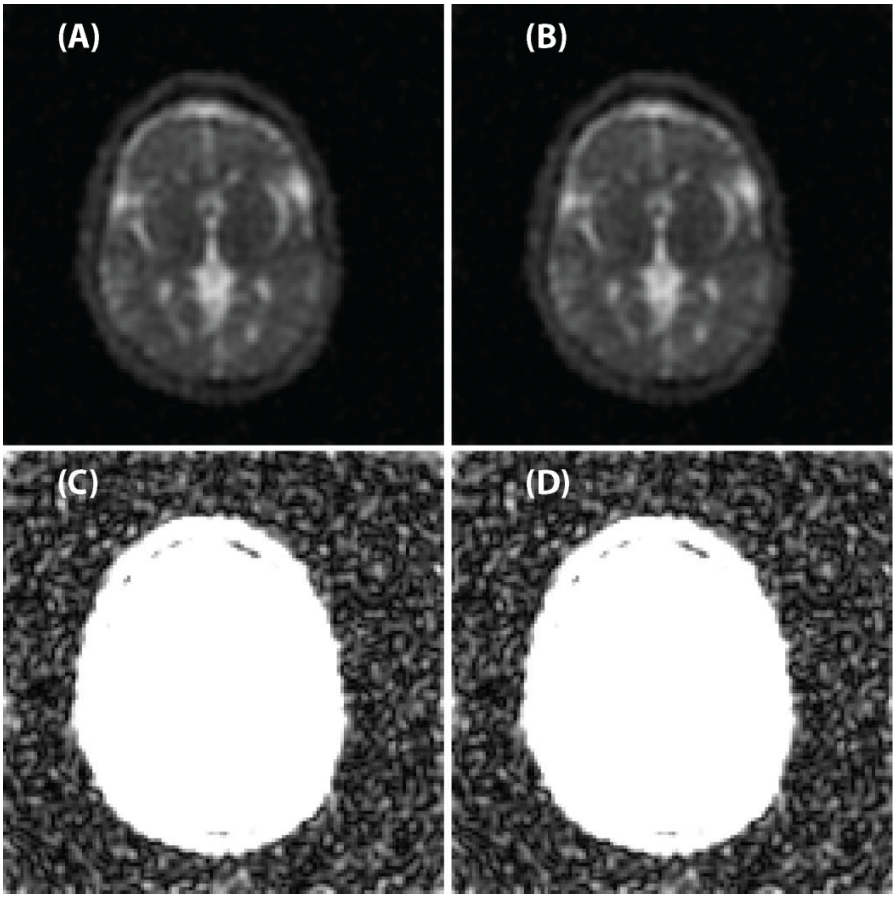

Figure A2-6: Comparing the amplified replication based error for convolution gridding using the width 4 and β = 6.5 kernel (A, C) and the width 6 and β = 10.5 kernel (B, D). Very small difference can be seen in the corner of the images windowed to highlight noise. However, this tiny difference is beyond the FoV and of very little interest.

Appendix 3

Arbitrary Imaging Development (AID) Software

Matlab based software was developed for the design and implementation of non-Cartesian k-space sampling. This software, named AID (Arbitrary Imaging Development), is intended to be independent of the actual k-space projection design and so provide utility for any and all non-Cartesian trajectories that could be conceived. The purpose of the AID software is to provide a platform for k-space projection design (i.e. to load, display editable design parameters for, and execute projection designs), to appropriately quantize each k-space projection design produced, to generate the gradient files to be implemented by the system, to recalculate sampled k-space locations based on gradient field step transition shapes, and to calculate the appropriate weighting parameters required for sampling density compensation.

The AID software is at the heart of the non-Cartesian imaging performed. The Varian Inova scanner was programmed as a 'dumb' participant in k-space acquisition, loading and 'playing' gradient files previously generated by AID, and storing acquired data for subsequent processing. In this manner, each (and any) type of k-space acquisition developed with AID can be implemented for any given Varian Inova program file. Different Varian Inova program files (each with the same 'dumb' k-space acquisition) are required only for different types of NMR sequences, i.e. sequences with different numbers of RF pulses and phases preceding acquisition. Use of the AID software is only required when k-space acquisition characteristics are to be changed; following development only the saved files generated by AID are needed for image generation.

Design files for numerous k-space acquisition methodologies were created during the tenure of this thesis including designs for: 'standard' TPI and sampling density apodized k-space acquisition (Chapter 2), relaxation compensating k-space acquisition (Chapter 4), and a novel 'Free-Twisting' TPI technique (not included in this thesis, but presented at the Non-Cartesian workshop in Sedona (144)).

Figure A3-1: Screenshot of the AID software user interface. The left column contains user input and projection characteristics dependent on the k-space projection design files loaded. The remaining columns are associated with the creation (of gradient and image construction files) and projection set analysis.

Appendix 4

Arbitrary Image Creation (AIC) Software

Images were created using another piece of software developed during this thesis labelled Arbitrary Image Creation (AIC) software. The purpose of this software was to read and properly format the exported experimental data from the Varian Inova scanner, import the k-space matrix locations and sampling density compensation matrix associated with the projection set used (as previously generated by the AID software), and perform the convolution gridding image creation process as well as zero-filling and scaling. The AIC software offers some rudimentary image visualization as well as export capability to the 'analyze' format.

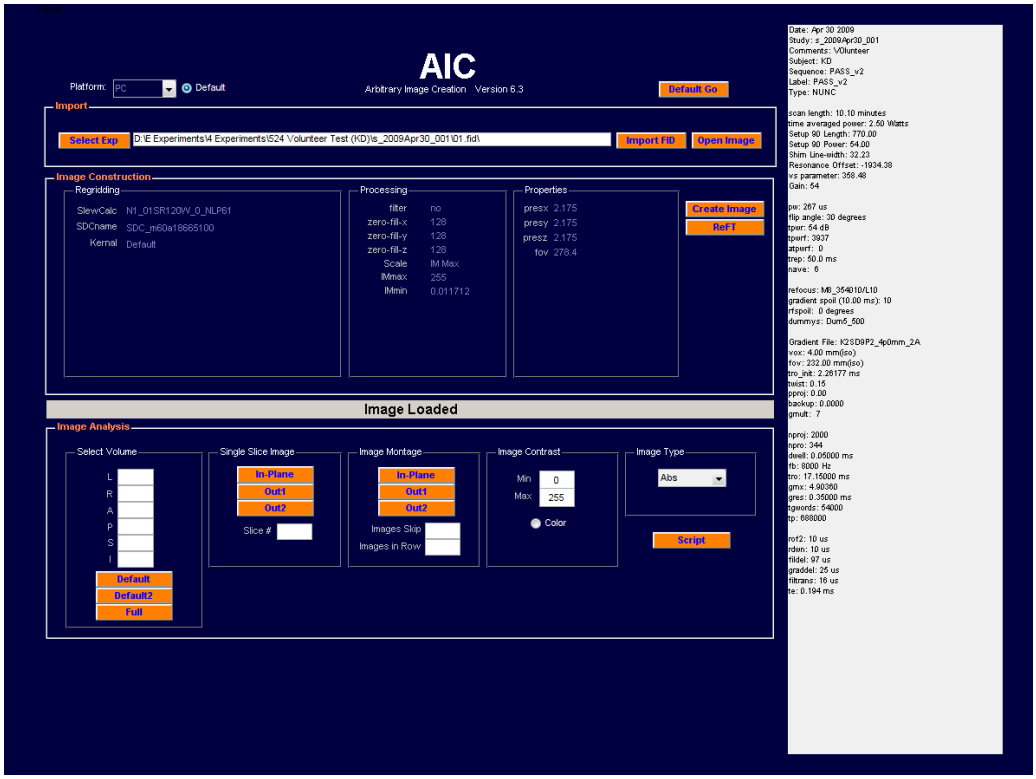

Figure A4-1: Screenshot of the AIC software user interface. Various image parameters are displayed on the right. Some rudimentary image display functions are offered along with image export.

Appendix 5

Galileo (Image Analysis) Software

Image analysis software was created to fill the need for an appropriately functional and flexible tool for the stroke study of Chapter 6. This software, named Galileo, has many region of interest drawing, analysis, and saving features not present on other software tools available during the tenure of this thesis. All the features of this software are keyboard and mouse based to facilitate accelerated analysis capability.

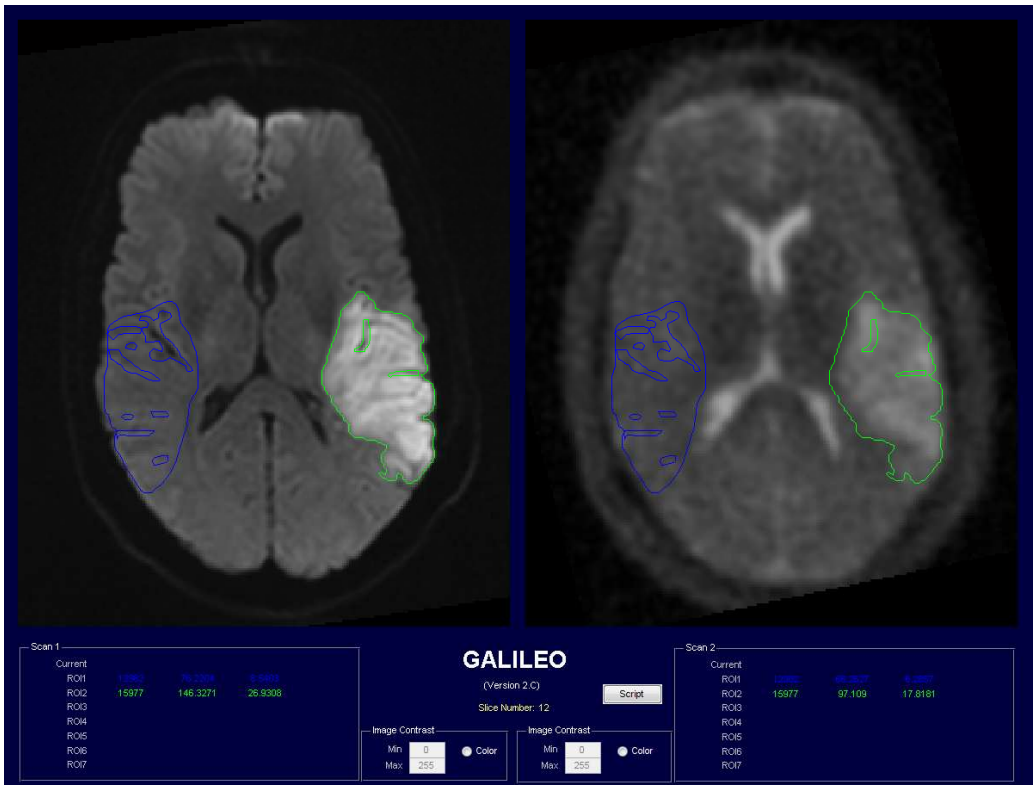

Figure A5-1: Screenshot of the Galileo software user interface. For this example the stroke lesion was drawn on the DWI image and visible CSF contributions to each ROI drawn on coregistered T_2 images. Encircled regions within a greater ROI are exclusionary. The Galileo displays ROI volumes as well as average intensity measures and standard deviation. However, any other analysis feature that could be created in Matlab is available through the 'script' button.

Appendix 6

Sodium Spin Simulation (Triple-S) Software

A sodium spin simulator was developed to help understand, visualize, and optimize sodium NMR sequence. This simulator solves the coupled differential equations describing the evolution of the sodium spin ensemble density operator under all relevant Hamiltonians (these coupled equations come directly from (71,145,146) and are described in Chapter 1.5). The simulations of Chapters 5 and 7 were performed using this software.

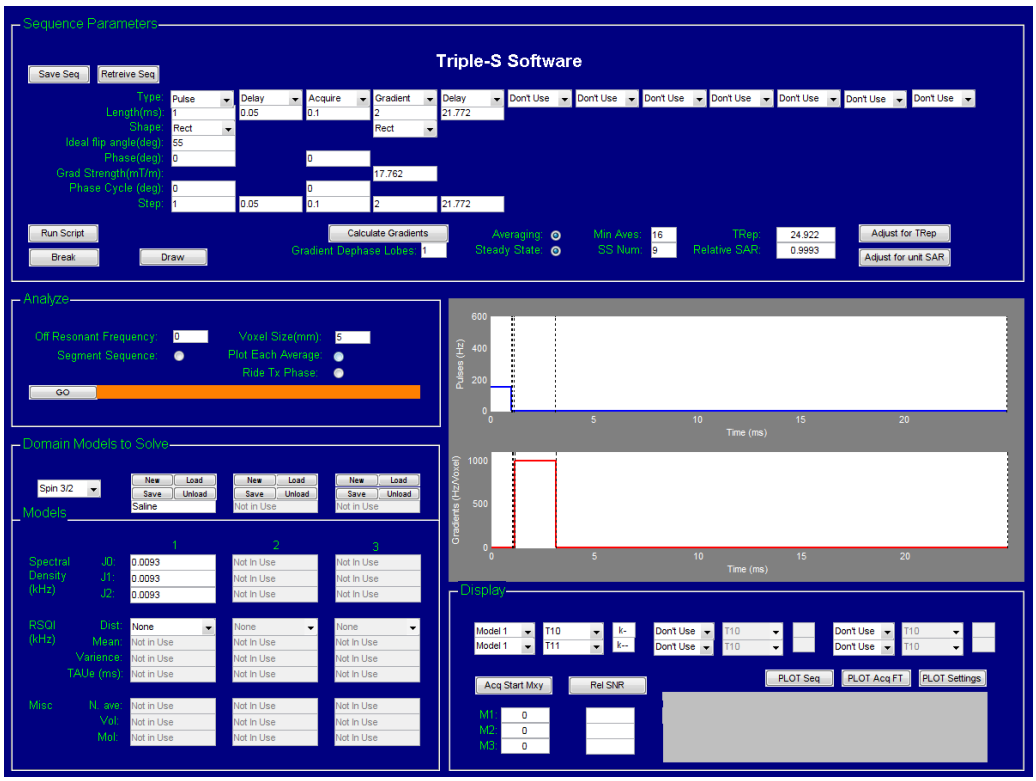

Figure A6-1: Screenshot of the Triple-S software user interface. This simple pulse sequence contains one RF pulse and a spoiling gradient. Considerably longer more complicated sequences, including multiple quantum filtering can be assessed. The evolution of all of the spin ensemble polarizations, as described by the irreducible tensor operator, can plotted throughout the pulse sequences. Spin 3/2 relaxation, as described by the spectral density parameters, as well as residual static quadrupole interaction effects can be simultaneously considered.

Appendix 7

4.7 Tesla Sodium Radio Frequency Head Coil

A simple, 16-rung, high-pass, quadrature sodium birdcage head coil was built early in this thesis for the sodium Larmor frequency of the 4.7 Tesla Varian system, 53 MHz, and was used exclusively for the experiments in this thesis (**Figure A7-1**). This coil, intended as a temporary coil until a professionally manufactured coil was to be completed, remains in use at the end of the tenure of this thesis.

Figure A7-1: A picture of the sodium birdcage head coil constructed and used during this thesis.

This 4.7 Tesla sodium head coil has a diameter of 30 cm, a rung length of 18 cm, and an end rung capacitance is 202 pF. The balun matching (**Figure A7-2**) (313) for human head loading includes 90 nH inductors and 100 pF capacitors. The loaded quality factor for the coil is 39.

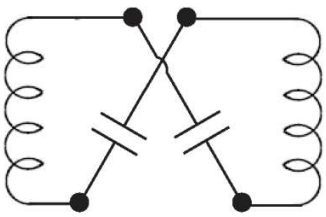

Figure A7-2: The balun matching circuit used in the sodium birdcage head coil.

Appendix 8

Sampling Efficiency Derivation

k-Space sampling efficiency is a measure of relative SNR concerning the generation of a desired $\Gamma[m]$ shape. An equation defining the decrease in noise variance for generation of a k-space filtering shape when designed sampling density is used instead of post-acquisition weighting is simply stated in the introduction of Chapter 2. The simple derivation of this equation, which was cut from the paper in revision for length related reasons is given below, as it is not listed elsewhere (to the author's knowledge).

The generation of $\Gamma[m]$ k-space transfer function is reflected in the relative noise power spectral density (rPSD) introduced in Chapter 1.3, where SD is the sampling density, W is post-acquisition weighting

$$\mathrm{rPSD}[m] \propto \mathrm{SD}[m] \cdot \mathrm{W}^2[m] \qquad \text{[A8-1]}$$

Consider first for the case of k-space filtering by post-acquisition weighting that $\mathrm{N_{ave}}$ samples have been acquired for each k-space location in a uniform manner, i.e.

$$\mathrm{SD}[m] = \mathrm{N_{ave}}. \qquad \text{[A8-2]}$$

The weighting required to produce the $\Gamma[m]$ shape with a value of one at the centre of k-space must be

$$\mathrm{W}[m] = \frac{\Gamma[m]}{\mathrm{N_{ave}}}, \qquad \text{[A8-3]}$$

yielding the relative noise power spectral density

$$\mathrm{rPSD}[m] \propto \frac{\Gamma^2[m]}{\mathrm{N_{ave}}}, \qquad \text{[A8-4]}$$

and the image noise variance dependence for k-space filtering by post-acquisition weighting

$$\sigma^2_{\mathrm{PAW}} \propto \frac{1}{\mathrm{N_{ave}}} \sum_{\mathrm{A}} \Gamma^2[m] \ . \qquad \text{[A8-5]}$$

Now consider that k-space has been sampled in such a manner that the same total number of data points ($\mathrm{N_{ave}} \cdot \mathrm{A}$), where A describes the k-space matrix dimensions, have been acquired covering the same k-space volume. However, the excess data points at the edges of k-space have been redistributed toward the central region to generate a sampling density shape that is a scaled version of $\Gamma[m]$

$$\mathrm{N_{ave}A} = b \cdot \sum_{\mathrm{A}} \Gamma[m] \ . \qquad \text{[A8-6]}$$

The sampling density with thus be

$$\mathrm{SD}[m] = b \cdot \Gamma[m] \ , \qquad \text{[A8-7]}$$

and the required constant weighting to maintain a constant value of one at the centre of k-space

$$\mathrm{W}[m] = \frac{1}{b} \ . \qquad \text{[A8-8]}$$

The relative PSD will be

$$\mathrm{rPSD}[m] \propto \left(\frac{\sum_{\mathrm{A}} \Gamma[m]}{\mathrm{N_{ave}A}} \right) \cdot \Gamma[m] \ , \qquad \text{[A8-9]}$$

and the image noise variance dependence for sampling density designed k-space filtering

$$\sigma^2_{\mathrm{SD}} \propto \frac{1}{\mathrm{N_{ave}A}} \left(\sum_{\mathrm{M}} \Gamma[m] \right)^2 \ . \qquad \text{[A8-10]}$$

The relative noise difference between the two methods of producing k-space filtering is

$$\frac{\sigma^2_{\mathrm{PAW}}}{\sigma^2_{\mathrm{SD}}} = \frac{\mathrm{A} \cdot \sum_{\mathrm{A}} \Gamma^2[m]}{(\sum_{\mathrm{A}} \Gamma[m])^2}\,. \qquad \text{[A8-11]}$$

While this simple derivation is related to the generation of a k-space filter it can conceptually be applied to the weighting of individual sampling points regardless of their location. The expression of Eq. [A8-12] (in its essence) has been presented previously with different derivation (55)

$$\frac{\sigma^2_{\mathrm{PAW}}}{\sigma^2_{\mathrm{SD}}} = \frac{\mathrm{L} \cdot \sum_{\lambda} \mathrm{W}^2[\lambda]}{(\sum_{\lambda} \mathrm{W}[\lambda])^2} \qquad \text{[A8-12]}$$

In this case $\mathrm{W}[p]$ is the post-acquisition weighting applied to any given sampling point acquired, and (L) is the total number of samples acquired. The most SNR efficient k-space acquisition is attained when no post-acquisition weighting is required. Previously this has been discussed in terms of weighting required to produce a uniform $\Gamma[\mathrm{m}]$ when sampling density is non-uniform (55), but the production of uniform $\Gamma[\mathrm{m}]$ may not always be optimal.

References

1. Hilal SK, Maudsley AA, Ra JB, Simon HE, Roschmann P, Wittekoek S, Cho ZH, Mun SK. Invivo Nmr Imaging of Na-23 in the Human Head. J Comput Assist Tomo 1985;9(1):1-7.

2. Jacobs MA, Ouwerkerk R, Kamel I, Bottomley PA, Bluemke DA, Kim HS. Proton, Diffusion-Weighted Imaging, and Sodium (Na-23) MRI of Uterine Leiomyomata after MR-Guided High-Intensity Focused Ultrasound: A Preliminary Study. J Magn Reson Imaging 2009;29(3):649-656.

3. Bartha R, Megyesi JF, Watling CJ. Low-grade glioma: Correlation of short echo time H-1-MR spectoscopy with Na-23 MR imaging. Am J Neuroradiol 2008;29(3):464-470.

4. Ouwerkerk R, Jacobs MA, Macura KJ, Wolff AC, Stearns V, Mezban SD, Khouri NF, Bluemke DA, Bottomley PA. Elevated tissue sodium concentration in malignant breast lesions detected with non-invasive Na-23 MRI. Breast Cancer Res Tr 2007;106(2):151-160.

5. Nielles-Vallespin S, Weber MA, Bock M, Bongers A, Speier P, Combs SE, Wohrle J, Lehmann-Horn F, Essig M, Schad LR. 3D radial projection technique with ultrashort echo times for sodium MRI: Clinical applications in human brain and skeletal muscle. Magn Reson Med 2007;57(1):74-81.

6. Ouwerkerk R, Bleich KB, Gillen JS, Pomper MG, Bottomley PA. Tissue sodium concentration in human brain tumors as measured with Na-23 MR imaging. Radiology 2003;227(2):529-537.

7. Thulborn KR, Davis D, Adams H, Gindin T, Zhou J. Quantitative tissue sodium concentration mapping of the growth of focal cerebral tumors with sodium magnetic resonance imaging. Magn Reson Med 1999;41(2):351-359.

8. Schuierer G, Ladebeck R, Barfuss H, Hentschel D, Huk WJ. Na-23 Imaging of Supratentorial Lesions at 4.0-T. Magnet Reson Med 1991;22(1):1-9.

9. Grodd W, Klose U. Sodium-Mr-Imaging of the Brain - Initial Clinical-Results. Neuroradiology 1988;30(5):399-407.

10. Turski PA, Houston LW, Perman WH, Hald JK, Turski D, Strother CM, Sackett JF. Experimental and Human-Brain Neoplasms - Detection with Invivo Sodium Mr Imaging. Radiology 1987;163(1):245-249.

11. Thulborn KR, Davis D, Snyder J, Yonas H, Kassam A. Sodium MR imaging of acute and subacute stroke for assessment of tissue viability. Neuroimag Clin N Am 2005;15(3):639-+.

12. Thulborn KR, Gindin TS, Davis D, Erb P. Comprehensive MR imaging protocol for stroke management: Tissue sodium concentration as a measure of tissue viability in nonhuman primate studies and in clinical studies. Radiology 1999;213(1):156-166.

13. Shimizu T, Naritomi H, Sawada T. Sequential-Changes on Na-23 Mri after Cerebral Infarction. Neuroradiology 1993;35(6):416-419.

14. Ouwerkerk R, Bottomley PA, Solaiyappan M, Spooner AE, Tomaselli GF, Wu KC, Weiss RG. Tissue sodium concentration in myocardial infarction in humans: A quantitative Na-23 MR imaging study. Radiology 2008;248(1):88-96.

15. Sandstede JJW, Hillenbrand H, Beer M, Pabst T, Butter F, Machann W, Bauer W, Hahn D, Neubauer S. Time course of Na-23 signal intensity after myocardial infarction in humans. Magnet Reson Med 2004;52(3):545-551.

16. Sandstede JJW, Pabst T, Beer M, Lipke C, Baurle K, Butter F, Harre K, Kenn W, Voelker W, Neubauer S, Hahn D. Assessment of myocardial infarction in humans with Na-23 MR imaging: Comparison with cine MR imaging and delayed contrast enhancement. Radiology 2001;221(1):222-228.

17. Weber MA, Nielles-Vallespin S, Essig M, Jurkat-Rott K, Kauczor HU, Lehmann-Horn F. Muscle Na+ channelopathies - MRI detects intracellular Na-23 accumulation during episodic weakness. Neurology 2006;67(7):1151-1158.

18. Weber MA, Nielles-Vallespin S, Huttner HB, Wohrle JC, Jurkat-Rott K, Lehmann-Horn F, Schad LR, Kauczor HU, Essig M, Meinck HM. Evaluation of patients with paramyotonia at Na-23 MR imaging during cold-induced weakness. Radiology 2006;240(2):489-500.

19. Wheaton AJ, Borthakur A, Shapiro EM, Regatte RR, Akella SVS, Kneeland JB, Reddy R. Proteoglycan loss in human knee cartilage: Quantitation with sodium MR imaging - Feasibility study. Radiology 2004;231(3):900-905.

20. Wang LG, Wu Y, Chang G, Oesingmann N, Schweitzer ME, Jerschow A, Regatte RR. Rapid Isotropic 3D-Sodium MRI of the Knee Joint In Vivo at 7T. J Magn Reson Imaging 2009;30(3):606-614.

21. Borthakur A, Mellon E, Niyogi S, Witschey W, Kneeland JB, Reddy R. Sodium and T-1 rho MRI for molecular and diagnostic imaging of articular cartilage. Nmr Biomed 2006;19(7):781-821.

22. Shimizu T, Naritomi H, Kuriyama Y, Sawada T. Sequential-Changes of Sodium Magnetic-Resonance Images after Cerebral-Hemorrhage. Neuroradiology 1992;34(4):301-304.

23. Mellon EA, Pilkinton DT, Clark CM, Elliott MA, Witschey WR, Borthakur A, Reddy R. Sodium MR Imaging Detection of Mild Alzheimer Disease: Preliminary Study. Am J Neuroradiol 2009;30(5):978-984.

24. Vander A, Sherman, J., Luciano, D. Human Physiology. New York: McGraw-Hill; 2001.

25. Bartha R, Menon RS. Long component time constant of Na-23 T*(2) relaxation in healthy human brain. Magn Reson Med 2004;52(2):407-410.

26. Clayton DB, Lenkinski RE. MR imaging of sodium in the human brain with a fast three-dimensional gradient-recalled-echo sequence at 4 T. Acad Radiol 2003;10(4):358-365.

27. Kohler S, Preibisch C, Nittka M, Haase A. Fast three-dimensional sodium imaging of human brain. Magn Reson Mater Phy 2001;13(2):63-69.

28. Hancu I, Boada FE, Shen GX. Three-dimensional triple-quantum-filtered Na-23 imaging of in vivo human brain. Magn Reson Med 1999;42(6):1146-1154.

29. Boada FE, Shen GX, Chang SY, Thulborn KR. Spectrally weighted twisted projection imaging: Reducing T-2 signal attenuation effects in fast three-dimensional sodium imaging. Magn Reson Med 1997;38(6):1022-1028.

30. Boada FE, Gillen JS, Shen GX, Chang SY, Thulborn KR. Fast three dimensional sodium imaging. Magn Reson Med 1997;37(5):706-715.

31. Winkler SS. Na-23 Magnetic-Resonance Brain Imaging. Neuroradiology 1990;32(5):416-420.

32. Winkler SS, Thomasson DM, Sherwood K, Perman WH. Regional T2 and Sodium Concentration Estimates in the Normal Human-Brain by Na-23 Mr Imaging at 1.5 T. J Comput Assist Tomo 1989;13(4):561-566.

33. Turski PA, Perman WH, Hald JK, Houston LW, Strother CM, Sackett JF. Clinical and Experimental Vasogenic Edema - Invivo Sodium Mr Imaging. Radiology 1986;160(3):821-825.

34. Perman WH, Turski PA, Houston LW, Glover GH, Hayes CE. Methodology of Invivo Human Sodium Mr Imaging at 1.5 T. Radiology 1986;160(3):811-820.

35. Qian YX, Stenger VA, Boada FE. Parallel imaging with 3D TPI trajectory: SNR and acceleration benefits. Magn Reson Imaging 2009;27(5):656-663.

36. Nagel AM, Laun FB, Weber MA, Matthies C, Semmler W, Schad LR. Sodium MRI Using a Density-Adapted 3D Radial Acquisition Technique. Magn Reson Med 2009;62(6):1565-1573.

37. Fleysher L, Oesingmann N, Stoeckel B, Grossman RI, Inglese M. Sodium Long-Component T-2* Mapping in Human Brain at 7 Tesla. Magnet Reson Med 2009;62(5):1338-1341.

38. Augath M, Heiler P, Kirsch S, Schad LR. In vivo K-39, Na-23 and H-1 MR imaging using a triple resonant RF coil setup. J Magn Reson 2009;200(1):134-136.

39. Romanzetti S, Halse M, Kaffanke J, Zilles K, Balcom BJ, Shah NJ. A comparison of three SPRITE techniques for the quantitative 3D imaging of the Na-23 spin density on a 4T whole-body machine. J Magn Reson 2006;179(1):64-72.

40. Feinberg DA, Crooks LA, Kaufman L, Brant-Zawadzki M, Posin JP, Arakawa M, Watts JC, Hoenninger J. Magnetic resonance imaging performance: a comparison of sodium and hydrogen. Radiology 1985;156(1):133-138.

41. Hussain MS, Stobbe RW, Bhagat YA, Emery D, Butcher KS, Manawadu D, Rizvi N, Maheshwari P, Scozzafava J, Shuaib A, Beaulieu C. Sodium Imaging Intensity Increases with Time after Human Ischemic Stroke. Ann Neurol 2009;66(1):55-62.

42. Stobbe R, Beaulieu C. Sodium imaging optimization under specific absorption rate constraint. Magn Reson Med 2008;59(2):345-355.

43. Stobbe R, Beaulieu C. Advantage of sampling density weighted apodization over postacquisition filtering apodization for sodium MRI of the human brain. Magn Reson Med 2008;60(4):981-986.

44. Stobbe R, Beaulieu C. In vivo sodium magnetic resonance imaging of the human brain using soft inversion recovery fluid attenuation. Magn Reson Med 2005;54(5):1305-1310.

45. Stobbe R, Beaulieu C. Sodium Relaxometry: Towards the Characterization of the Sodium NMR Environment in the Human Brain Using a Novel Relaxometry Technique. Proceedings of the 14th Annual Meeting of ISMRM, Seattle, Washington, USA 2006:3104.

46. Dizon JM, Tauskela JS, Wise D, Burkhoff D, Cannon PJ, Katz J. Evaluation of triple-quantum-filtered Na-23 NMR in monitoring of intracellular Na content in the perfused rat heart: Comparison of intra- and extracellular transverse relaxation and spectral amplitudes. Magn Reson Med 1996;35(3):336-345.

47. Colet JM, Bansal N, Malloy CR, Sherry AD. Multiple quantum filtered Na-23 NMR spectroscopy of the isolated, perfused rat liver. Magn Reson Med 1999;41(6):1127-1135.

48. Perman WH, Thomasson DM, Bernstein MA, Turski PA. Multiple Short-Echo (2.5-Ms) Quantitation of Invivo Sodium T2 Relaxation. Magn Reson Med 1989;9(2):153-160.

49. Winter PM, Bansal N. Triple-quantum-filtered Na-23 NMR spectroscopy of subcutaneously implanted 9L gliosarcoma in the rat in the presence of TmDOTP5-. J Magn Reson 2001;152(1):70-78.

50. Winter PM, Bansal N. TmDOTP5- as a Na-23 shift reagent for the subcutaneously implanted 9L gliosarcoma in rats. Magn Reson Med 2001;45(3):436-442.

51. Pabst T, Sandstede J, Beer M, Kenn W, Neubauer S, Hahn D. Sodium T2* relaxation times in human heart muscle. J Magn Reson Imaging 2002;15(2):215-218.

52. Van Emous JG, Van Echteld GJA. Changes of intracellular sodium T-2 relaxation times during ischemia and reperfusion in isolated rat hearts. Magn Reson Med 1998;40(5):679-683.

53. Seshan V, Sherry AD, Bansal N. Evaluation of triple quantum-filtered Na-23 NMR spectroscopy in the in situ rat liver. Magn Reson Med 1997;38(5):821-827.

54. Haacke EM, Brown RW, Thompson MR, R. V. Magnetic Resonance Imaging. New York: John Wiley & Sons; 1999.

55. Pipe JG, Duerk JL. Analytical Resolution and Noise Characteristics of Linearly Reconstructed Magnetic-Resonance Data with Arbitrary K-Space Sampling. Magn Reson Med 1995;34(2):170-178.

56. Jackson JI, Nishimura DG, Macovski A. Twisting Radial Lines with Application to Robust Magnetic-Resonance-Imaging of Irregular Flow. Magn Reson Med 1992;25(1):128-139.

57. Haacke EM, Tkach JA. Fast Mr-Imaging - Techniques and Clinical-Applications. Am J Roentgenol 1990;155(5):951-964.

58. Young W, Rappaport ZH, Chalif DJ, Flamm ES. Regional Brain Sodium, Potassium, and Water Changes in the Rat Middle Cerebral-Artery Occlusion Model of Ischemia. Stroke 1987;18(4):751-759.

59. Siesjo BK, Deshpande JK. Electrolyte Shifts between Brain and Plasma in Hypoglycemic Coma. J Cerebr Blood F Met 1987;7(6):789-793.

60. Stobbe R, Beaulieu, C. Advantage of Sampling Density Weighted Apodization Over Postacquisition Filtering Apodization for Sodium MRI of the Human Brain. Magn Reson Med 2008;60(4):981-986.

61. Devore J, Peck, R. Statistics, The Exploration and Analysis of Data. Toronto, Canada: Nelson; 2005.

62. Peebles P. Probability, Random Variables, and Random Signal Properties. New York: McGraw-Hill; 1993.

63. Buxton R. Introduction to Functional Magnetic Resonance Imaging: Principles and Techniques. Cambridge: University Press; 2002.

64. Jones SC, Kharlamov A, Yanovski B, Kim DK, Easley KA, Yushmanov VE, Ziolko SK, Boada FE. Stroke onset time using sodium MRI in rat focal cerebral ischemia. Stroke 2006;37(3):883-888.

65. Bartha R, Lee TY, Hogan MJ, Hughes S, Barberi E, Rajakumar N, Menon RS. Sodium T-2*-weighted MR imaging of acute focal cerebral ischemia in rabbits. Magn Reson Imaging 2004;22(7):983-991.

66. Thulborn KR, Davis D, Snyder J, Yonas H, Kassam A. Sodium MR imaging of acute and subacute stroke for assessment of tissue viability. Neuroimag Clin N Am 2005;15(3):639-653.

67. Lin SP, Song SK, Miller JP, Ackerman JJH, Neil JJ. Direct, longitudinal comparison of H-1 and Na-23 MRI after transient focal cerebral ischemia. Stroke 2001;32(4):925-932.

68. Gotoh O, Asano T, Koide T, Takakura K. Ischemic Brain Edema Following Occlusion of the Middle Cerebral-Artery in the Rat .1. The Time Courses of the Brain Water, Sodium and Potassium Contents and Blood-Brain-Barrier Permeability to I-125 Albumin. Stroke 1985;16(1):101-109.

69. Tanase C, Boada FE. Triple-quantum-filtered imaging of sodium in presence of B-0 inhomogeneities. Journal of Magnetic Resonance 2005;174(2):270-278.

70. Winter PM, Poptani H, Bansal N. Effects of chemotherapy by 1,3-bis(2-chloroethyl)-1-nitrosourea on single-quantum- and triple-quantum-filtered Na-23 and P-31 nuclear magnetic resonance of the subcutaneously implanted 9L glioma. Cancer Res 2001;61(5):2002-2007.

71. Hancu I, van der Maarel JRC, Boada FE. A model for the dynamics of spins 3/2 in biological media: Signal loss during radiofrequency excitation in triple-quantum-filtered sodium MRI. Journal of Magnetic Resonance 2000;147(2):179-191.

72. Borthakur A, Hancu I, Boada FE, Shen GX, Shapiro EM, Reddy R. In vivo triple quantum filtered twisted projection sodium MRI of human articular cartilage. Journal of Magnetic Resonance 1999;141(2):286-290.

73. Schepkin VD, Choy IO, Budinger TF, Obayashi DY, Taylor SE, DeCampli WM, Amartur SC, Young JN. Sodium TQF NMR and intracellular sodium in isolated crystalloid perfused rat heart. Magnet Reson Med 1998;39(4):557-563.

74. Kalyanapuram R, Seshan V, Bansal N. Three-dimensional triple-quantum-filtered Na-23 imaging of the dog head in vivo. Jmri-J Magn Reson Im 1998;8(5):1182-1189.

75. Jaccard G, Wimperis S, Bodenhausen G. Multiple-Quantum Nmr-Spectroscopy of S=3/2 Spins in Isotropic-Phase - a New Probe for Multiexponential Relaxation. J Chem Phys 1986;85(11):6282-6293.

76. Yepes M, Roussel BD, Ali C, Vivien D. Tissue-type plasminogen activator in the ischemic brain: more than a thrombolytic. Trends Neurosci 2009;32(1):48-55.

77. Wahlgren N, Ahmed N, Davalos A, Ford GA, Grond M, Hacke W, Hennerici MG, Kaste M, Kuelkens S, Larrue V, Lees KR, Roine RO, Soinne L, Toni D, Vanhooren G, Investigators S-M. Thrombolysis with alteplase for acute ischaemic stroke in the Safe implementation of Thrombolysis in Stroke-Monitoring Study (SITS-MOST): an observational study. Lancet 2007;369(9558):275-282.

78. Hacke W. Guidelines for management of ischaemic stroke and transient ischaemic attack 2008 - The European Stroke Organisation (ESO) Executive Committee and the ESO Writing Committee. Cerebrovasc Dis 2008;25(5):457-507.

79. Adams HP, del Zoppo G, Alberts MJ, Bhatt DL, Brass L, Furlan A, Grubb RL, Higashida RT, Jauch EC, Kidwell C, Lyden PD, Morgenstern LB, Qureshi AI, Rosenwasser RH, Scott PA, Wijdicks EFM. Guidelines for the early management of adults with ischemic stroke - A guideline from the American Heart Association/American Stroke Association Stroke Council, Clinical Cardiology Council, Cardiovascular Radiology and Intervention Council, and the atherosclerotic peripheral vascular disease and quality of care outcomes in research interdisciplinary working groups. Stroke 2007;38(5):1655-1711.

80. The_National_Institute_of_Neurological_Disorders_and_Stroke_rt-PA_Stroke_Study_Group. Tissue-Plasminogen Activator for Acute Ischemic Stroke. New Engl J Med 1995;333(24):1581-1587.

81. Ingall TJ, O'Fallon WM, Asplund K, Goldfrank LR, Hertzberg VS, Louis TA, Christianson TJH. Findings from the reanalysis of the NINDS tissue plasminogen activator for acute ischemic stroke treatment trial. Stroke 2004;35(10):2418-2424.

82. Saver JL. Number needed to treat estimates incorporating effects over the entire range of clinical outcomes - Novel derivation method and application to thrombolytic therapy for acute stroke. Arch Neurol-Chicago 2004;61(7):1066-1070.

83. Saver JL. Hemorrhage after thrombolytic therapy for stroke - The clinically relevant number needed to harm. Stroke 2007;38(8):2279-2283.

84. Hacke W, Kaste M, Fieschi C, Toni D, Lesaffre E, Vonkummer R, Boysen G, Bluhmki E, Hoxter G, Mahagne MH, Hennerici M. Intravenous Thrombolysis with Recombinant Tissue-Plasminogen Activator for Acute Hemispheric Stroke - the European Cooperative Acute Stroke Study (Ecass). Jama-J Am Med Assoc 1995;274(13):1017-1025.

85. Hacke W, Kaste M, Fieschi C, von Kummer R, Davalos A, Meier D, Larrue V, Bluhmki E, Davis S, Donnan G, Schneider D, Diez-Tejedor E, Trouillas P, Study SEAAS. Randomised double-blind placebo-controlled trial of thrombolytic therapy with intravenous alteplase in acute ischaemic stroke (ECASS II). Lancet 1998;352(9136):1245-1251.

86. Clark WM, Wissman S, Albers GW, Jhamandas JH, Madden KP, Hamilton S, Investigators AS. Recombinant tissue-type plasminogen activator (alteplase) for ischemic stroke 3 to 5 hours after symptom onset - The ATLANTIS study: A randomized controlled trial. Jama-J Am Med Assoc 1999;282(21):2019-2026.

87. Clark WM, Albers GW, Madden KP, Hamilton S, Ischemi TTA. The rtPA (Alteplase) 0- to 6-hour acute stroke trial, part A (A0276g) - Results of a double-blind, placebo-controlled, multicenter study. Stroke 2000;31(4):811-816.

88. Hacke W, Donnan G, Fieschi C, Kaste M, von Kummer R, Broderick JP, Brott T, Frankel M, Grotta JC, Haley EC, Kwiatkowski T, Levine SR, Lewandowski C, Lu M, Lyden P, Marler JR, Patel S, Tilley BC, Albers G, Brott T, Grotta J, Bluhmki PE, Wilhelm M, Hamilton S, Investigators ASG, Investigators ESG, Investigato NR-PSG. Association of outcome with early stroke treatment: pooled analysis of ATLANTIS, ECASS, and NINDS rt-PA stroke trials. Lancet 2004;363(9411):768-774.

89. Hacke W, Kaste M, Bluhmki E, Brozman M, Davalos A, Guidetti D, Larrue V, Lees KR, Medeghri Z, Machnig T, Schneider D, von Kummer R, Wahlgren N, Toni D, Investigators E. Thrombolysis with alteplase 3 to 4.5 hours after acute ischemic stroke. New Engl J Med 2008;359(13):1317-1329.

90. Moseley ME, Cohen Y, Mintorovitch J, Chileuitt L, Shimizu H, Kucharczyk J, Wendland MF, Weinstein PR. Early Detection of Regional Cerebral-Ischemia in Cats - Comparison of Diffusion-Weighted and T2-Weighted Mri and Spectroscopy. Magn Reson Med 1990;14(2):330-346.

91. Warach S, Chien D, Li W, Ronthal M, Edelman RR. Fast Magnetic-Resonance Diffusion-Weighted Imaging of Acute Human Stroke. Neurology 1992;42(9):1717-1723.

92. Hjort N, Christensen S, Solling C, Ashkanian M, Wu O, Rohl L, Gyldensted C, Andersen G, Ostergaard L. Ischemic injury detected by diffusion imaging 11 minutes after stroke. Ann Neurol 2005;58(3):462-465.

93. Fiehler J, Knudsen K, Kucinski T, Kidwell CS, Alger JR, Thomalla G, Eckert B, Wittkugel O, Weiller C, Zeumer H, Rother J. Predictors of apparent diffusion coefficient normalization in stroke patients. Stroke 2004;35(2):514-519.

94. Astrup J, Siesjo BK, Symon L. Thresholds in Cerebral-Ischemia - the Ischemic Penumbra. Stroke 1981;12(6):723-725.

95. Lipton P. Ischemic cell death in brain neurons. Physiol Rev 1999;79(4):1431-1568.

96. Baird AE, Benfield A, Schlaug G, Siewert B, Lovblad KO, Edelman RR, Warach S. Enlargement of human cerebral ischemic lesion volumes measured by diffusion-weighted magnetic resonance imaging. Ann Neurol 1997;41(5):581-589.

97. Barber PA, Darby DG, Desmond PM, Yang Q, Gerraty RP, Jolley D, Donnan GA, Tress BM, Davis SM. Prediction of stroke outcome with echoplanar perfusion- and diffusion-weighted MRI. Neurology 1998;51(2):418-426.

98. Beaulieu C, de Crespigny A, Tong DC, Moseley ME, Albers GW, Marks MP. Longitudinal magnetic resonance imaging study of perfusion and diffusion in stroke: Evolution of lesion volume and correlation with clinical outcome. Ann Neurol 1999;46(4):568-578.

99. Albers GW, Thijs VN, Wechsle L, Kemp S, Schlaug G, Skalabrin E, Bammer R, Kakuda W, Lansberg MG, Shuaib A, Coplin W, Scott H, Moseley M, Marks MP, Investigtion D. Magnetic resonance imaging profiles predict clinical response to early reperfusion: The diffusion and perfusion imaging evaluation for understanding stroke evolution (DEFUSE) study. Ann Neurol 2006;60(5):508-517.

100. Davis SM, Donnan GA, Parsons MW, Levi C, Butcher KS, Peeters A, Barber PA, Bladin C, De Silva DA, Byrnes G, Chalk JB, Fink JN, Kimber TE, Schultz D, Hand PJ, Frayne J, Hankey G, Muir K, Gerraty R, Tress BM, Desmond PM, Investigators E. Effects of alteplase beyond 3 h after stroke in the Echoplanar Imaging Thrombolytic Evaluation Trial (EPITHET): a placebo-controlled randomised trial. Lancet Neurol 2008;7(4):299-309.

101. Barber PA, Zhang J, Demchuk AM, Hill MD, Buchan AM. Why are stroke patients excluded from TPA therapy? An analysis of patient eligibility. Neurology 2001;56(8):1015-1020.

102. Schuier FJ, Hossmann KA. Experimental Brain Infarcts in Cats .2. Ischemic Brain Edema. Stroke 1980;11(6):593-601.

103. Ito U, Ohno K, Nakamura R, Suganuma F, Inaba Y. Brain Edema During Ischemia and after Restoration of Blood-Flow - Measurement of Water, Sodium, Potassium Content and Plasma-Protein Permeability. Stroke 1979;10(5):542-547.

104. Katzman R, Clasen R, Klatzo I, Meyer JS, Pappius HM, Waltz AG. Report of Joint Committee for Stroke Resources .4. Brain Edema in Stroke - Study-Group. Stroke 1977;8(4):509-540.

105. Betz AL, Keep RF, Beer ME, Ren XD. Blood-Brain-Barrier Permeability and Brain Concentration of Sodium, Potassium, and Chloride During Focal Ischemia. J Cerebr Blood F Met 1994;14(1):29-37.

106. Menzies SA, Betz AL, Hoff JT. Contributions of Ions and Albumin to the Formation and Resolution of Ischemic Brain Edema. J Neurosurg 1993;78(2):257-266.

107. Hatashita S, Hoff JT. Brain Edema and Cerebrovascular Permeability During Cerebral-Ischemia in Rats. Stroke 1990;21(4):582-588.

108. Lo WD, Betz AL, Schielke GP, Hoff JT. Transport of Sodium from Blood to Brain in Ischemic Brain Edema. Stroke 1987;18(1):150-157.

109. LaVerde G, Nemoto E, Jungreis CA, Tanase C, Boada FE. Serial triple quantum sodium MRI during non-human primate focal brain ischemia. Magn Reson Med 2007;57(1):201-205.

110. Boada FE, LaVerde G, Jungreis C, Nemoto E, Tanase C, Hancu F. Loss of cell ion homeostasis and cell viability in the brain: What sodium MRI can tell us. Curr Top Dev Biol 2005;70:77-101.

111. Tyson RL, Sutherland GR, Peeling J. (23)Na nuclear magnetic resonance spectral changes during and after forebrain ischemia in hypoglycemic, normoglycemic, and hyperglycemic rats. Stroke 1996;27(5):957-964.

112. Wang Y, Hu WX, Perez-Trepichio AD, Ng TC, Furlan AJ, Majors AW, Jones SC. Brain tissue sodium is a ticking clock telling time after arterial occlusion in rat focal cerebral ischemia. Stroke 2000;31(6):1386-1391.

113. Lees GJ. Inhibition of Sodium-Potassium-Atpase - a Potentially Ubiquitous Mechanism Contributing to Central-Nervous-System Neuropathology. Brain Res Rev 1991;16(3):283-300.

114. Stys PK. General mechanisms of axonal damage and its prevention. J Neurol Sci 2005;233(1-2):3-13.

115. Hansen AJ. Effect of Anoxia on Ion Distribution in the Brain. Physiol Rev 1985;65(1):101-148.

116. Breder J, Sabelhaus CF, Opitz T, Reymann KG, Schroder UH. Inhibition of different pathways influencing Na+ homeostasis protects organotypic hippocampal slice cultures from hypoxic/hypoglycemic injury. Neuropharmacology 2000;39(10):1779-1787.

117. Lee JM, Zipfel GJ, Choi DW. The changing landscape of ischaemic brain injury mechanisms. Nature 1999;399(6738):A7-A14.

118. Rothman SM, Olney JW. Glutamate and the Pathophysiology of Hypoxic Ischemic Brain-Damage. Ann Neurol 1986;19(2):105-111.

119. Dingledine R, Borges K, Bowie D, Traynelis SF. The glutamate receptor ion channels. Pharmacol Rev 1999;51(1):7-61.

120. MacGregor DG, Avshalumov MV, Rice ME. Brain edema induced by in vitro ischemia: causal factors and neuroprotection. J Neurochem 2003;85(6):1402-1411.

121. Czyz A, Baranauskas G, Kiedrowski L. Instrumental. role of Na+ in NMDA excitotoxicity in glucose-deprived and depolarized cerebellar granule cells. J Neurochem 2002;81(2):379-389.

122. Choi DW. Ionic Dependence of Glutamate Neurotoxicity. J Neurosci 1987;7(2):369-379.

123. Nicholls D, Attwell D. The Release and Uptake of Excitatory Amino-Acids. Trends Pharmacol Sci 1990;11(11):462-468.

124. Kahle KT, Simard JM, Staley KJ, Nahed BV, Jones PS, Sun DD. Molecular Mechanisms of Ischemic Cerebral Edema: Role of Electroneutral Ion Transport. Physiology 2009;24(4):257-265.

125. Fung ML. Role of voltage-gated Na+ channels in hypoxia-induced neuronal injuries. Clin Exp Pharmacol P 2000;27(8):569-574.

126. Nikolaeva MA, Mukherjee B, Stys PK. Na+-dependent sources of intra-axonal Ca2+ release in rat optic nerve during in vitro chemical ischemia. J Neurosci 2005;25(43):9960-9967.

127. Banasiak KJ, Burenkova O, Haddad GG. Activation of voltage-sensitive sodium channels during oxygen deprivation leads to apoptotic neuronal death. Neuroscience 2004;126(1):31-44.

128. Leppanen L, Stys PK. Ion transport and membrane potential in CNS myelinated axons .2. Effects of metabolic inhibition. J Neurophysiol 1997;78(4):2095-2107.

129. Stys PK, Waxman SG, Ransom BR. Na+-Ca2+ Exchanger Mediates Ca2+ Influx during Anoxia in Mammalian Central-Nervous-System White Matter. Ann Neurol 1991;30(3):375-380.

130. Simard JM, Kent TA, Chen MK, Tarasov KV, Gerzanich V. Brain oedema in focal ischaemia: molecular pathophysiology and theoretical implications. Lancet Neurol 2007;6(3):258-268.

131. Sheldon C, Diarra A, Cheng YM, Church J. Sodium influx pathways during and after anoxia in rat hippocampal neurons. J Neurosci 2004;24(49):11057-11069.

132. Beck J, Lenart B, Kintner DB, Sun D. Na-K-Cl cotransporter contributes to glutamate-mediated excitotoxicity. J Neurosci 2003;23(12):5061-5068.

133. Simard JM, Chen M, Tarasov KV, Bhatta S, Ivanova S, Melnitchenko L, Tsymbalyuk N, West GA, Gerzanich V. Newly expressed SUR1-regulated NCCa-ATP channel mediates cerebral edema after ischemic stroke. Nat Med 2006;12(4):433-440.

134. Rosenberg GA. Ischemic brain edema. Prog Cardiovasc Dis 1999;42(3):209-216.

135. Ayata C, Ropper AH. Ischaemic brain oedema. J Clin Neurosci 2002;9(2):113-124.

136. Klatzo I. Neuropathological Aspects of Brain Edema. J Neuropath Exp Neur 1967;26(1):1-&.

137. Neumar RW. Molecular mechanisms of ischemic neuronal injury. Ann Emerg Med 2000;36(5):483-506.

138. Stys PK. White matter injury mechanisms. Curr Mol Med 2004;4(2):113-130.

139. O'Donnell ME, Tran L, Lam TI, Liu XB, Anderson SE. Bumetanide inhibition of the blood-brain barrier Na-L-Cl cotransporter reduces edema formation in the rat middle cerebral artery occlusion model of stroke. J Cerebr Blood F Met 2004;24(9):1046-1056.

140. Betz AL. Alterations in cerebral endothelial cell function in ischemia. Cellular and Molecular Mechanisms of Ischemic Brain Damage 1996;71:301-313.

141. Oppenheim AV. Discrete Time Processing. Upper Saddle River, New Jersey: Prentice-Hall; 1999.

142. Bose T. Digital Signal and Image Processing; 2004.

143. Lathi BP. Linear Systems and Signals. Carmichael, CA: Berkeley-Cambridge Press.; 1992.

144. Stobbe R, Beaulieu C. A New Approach to 3D Twisted Projection Imaging Using Projections that Twist with 3 Degrees of Freedom. ISMRM Workshop on Non-Caresian MR, Sedona, Arizona, USA 2007.

145. Van der Maarel JRC. Thermal relaxation and coherence dynamics of spin 3/2. I. Static and fluctuating quadrupolar interactions in the multipole basis. Concept Magn Reson A 2003;19A(2):97-116.

146. van der Maarel JRC. Thermal relaxation and coherence dynamics of spin 3/2. II. Strong radio-frequency field. Concept Magn Reson A 2003;19A(2):117-133.

147. Jerschow A. From nuclear structure to the quadrupolar NMR interaction and high-resolution spectroscopy. Prog Nucl Mag Res Sp 2005;46(1):63-78.

148. Friedlander G. Nuclear and Radiochemistry; 1966.

149. Krane K. Nuclear Physics; 1987.

150. Rose ME. Elementary Theory of Angular Momentum. New York: John Wiley & Sons; 1957.

151. Serway. Modern Physics. Toronto: Nelson Thomson Learning; 1997.

152. Allen P. 675 Class Notes. 2004.

153. Slichter C. Principles of Magnetic Resonance. New York: Springer-Verlag; 1963.

154. Ernst RR. Principles of Nuclear Magnetic Resonance in One and Two Dimensions. New York: Oxford Press; 1987.

155. Thompson RI. The Tools of Quantum Mechanics. Quantum Mechanics Class Notes (Physics 443 - Calgary); 2002.

156. Blum K. Density Matrix Theory and Applications. New York: Plenum Press; 1981.

157. Abragam A. Principles of Nuclear Magnetism. New York: Oxford University Press; 1961.

158. Sternheimer RM. Shielding and Antishielding Effects for Various Ions and Atomic Systems. Phys Rev 1966;146(1):140-&.

159. Pyykko P. Year-2008 nuclear quadrupole moments. Mol Phys 2008;106(16-18):1965-1974.

160. Rooney WD, Springer CS. A Comprehensive Approach to the Analysis and Interpretation of the Resonances of Spins 3/2 from Living Systems. NMR Biomed 1991;4(5):209-226.

161. Springer CS. Biological Systems: Spin 3/2 Nuclei. The Encyclopedia of Nuclear Magnetic Resonance 1996:940-951.

162. Harris R. Nuclear Magnetic Resonance Spectroscopy. Toronto, Canada: Pitman Publishing; 1983.

163. Berendsen, Edzes HT. Observation and General Interpretation of Sodium Magnetic-Resonance in Biological-Material. Ann Ny Acad Sci 1973;204(MAR30):459-485.

164. Stobbe R, Beaulieu C. Sodium 'Invisibility' in Signal Quantum Sodium Imaging of the Human Brain at High Field. Proceedings of the 16th Annual Meeting of ISMRM, Honolulu, Hawaii, USA 2009.

165. Sanctuary BC. Multipole Nmr .3. Multiplet Spin Theory. Mol Phys 1983;48(6):1155-1176.

166. Edmonds AR. Angular Momentum in Quantum Mechanics. New Jersey: Princeton University Press; 1957.

167. Bowden GJ, Hutchison WD. Tensor Operator-Formalism for Multiple-Quantum Nmr .1. Spin-1 Nuclei. J Magn Reson 1986;67(3):403-414.

168. Muller N, Bodenhausen G, Ernst RR. Relaxation-Induced Violations of Coherence Transfer Selection-Rules in Nuclear-Magnetic-Resonance. J Magn Reson 1987;75(2):297-334.

169. Bowden GJ, Hutchison WD, Khachan J. Tensor Operator-Formalism for Multiple-Quantum Nmr .2. Spins-3/2,Spin-2, and Spin-5/2 and General-I. J Magn Reson 1986;67(3):415-437.

170. Philp DJ, Kuchel PW. A way of visualizing NMR experiments on quadrupolar nuclei. Concept Magn Reson A 2005;25A(1):40-52.

171. Halstead TK, Osment PA, Sanctuary BC. Multipole Nmr .9. Polar Graphical Representation of Nuclear-Spin Polarizations. J Magn Reson 1984;60(3):382-396.

172. van der Maarel JRC, Jesse W, Hancu I, Woessner DE. Dynamics of spin I=3/2 under spin-locking conditions in an ordered environment. J Magn Reson 2001;151(2):298-313.

173. van der Maarel JRC, Woessner DE, Merritt ME. Extremely slow counterion dynamics in xanthan liquid crystal through Na-23 and N-14 NMR. J Phys Chem B 2002;106(15):3864-3871.

174. Vandermaarel JRC. The Relaxation Dynamics of Spin L=1 Nuclei with a Static Quadrupolar Coupling and a Radiofrequency Field. J Chem Phys 1993;99(8):5646-5653.

175. Vandermaarel JRC. Relaxation of Spin S=3/2 in the Doubly Rotating Tilted Frame. J Chem Phys 1989;91(3):1446-1450.

176. Vandermaarel JRC. Relaxation of Spin 3/2 in a Nonzero Average Electric-Field Gradient. Chem Phys Lett 1989;155(3):288-296.

177. KempHarper R, Brown SP, Hughes CE, Styles P, Wimperis S. Na-23 NMR methods for selective observation of sodium ions in ordered environments. Prog Nucl Mag Res Sp 1997;30:157-181.

178. Eliav U, Shinar H, Navon G. The Formation of a 2nd-Rank Tensor in Na-23 Double-Quantum-Filtered Nmr as an Indicator for Order in a Biological Tissue. J Magn Reson 1992;98(1):223-229.

179. Navon G, Shinar H, Eliav U, Seo Y. Multiquantum filters and order in tissues. NMR Biomed 2001;14(2):112-132.

180. Campolieti G, Sanctuary BC, Cole HBR. Multipole Theory of Soft Pulses in Nmr of Quadrupolar Solids. J Magn Reson 1990;88(3):457-472.

181. Pandey L, Towta S, Hughes DG. Nmr Pulse Response and Measurement of the Quadrupole Coupling-Constant of 1=3/2 Nuclei. J Chem Phys 1986;85(12):6923-6927.

182. Mclachlan AD. Line Widths of Electron Resonance Spectra in Solution. Proc R Soc Lon Ser-A 1964;280(138):271-&.

183. Lurcat F, Debroglie L. Sur La Relation Entre Les Temps De Relaxation Et Les Probabilites De Transition En Resonance Nucleaire (Magnetique Et Quadrupolaire) .2. Cr Hebd Acad Sci 1955;240(26):2517-2518.

184. Hubbard PS. Nonexponential Nuclear Magnetic Relaxation by Quadrupole Interactions. J Chem Phys 1970;53(3):985-&.

185. Engstrom S, Jonsson B, Jonsson B. A Molecular Approach to Quadrupole Relaxation - Monte-Carlo Simulations of Dilute Li+, Na+, and Cl- Aqueous-Solutions. J Magn Reson 1982;50(1):1-20.

186. Engstrom S, Jonsson B, Impey RW. Molecular Dynamic Simulation of Quadrupole Relaxation of Atomic Ions in Aqueous-Solution. J Chem Phys 1984;80(11):5481-5486.

187. Eliav U, Baram A, Navon G. Nuclear Magnetic-Resonance Line-Shapes of Exchanging Spin 3/2 Nuclei. J Chem Phys 1988;89(9):5584-5588.

188. Mocci F, Laaksonen A, Lyubartsev A, Saba G. Molecular dynamics investigation of Na-23 NMR relaxation in oligomeric DNA aqueous solution. J Phys Chem B 2004;108(41):16295-16302.

189. Denisov VP, Halle B. Sequence-specific binding of counterions to B-DNA. P Natl Acad Sci USA 2000;97(2):629-633.

190. Young MA, Jayaram B, Beveridge DL. Intrusion of counterions into the spine of hydration in the minor groove of B-DNA: Fractional occupancy of electronegative pockets. J Am Chem Soc 1997;119(1):59-69.

191. Shui XQ, McFail-Isom L, Hu GG, Williams LD. The B-DNA dodecamer at high resolution reveals a spine of water on sodium. Biochemistry-Us 1998;37(23):8341-8355.

192. Dong Q, Stellwagen E, Stellwagen NC. Monovalent Cat-ion Binding in the Minor Groove of DNA A-Tracts. Biochemistry-Us 2009;48(5):1047-1055.

193. Page MJ, Di Cera E. Role of Na+ and K+ in enzyme function. Physiol Rev 2006;86(4):1049-1092.

194. Di Cera E. A structural perspective on enzymes activated by monovalent cations. J Biol Chem 2006;281(3):1305-1308.

195. Nayal M, DiCera E. Valence screening of water in protein crystals reveals potential Na+ binding sites. J Mol Biol 1996;256(2):228-234.

196. Reuben J, Shporer M, Gabbay EJ. Alkali Ion DNA Interaction as Reflected in Nuclear-Relaxation Rates of Na-23 and Rb-87. P Natl Acad Sci USA 1975;72(1):245-247.

197. James TL, Noggle JH. Sodium-23 Nuclear Magnetic Resonance Studies of Sodium Aminocarboxylic Acid Complexes. J Am Chem Soc 1969;91(13):3424-&.

198. Bleam ML, Anderson CF, Record MT. Na-23 Nuclear Magnetic-Resonance Studies of Cation Deoxyribonucleic-Acid Interactions. Biochemistry-Us 1983;22(23):5418-5425.

199. Torres AM, Philp DJ, Kemp-Harper R, Garvey C, Kuchel PW. Determination of Na+ binding parameters by relaxation analysis of selected Na-23 NMR coherences: RNA, BSA and SDS. Magn Reson Chem 2005;43(3):217-224.

200. Chen SWW, Rossky PJ. Influence of Solvent and Counterion on Na-23+ Spin Relaxation in Aqueous-Solution. J Phys Chem-Us 1993;97(41):10803-10812.

201. Whitfield DM, Stojkovski S, Sarkar B. Metal Coordination to Carbohydrates - Structures and Function. Coordin Chem Rev 1993;122(1-2):171-225.

202. Lerner L, Torchia DA. A Multinuclear Nmr-Study of the Interactions of Cations with Proteoglycans, Heparin, and Ficoll. J Biol Chem 1986;261(27):2706-2714.

203. Wennerstrom H, Lindblom G, Lindman B. Theoretical Aspects on Nmr of Quadrupolar Ionic Nuclei in Micellar Solutions and Amphiphilic Liquid-Crystals. Chem Scripta 1974;6(3):97-103.

204. Halle B. Theory of Intramolecular Spin Relaxation by Translational Diffusion in Locally Ordered Fluids .1. Continuum Diffusion Versus Discrete-State Exchange in Systems with Planar Interfaces. Mol Phys 1984;53(6):1427-1461.

205. Reddy MR, Rossky PJ, Murthy CS. Counterion Spin Relaxation in DNA Solutions - a Stochastic Dynamics Simulation Study. J Phys Chem-Us 1987;91(19):4923-4933.

206. Halle B, Wennerstrom H, Piculell L. Interpretation of Counterion Spin Relaxation in Poly-Electrolyte Solutions. J Phys Chem-Us 1984;88(12):2482-2494.

207. Linse P, Halle B. Counterion Nmr in Heterogeneous Aqueous Systems - a Molecular-Dynamics Simulation Study of the Electric-Field Gradient. Mol Phys 1989;67(3):537-573.

208. Forester TR. A Molecular-Dynamics Study of Electric-Field Gradients in Condensed B-DNA Systems. Mol Phys 1991;73(6):1335-1347.

209. Woessner DE. NMR relaxation of spin-(3)/(2) nuclei: Effects of structure, order, and dynamics in aqueous heterogeneous systems. Concept Magnetic Res 2001;13(5):294-325.

210. Rooney WD, Springer CS. The Molecular Environment of Intracellular Sodium - Na-23 Nmr Relaxation. NMR Biomed 1991;4(5):227-245.

211. Jayaram B, Beveridge DL. Modeling DNA in aqueous solutions: Theoretical and computer simulation studies on the ion atmosphere of DNA. Annu Rev Bioph Biom 1996;25:367-394.

212. Grieve SM, Wickstead B, Torres AM, Styles P, Wimperis S, Kuchel PW. Multiple-quantum filtered O-17 and Na-23 NMR analysis of mitochondrial suspensions. Biophys Chem 1998;73(1-2):137-143.

213. Cope FW. Nmr Evidence for Complexing of Na+ in Muscle Kidney and Brain and by Actomyosin . Relation of Cellular Complexing of Na+ to Water Structure and to Transport Kinetics. J Gen Physiol 1967;50(5):1353-&.

214. Cope FW. Spin-Echo Nuclear Magnetic Resonance Evidence for Complexing of Sodium Ions in Muscle, Brain, and Kidney. Biophys J 1970;10(9):843-&.

215. Navon G, Werrmann JG, Maron R, Cohen SM. P-31 Nmr and Triple Quantum Filtered Na-23 Nmr-Studies of the Effects of Inhibition of Na+/H+ Exchange on Intracellular Sodium and Ph in Working and Ischemic Hearts. Magn Reson Med 1994;32(5):556-564.

216. Foy BD, Burstein D. Interstitial Sodium Nuclear-Magnetic-Resonance Relaxation-Times in Perfused Hearts. Biophys J 1990;58(1):127-134.

217. Tauskela JS, Dizon JM, Whang J, Katz J. Evaluation of multiple-quantum-filtered Na-23 NMR in monitoring intracellular Na content in the isolated perfused rat heart in the absence of a chemical-shift reagent. J Magn Reson 1997;127(1):115-127.

218. Cameron IL, Smith NKR, Pool TB, Sparks RL. Intracellular Concentration of Sodium and Other Elements as Related to Mitogenesis and Oncogenesis Invivo. Cancer Res 1980;40(5):1493-1500.

219. Koch KS, Leffert HL. Increased Sodium-Ion Influx Is Necessary to Initiate Rat Hepatocyte Proliferation. Cell 1979;18(1):153-163.

220. Gupta RK, Gupta P. Direct Observation of Resolved Resonances from Intra-Cellular and Extracellular Na-23 Ions in Nmr-Studies of Intact-Cells and Tissues Using Dysprosium(Iii)Tripolyphosphate as Paramagnetic Shift-Reagent. J Magn Reson 1982;47(2):344-350.

221. Sherry AD, Malloy CR, Jeffrey FMH, Cacheris WP, Geraldes CFGC. Dy(Dotp)5- - a New, Stable Na-23 Shift-Reagent. J Magn Reson 1988;76(3):528-533.

222. Buster DC, Castro MMCA, Geraldes CFGC, Malloy CR, Sherry AD, Siemers TC. Tm(Dotp)5--a 23na+ Shift Agent for Perfused Rat Hearts. Magn Reson Med 1990;15(1):25-32.

223. Bansal N, Germann MJ, Seshan V, Shires GT, Malloy CR, Sherry AD. Thulium 1,4,7,10-Tetraazacyclododecane-1,4,7,10-Tetrakis(Methylene Phosphonate) as a Na-23 Shift-Reagent for the Invivo Rat-Liver. Biochemistry-Us 1993;32(21):5638-5643.

224. Bansal N, Germann MJ, Lazar I, Malloy CR, Sherry AD. Invivo Na-23 Mr Imaging and Spectroscopy of Rat-Brain During Tmdotp5- Infusion. Jmri-Journal of Magnetic Resonance Imaging 1992;2(4):385-391.

225. Eleff SM, Mclennan IJ, Hart GK, Maruki Y, Traystman RJ, Koehler RC. Shift-Reagent Enhanced Concurrent Na-23 and H-1 Magnetic-Resonance Spectroscopic Studies of Transcellular Sodium Distribution in the Dog Brain in-Vivo. Magn Reson Med 1993;30(1):11-17.

226. Lyon RC, Pekar J, Moonen CTW, Mclaughlin AC. Double-Quantum Surface-Coil Nmr-Studies of Sodium and Potassium in the Rat-Brain. Magn Reson Med 1991;18(1):80-92.

227. Hrabetova S, Nicholson C. Contribution of dead-space microdomains to tortuosity of brain extracellular space. Neurochem Int 2004;45(4):467-477.

228. Nicholson C. Diffusion and related transport mechanisms in brain tissue. Rep Prog Phys 2001;64(7):815-884.

229. Nicholson C, Sykova E. Extracellular space structure revealed by diffusion analysis. Trends Neurosci 1998;21(5):207-215.

230. Boulanger Y, Vinay P, Desroches M. Measurement of a Wide-Range of Intracellular Sodium Concentrations in Erythrocytes by Na-23 Nuclear Magnetic-Resonance. Biophys J 1985;47(4):553-561.

231. Nissen H, Jacobsen JP, Horder M. Assessment of the Nmr Visibility of Intraerythrocytic Sodium by Flame Photometric and Ion-Competitive Studies. Magn Reson Med 1989;10(3):388-398.

232. Buist RJ, Deslauriers R, Saunders JK, Mainwood GW. Na-23 and Flame Photometric Studies of the Nmr Visibility of Sodium in Rat Muscle. Can J Physiol Pharm 1991;69(11):1663-1669.

233. Furo I, Halle B, Quist PO. A New Method for Selective Detection of Invisible Quadrupolar Satellites in Heterogeneous Systems. J Magn Reson Ser B 1993;102(1):84-90.

234. Boada FE, Christensen JD, Huanghellinger FR, Reese TG, Thulborn KR. Quantitative in-Vivo Tissue Sodium Concentration Maps - the Effects of Biexponential Relaxation. Magn Reson Med 1994;32(2):219-223.

235. Christensen JD, Barrere BJ, Boada FE, Vevea JM, Thulborn KR. Quantitative tissue sodium concentration mapping of normal rat brain. Magn Reson Med 1996;36(1):83-89.

236. Joseph PM, Summers RM. The Flip-Angle Effect - a Method for Detection of Na-23 Quadrupole Splitting in Tissue. Magn Reson Med 1987;4(1):67-77.

237. Pekar J, Leigh JS. Detection of Biexponential Relaxation in Na-23 Facilitated by Double-Quantum Filtering. J Magn Reson 1986;69(3):582-584.

238. Kempharper R, Wimperis S. Detection of the Interaction of Sodium-Ions with Ordered Structures in Biological-Systems - Use of the Jeener-Broekaert Experiment. J Magn Reson Ser B 1993;102(3):326-331.

239. Eliav U, Navon G. Analysis of Double-Quantum-Filtered Nmr-Spectra of Na-23 in Biological Tissues. J Magn Reson Ser B 1994;103(1):19-29.

240. Kemp-Harper R, Wickstead B, Wimperis S. Sodium ions in ordered environments in biological systems: Analysis of Na-23 NMR spectra. J Magn Reson 1999;140(2):351-362.

241. Reddy R, Li SC, Noyszewski EA, Kneeland JB, Leigh JS. In vivo sodium multiple quantum spectroscopy of human articular cartilage. Magn Reson Med 1997;38(2):207-214.

242. Shinar H, Knubovets T, Eliav U, Navon G. Sodium Interaction with Ordered Structures in Mammalian Red-Blood-Cells Detected by Na-23 Double Quantum Nmr. Biophys J 1993;64(4):1273-1279.

243. Tauskela JS, Shoubridge EA. Response of the Na-23-Nmr Double-Quantum Filtered Signal to Changes in Na+ Ion Concentration in Model Biological Solutions and Human Erythrocytes. Biochim Biophys Acta 1993;1158(2):155-165.

244. Knubovets T, Shinar H, Eliav U, Navon G. A Na-23 multiple-quantum-filtered NMR study of the effect of the cytoskeleton conformation on the anisotropic motion of sodium ions in red blood cells. J Magn Reson Ser B 1996;110(1):16-25.

245. Reddy R, Bolinger L, Shinnar M, Noyszewski E, Leigh JS. Detection of Residual Quadrupolar Interaction in Human Skeletal-Muscle and Brain in-Vivo Via Multiple-Quantum Filtered Sodium Nmr-Spectra. Magn Reson Med 1995;33(1):134-139.

246. Shporer M, Civan MM. Nuclear Magnetic-Resonance of Sodium-23 Linoleate-Water - Basis for an Alternative Interpretation of Sodium-23 Spectra within Cells. Biophys J 1972;12(1):114-&.

247. Pandey L, Hughes DG. Rf Pulse Response of a System of I=3/2 Nuclei in the Presence of Quadrupole Splitting. J Mol Struct 1983;111(DEC):91-96.

248. Schmidt VH. Pulsed Magnetic and Optical Resonance. In: Blinc R, editor; 1971; University of Ljubljana, Yugoslavia. p 75-83.

249. Stobbe R, Beaulieu C. Sodium MRI of the Human Brain Using Projection Acquisition in the Steady-State with Coherent Magnetization (Na-PACMAN). Proceedings of the 15th Annual Meeting of ISMRM, Toronto, Ontario, Canada 2008.

250. Brooker HR, Mareci TH, Mao JT. Selective Fourier-Transform Localization. Magn Reson Med 1987;5(5):417-433.

251. Parker DL, Gullberg GT, Frederick PR. Gibbs Artifact Removal in Magnetic-Resonance-Imaging. Med Phys 1987;14(4):640-645.

252. Jensen JE, Drost DJ, Menon RS, Williamson PC. In vivo brain P-31-MRS: measuring the phospholipid resonances at 4 Tesla from small voxels. NMR Biomed 2002;15(5):338-347.

253. Hugg JW, Maudsley AA, Weiner MW, Matson GB. Comparison of k-space sampling schemes for multidimensional MR spectroscopic imaging. Magn Reson Med 1996;36(3):469-473.

254. Sarkar S, Heberlein K, Hu XP. Truncation artifact reduction in spectroscopic imaging using a dual-density spiral k-space trajectory. Magn Reson Imaging 2002;20(10):743-757.

255. Pohmann R, von Kienlin M. Accurate phosphorus metabolite images of the human heart by 3D acquisition-weighted CSI. Magn Reson Med 2001;45(5):817-826.

256. Greiser A, von Kienlin M. Efficient k-space sampling by density-weighted phase-encoding. Magn Reson Med 2003;50(6):1266-1275.

257. Star-Lack JM. Optimal gradient waveform design for projection imaging and projection reconstruction echoplanar spectroscopic imaging. Magn Reson Med 1999;41(4):664-675.

258. Greiser A, Haase A, von Kienlin M. Improved cardiac sodium MR imaging by density-weighted phase-encoding. J Magn Reson Imag 2005;21(1):78-81.

259. Neuberger T, Greiser A, Nahrendorf M, Jakob PM, Faber C, Webb AG. Na-23 microscopy of the mouse heart in vivo using density-weighted chemical shift imaging. Magn Reson Mater Phy 2004;17(3-6):196-200.

260. Pipe JG, Menon P. Sampling density compensation in MRI: Rationale and an iterative numerical solution. Magn Reson Med 1999;41(1):179-186.

261. Beatty PJ, Nishimura DG, Pauly JM. Rapid gridding reconstruction with a minimal oversampling ratio. Ieee T Med Imaging 2005;24(6):799-808.

262. Pipe JG. Reconstructing MR images from undersampled data: Data-weighting considerations. Magn Reson Med 2000;43(6):867-875.

263. Gurney PT, Hargreaves BA, Nishimura DG. Design and analysis of a practical 3D cones trajectory. Magn Reson Med 2006;55(3):575-582.

264. Rahmer J, Bornert P, Groen J, Bos C. Three-dimensional radial ultrashort echo-time imaging with T-2 adapted sampling. Magn Reson Med 2006;55(5):1075-1082.

265. Hilal SK, Maudsley AA, Simon HE, Perman WH, Bonn J, Mawad ME, Silver AJ, Ganti SR, Sane P, Chien IC. Invivo Nmr Imaging of Tissue Sodium in the Intact Cat before and after Acute Cerebral Stroke. Am J Neuroradiol 1983;4(3):245-249.

266. Pabst T, Sandstede J, Beer M, Kenn W, Greiser A, von Kienlin M, Neubauer S, Hahn D. Optimization of ECG-triggered 3D Na-23 MRI of the human heart. Magn Reson Med 2001;45(1):164-166.

267. Maril N, Rosen Y, Reynolds GH, Ivanishev A, Ngo L, Lenkinski RE. Sodium MRI of the human kidney at 3 tesla. Magn Reson Med 2006;56(6):1229-1234.

268. Steidle G, Graf H, Schick F. Sodium 3-D MRI of the human torso using a volume coil. Magn Reson Imaging 2004;22(2):171-180.

269. Insko EK, Clayton DB, Elliott MA. In vivo sodium MR imaging of the intervertebral disk at 4 T. Acad Radiol 2002;9(7):800-804.

270. Constantinides CD, Gillen JS, Boada FE, Pomper MG, Bottomley PA. Human skeletal muscle: Sodium MR imaging and quantification-potential applications in exercise and disease. Radiology 2000;216(2):559-568.

271. Damen F, Holdsworth S, Atkinson I, Boskamp E, Claiborne T, Nauerth A, Li B, Zhou XJ, Liang ZP, Thulborn KR. Initial Experience with Sodium MRI of Phantoms and Human Brain at 9.4 Tesla. Proceedings of the 14th Annual Meeting of ISMRM, Seattle, Washington, USA 2006:3103.

272. Liu H, Snyder C, Vaughan JT, Ugurbil K. A practical sodium imaging method at 7T. Proceedings of the 13th Annual Meeting of ISMRM, Miami, Florida, USA 2005:1253.

273. Zaremba LA. Criteria for Significant Risk Investigations of Magnetic Resonance Diagnostic Devices. U.S. Department of Health and Human Services Food and Drug Administration Center for Devices and Radiological Health; 2003.

274. Babsky AM, Hekmatyar SK, Zhang H, Solomon JL, Bansal N. Predicting and monitoring response to chemotherapy by 1,3-bis(2-chloroethyl)-1-nitrosourea in subcutaneously implanted 9L glioma using the apparent diffusion coefficient of water and Na-23 MRI. J Magn Reson Imag 2006;24(1):132-139.

275. Pekar J, Renshaw PF, Leigh JS. Selective Detection of Intracellular Sodium by Coherence-Transfer Nmr. J Magn Reson 1987;72(1):159-161.

276. Wintermark M, Albers GW, Alexandrov AV, Alger JR, Bammer R, Baron JC, Davis S, Demaerschalk BM, Derdeyn CP, Donnan GA, Eastwood JD, Fiebach JB, Fisher M, Furie KL, Goldmakher GV, Hacke W, Kidwell CS, Kloska SP, Kohrmann M, Koroshetz W, Lee TY, Lees KR, Lev MH, Liebeskind DS, Ostergaard L, Powers WJ, Provenzale J,

Schellinger P, Silbergleit R, Sorensen AG, Wardlaw J, Warach S. Acute stroke imaging research roadmap. Stroke 2008;39(5):1621-1628.

277. Kohrmann M, Juttler E, Fiebach JB, Huttner HB, Siebert S, Schwark C, Ringleb PA, Schellinger PD, Hacke W. MRI versus CT-based thrombolysis treatment within and beyond the 3 h time window after stroke onset: a cohort study. Lancet Neurol 2006;5(8):661-667.

278. Schlaug G, Siewert B, Benfield A, Edelman RR, Warach S. Time course of the apparent diffusion coefficient (ADC) abnormality in human stroke. Neurology 1997;49(1):113-119.

279. Moseley M. In vivo sodium-23 magnetic resonance surface coil imaging: observing experimental cerebral ischemia in the rat. Magn Reson Imaging 1985;3:383-387.

280. Ra JB, Hilal SK, Cho ZH. A method for in vivo MR imaging of the short T2 component of sodium-23. Magn Reson Med 1986;3(2):296-302.

281. Hilal SK, Maudsley AA, Ra JB, Simon HE, Roschmann P, Wittekoek S, Cho ZH, Mun SK. In vivo NMR imaging of sodium-23 in the human head. J Comput Assist Tomogr 1985;9(1):1-7.

282. Ginsberg MD, Palesch YY, Hill MD. The ALIAS (ALbumin In Acute Stroke) Phase III randomized multicentre clinical trial: design and progress report. Biochemical Society transactions 2006;34(Pt 6):1323-1326.

283. Ratkowsky DA. Handbook of Nonlinear Regression Models. New York: Marcel Dekker, inc.; 1990.

284. Kline RP, Wu EX, Petrylak DP, Szabolcs M, Alderson PO, Weisfeldt ML, Cannon P, Katz J. Rapid in vivo monitoring of chemotherapeutic response using weighted sodium magnetic resonance imaging. Clin Cancer Res 2000;6(6):2146-2156.

285. Patt SL, Sykes BD. Water Eliminated Fourier-Transform Nmr-Spectroscopy. J Chem Phys 1972;56(6):3182-&.

286. Allis JL, Seymour AML, Radda GK. Absolute Quantification of Intracellular Na+ Using Triple-Quantum-Filtered Na-23 Nmr. J Magn Reson 1991;93(1):71-76.

287. Navon G. Complete Elimination of the Extracellular Na-23 Nmr Signal in Triple Quantum Filtered Spectra of Rat Hearts in the Presence of Shift-Reagents. Magn Reson Med 1993;30(4):503-506.

288. Stobbe R, Beaulieu C. 'High Resolution' Sodium Imaging Using Sampling Density Weigted Oblate-Spheroidal 3D Twisted Projection Imaging. ISMRM Workshop on Non-Caresian MR, Sedona, Arizona, USA 2007.

289. Tsang A, Stobbe R, Beaulieu C. Triple-Quantum-Filtered Sodium MRI of the Human Brain at 4.7T. Proceedings of the 16th Annual Meeting of ISMRM, Honolulu, Hawaii, USA 2009.

290. Bortner CD, Cidlowski JA. Uncoupling cell shrinkage from apoptosis reveals that Na+ influx is required for volume loss during programmed cell death. J Biol Chem 2003;278(40):39176-39184.

291. Albers G, Thijs V, Wechsler L, Kemp S, Schlaug G, Skalabrin E, Bammer R, Lansberg M, Shuaib A, Coplin W, Kakuda W, Moseley M, Marks M. Diffusion weighted imaging evaluation for understanding stroke evolution: The DEFUSE study. Neurology 2006;66(5):315-316.

292. Tanne D. Imaging blood-brain barrier disruption: an evolving tool for assessing the risk of hemorrhage after thrombolysis. Nat Clin Pract Neuro 2008;4(12):644-645.

293. Tanne D, Kasner SE, Demchuk AM, Koren-Morag N, Hanson S, Grond M, Levine SR, Survey Mr-PAS. Markers of increased risk of intracerebral hemorrhage after intravenous recombinant tissue plasminogen activator therapy for acute ischemic stroke in clinical practice The multicenter rt-PA acute stroke survey. Circulation 2002;105(14):1679-1685.

294. Dzialowski I, Hill MD, Coutts SB, Demchuk AM, Kent DM, Wunderlich O, von Kummer R. Extent of early ischemic changes on computed tomography (CT) before thrombolysis - Prognostic value of the Alberta Stroke Program Early CT Score in ECASS II. Stroke 2006;37(4):973-978.

295. Singer OC, Humpich MC, Fiehler J, Albers GW, Lansberg MG, Kastrup A, Rovira A, Liebeskind DS, Gass A, Rosso C, Derex L, Kim JS, Neumann-Haefelin T, Invest MSSG. Risk for symptomatic intracerebral hemorrhage after thrombolysis assessed by diffusion-weighted magnetic resonance imaging. Ann Neurol 2008;63(1):52-60.

296. Lansberg MG, Thijs VN, Bammer R, Kemp S, Wijman CAC, Marks MP, Albers GW, Investigators D. Risk factors of symptomatic intracerebral hemorrhage after tPA therapy for acute stroke. Stroke 2007;38(8):2275-2278.

297. Singer OC, Kurre W, Humpich MC, Lorenz MW, Kastrup A, Liebeskind DS, Thomalla G, Fiehler J, Berkefeld J, Neumann-Haefelin T, Investigators SSG. Risk Assessment of Symptomatic Intracerebral Hemorrhage After Thrombolysis Using DWI-ASPECTS. Stroke 2009;40(8):2743-2748.

298. Neumann-Haefelin T, Hoelig S, Berkefeld J, Fiehler J, Gass A, Humpich M, Kastrup A, Kucinski T, Lecei O, Liebeskind DS, Rother J, Rosso C, Samson Y, Saver JL, Yan B, Grp MS. Leukoaraiosis is a risk factor for symptomatic intracerebral hemorrhage after thrombolysis for acute stroke. Stroke 2006;37(10):2463-2466.

299. del Zoppo GJ, Von Kummer R, Hamann GF. Ischaemic damage of brain microvessels: inherent risks for thrombolytic treatment in stroke. J Neurol Neurosur Ps 1998;65(1):1-9.

300. Latour LL, Kang DW, Ezzeddine MA, Chalela JA, Warach S. Early blood-brain barrier disruption in human focal brain ischemia. Ann Neurol 2004;56(4):468-477.

301. Warach S, Latour LL. Evidence of reperfusion injury, exacerbated by thrombolytic therapy, in human focal brain ischemia using a novel imaging marker of early blood-brain barrier disruption. Stroke 2004;35(11):2659-2661.

302. Bang OY, Buck BH, Saver JL, Alger JR, Yoon SR, Starkman S, Ovbiagele B, Kim D, Ali LK, Sanossian N, Jahan R, Duckwiler GR, Vinuela F, Salamon N, Villablanca JP, Liebeskind DS. Prediction of hemorrhagic transformation after recanalization therapy using T2*- Permeability magnetic resonance imaging. Ann Neurol 2007;62(2):170-176.

303. Aubert A, Costalat R. A model of the coupling between brain electrical activity, metabolism, and hemodynamics: Application to the interpretation of functional neuroimaging. Neuroimage 2002;17(3):1162-1181.

304. Paxinos G, Jurgen, K.M. The Human Nervous System. San Diego, California: Elsevier Academic Press; 2004.

305. Le Bihan D, Urayama S, Aso T, Hanakawa T, Fukuyama H. Direct and fast detection of neuronal activation in the human brain with diffusion MRI. P Natl Acad Sci USA 2006;103(21):8263-8268.

306. Elmallakh RS, Wyatt RJ. The Na,K-Atpase Hypothesis for Bipolar Illness. Biol Psychiat 1995;37(4):235-244.

307. Hamid H, Gao YL, Lei ZM, Hougland MT, El-Mallakh RS. Effect of ouabain on sodium pump alpha-isoform expression in an animal model of mania. Prog Neuro-Psychoph 2009;33(7):1103-1106.

308. Huang X, Lei ZM, El-Mallakh RS. Lithium normalizes elevated intracellular sodium. Bipolar Disord 2007;9(3):298-300.

309. El-Mallakh RS. Ion homeostasis and the mechanism of action of lithium. Clin Neurosci Res 2004;4(3-4):227-231.

310. Boada FE, Gillen JS, Noll DC, Shen GX, Thulborn KR. Data acquisition and postprocessing strategies for fast quantitative sodium imaging. Int J Imag Syst Tech 1997;8(6):544-550.

311. Jackson JI, Meyer CH, Nishimura DG, Macovski A. Selection of a Convolution Function for Fourier Inversion Using Gridding. Ieee T Med Imaging 1991;10(3):473-478.

312. Osullivan JD. A Fast Sinc Function Gridding Algorithm for Fourier Inversion in Computer-Tomography. Ieee T Med Imaging 1985;4(4):200-207.

313. Frankel S. Reactance Networks for Coupling Between Unbalanced and Balanced Circuits. Proceedings of the IRE 1941:486-493.